Ring Current Ion Populations during Geomagnetically Disturbed Periods

David Robert Forster
Institute of Mathematics and Physics
Aberystwyth University

Supervised By:
Prof. Manuel Grande
and
Dr. Balázs Pintér

Thesis submitted for the degree of Doctor of Philosophy at
Aberystwyth University

22nd September, 2011

Abstract

Charge exchange is investigated as a source of magnetospheric He^+. Ionic data from the Magnetospheric Ion Composition Spectrometer (MICS) on the Combined Release and Radiation Effects Satellite (CRRES) are investigated during storm and quiet periods. A He^+/He^{++} maximum is observed at Ring Current altitudes, where particle trapping is relatively stable. A study of ionic number density across the main and recovery phases of geomagnetic storms provides evidence of a recovery phase source of He^+ that does not include the other species. It is suggested that charge exchange of trapped He^{++} ions with exospheric neutral hydrogen is the source of this He^+.

Cross sections are obtained for the $He^{++} \rightarrow He^+$ charge exchange reaction. A new population of He^+ ions is observed within the drift echo of an injection which occurred during orbit 497 of CRRES, at E/q values not present in the injection. The possibility of this new He^+ population having arisen due to charge exchange is discussed, and charge exchange cross sections are calculated for the reaction. The cross sections calculated for these data are larger than those found by previous work, and it is concluded that the observed effect cannot be explained entirely by charge exchange.

Solar wind precursors to pseudobreakups are compared to those of substorms. [Tsurutani et al., 2003] gave examples of stormtime periods which did not contain substorm expansion phases. These are investigated for evidence of electron injections at geosynchronous altitude. It is shown that injections did occur during these periods, though generally at lower energy than those with expansions. The injections are attributed to pseudobreakup activity rather than full substorms. Solar wind parameters are compared to injection energy for storms with expansions and without. It is shown that the occurrence of expansions is associated with spikes in solar wind density, though a time lag of up to 20 minutes is required. This is explained in relation to the pressure catastrophe ([Erickson and Wolf, 1980]), whereby some time is required for magnetospheric convection.

Declaration

This work has not previously been accepted in substance for any degree and is not being concurrently submitted in candidature for any degree.

Signed ..... (candidate)

Date ..... 21st February, 2012 .....

STATEMENT 1

This thesis is the result of my own investigations, except where otherwise stated. Where correction services have been used, the extent and nature of the correction is clearly marked in a footnote(s).

Other sources are acknowledged by footnotes giving explicit references.
A bibliography is appended.

Signed ..... (candidate)

Date ..... 21st February, 2012 .....

STATEMENT 2

I hereby give consent for my thesis, if accepted, to be available for photocopying and for inter-library loan, and for the title and summary to be made available to outside organisations.

Signed ..... (candidate)

Date ..... 21st February 2012 .....

Acknowledgements

This PhD was funded by the Science and Technology Facilities Council (STFC).

I would like to thank my supervisors, Prof. Manuel Grande and Dr. Balázs Pintér, for their support and guidance during my PhD. I would also like to thank all of the staff at the Institute of Maths and Physics, Aberystwyth University for their support.

I give my thanks to my fellow PhD students for their company and assistance; Jimmy Carter, Ian Whittaker, Gemma Guymer, Thomas Knight, Claire Q, Alex Leatherland, Martin Vickers and Gareth Dorrian. Special thanks go to Jimmy Carter for his culling of the excess commas in my Thesis.

I would like to thank my family for their support throughout my PhD; Mrs. Elaine Forster, Dr. Graeme Forster, Mr. Arthur Davies and Miss Heather Roberts.

Finally, my thanks go to people who have shown great kindness towards me during my PhD, and have gone out of their way in helping me to complete it; Mrs. Pippa Knight and family, Dr. Richard Evans, Dr. Amy Staniforth, Megan and Rupert.

Contents

Abstract 1
Declaration 2
Acknowledgements 3
Contents 4
List of Figures 9

1 Magnetospheric Processes and Ionic Populations 15

1.1 The Radiation Belts…… 15
1.2 Trapping and Adiabatic Invariants…… 16
1.2.1 The First Invariant…… 16
1.2.2 The Second Invariant…… 16
1.2.2.1 Pitch Angle and the Loss Cone…… 17
1.2.3 The Third Invariant…… 18
1.2.3.1 Gradient-Curvature Drift…… 18
1.3 Sources of the Radiation Belt…… 19
1.3.1 Charge Exchange as both a Source and Loss Process…
…… 20
1.4 Geomagnetic Storms and Substorms…… 22
1.4.1 Substorms and the Pressure Catastrophe…… 22
1.4.2 Pseudobreakups…… 25
1.4.3 Dispersionless Substorm Injections…… 26
1.5 D_{ST} and the Ring Current…… 27
1.6 Current Interest in Magnetospheric Physics…… 27
1.6.1 Models of the Substorm…… 27
1.6.2 High Energy Electrons and Solar Wind Velocity…… 30
1.7 The Work Presented in this Thesis…… 30

2 Missions and Instrumentation 32

2.1 The CRRES Satellite: Mission and Orbit…… 32
2.2 The CRRES MICS Instrument……... 33
2.3 Previous Studies Using CRRES MICS Data……... 35
2.4 Overview of the LANL Satellites…… 36
2.5 Overview of the THEMIS Mission…… 38

3 The Origin of Magnetospheric Singly Charged Helium 40

3.1 The Origin of Magnetospheric Ions…….. 40
3.2: The Ring Current in Invariant Latitude……... 40
3.2.1 Ion Populations in Invariant Latitude…… 40
3.2.2 CRRES Electron Plots…… 43
3.2.3 He^{+}/He^{++} Maximum in the Outer Belt……..…. 46
3.2.4 CRRES Charge Parameter Plots…….. 48
3.3 Stormtime Dynamics of the Charge Parameter Maximum……... 53
3.3.1 CRRES Helium Ratio vs. D_{ST}……. 53
3.3.2 Charge Parameter vs. L and D_{ST}……... 54
3.4 Charge Exchange in CRRES Injections and Drift Echoes…… 56
3.5 Average Helium Ratio with MLT between L of 4 and 5 R_E…… 57
3.6 The Shift in Number Density after a Single CRRES Orbit……..… 59
3.6.1 Introduction to the Investigation……..59
3.6.2 Shifts in Number Density and What They May Mean…. 60
3.6.3 Example Orbits for Different Storm Phases……..63
3.6.4 Number Density Shifts for Storm and Quiet Time……66
3.6.5 Number Density Shifts across Different Storm Phases.. 69
3.6.5.1 Locating Main Phases in the Data……. 69
3.7 Chapter Summary…… 73

4 Calculating Charge Exchange Cross Sections Using Injections and Drift Echoes 75

4.1 Introduction: Injections, Drift Echoes and Charge Exchange…... 75
4.1.1 A Feasibility Study for Charge Exchange of Trapped Ions ……... 75
4.2 The Method of Calculation……..78
4.2.1 Charge Exchange Cross Sections……....78
4.2.2 Dispersionless Injections and Drift Echoes: Orbit 497… 80
4.2.3 The Other Injections Included in the Investigation…….. 82
4.2.4 The Drift Period…… 83
4.2.5 N_H and Altitude across a Drift Path…… 85
4.2.5.1 The Altitude of a Bouncing Ion…… 87
4.2.6 How Charge Exchange Would Appear in a CRRES Spectrogram…….. 89
4.2.6.1 The Location of Charge Exchanged He^+ on a CRRES Spectrogram…… 93
4.2.7 Accounting for E/q Range Spreading……....94
4.2.7.1 Relative He++ to He+ Input for E/q bin 15: 200-240 keV……94
4.2.7.2 Relative Input Equations for the Other Energy Bins…….. 95
4.2.8 The Energy of a Charge Exchange Reaction: Quantum Effects……95
4.2.9 Modelled Magnetic Field Data…… 96
4.3 Results…….. 98
4.3.1 The Cross Sections from Orbit 497…….....98
4.3.2 The Cross sections from Orbit 490…… 101
4.3.3 The Average Cross Section…… 102
4.3.4 Comparison of Cross Sections with Recent Work…..... 106
4.3.5 Consequences of the Assumptions……108

4.4 Discussion and Conclusions……..... 112

5 Geomagnetic Storms which do not Contain Substorms 115

5.1 Storms with no Substorms……. 115
5.1.1 Introduction……..... 115
5.1.2 ICMEs with Magnetic Clouds……..... 115
5.2 Geosynchronous Altitude Electrons during the Substormless Storms of 1997…….…..... …….. 117
5.2.1 LANL Electron Spectrograms……. 117
5.2.2 Pseudobreakups……... 127
5.3 The Energies of Injected Electrons……128
5.3.1 Injections during Substormless Storms……. 129
5.3.2 Injections during Storms with Substorms…….....130
5.3.3 Solar Wind Correlation with Injections……..132
5.3.4 Maximum Gradient of the Solar Wind Pressure and Bz for the events of 1997……135
5.4 Pseudobreakup or Substorm Occurrence: A Brief Summary……139
5.5 Storms with No Substorms: 2000 – 2003……140
5.5.1 Geomagnetic Storms during the Period……..……..140
5.5.2 Electron Injections during the Storms of 2000-2003….. 143
5.5.3 IMAGE Data for 2000 – 2003…….....145
5.5.4 All-Sky Keograms for 2000 – 2003…….…….. 146
5.5.5 Results of the 2000 – 2003 Study…….. 149
5.5.6 Storms with No Substorm: A Feature of Slow Magnetic Clouds?..... 152
5.5.7 A Theory for Slow CMEs and Substorm Occurrence…. ……152
5.5.8 Storms with no Substorms during the THEMIS Era…… ……..…….. 154
5.6 Chapter Conclusions……154

6 Conclusions and Further Work 156

6.1 Summary of the Work……..156
6.1.1 Charge Exchange as a Source of Outer Belt He^+……156
6.1.2 Calculating the Charge Exchange Cross Section Using Distinct Populations of Drifting Particles……157
6.1.3 Storms with No Substorms: A Study of Substorm and Pseudobreakup Occurrence……158
6.2 Conclusions and Further Work…….. 159
6.2.1 Charge Exchange as a Source of Outer Belt He^+……159
6.2.2 Calculating the Charge Exchange Cross Section Using Distinct Populations of Drifting Particles……160
6.2.3 Storms with No Substorms: A Study of Substorm and Pseudobreakup Occurrence……161
6.3 Summary of Conclusions…… 162

Bibliography 163

Appendix 174

A Number Density Shifts in Helium…… 174
B Cross Sections for Individual Orbits……179
C LANL Injections during the Period 2000 – 2003…… 181

Figures

1.1 Illustration of Earth's Radiation Belts……15
1.2 Vector diagram of equatorial Pitch Angle……..…. 18
1.3 Grad-B drift for ions and electrons…….....19
1.4 The charge exchange process in the Radiation Belts…….. 21
1.5 Illustration of the Dungey Cycle…… ……23
1.6 Near-Earth magnetotail topology due to the pressure catastrophe....24
1.7 Formation of a Near-Earth Neutral line……25
1.8 CRRES orbit 604: O^+ spectrogram…….. 26
1.9 The Current Disruption Model for Substorms……28
1.10 The Near Earth Neutral Line Model for Substorms…….. 29

2.1 Geometry of the CRRES MICS analyser/detector assembly…….....34
2.2 Orientation and look direction of MICS……35
2.3 Orbit layout of the THEMIS probes during Tail Science Periods…… 38

3.1 CRRES He^+ number density against invariant latitude and local time ……... 41
3.2 CRRES He^{++} number density against invariant latitude and local time ……... 42
3.3 CRRES O^+ number density against invariant latitude and local time ……... 43
3.4 CRRES high energy electron counts against invariant latitude and local time……..……..……44
3.5 CRRES low energy electron counts against invariant latitude and local time……..……..44
3.6 CRRES low energy electrons vs. time; comparison with D_{ST}……..... 45
3.7 VIKING plot of helium charge and anisotropy parameters against invariant latitude and local time…… 47

3.8 CRRES helium charge parameter against invariant latitude and local time during quiet periods……... 48
3.9 CRRES helium charge parameter against invariant latitude and local time during storm periods……..... 49
3.10 CRRES O^+/He^{++} against invariant latitude and local time during both quiet and storm periods…….50
3.11 CRRES O^+/He^+ against invariant latitude and local time during both quiet and storm periods…….51
3.12 2-hour MLT radial averages through invariant latitude ion ratio plots for 14:00 to 16:00 MLT and 20:00 to 22:00 MLT……..…… 51
3.13 Overall radial average of ion ratio plots between 18:00 MLT and 00:00 MLT…… 52
3.14 Helium charge ratio against L-Shell and D_{ST}……..53
3.15 Helium charge parameter against L-Shell and D_{ST}..... 54
3.16 O^+ / He^+ Parameter against L-Shell and D_{ST}……..55
3.17 Spectrograms of heavy ion data for orbit 497 of CRRES…….56
3.18 2-hour local time average histograms of helium charge parameter within the Ring Current region…….. 58
3.19 Diagram showing the details of the orbit-by-orbit CRRES investigation Of shifts in helium number density…….. 60
3.20 Diagram showing possible shifts in helium number density…… 61
3.21 Ionic helium species shift across the main phase of a geomagnetic storm……. 63
3.22 Ionic helium species shift across the initial rapid recovery phase of a geomagnetic storm……. 64
3.23 Ionic helium species shift across the later smooth recovery phase of a geomagnetic storm……. 65
3.24 Ionic helium species shifts during storm and quiet periods, showing All data and overall average……..66
3.25 Average shift in O^+ and He^{++} during storm and quiet periods……. 68
3.26 D_{ST} index during 1991 and its 5-hour gradient……...70

3.27 Ionic helium species shifts during main and recovery phases, showing all data and overall average…….. 71
3.28 Average shift in O^+ and He^{++} during main and recovery phases…….73

4.1 Charge exchange cross sections for various ions……. 77
4.2 Modelled decay of He^{++} due to charge exchange, alongside the source and loss rate of He^+ due to charge exchange…….. 78
4.3 The cylindrical volume in which charge exchange can occur……. 79
4.4 Heavy ion spectrograms for orbit 497 of CRRES…….. 81
4.5 He^+ spectrogram for orbit 497 of CRRES with drift echo boundaries marked……..81
4.6 He^{++} spectrograms for the orbits containing the other injections used in the study…….. 82
4.7 Orbit 497 spectrogram with modelled drift period plotted……84
4.8 He^{++} spectrogram for orbit 497, showing handpicked drift echoes… 85
4.9 Neutral hydrogen density, N_H, against altitude…….. 86
4.10 Pitch angle against mirror altitude for ions trapped at L = $6R_E$……88
4.11 Cartoon showing the expected time-spreading effect due to charge exchange……..90
4.12 Cartoon showing the expected energy-bin spreading due to charge exchange……..91
4.13 Cartoon showing the complete region in which an injected ion could end up on a CRRES spectrogram……92
4.14 Orbit 497 He^+ and He^{++} spectrograms with the injected population under study and the drift period marked……. 93
4.15 Spectrogram of modelled B magnitude…….. 96
4.16 Modelled magnetic field topology for 14th February, 1991…….. 97
4.17 Helium ratio against time for injected energy ranges in orbit 497….. 98
4.18 Percentage of He^+ due to charge exchange against time…….. 99
4.19 Calculated velocity-charge exchange cross section for drift 1 of orbit 497……101

4.20 Calculated velocity-charge exchange cross section for drift 1 of orbit 490……102
4.21 The average calculated velocity-charge exchange cross section for Drift 1…….. ….....103
4.22 Cross section from previous work with relevant energies marked…. 104
4.23 The average calculated velocity-charge exchange cross section for Drift 2…….. ….....105
4.24 Graph showing previously calculated cross sections……... 106
4.25 Calculated average cross sections for drift 1……. 107
4.26 Modelled drift period with partial drift accounted for……..108
4.27 Calculated cross sections with partial drift accounted for…….109
4.28 Calculated cross sections; comparison between partial and full Drift…… 110
4.29 Partial drift cross sections, showing the effect of changing the N_H value by a factor of 5…….. 111

5.1 Cartoon showing the features of an ICME containing a magnetic Cloud……116
5.2a LANL electron spectrogram for January 10th, 1997…….. 118
5.2b B_z data for January 10th, 1997…….. 119
5.3a LANL electron spectrogram for February 10th, 1997……120
5.3b B_z data for February 10th, 1997……121
5.4a LANL electron spectrogram for June 9th, 1997…….. 122
5.4b B_z data for June 9th, 1997…….. 123
5.5a LANL electron spectrogram for July 15th, 1997……..124
5.5b B_z data for July 15th, 1997……. 125
5.6a LANL electron spectrogram for August 3rd, 1997…….. 126
5.6b B_z data for August 3rd, 1997…….. 127
5.7a Visual analysis of B_z and B_{mag} precursor to pseudobreakups and Substorms, 1997…… 132

5.7b Visual analysis of P_{ram} and flow speed precursor to pseudobreakups and Substorms, 1997……. 133
5.8 Maximum gradient in IMF B_z vs. injection energy, 1997…….. 136
5.9 Maximum gradient in P_{ram} vs. injection energy, 1997……137
5.10 Maximum gradient in density vs. injection energy, 1997……..138
5.11 Solar wind data from January 22nd and 23rd, 2000…… 142
5.12 LANL electron spectrogram for January 22nd, 2000……..144
5.13 IMAGE electron data for April 22nd, 2001……145
5.14 Abisko All-Sky Keogram from 22nd January, 2000…… 146
5.15 Abisko All-Sky Keogram from 23rd March, 2002…… 147
5.16 Maximum gradient in IMF B_z vs. injection energy, 2000-2003…… 149
5.17 Maximum gradient in P_{ram} vs. injection energy, 2000-2003…… 150
5.18 Maximum gradient in density vs. injection energy, 2000-2003…… 151
5.19 Solar wind features of a Slow CME…… 153

A.1 O^+ vs. He^{++} number density all vectors for storm and quiet…… 174
A.2 O^+ vs. He^+ number density all vectors for storm and quiet…….. 175
A.3 O^+ vs. He^+ number density average for storm and quiet…….. 175
A.4 O^+ vs. He^{++} number density all vectors for main phase…… 176
A.5 O^+ vs. He^{++} number density all vectors for recovery phase…… 176
A.6 O^+ vs. He^+ number density all vectors for main phase…….. 177
A.7 O^+ vs. He^+ number density all vectors for recovery phase……. 177
A.8 O^+ vs. He^+ number density average for storm and quiet…….. 178

B.1 Charge exchange cross section, orbit 548……..179
B.2 Charge exchange cross section, orbit 604……..180
B.3 Charge exchange cross section, orbit 612……..180

C.1 Solar wind data: 5th – 6th February, 2000…… 184
C.2 Solar wind data: 12th – 13th February, 2000……185
C.3 Solar wind data: 1st – 2nd March, 2000……... 186

C.4 Solar wind data: 3rd – 4th October, 2000……..187
C.5 LANL electron spectrogram, 5th February, 2000……188
C.6 LANL electron spectrogram, 12th February, 2000…….. 189
C.7 LANL electron spectrogram, 1st March, 2000……190
C.8 LANL electron spectrogram, 4th October, 2000…….. 191
C.9 Kilpisjarvi All-Sky keogram for 5th February, 2000……192
C.10 Muonio All-Sky keogram for 5th February, 2000…… 192
C.11 Kevo All-Sky keogram for 12th February, 2000…….. 192
C.12 Kevo All-Sky keogram for 12th February, 2000…….. 193
C.13 Abisko All-Sky keogram for 1st March, 2000…….. 193
C.14 Kilpasjarvi All-Sky keogram for 1st March, 2000…… 193
C.15 Kevo All-Sky keogram for 4th October, 2000…….. 194

Chapter 1: Magnetospheric Processes and Ionic Populations

1.1 The Radiation Belts

The Radiation Belts are toroidal structures, made up of ions and electrons drifting around the Earth. The inner belt exists at altitudes ranging from L = ~1.1R_E to 2.0R_E, and is composed mainly of protons, sourced from upper atmospheric neutron decay, due to cosmic ray albedo ([Freden, 1968]). This is a slow source, but the stability of the particle trapping at the relatively low altitude of the belt makes it a permanent and intense feature. The outer radiation belt exists between L shells of ~4.0R_E and 7.0R_E, moving to lower altitudes with increasing storm activity ([Daglis et al., 1999]). The sources for this belt are both the solar wind and terrestrial ionosphere.

The Radiation Belts were first discovered in 1958 by [Van Allen et al., 1958]. The payload of the Explorer 1 spacecraft included a Geiger Müller tube with the purpose of studying cosmic rays. The discovery of intense radiation caused Eric Ray, one of Van Allen's colleagues, to state, "Space is radioactive!" as the spacecraft passed into the region.

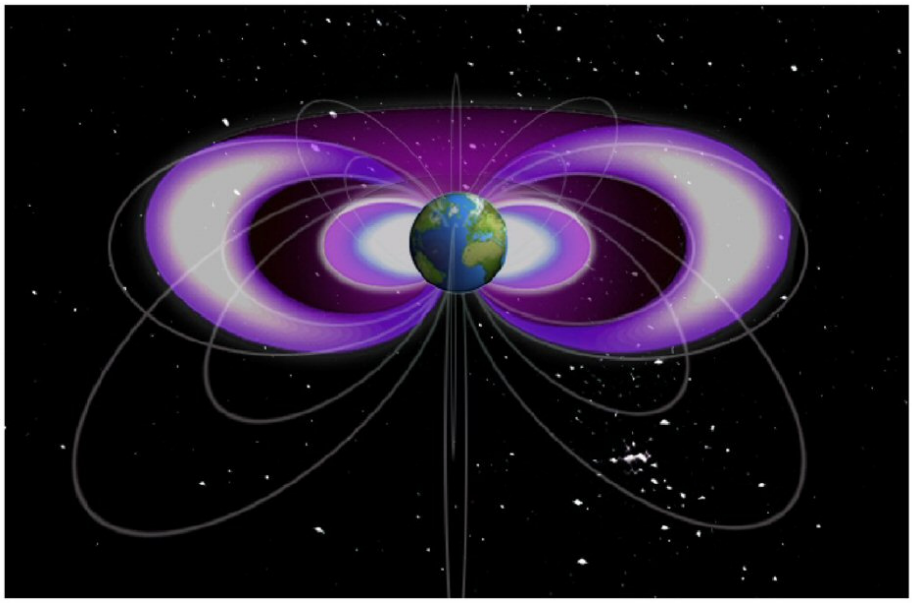

Figure 1.1: Earth's inner and outer Radiation Belts ([Hudson et. al, 2008]).

1.2 Trapping and Adiabatic Invariants

Particles within the Radiation Belts are referred to as 'trapped'. The motion of trapped particles is described using three adiabatic invariants, which allow the particle to remain stably trapped as long as their conditions are unviolated.

1.2.1 The First Invariant

The first adiabatic invariant defines the gyration of a particle around a magnetic field line. The period of gyration, T_c is given in equation 1.1.

$$T_c = \frac{2\pi m\mu}{|q|} \qquad \text{Equation 1.1}$$

In equation 1.1, m is the mass of the particle and q is the charge. The magnetic moment, μ, is given in equation 1.2. In this equation, B is the magnetic field density.

$$\mu = \frac{m.v_{\perp}^2}{2.B} \qquad \text{Equation 1.2}$$

The first adiabatic invariant is unviolated as long as μ changes slowly relative to the global magnetic field. The gyroperiod is of the order 10^{-3} or 10^{-4}s for electrons. This timescale is far shorter than that of the bounce motion, defined by the second invariant.

1.2.2 The Second Invariant

The second adiabatic invariant defines the bounce motion of particles between the regions of greater magnetic field density at the poles. The density of field at a 'mirror point' is given in equation 1.3.

$$B_m = \frac{W}{\mu}$$ Equation 1.3

where:

$$W = \frac{1}{2} m\left(v_{\perp}^2 + v_{\parallel}^2\right)$$ Equation 1.4

In equation 1.4, $v_{\perp}$ and $v_{||}$ are, respectively, the perpendicular and parallel components of the velocity, relative to the magnetic field. As the particle comes near to its mirror point, the parallel component of the velocity goes to zero, while the perpendicular velocity reaches its maximum. At the mirror point, the direction of motion along the field line reverses, creating a 'bounce motion' between the poles of the Earth's magnetic field.

1.2.2.1 Pitch Angle and the Loss Cone

It can be seen that particles with different equatorial velocities will have their mirror points at different altitudes. The pitch angle, defined at the equator, is given in equation 1.5.

$$\alpha = \tan^{-1}\left(\frac{v_{\perp}}{v_{\parallel}}\right)$$ Equation 1.5

α is the angle between the components of the velocity vector at the magnetic equator, shown in figure 1.2.

Particles with low pitch angles will have low altitude mirror points. For very low pitch angles, the mirror altitude will be in regions of dense atmosphere, where loss due to collisions is likely. This defines a loss cone, which is a solid angle, defined at the equator, in which all particles will be lost due to atmospheric collisions.

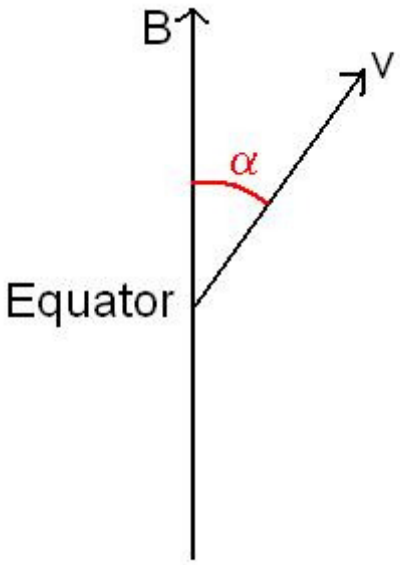

Figure 1.2: The equatorial pitch angle; the angle between the magnetic field and particle velocity vector at the magnetic equator.

1.2.3 The Third Invariant

The third adiabatic invariant defines the drift of particles around the Earth, known as Gradient-Curvature drift. This drift is westward for ions and eastward for electrons. This motion of these particles causes a current around the Earth, known as the ring current. As the current is proportional to the energy density of the charge-carriers, the ring current is mostly due to the ionic population within the belt ([Williams, 1987]). The term 'ring current' is, therefore, usually used in reference to the ions rather than electrons.

'Gradient' and 'Curvature' refer to the mechanisms by which particles drift around the earth, these being approximately equal in their contribution towards the motion, and in the same direction.

1.2.3.1 Gradient-Curvature Drift

Across its path of gyration around a field line, a particle will cover a small altitude range. The density of the magnetic field drops with altitude, meaning that

B across the inner part of the gyro-orbit will be greater than B across the outer part. Equation 1.6 shows that an increase in B would lead to a decrease in gyroradius, resulting in a shorter gyro-circumference for that half of the orbit. The particle would, therefore, travel further during the outer part of its gyration than during the inner. This effect is shown in figure 1.3.

$$r_g = \frac{mv_\perp}{|q|B} \qquad \text{Equation 1.6}$$

The curvature of the magnetic field lines leads to a centrifugal force, which causes a sideways drift for the particle.

In order for stable trapping, Earth's magnetic field must not undergo changes on the timescale of any of these invariants. Due to its relatively long timescale, the third invariant is violated most often. Violation of the third invariant is the mechanism thought to be responsible for radial diffusion (e.g. [Nakada and Mead, 1965]).

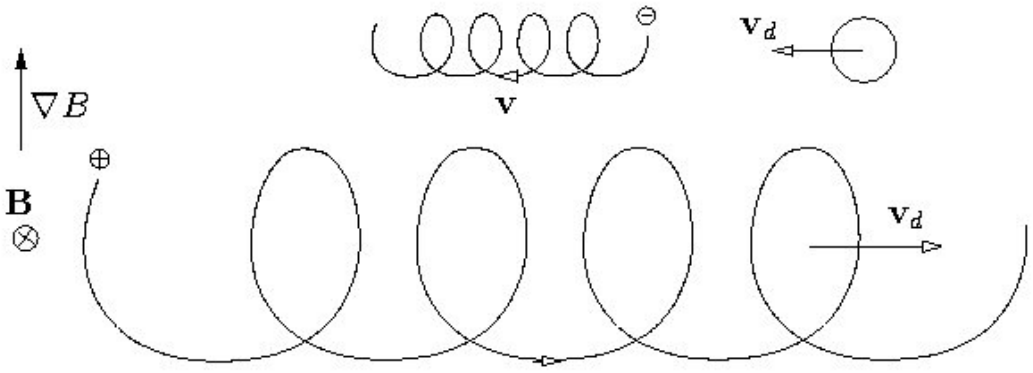

Figure 1.3: Grad-B drift ([1]); a magnetic field density gradient across the gyro-orbit will result in a varied gyroradius, it being shorter in regions of higher B. This effect will cause the particles to drift around the Earth.

1.3 Sources of the Outer Radiation Belt

The outer radiation belt is sourced from both the solar wind and terrestrial ionosphere, with both sources initially populating the plasma sheet. The main

ionic species are H^+, O^+, He^{++} and He^+. H^+ is the most dominant ion, and could feasibly come from either source. The second-most abundant ion is O^+ ([Daglis et al., 1999]), a heavy, weakly ionised species which is not vastly present in the solar wind. O^+ is, therefore, often used as evidence of ionospheric input to the outer belt, and it has been shown that O^+ increases notably in number density during geomagnetic storms. In contrast, He^{++} is not strongly present terrestrially due to its high charge state, which is a result of the hotter nature of the sun than the Earth. He^{++} is, therefore, used as evidence of solar wind input to the belt. He^+ could feasibly be sourced terrestrially, as it is present in the ionosphere, but it is also possible that the solar wind could act as a source of He^+ via the trapping of He^{++} followed by a charge exchange reaction with neutral Hydrogen within Earth's exosphere.

1.3.1 Charge Exchange as Both a Source and Loss Process

Within the altitude range of the outer belt, the number density of neutral hydrogen is large enough for charge exchange to be expected to occur.

$$H^+ + H \rightarrow H + H^+ \qquad \text{Equation 1.7}$$

$$O^+ + H \rightarrow O + H^+ \qquad \text{Equation 1.8}$$

$$He^{++} + H \rightarrow He^+ + H^+ \qquad \text{Equation 1.9}$$

$$He^+ + H \rightarrow He + H^+ \qquad \text{Equation 1.10}$$

For all singly ionised species, charge exchange will act as a loss mechanism. This is illustrated in figure 1.4, taken from [Daglis et al., 1999]. In the figure, an energetic ion trapped in the magnetosphere undergoes a charge exchange reaction with a neutral atom in the thermal energy range. The ion would then become an energetic neutral, which would no longer be magnetically bound and

would hence be lost. The thermal ion may become stably trapped, but would be at a far lower energy than the original ion, reducing the effective ring current. In the case of the high-altitude exosphere, every resulting thermal ion would be H^+.

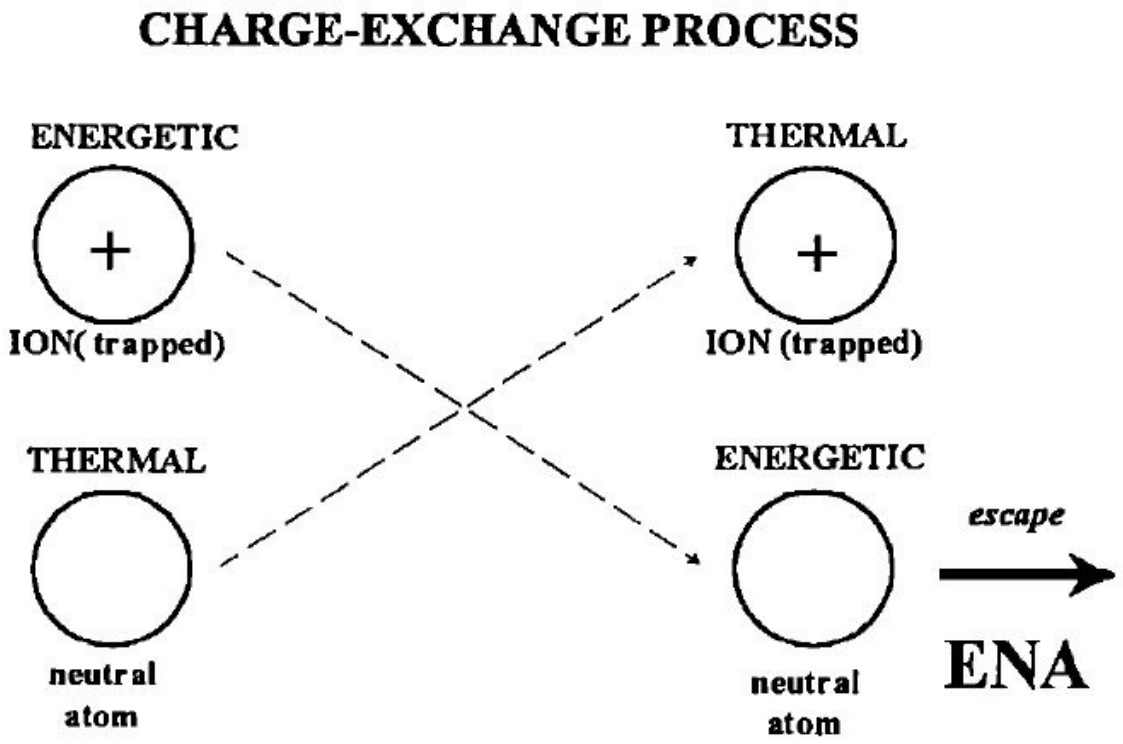

Figure 1.4: The charge exchange input and output, from [Daglis et al., 1999]; if a trapped, energetic, singly-charged ion undergoes charge exchange with a thermal-energy neutral, the result would be an energetic neutral and a thermal-energy trapped ion.

Equation 1.9 acts as a loss mechanism for He^{++}, but would also act as a source mechanism for He^+. If the theory of figure 1.4 is applied to this particular reaction the product would not contain a neutral. Instead, a thermal H^+ and a He^+ of the same energy as the original He^{++} ion would result. The change in the charge of the ion would result in a halving of the gyroperiod, gyroradius and drift period, but the actual energy of the ion would not be notably changed. It has been suggested that, due to charge exchange, He^+ becomes the dominant species in the outer radiation belt during the recovery phase of geomagnetic storms ([Tinsley, 1976]). Other high charge state solar wind ions, such as highly

ionised iron and oxygen, also undergo charge exchange reactions, but their relatively low abundance in the solar wind means that they contribute little to the outer belt population.

1.4 Geomagnetic Storms and Substorms

Geomagnetic storms are periods of intense activity within Earth's magnetosphere, the primary signature being a decrease in horizontal surface magnetic field due to an enhanced ring current. In 1961, Dungey proposed his model for magnetospheric energisation due to reconnection with the IMF. It was shown by [Gonzalez et al., 1994] that periods of southward IMF B_z are a requirement for magnetic storms. It has also been shown that magnetic storms arise due to solar wind discontinuities, such as Interplanetary Coronal Mass Ejections (ICMEs) and Corotating Interaction Regions (CIRs) (e.g. [Gonzalez and Tsurutani, 1987], [Gosling et al., 1991], [Gonzalez et al., 1994]).

Magnetospheric substorms involve a large scale restructuring of the magnetotail, and are perhaps the longest known magnetospheric phenomenon due to their observable nature at visible wavelengths in the form of the aurora. In their early work on the subject, [Chapman, 1962] and [Akasofu, 1968] believed that geomagnetic storms were simply made up of collections of substorms, treating them as magnetospheric pumps which inflate the inner magnetosphere with plasma. Since their initial papers it has become apparent that geomagnetic storms cannot be made only of substorms ([Daglis, 1999]). The substorm is still not completely understood, but it is known to be a fundamental magnetospheric process. The knowledge of substorms is vital in understanding the dynamics of the magnetosphere.

1.4.1 Substorms and the Pressure Catastrophe

If a substorm is not a single unit of a geomagnetic storm, what is it and what purpose does it serve? This is presently a debated subject in

magnetospheric physics. It has been suggested that the substorm is the mechanism by which the magnetosphere releases mass and energy when some unknown threshold is met, and is a solution to the pressure catastrophe, first theorised by [Erickson and Wolf, 1980].

The Dungey cycle ([Dungey, 1961]), depicted in figure 1.5, predicts that southwardly directed IMF B_z can reconnect with Earth's magnetosphere on the dayside, and that field lines will be dragged across the poles of the Earth, eventually stretching out into a distant magnetotail. Far down the tail a neutral line is thought to exist, at which IMF-connected field lines are reconnected to the geomagnetic field and subsequently retract earthward.

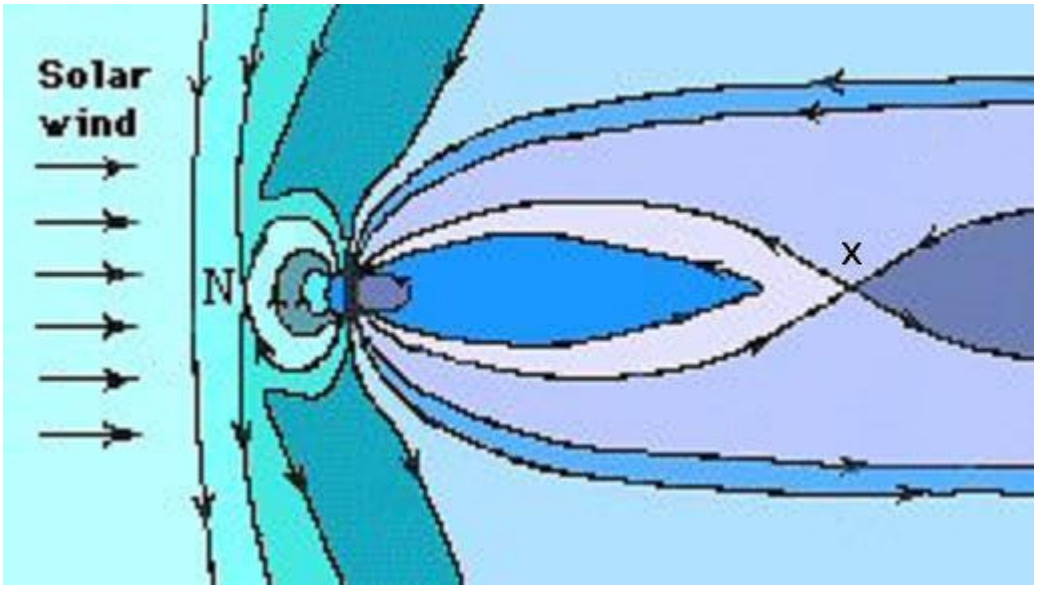

Figure 1.5: Diagram of the Dungey cycle ([2]), with dayside reconnection dragging B-field lines over the poles, and eventually reconnecting at point x, the hones point. Following reconnection, the B-field lines retract earthward.

This point, sometimes called the Hones point, is shown as point x in figure 1.5, taken from [2]. The point itself was found to be located ~100R_E downtail ([Baker et al., 1984]). After reconnection at this neutral line, the field line (and the plasma bound to it) will convect earthward. In the distant tail the magnetic field density is relatively low, making the volume of each retracting flux tube large (volume ~ 1/B). As the field line moves earthward, B increases dramatically, and

consequently the flux tube volume will rapidly decrease. For a flux tube of pressure P and volume V, P/V would be constant; a decrease in V would lead to an increase in P. The pressure would eventually inhibit the convective flow, and a so called 'pressure catastrophe' would occur ([Erickson & Wolf, 1980]).

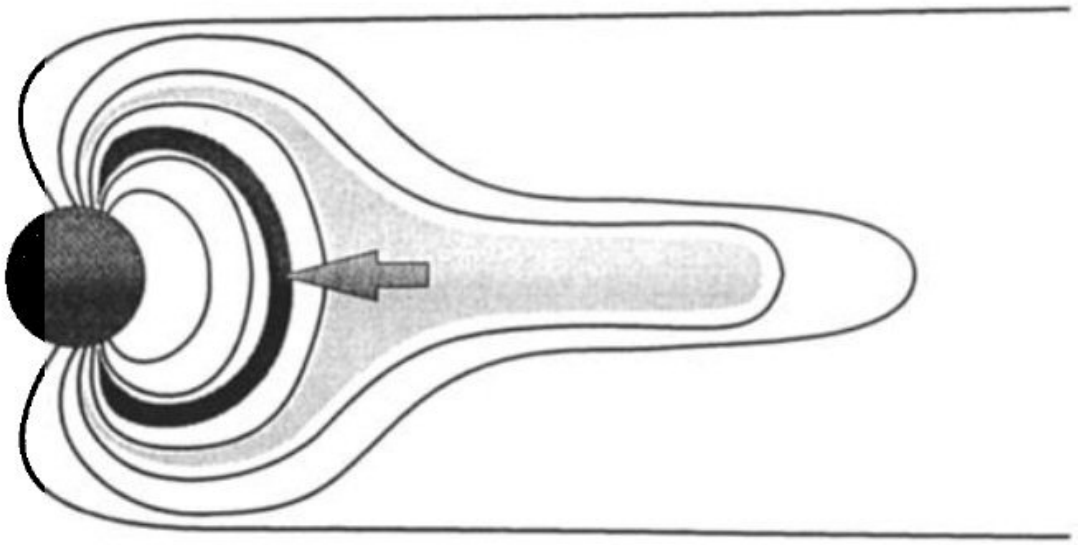

Figure 1.6: The expected topology of the near-earth magnetotail as a result of the pressure catastrophe, from [Daglis et al., 1999]. A buildup of pressure will impede the earthward flow of flux tubes retracting from reconnection in the distant tail.

Figure 1.6 shows the expected magnetotail configuration due to a pressure buildup. [Erickson and Wolf, 1980] suggested that the substorm was the process by which the pressure crisis was solved, alongside theoretical evidence that persistent steady magnetospheric convection was not possible. Substorms involve the formation of a near-earth neutral line (NENL) between $15R_E$ and $25R_E$ downtail ([Hones et al., 1972]). The released plasmoid, shown in figure 1.7, would significantly reduce the amount of mass, and hence the pressure, within the flux tubes in the region, and flow would be unclogged.

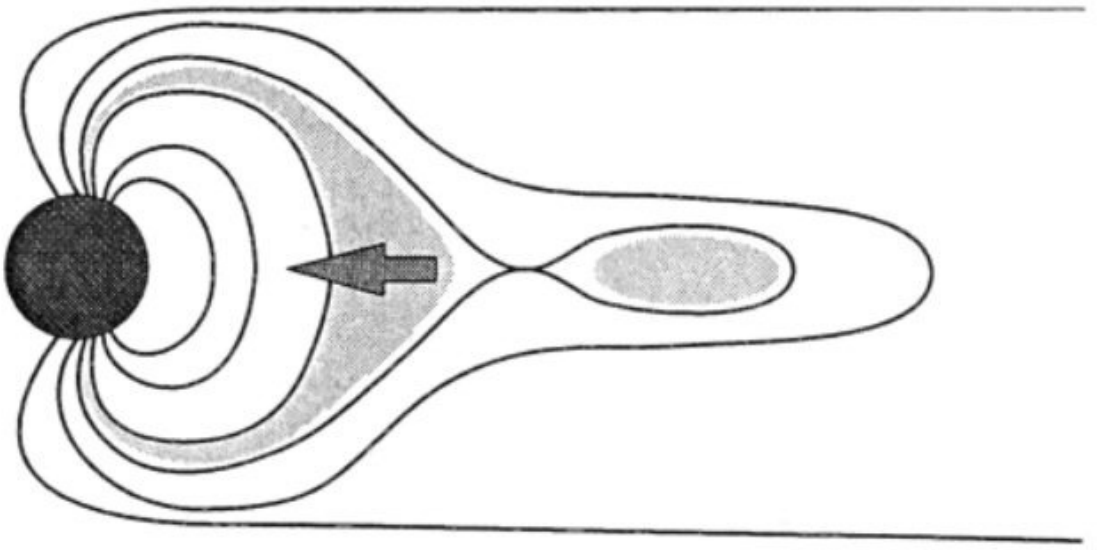

Figure 1.7: The formation of a near-earth neutral line as a means of reducing the pressure buildup, suggested by [Erickson and Wolf, 1980] as the function of a magnetospheric substorm (taken from [Daglis et al., 1999]).

1.4.2 Pseudobreakups

Substorms manifest themselves in the aurora with a relocation to lower latitudes (growth phase) followed by a sudden brightening and breakup of the aurora and an expansion back to higher latitudes (an onset followed by expansion phase, [Akasofu, 1968]). Sometimes, the brightening at onset is not followed by an expansion phase. This phenomenon is referred to as a pseudobreakup.

Pseudobrakups were initially observed to occur during the growth phase of substorms (e.g. [Elvey, 1957], [Akasofu, 1968]), but have since been shown to occur as isolated events during quiet time ([Fillingim et al., 2000]), and after substorm recovery ([Aikio et al., 1999]). It was pointed out by [Rostoker, 1998] that the characteristics of pseudobreakups have not been clearly defined, and many papers use different definitions as to what makes a pseudobreakup. Examples of this include [McPherron, 1991], who defined a pseudobreakup as a “non expanding breakup”; [Lyons et al., 1999], who required the onset to occur

on the equatorward edge of the aurora; and [Voronkov et al., 2003], who required there be “No considerable poleward motion after onset”.

Pseudobreakups share many of the properties of substorms, such as magnetotail dipolarisation and geosynchronous particle injections. Recently, [Kullen and Karlsson, 2004] published work which gave evidence that pseudobreakups and substorms were the same phenomenon, with pseudobreakups simply being the weakest form of substorm.

1.4.3 Dispersionless Substorm Injections

Around substorm onset, populations of particles are observed to be injected across midnight MLT at geosynchronous altitudes. These injections have been discussed by [DeForest and Mcilwain, 1971], who noted that “a hot cloud of plasma is injected into the midnight sector during each substorm”. Provided the satellite was near midnight, in an energy spectrogram an injection would appear as an indispersed signature, with particles of all energies reaching the detector simultaneously. Figure 1.8 shows O^+ data from orbit 604 of CRRES, taken on 30th March, 1991. A clear injection signature is observed at ~21:30 UT.

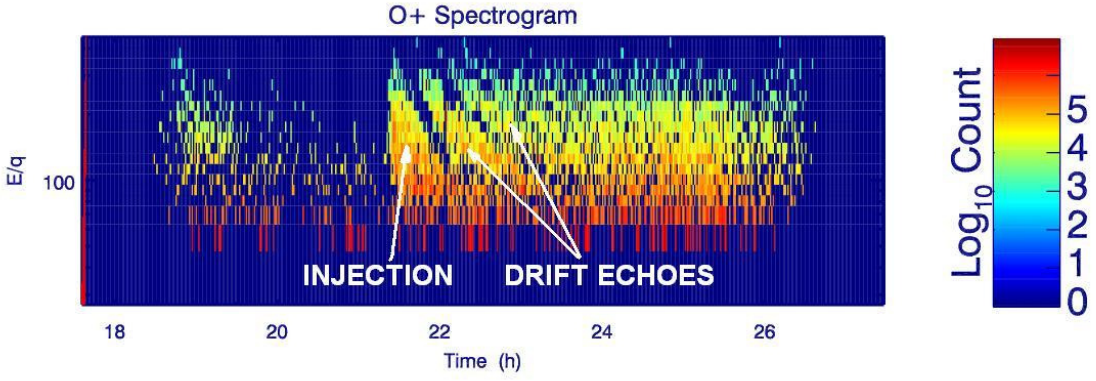

Figure 1.8: O^+ spectrogram from orbit 604 of CRRES, with the injection and drift echoes marked. Two clear drift echoes are observed.

The injected population is often observed again, after the particles have drifted around the earth, as a dispersed signature. These signatures are known as drift echoes. Two clear drift echoes can be seen after the injection in figure 1.8.

1.5 D_{ST} and the Ring Current

The Disturbance Storm-Time (D_{ST}) index is an hourly index of equatorial horizontal magnetic field perturbation, calculated using data from an array of near-equatorial magnetometers. The perturbation of the field is due to an enhanced ring current, and during geomagnetic storms the D_{ST} is observed to rapidly drop to negative values reaching hundreds of nT, and slowly return to near-zero. This signature is explained by the rapid energisation of the ring current associated with storms and the following loss of energy as the ring current decays. The level of perturbation must then be a function of the amount of energy within the ring current. A mathematical theorem relating the disturbed magnetic field to the amount of energy in the ring current (and other magnetospheric currents, though it is expected that the ring current causes the greatest equatorial perturbation during stormtime) was first derived by [Dessler and Parker, 1959], and [Sckopke, 1966].

1.6 Current Interest in Magnetospheric Physics

1.6.1 Models of the Substorm

A long standing question in magnetospheric physics relates to the order in which observed events take place during a substorm. There are three components of the substorm instability. These are Auroral Breakup, Current Disruption and Reconnection. Auroral Breakup and expansion are the classical method for the determination of substorm occurrence, with the aurora visibly breaking up and expanding to high latitudes. Current Disruption occurs at ~$10R_E$ downtail, whereby an abrupt increase in $B_{z(gsm)}$ initiates the formation of a wedge

in the cross-tail current ([McPherron et al., 1973]), which then flows along field lines and through the ionosphere. Reconnection occurs at ~25R_E ([Nagai et al., 1998]), with the formation of a Near-Earth Neutral-Line (NENL) leading to bursty earthward flows and tailward plasmoids.

It is generally agreed that Auroral Breakup follows Current Disruption, but there are different views relating to whether the NENL is the cause, or an effect of, Current Disruption. There are two conflicting models for the substorm: the Current Disruption and the Near-Earth Neutral-Line models.

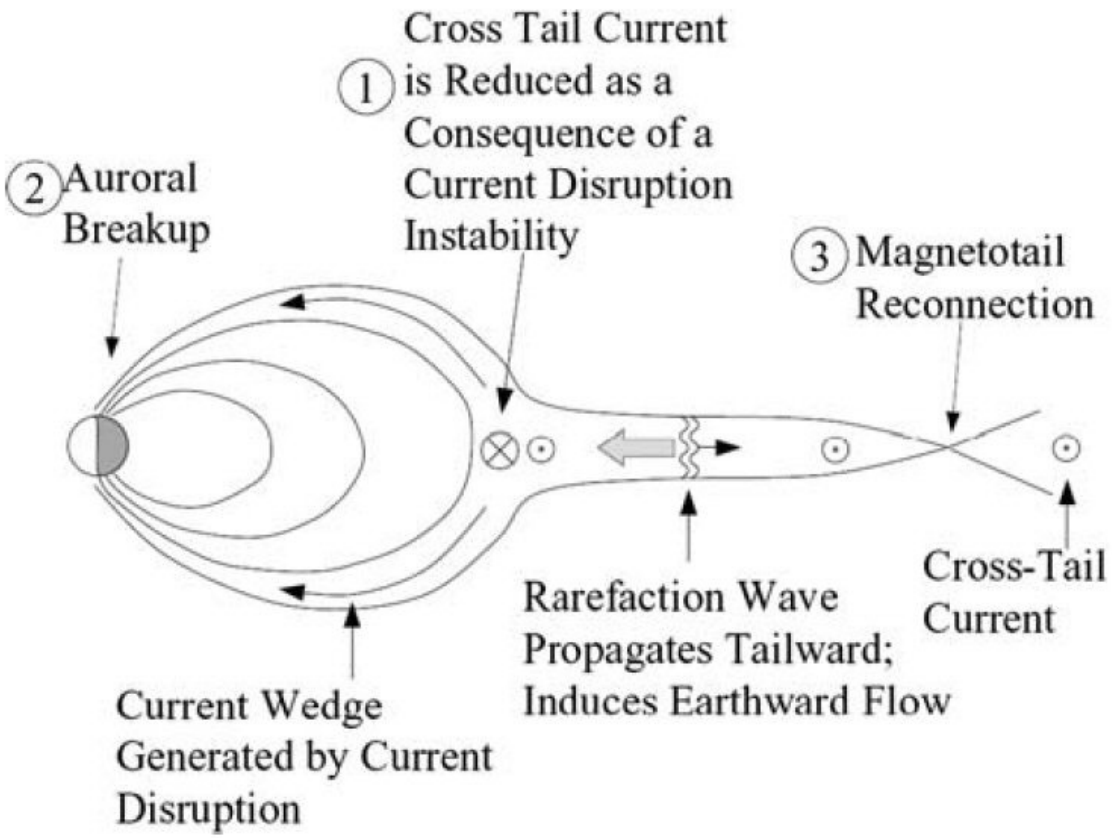

Figure 1.9: The order of events according to the Current Disruption model ([Angelopoulos, 2008]). Numbers indicate the chronological sequence of events.

In the Current Disruption model, an instability within the current disruption region (8-10R_E) is responsible for substorm onset ([Lui, 1996]). The formation of the NENL would then occur as a result of a tailward rarefaction wave, though no

evidence of such a wave has ever been reported. Evidence in favour of this model includes the observation that the breakup auroral arc is equatorward, i.e. near-earth ([Lui and Burrows, 1978]), and also that there is a rapid increase in the cross-tail current density in the region, prior to substorm onset ([Kaufmann, 1987]). The order of events in the Current Disruption model is shown in figure 1.9, taken from [Angelopoulos, 2008].

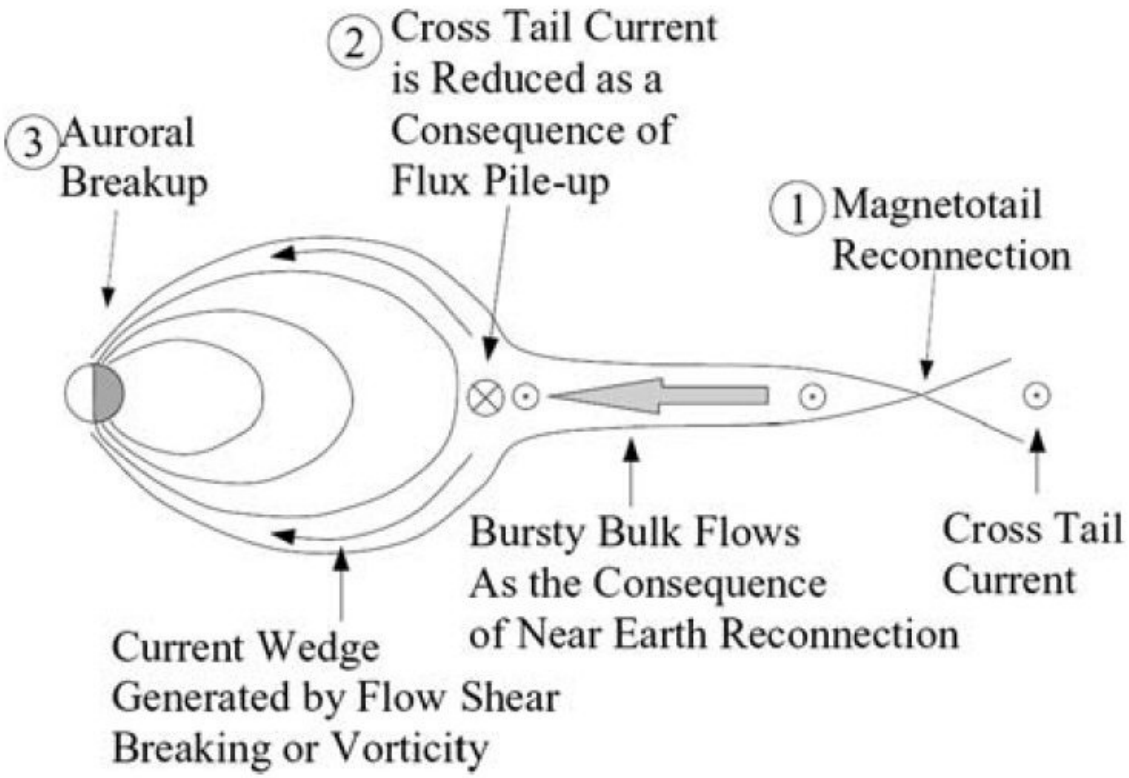

Figure 1.10: The order of events according to the NENL model ([Angelopoulos, 2008]). Numbers indicate the chronological sequence of events.

In the NENL model for the substorm ([Hones, 1976], [Baker et al., 1996]), the reconnection occurs first. Bursty earthward flow ([Baumjohann et al., 1989]) then leads to a buildup of flux within the cross-tail current region, causing Current Disruption, which leads to Auroral Breakup. Observations made by [Angelopoulos et al., 1997] of earthward flows occurring from 12 – 18R_E downtail

within 1 minute of onset are in support of this model. The order of events in the NENL model is shown in figure 1.10, taken from [Angelopoulos, 2008].

1.6.2 High Energy Electrons and Solar Wind Velocity

One of the best known results in Radiation Belt research is that of [Paulikas and Blake, 1979], which showed a linear relationship between solar wind velocity and relativistic electron flux in the Outer Radiation Belt. In a recent paper, [Reeves et al., 2011] further investigated this effect using a far larger statistical dataset (from 1989 to 2010). It was found that the relationship between solar wind speed and high-energy electron flux in the Outer Radiation Belt is more complex than previously believed, with a velocity-dependant lower limit to electron flux but no velocity-dependant upper limit. This is referred to in their paper as a “triangular relationship” between solar wind velocity and high energy electron flux.

1.7 The Work Presented in this Thesis

Presented in this thesis are studies of ionic populations in the Ring Current during periods of storm (D_{ST} < -30nT) and Quiet (D_{ST} > -30nT). In chapter 3, evidence suggesting that charge exchange is a primary source of Ring Current He^+ is presented and discussed, including evidence of a source mechanism for He^+ during the recovery phase of geomagnetic storms.

Chapter 4 attempts to find the charge exchange cross section for the reaction displayed in equation 1.9 using the distinct ionic populations associated with substorm injections and subsequent drift echoes. While a shift from He^{++} toward He^+ is evident, the cross sections are found to be too large for the effect to be due solely to charge exchange.

The differences in solar wind precursors leading to substorms and pseudobreakups are investigated in chapter 5. Stormtime periods which lacked substorm expansion phases in aurora are shown to contain dispersionless

injections in electron data, attributed to pseudobreakups. It is then shown that substorm occurrence is dependant on large solar wind density enhancements, with larger spikes leading to higher energy injections.

Chapter 2: Missions and Instrumentation

2.1 The CRRES Satellite: Mission and Orbit

The Combined Release and Radiation Effects Satellite (CRRES) was a joint NASA and US Department of Defence mission aiming to study the near-earth radiation environment. It was launched on 25th July, 1990, into a near-equatorial geosynchronous transfer orbit, with inclination of 18.1^{o} and an orbital period of 9 hours and 50 minutes. Of the planned 3-year mission, CRRES lasted only a single year. It was lost on 12th October, 1991, presumed to be a result of onboard battery failure. ([Johnson et al., 1992]).

The geosynchronous transfer orbit of CRRES passed through a range of L-shells, from its perigee at around 1.2R_E on the dayside of Earth, to its apogee, which fell between 7.0R_E and 8.0R_E across the mission. The Magnetic Local Time (MLT) location of the apogee began at 0830MLT, and had progressed to 1530MLT by the end of the mission. This gave excellent spatial coverage of the outer radiation belt, and the often near-midnight location of CRRES at geosynchronous altitudes allowed detailed study of many dispersionless injections which occurred during the period ([Hall et al., 1998], [Grande et al., 1997]). The rotation of CRRES was about the Sun-Earth axis.

The CRRES mission held three primary objectives:

1. To study the effects of the natural radiation environment on microelectronic components and on high-efficiency gallium arsenide solar cells and to map this environment;
2. To conduct low-altitude satellite studies of ionospheric irregularities (LASSII); and
3. To conduct a series of chemical release experiments in the ionosphere and magnetosphere.

The 'Release' part of CRRES's title related to 24 chemical canisters that were part of the payload, in order that the third objective be fulfilled. This involved releasing chemicals which would subsequently be ionised by solar UV radiation, and mapping their motion as they travelled along the magnetic field lines. The purpose of this was to study the propagation of electric fields and waves.

The full payload of CRRES involved more than 40 instruments. The main instrument of importance in this study is the Magnetospheric Ion Composition Spectrometer (MICS), though data from the Medium Electrons A device are also presented.

2.2 The CRRES MICS Instrument

The MICS device on the CRRES satellite was capable of full identification of ionic species ranging from Hydrogen to Iron in the energy range 1.2 keV/charge to 426.5 keV/charge. For a full description of the device and its components, the reader is directed toward the paper by [Wilken et al., 1992] entitled "Magnetospheric Ion Composition Spectrometer Onboard the CRRES Spacecraft". The operation of the device will be briefly discussed here, using the paper by Wilken et al. as reference.

The technique of ion identification employed by the CRRES MICS instrument involves a time-of-flight, T, and energy, E, measurement, with the mass, A, being proportional to ET^2. The charge, Q, of an ion is determined using an E/Q filter at the entry point of the spectrometer, which will only accept ions with a defined energy per charge ratio. Beyond the E/Q filter, ions pass through an accelerating voltage, in order to improve instrument resolution at low energies. The mass resolution is a function of particle mass and energy, increasing as a function of energy to mass ratio. With the accelerating voltage, the observed ion energy will be given by equation 2.1. In the equation, E_0 is the energy of the incident particle and U is the accelerating voltage.

$$E = E_0 + UQ = Q\left[\left(\frac{E_0}{Q}\right) + U\right] \qquad \text{Equation 2.1}$$

The benefit of the accelerating voltage, U, can be seen in this equation for low E_0/Q values.

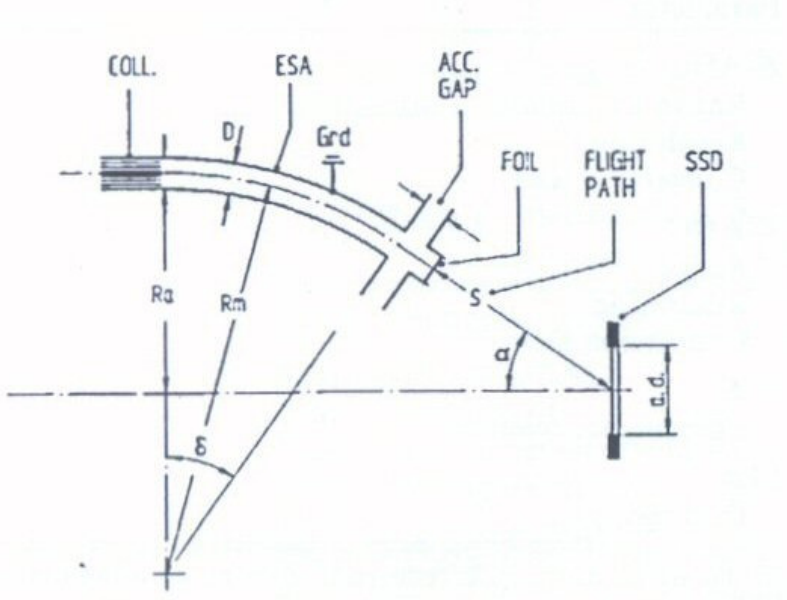

Figure 2.1: Geometry of the analyser/detector assembly, from [Wilken et al., 1992].

Figure 2.1 shows the chosen design for the analyser/detector assembly. At the opening of the ESA, incident ions first pass through the collimator, which reduces scattering within the ESA and removes ions with indirect trajectories. Provided the ions have an accepted E/Q value, they will then pass through the ESA and into the post-acceleration region, where the accelerating voltage is applied in order to improve resolution. Following the acceleration, ions are directed into a thin carbon foil. Any ion passing through the foil will induce an

ejection of secondary electrons from the surface, which are accelerated to 1 keV. These electrons are collected on a microchannel plate (MCP), and the start signal for the time-of-flight (T) is given. The ion will continue on its path across the distance (s) and then will collide with the Solid State Detector (SSD). The electrons ejected from the SSD are collected by another MCP to provide the stop signal for the T measurement.

The MICS device's orientation and viewing direction, in the spacecraft frame, are shown in figure 2.2 (taken from [Wilken et al., 1992]). The satellite's spin axis is the Earth-Sun line, with the rate of rotation being ~2.0 rpm. The pitch angle distribution sampled by this rotation is limited to the YZ plane, meaning that the observed pitch angle range would depend upon the field orientation.

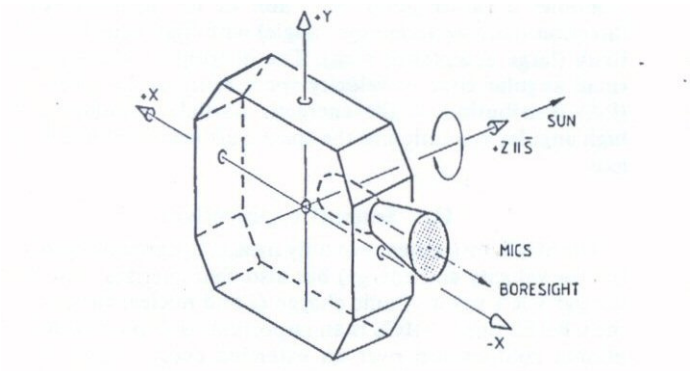

Figure 2.2: Orientation and look direction of MICS, with CRRES' spin marked, from [Wilken et al., 1992].

2.3 Previous Studies Using CRRES MICS Data

The orbit of CRRES sampled a wide range of L-Shells, making it ideal for spatial and temporal studies of particle populations in the outer belt. [Hall et al., 1998] used data from the MICS instrument in a study of 87 dispersionless substorm injections from the first half of 1991. It was found that the spatial scale of the injections was large and that quiet time injections were generally solar

wind rich (He^{++}), as opposed to storm time injections containing more terrestrial material (O^{+}).

[Grande et al., 1997] used CRRES MICS data to study the composition of the ring current during storm time, showing that ring current enhancements strongly correlated with the D_{ST} index, and that, with decreasing D_{ST}, there is a progression to lower altitudes of the maxima in number density of each species. Analysis of the 87 injections from [Hall et al., 1998] showed that injections generally did not contain He^{+}, and that they generally occurred at higher altitudes than the large stormtime enhancement. It was hence shown that the enhancement could not be due to substorm injections.

The intense magnetic storm of March, 1991, was also studied using CRRES MICS data. [Grande et al., 1996] published work investigating high charge-state heavy ions observed by CRRES following the storm's commencement, such as Fe, Mg and Si. Fe was observed to change abruptly from q = +9 to +16, which was attributed to two separate solar wind source populations rather than charge exchange. These ions must have been rapidly able to access the region of CRRES after entering the plasma sheet, which would not have been possible under average geomagnetic conditions. The change in charge state was explained as being due to a fast solar wind stream tamped by a slow one, i.e. a Corotating Interaction Region (CIR). The shift in Fe charge state in the solar wind was confirmed by Ulysses measurements.

2.4 Overview of the LANL Satellites

Electron data from the Los Alamos National Laboratory (LANL) satellites are used in chapter 5, and will briefly be discussed here. At present, LANL have over 10 satellites in geosynchronous orbits. Data is received continually, usually from 3 or 4 different satellites simultaneously. The orbital period of the satellites is 24 hours, meaning they are fixed in longitude, and the near equatorial orbits reach a maximum latitude of 11°.

Electron instruments onboard the LANL satellites include the Magnetospheric Plasma Analyser (MPA), which detects electrons between ~1eV/e and 40keV/e; the Synchronous Orbit Particle Analyser (SOPA), which can detect electrons from 50keV to above 1.5MeV; and the Energetic Spectrometer for Particles (ESP), which detects electrons ranging from 0.7MeV to 26MeV. Substorm injections generally occur within the SOPA energy range. Table 2.1 gives the SOPA electron energy bins.

SOPA Electron Channels

Channel Name	Nominal Energies
E1	50-75 keV
E2	75-105 keV
E3	105-150 keV
E4	150-225 keV
E5	225-315 keV
E6	315-500 keV
E7	500-750 keV
E8	0.75-1.1 MeV
E9	1.1-1.5 MeV
E10	above 1.5 MeV
ESP1	0.7-1.8 MeV
ESP2+3+4	1.8-3.5 MeV
ESP5+6	3.5-6.0 MeV
ESP7	6.0-7.8 MeV
ESP8	7.8-10.8 MeV
ESP9	10.8-26 MeV

Table 2.1: Electron energy channels for the LANL SOPA device ([3]).

The LANL satellites' geosynchronous orbit altitude makes them ideal for the investigation of substorm occurrence, as the presence of multiple satellites makes it likely that at least one will be near enough to midnight (MLT) to observe the dispersionless particle injections which occur at substorm onset. LANL data are used in the work for chapter 5 of this thesis as a means of detecting substorm occurrence in particle data.

2.5 Overview of the THEMIS Mission

In February, 2007, the mission Time History of Events and Macroscale Interactions during Substorms (THEMIS) launched, its objective being to discover the series of events which lead up to the occurrence of the magnetospheric substorm. The mission involved five identical probes. All probes were put into elliptical orbits, with the MLT location of the apogee dependant on the particular mission phase. In the tail science phase, the apogees were all downtail. Three of the probes had their apogee at $10R_E$, with an orbital period of ~1 day. The remaining two probes had apogees at $20R_E$ and $30R_E$, their orbital periods being ~2 days and ~4 days, respectively. Once every 4 days, the satellites would align in the tail. The inner three probes would search for evidence of current disruption, while the outer pair would look for evidence of reconnection, such as opposing plasma flows and magnetic dipolarisation (see [Angelopoulos, 2008]). The orbital layout of the THEMIS probes is shown in figure 2.3.

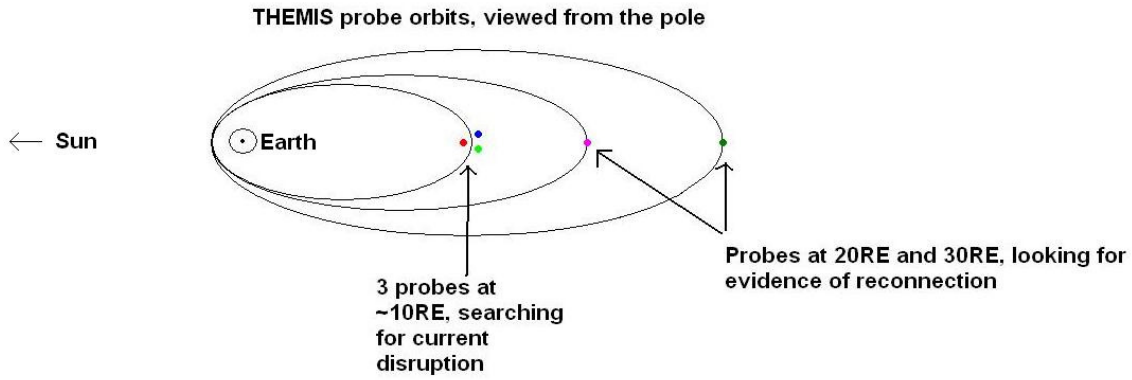

Figure 2.3: Orbit of the THEMIS probes during the tail science phases, looking for current disruption at $10R_E$ and reconnection between $20R_E$ and $30R_E$, downtail.

THEMIS data were planned for use in chapter 5 of this thesis, in a study of the differences in magnetotail development during storms caused by slow CMEs.

Unfortunately, during the Tail Science periods no storms were located which resulted from these.

Chapter 3: The Origin of Magnetospheric Singly Charged Helium

3.1: The Origin of Magnetospheric Ions

The ion composition of the magnetosphere is highly dynamic, being dependent upon conditions within the solar-terrestrial environment. The most common ion is H^+, but heavier species, such as Helium and Oxygen, also make up a significant fraction of the population. The energy and charge state of any species of ion can be used to determine its origin; completely ionised Helium (He^{++}) predominantly coming from the solar wind and singly ionised Oxygen (O^+) being evidence of a terrestrial source. Singly charged Helium (He^+) is known to exist within the ionosphere, but there is also an argument for it being sourced from the solar wind. This is that after becoming trapped within the magnetosphere, He^{++} undergoes a charge exchange reaction with exospheric neutral Hydrogen (H), leaving He^+ and H^+. This chapter investigates charge exchange as a major source of magnetospheric He^+ using ionic data from the CRRES MICS instrument.

3.2: The Ring Current in Invariant latitude

3.2.1: Ion Populations in Invariant Latitude

In this section, the ion composition of the magnetosphere will be investigated, focussing primarily on the Outer Radiation Belt. Figure 3.1 displays plots of the number density of He^+ against invariant latitude and local time during both quiet and storm conditions. The outer belt exists between L-Shells of $4R_E$ and $7R_E$, and hence maps down to invariant latitudes between 60^o and 66^o. It can be seen in both plots, though far more clearly during storm periods.

For the quiet time plot only data for $D_{ST} > -30nT$ is used. An approximation for the poleward boundary of the belt would be around 68^o, where there is a sudden jump of around an order of magnitude. The belt remains close to this

magnitude as far as the data remains clear, making the equatorward boundary hard to identify, though there is a drop in number density at around 55° that probably marks this point.

The storm-time plot, which contains data for D_{ST} < -30nT, shows a few differences. The belt appears to have expanded to lower latitudes, and the He^+ number density therein is greatly intensified. At 1200LT, the poleward boundary has shifted to around 66°. This effect does not persist around the belt, and a lack of data means that the dynamics of this boundary cannot be investigated with this dataset. The maximum He^+ density appears to be about an order of magnitude higher than during quiet periods, and is centred at approximately 60-61°.

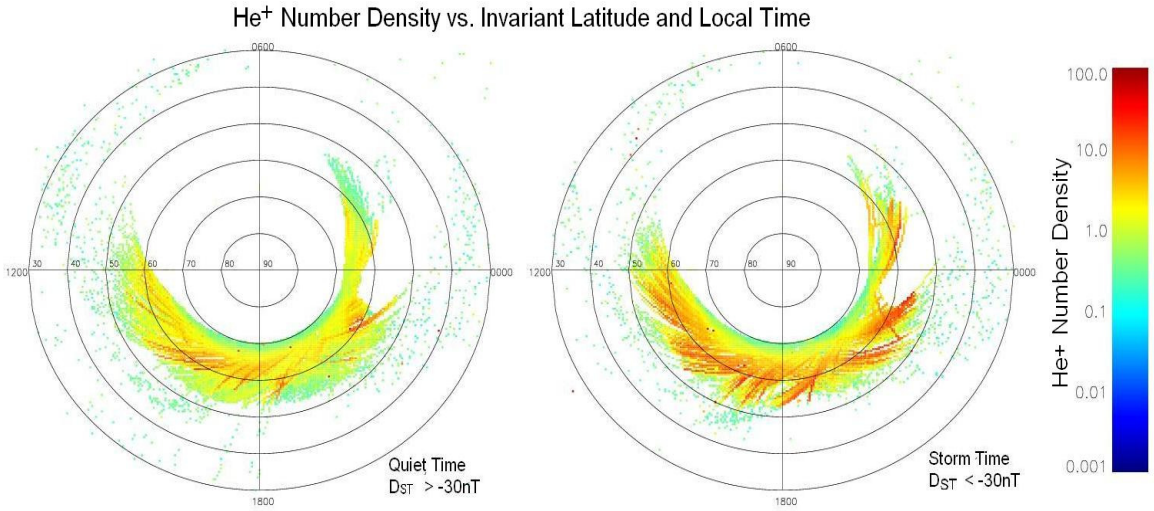

Fig. 3.1: He^+ number density vs. invariant latitude and local time for storm (right) and quiet (left). The ring current region can be seen between 55° and 70° during quiet time, and is more clearly visible during storm time with its density peak across 60°.

It is clear that during storm-time, the He^+ population of the outer radiation belt is intensified. This may be due to an outflow effect from the ionosphere, but it is also likely that there will be an increased rate of charge exchange for the reaction:

$$He^{++} + H \rightarrow He^{+} + H^{+} \qquad \text{Eq. 3.1}$$

This is probably due to the large influx of solar wind He^{++} associated with stormtime, alongside the earthward compression (and hence latitudinal decrease) of the belt, which moves into regions with a greater density of neutral hydrogen.

Figure 3.2 shows equivalent plots for He^{++}, in which outer belt boundaries are far more difficult to pinpoint. The range of number densities within these plots is similar to that of He^{+}. He^{++} is dominant over He^{+} at both high and low latitudes, but within the belt itself He^{+} exists in greater densities. This may be the result of the charge exchange reaction detailed in equation 3.1.

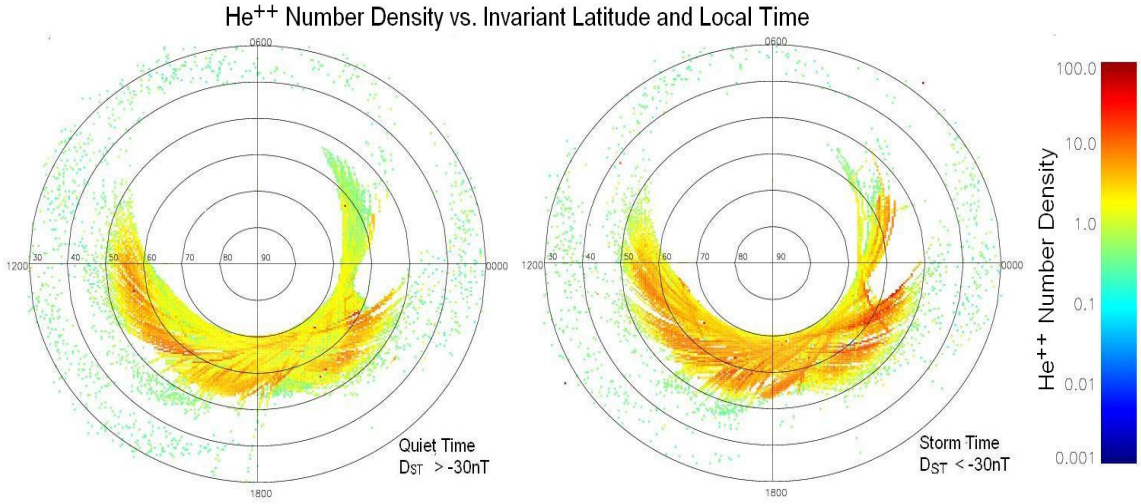

Fig. 3.2: He^{++} number density vs. invariant latitude and local time for storm (right) and quiet (left). The highly charged nature of He^{++} means it is not a terrestrial ion, its source being the Sun. A wider belt is observed in He^{++}, again increasing in number density during storm time. The migration to lower altitudes is less obvious in He^{++}.

A study of the number density of He^{++} compared to He^{+} across different storm phases will be conducted in section 3.6 of this chapter.

It has been well documented that a substantial amount of outer belt material is sourced from the ionosphere ([Daglis et al., 1999]), and much of the singly charged Helium may indeed have originated there. Figure 3.3 shows invariant latitude against local time and number density for O^{+}, a weakly ionised heavy element which is not present in the solar wind. It is clear from the plots that

O^+ is the dominant heavy ion in the outer belt, and far more so during storm time. Like He^{++}, distinct boundaries for the belt are hard to place. During quiet time, the largest O^+ number densities occur between 55° and 65°. Under storm conditions, the oxygen belt is intensified to a greater degree than both species of helium, and its equatorward boundary has shifted down to ~50°. From these plots it is clear that the ionosphere is responsible for a large percentage of the outer belt ion population for both storm and quiet periods.

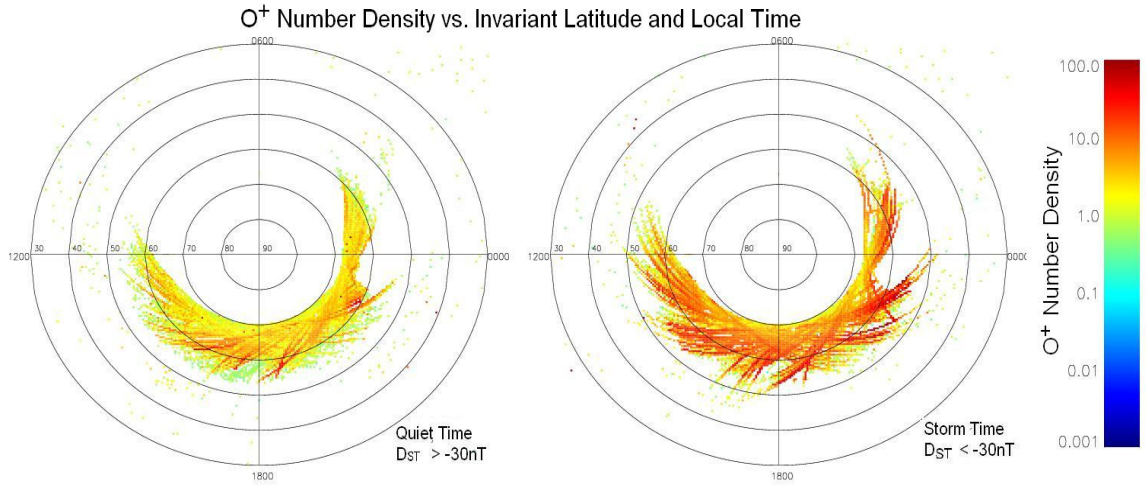

Fig. 3.3: O^+ number density vs. invariant latitude and local time for storm (right) and quiet (left). O^+ number density increases dramatically during storm time. As O^+ is a locally sourced ion, storm time must increase the rate of ionospheric outflow.

3.2.2 CRRES Electron Plots

Using the same method as above, electron data were also plotted. Figure 3.4 shows data for electrons of energy 4 – 5 MeV for storm and quiet time. The outer belt is very clear in this data, appearing as an enhancement in flux between 50° and 60°.

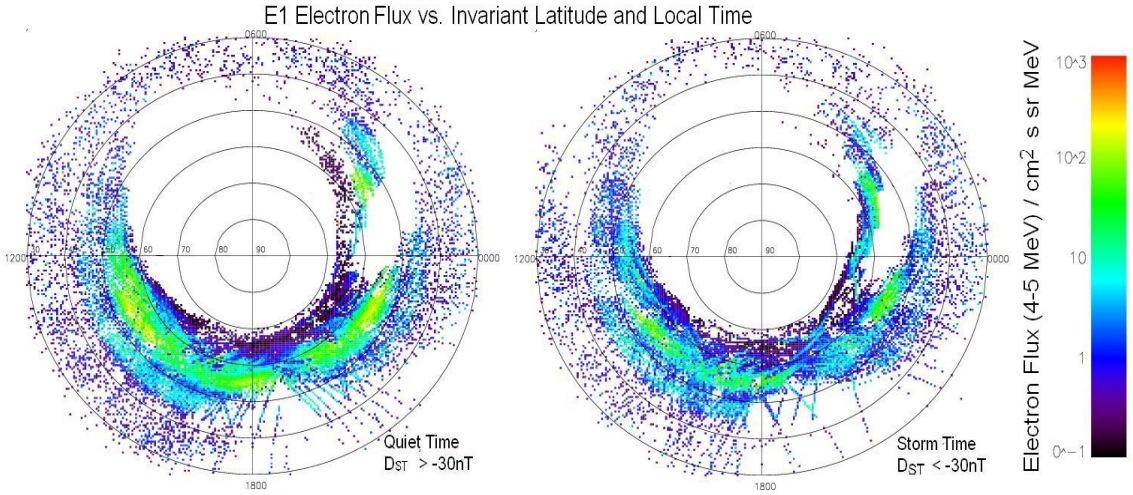

Figure 3.4: High-energy electron counts for storm (right) and quiet (left). Two clear belts are visible in these spectrograms, which are the result of the large magnetic storm of March, 1991. The latitude of the high energy electron belt is observed not to be dependant on storm index.

The maximum of the outer belt for these high energy electrons does not appear to be displaced by storm-level.

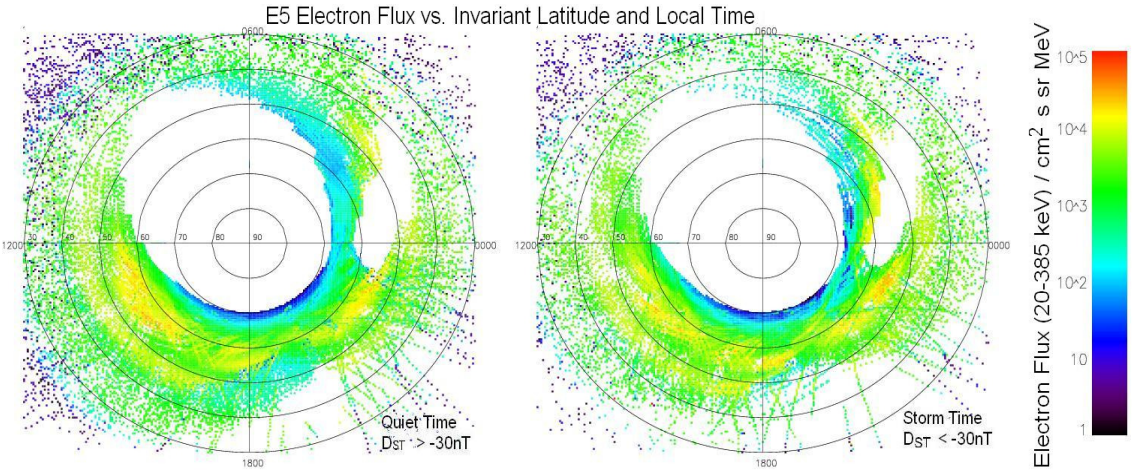

Figure 3.5: Low energy electron counts for storm (right) and quiet (left). These electrons are at the types of energies associated with substorm injections. Three belts are visible in these spectrograms, again the result of the large storm of March, 1991. During storm time, the electrons show a greater number density across midnight and in the dawn sector, but elsewhere the spectrograms do not show a great difference between storm and quiet.

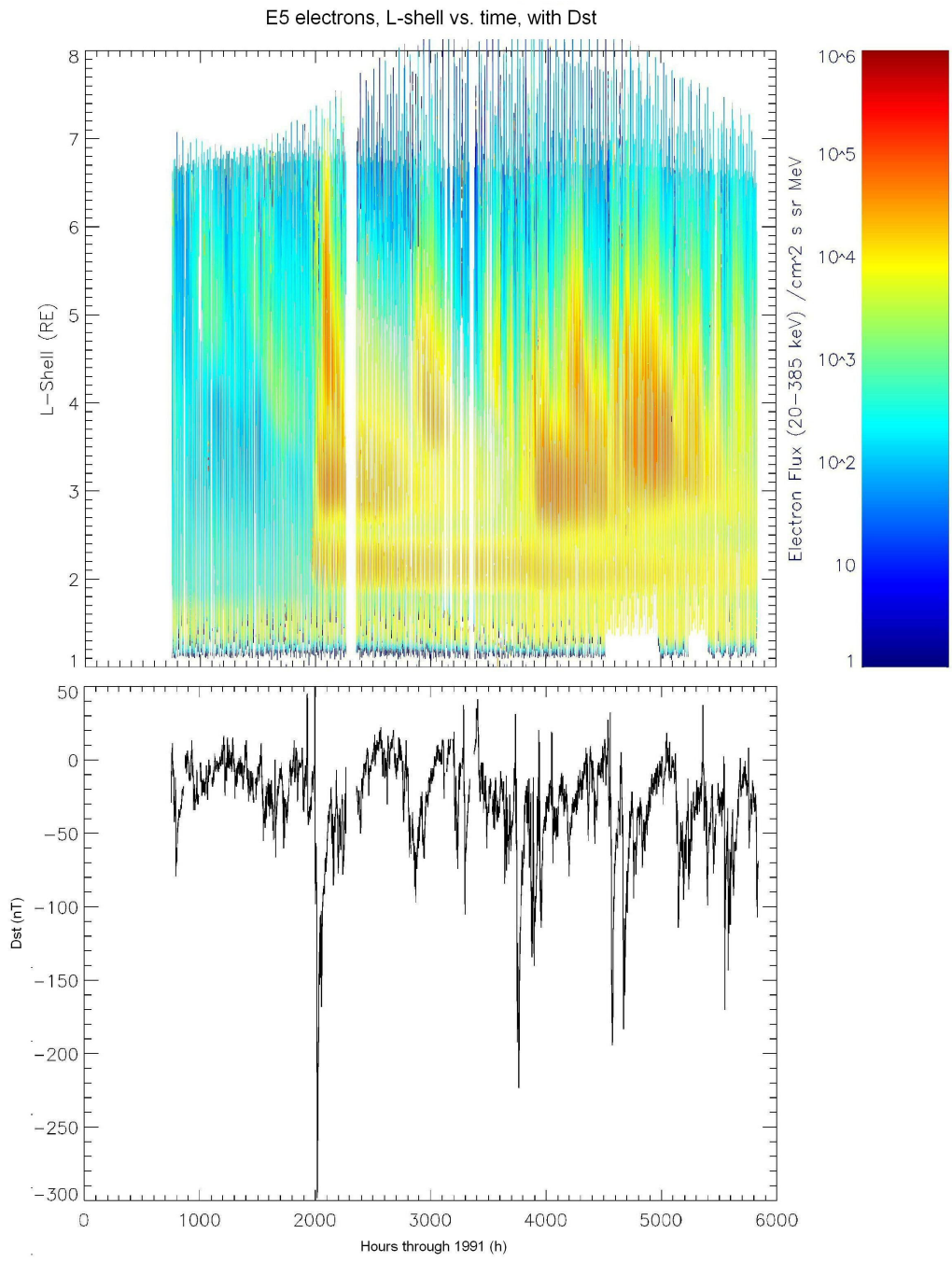

Figure 3.6: (Top) Low energy electron counts vs. L and time. (Bottom) D_{ST} across the same period. The magnetosphere is observed to fill with these substorm-energy electrons at storm onset. The large storm of March, 24th, 1991 (~2000 hours), creates multiple belts in L, the highest of which appears to move to lower latitudes with time. After each new storm, the belts refill.

Figure 3.5 shows data for electrons of energy 20 – 385 keV, which is the approximate energy range for substorm electrons. The outer belt appears to have split into two, with a dip in between. This occurred as a result of the large magnetic storm of March 24th, 1991. The number density of these low energy electrons is observed to greatly increase during storm time.

Figure 3.6 shows electrons of energy 20 – 385 keV, against L and time, as well as D_{ST} data for the period. At ~2000 hours, the large storm of March 1991 fills the magnetosphere with electrons. Initially the electrons appear to form three belts, which appear to diffuse inward, settling eventually into stable formations. The maximum altitude of belt formed appears to be a function of D_{ST}, with belts forming at higher altitudes during larger storms.

3.2.3 He^+/He^{++} Maximum in the Outer Radiation Belt

In a previous piece of work (unpublished), D. R. Lepine investigated the ratio of singly to doubly charged helium within the magnetosphere, using data from the MICS device on the VIKING satellite. In order for this, he used a quantity which he named the Charge Parameter:

$$Charge Parameter = \frac{N(He^+) - N(He^{++})}{N(He^+) + N(He^{++})} \qquad \text{Equation 3.2}$$

This is the difference in number density divided by the sum, and will always fall between 1.0 (He^+ dominant) and -1.0 (He^{++} dominant). Lepine also created an anisotropy parameter, which used the proton pitch angle distribution to determine the trapping stability in different regions.

Figure 3.7 is the result of his study, showing the average charge state distribution against invariant latitude and local time, using 80% of the quiet-time Viking dataset. A region of He^+ dominance over He^{++} is clearly visible within the region of highest trapping stability (the outer radiation belt). It was Lepine's belief that this maximum was primarily the result of the reaction given in equation 3.1.

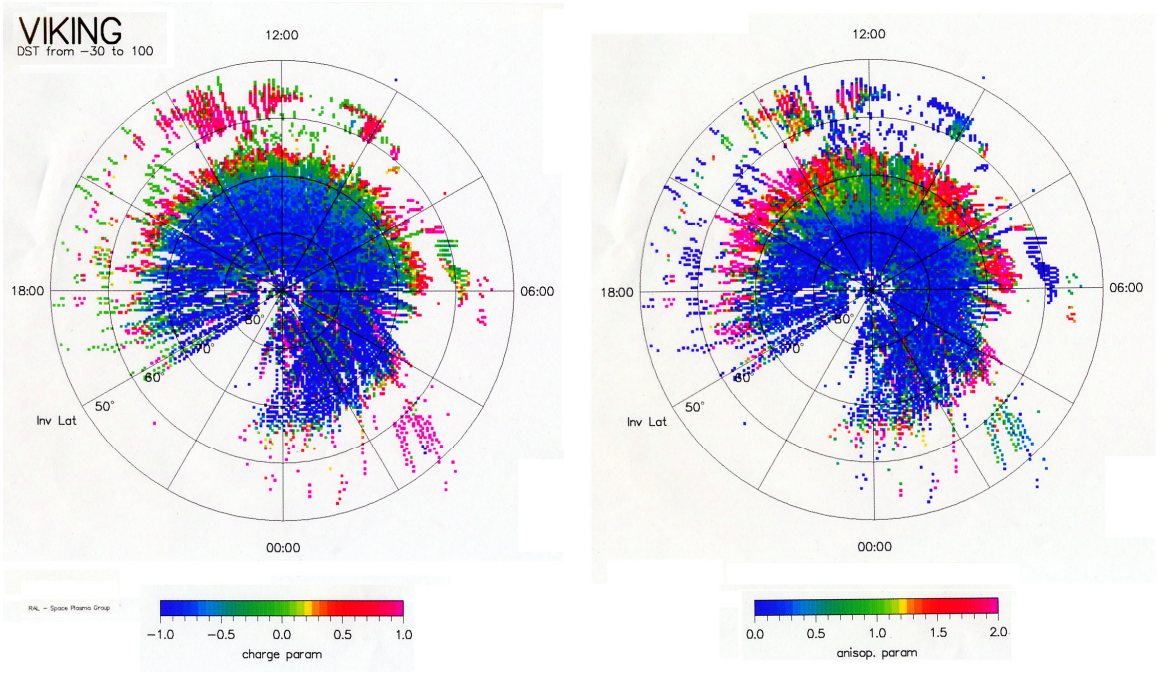

Figure 3.7: (Right) Anisotropy Parameter, showing the regions of greatest trapping stability. The location of the outer radiation belt can be clearly seen between approximately 65^o and 70^o latitude (from unpublished work by D. R. Lepine).
(Left) Charge parameter vs. invariant latitude and magnetic local time, using VIKING quiet time data. A clear He^+ maximum can be seen in the region of the outer radiation belt (as marked by the anisotropy parameter, centred at ~66^o), which Lepine believed was due to charge exchanged solar wind He^{++}.

Lepine's explanation of the effect observed in figure 3.7 involved inward radial diffusion of weakly trapped solar wind He^{++} ions, which would then undergo charge exchange with geocoronal neutral hydrogen within the region of stable trapping (the outer belt). Charge exchange lifetime was found to be a strong function of pitch angle, which may be explained by the higher density of neutral hydrogen at the altitudes of the mirror points associated with lower pitch angles. Within the paper, Lepine considers charge exchange to be the primary source of magnetospheric He^+.

3.2.4: CRRES Charge Parameter Plots

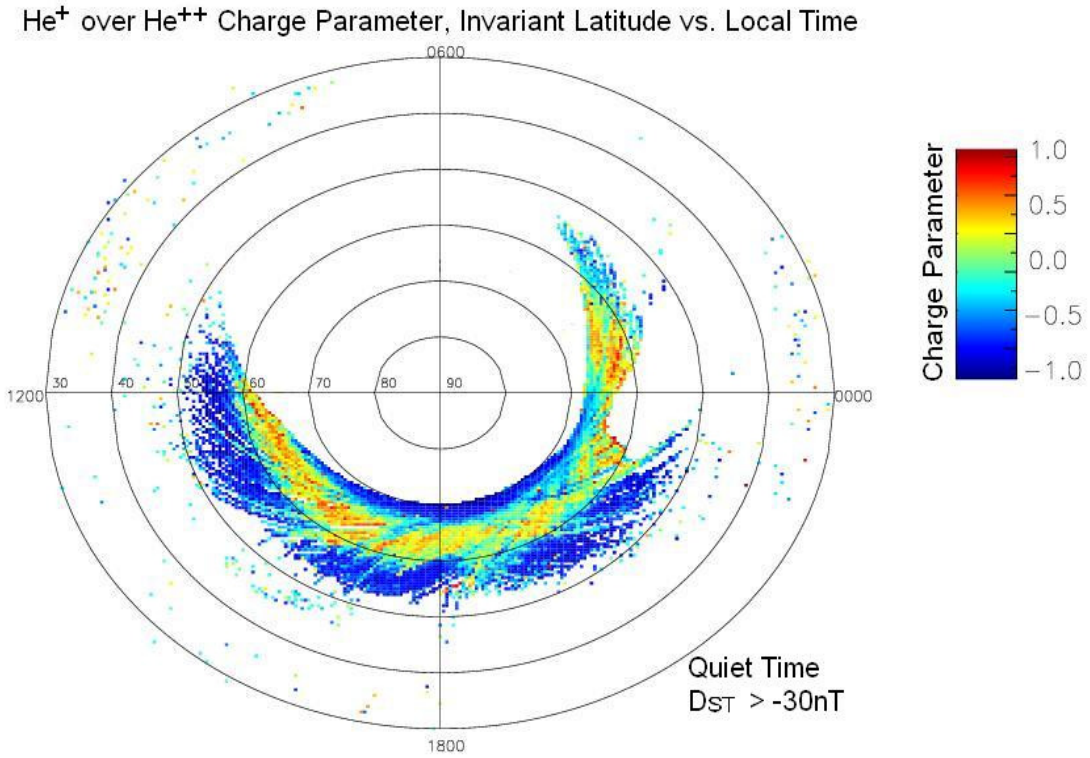

FIG. 3.8: Charge Parameter vs. Invariant Latitude and Local time during quiet time. He^{++} dominates over He^{+} at latitudes both lower and higher than the belt, but inside the belt, He^{+} is the ion of greater density. This is attributed to stable trapping of He^{++} followed by charge exchange with exospheric neutral Hydrogen.

Figure 3.8 shows the CRRES equivalent of Lepine's VIKING plot. It can immediately be seen that the maximum still exists; around 1500LT the belt is centred at approximately 63^{o}. The difference of ~4^{o} between this value and that measured by Lepine signifies a shift in L value of the central outer belt from $6.0R_E$ to $4.9R_E$. This is due to the stage of the solar cycle, with VIKING being in operation at solar minimum as opposed to CRRES at maximum. Due to the nature of CRRES's pitch angle sampling, no measurement of the degree of trapping stability could be made for the data. Figure 3.9 shows charge parameter against invariant latitude for stormtime data. The maximum is observed to move

to lower altitudes during periods of storm-activity, which is a feature of the outer belt. This gives evidence that the maximum is indeed located within this region.

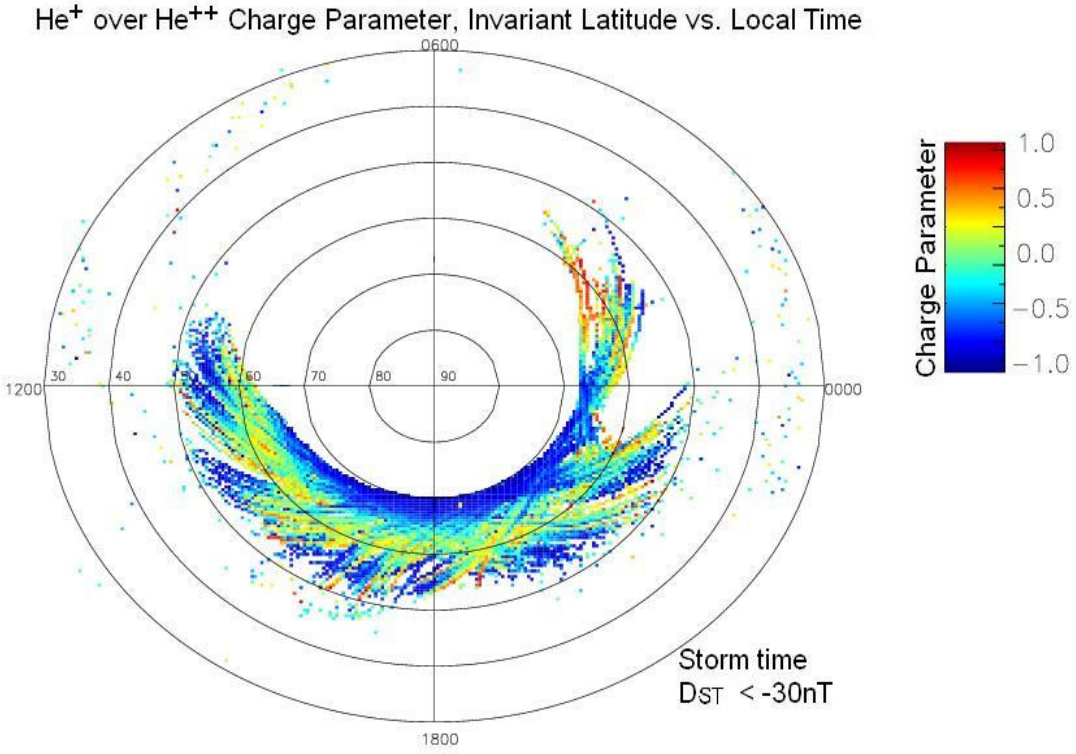

FIG. 3.9: Charge Parameter vs. Invariant Latitude and Local time during storm time. The He^+ maximum is observed to expand to lower latitudes, following the region of stable trapping. The highest latitude of the maximum is the same for storm and quiet.

In order to investigate the source of this magnetospheric Helium, the ratios of other ionic species were investigated. Figure 3.10 shows the ratio of O^+ to He^{++}, i.e. the ratio of particles of terrestrial to solar wind origin, for quiet and storm-time conditions. In both cases it can be seen that O^+ is dominant over He^{++} within the outer belt region, marking substantial ionospheric input regardless of storm conditions. The maximum is, however more pronounced in the stormtime plot, and the greatest values in the maximum region are certainly at lower latitudes during storm periods.

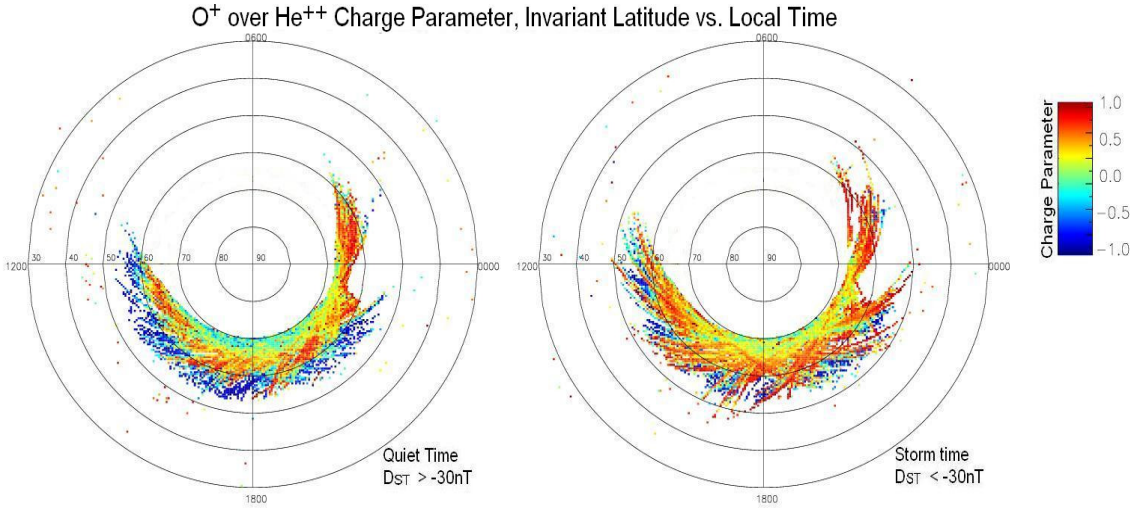

FIG 3.10: O^+/He^{++} parameter vs. invariant latitude and local time, for storm (right) and quiet (left). He^{++} again dominates at low latitudes, but within the belt O^+ exists in greater densities. Above the belt, O^+ is marginally more present than He^{++}.

It is clear that the ion population of the outer belt is strongly of ionospheric origin at all times, as evidenced by the high concentration of O^+ as compared to He^{++}. He^+ is also present within the ionosphere, and should, therefore, also enter the outer belt via the same processes which allow O^+ to do so. Figure 3.11 shows the ratio O^+/He^+ for both storm and quiet conditions. In the case that the He^+ was completely of ionospheric origin, one would expect to see a relatively flat ratio throughout the magnetosphere, as the outflow ratio for both ions should be the same. It can clearly be seen that this is not the case, with O^+ having substantially greater number densities at latitudes greater than the belt (higher altitudes), while in the region of the belt itself their number densities appear to be fairly similar.

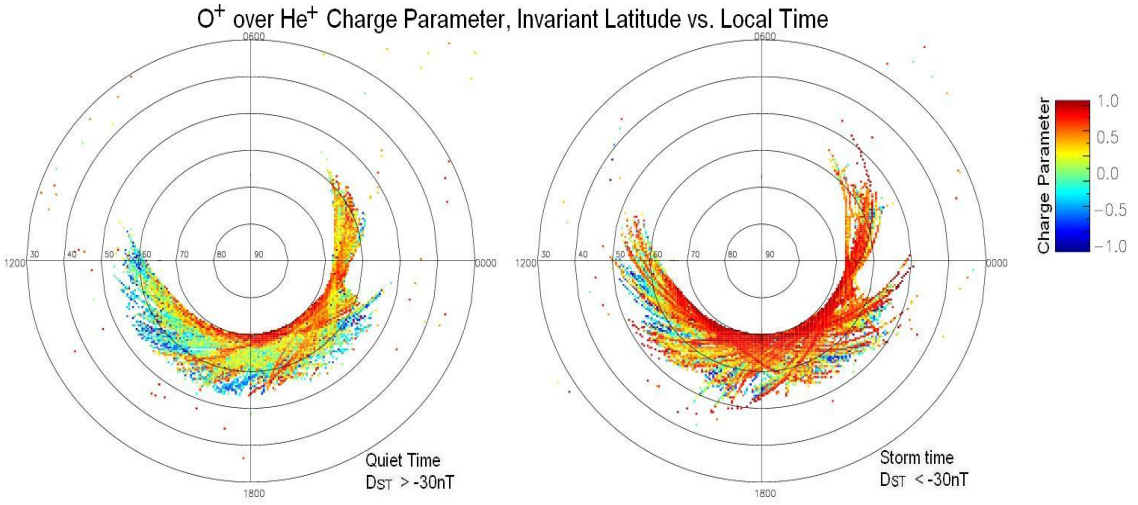

FIG. 3.11: O^+/He^+ parameter vs. Invariant Latitude and local time, for storm (right) and quiet (left). O^+ dominates over He^+ at high latitudes, indicating a large amount of terrestrial material at high altitudes. Within the belt region, He^+ exists at similar densities to O^+. The lack of a nearly-flat ratio across all L suggests a different source mechanism for these ions.

Charge exchange will only be observed for ionic populations trapped in stable drift-orbits. The plots of number density ratios against invariant latitude and local time give evidence that, in the region of greatest trapping stability, charge exchange acts as a source of He^+.

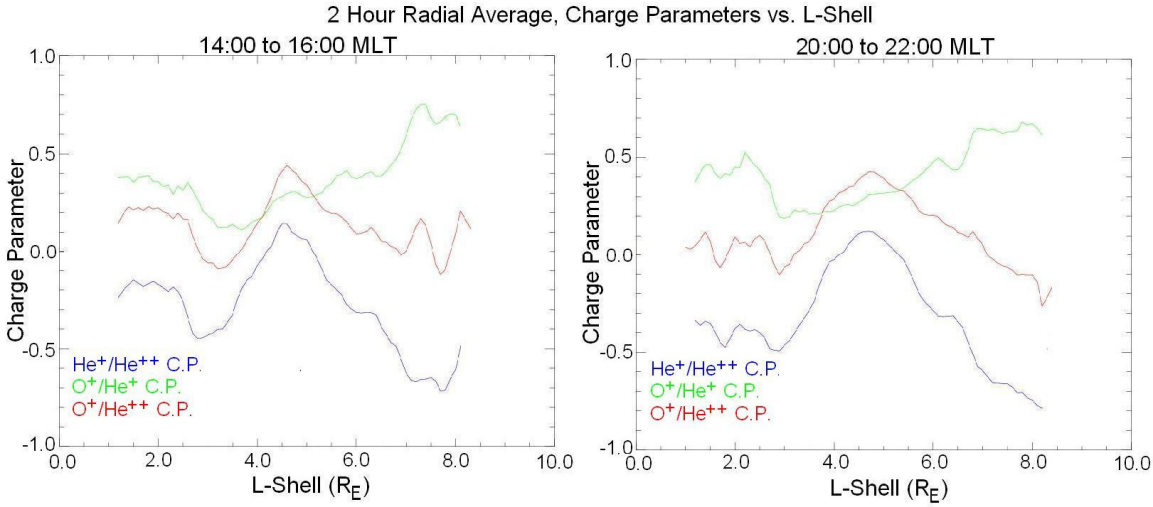

Fig 3.12: Radial plots of 2-hour Local time averages from 1400 to 1600 MLT (left); and 2000 to 2200 MLT (right). The red, green and blue lines show He^+/He^{++}, O^+/He^{++} and O^+/He^+, respectively. The Dip in O^+/He^+ is shown to correlate with the peak in He^+/He^{++}, indicating that they occur across the same latitudinal region.

Figure 3.12 shows two-hour radial averages during quiet time through the invariant latitude ratio plots, from 1400 to 1600 MLT (left) and 2000 to 2200 MLT (right). The latitude of the maximum charge parameter in He^+ / He^{++} is similar to that of O^+ / He^{++} (the outer belt region). At similar latitudes, O^+ / He^+ charge parameter appears to dip. This dip signifies that the source of the outer belt He^+ cannot be the ionosphere alone, or else O^+ / He^+ would display a flat ratio within the region.

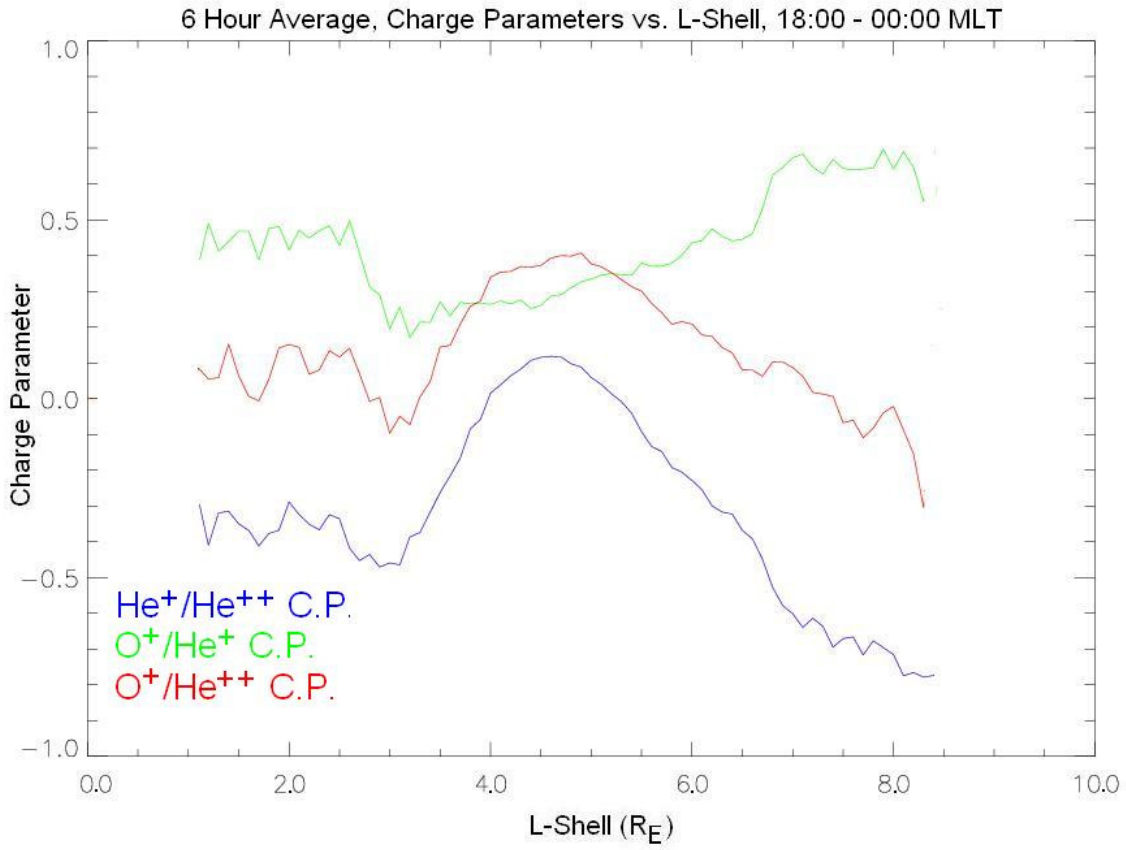

Figure 3.13: Overall radial average between local times of 1800 and 0000 MLT. O^+/He^+ (green) is shown to anticorrelate with the He^+/He^{++} (blue). The spike in O^+/He^{++} (red) in the same region confirms that the dip in O^+/He^+ is not due to a lack of O^+.

Figure 3.13 shows the average of three ratios between 1800 and 0000 MLT against latitude during quiet time. It is again clear that there must be a further source of He^+ in the outer belt region.

3.3: Stormtime Dynamics of the Charge Parameter maximum

3.3.1: CRRES Helium Ratio vs. D_{ST}

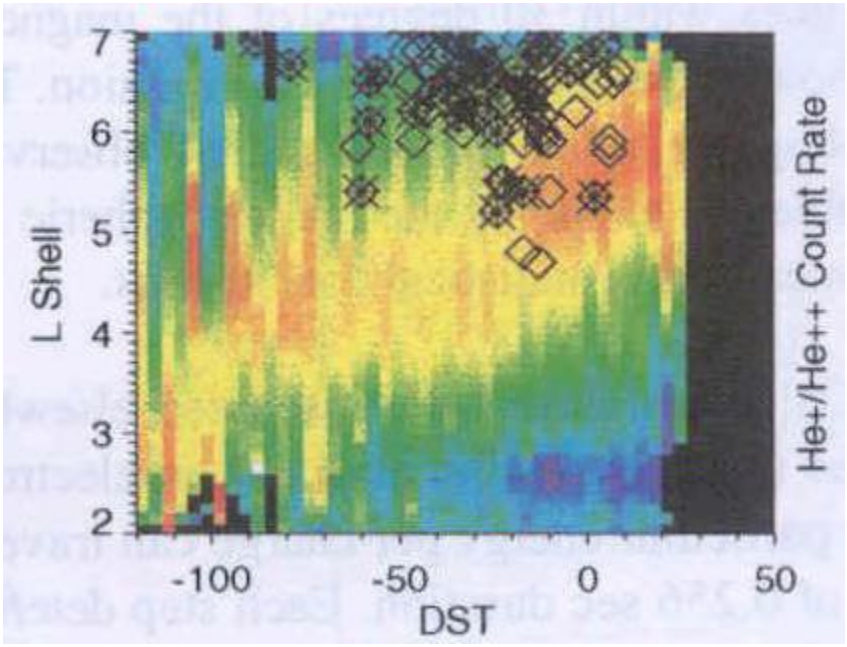

FIG. 3.14: [Grande et al., 1997] plot of Helium charge-state ratio vs. L and D_{ST}. The He^+ maximum is observed to drop to lower L-shells during storm periods, following the location of the region of stable trapping.

Figure 3.14 is a plot of He^+/He^{++} from previous work by [Grande et al., 1997]. Within this plot, the shifting in L of the maximum in number density ratio He^+/He^{++} with D_{ST} can be seen.

3.3.2: Charge Parameter vs. L and D_{ST}

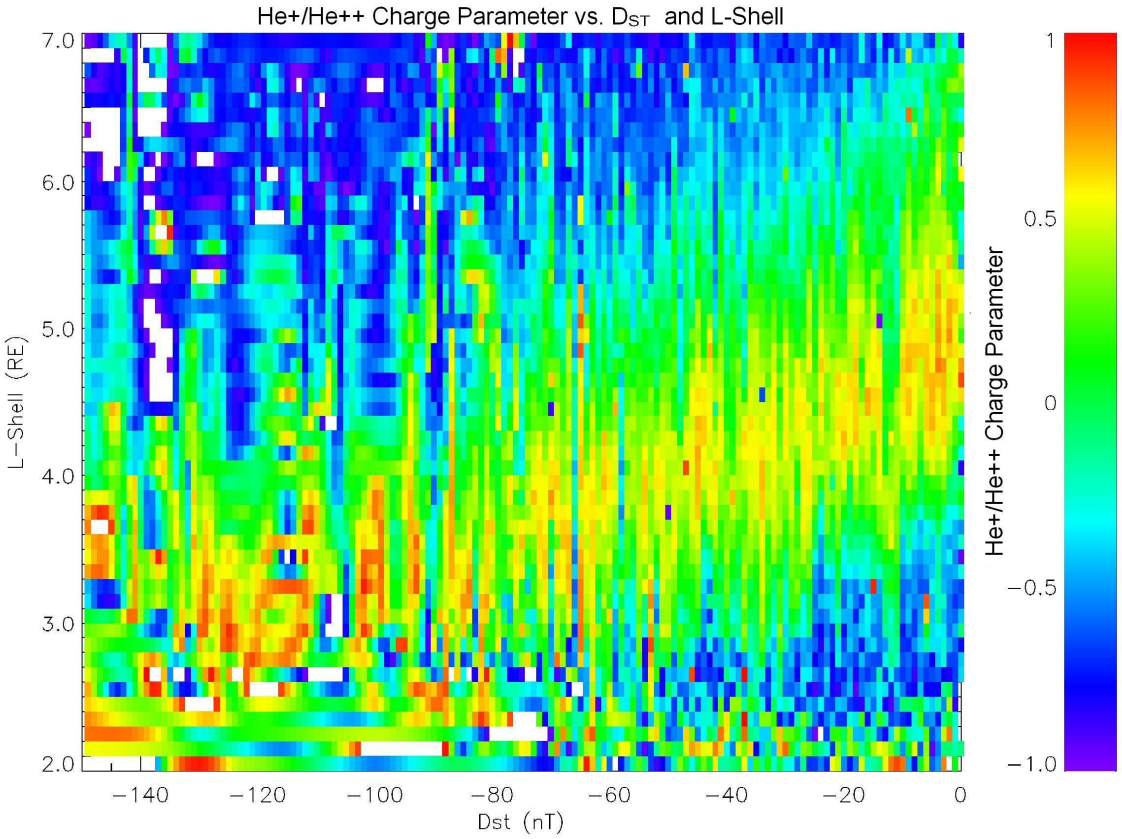

Figure 3.15: Helium Charge parameter vs. L and D_{ST}. The same correlation as can be seen in 3.14 is seen using the charge parameter, with the He^+ maximum moving to lower L-shells during storm time.

Figure 3.15 shows a CRRES plot of the helium charge parameter against L-shell and D_{ST}, using data from January to September, 1991. The region of He^+ dominance over He^{++} is again clearly visible, and is observed to move to lower altitudes with increasing storm activity. This is a well known feature of the outer belt during stormtime, and gives further evidence that the He^+ charge maximum exists within that region. The maximum in He^+ exists for all amounts of storm activity. It was predicted that less charge exchange would occur during quiet time, due to the greater altitude of the belt, but this appears not to be the case. It is possible that the difference in Hydrogen density due to the stormtime altitude

shift is small compared to the large Hydrogen densities reached by all low-pitch angle particles.

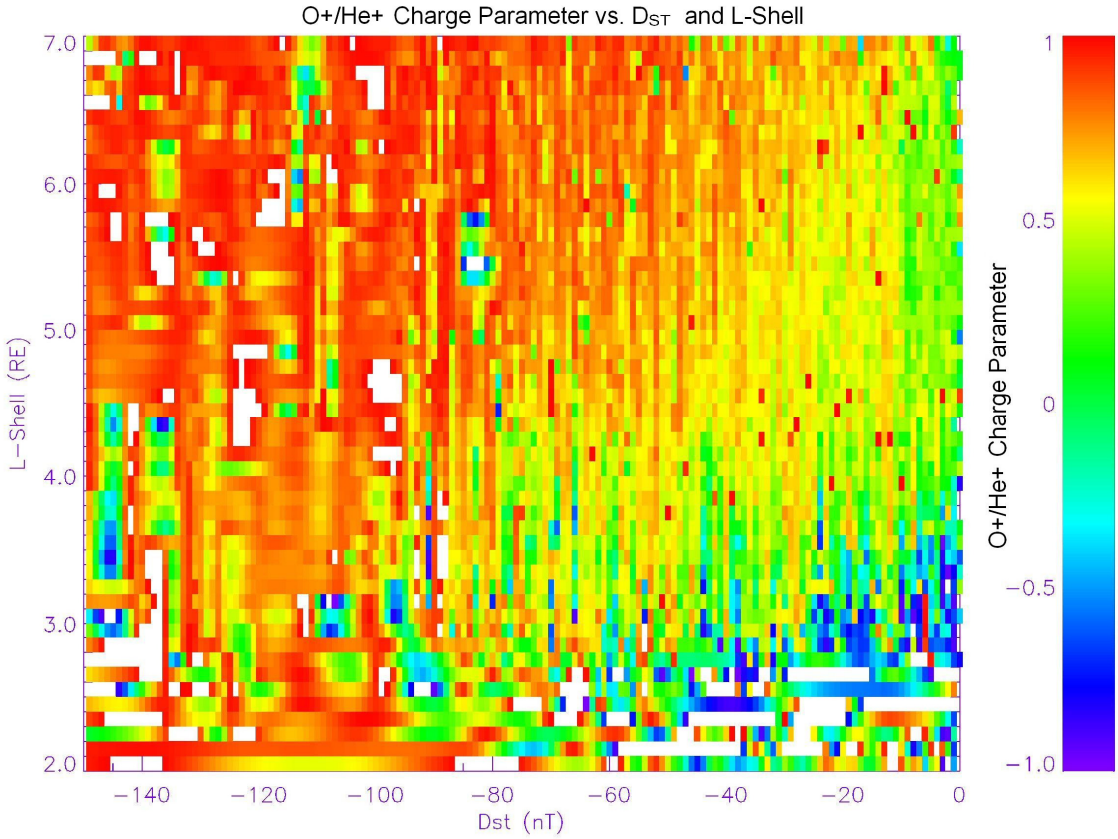

Figure 3.16: O^+ / He^+ parameter vs. L and D_{ST}. O^+ dominates over He^+ at high altitudes, especially during storm time. In the region of the belt, He^+ exists in approximately the same density as O^+. At L~3R_E, The dip in ratio shows a lack of O^+ rather than an abundance of He^+ (He^+ exists in greater density than the other species here). O^+ fills this region during storm time.

Figure 3.16 is the same type of plot as 3.15, showing O^+ against He^+. O^+ is observed to dominate over He^+ at high altitudes, and shows an increase in number density during stormtime. The He^+ maximum can also be seen in this plot, where the ratio begins to favour O^+ less.

3.4: Charge Exchange in CRRES Injections and Drift Echoes

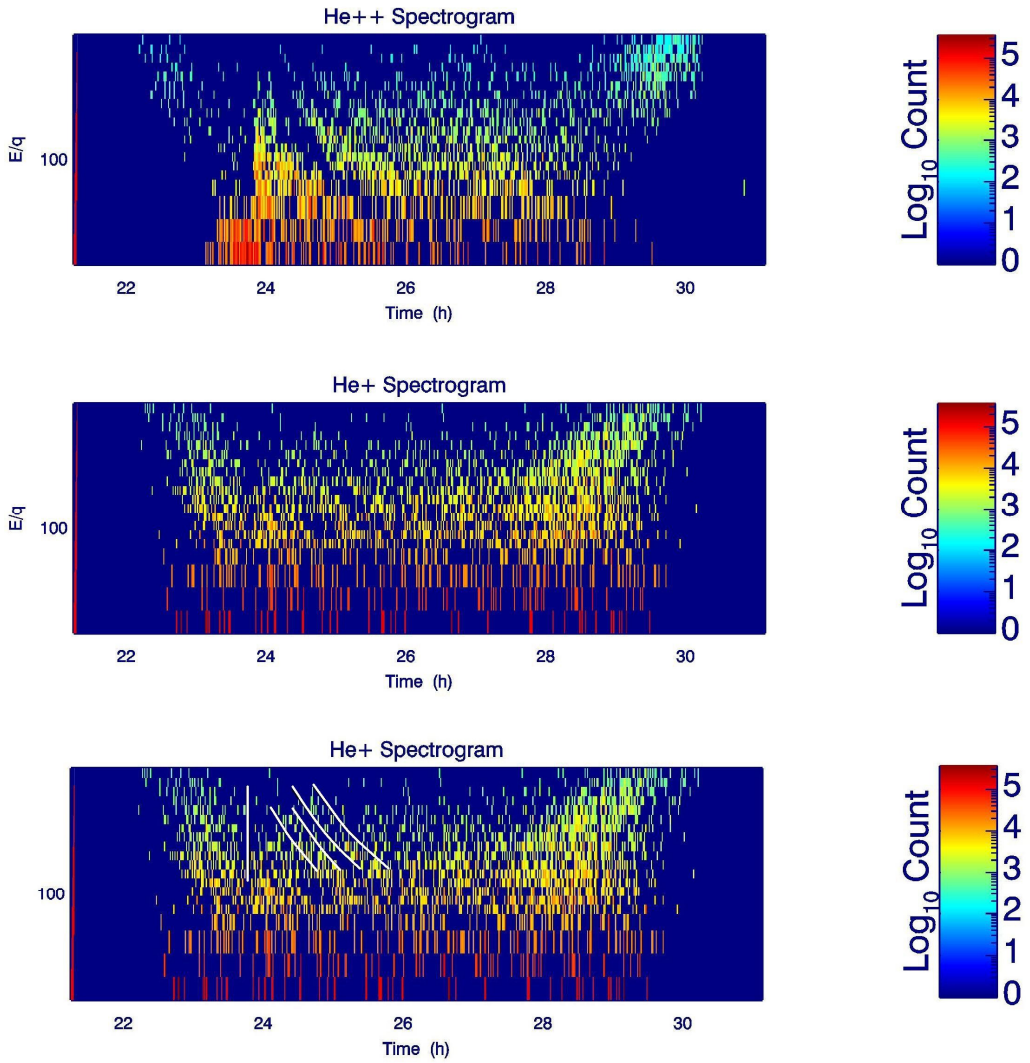

Figure 3.17: Spectrogram of Orbit 497 of CRRES, showing He^{++} (top), He^{+} (middle) and He^{+} with new population marked (bottom). Although He^{+} is not present in the injection, clear drift echoes are observed in after the ions have orbited. These are marked in the bottom spectrogram.

Figure 3.17 shows the E/q spectrograms of He^{+} and He^{++} for orbit 497 of CRRES, taken on 14th and 15th February, 1991. The dispersionless substorm injection that occurred at ~23:50 UT has been studied before by [Grande et al., 1992]. Following the injection, the newly introduced population drifts around the Earth, and is observed by CRRES again as a dispersed drift signature. The E/q range for the He^{++} in the injection reaches a maximum of ~240 keV, while the

He^+ reaches only ~140 keV. Within the first drift echo, however, a clear He^+ arc can be seen, reaching energies not observed in the injection. The possibility that this new He^+ population is the result of He^{++} undergoing charge exchange by the reaction in equation 3.1 is suggested. If charge exchange is responsible, it will be possible to calculate the cross section for the reaction. This is carried out in chapter 4 of this thesis.

3.5 Average Helium Ratio with MLT between L of 4 and $5R_E$

If the drift echo in orbit 497 does contain evidence of charge exchange, one would expect that, on the timescale of a single drift, there would be a small difference in the average number density either side of midnight. If injections are assumed to occur at exactly midnight (this would be a more reasonable assumption for quiet time, as during storm time the injection will often spread across midnight), the westward drift of the ions would imply that, as one travels anticlockwise through the belt, each MLT sector would be expected to contain more He^+ as compared to He^{++}, i.e. charge exchange could be mapped to occur as you follow a population of ions. The amount of He^{++} entering the outer belt due to inward radial diffusion is assumed not to differ with local time. Figure 3.18 shows the quarter-MLT average of charge parameter between L of 4 and $5R_E$ for quiet and storm time. The L-shell range of $4R_E$ to $5R_E$ is the approximate low-altitude section of the outer radiation belt, where the density of neutral hydrogen is greatest and the greatest rate of charge exchange would be expected.

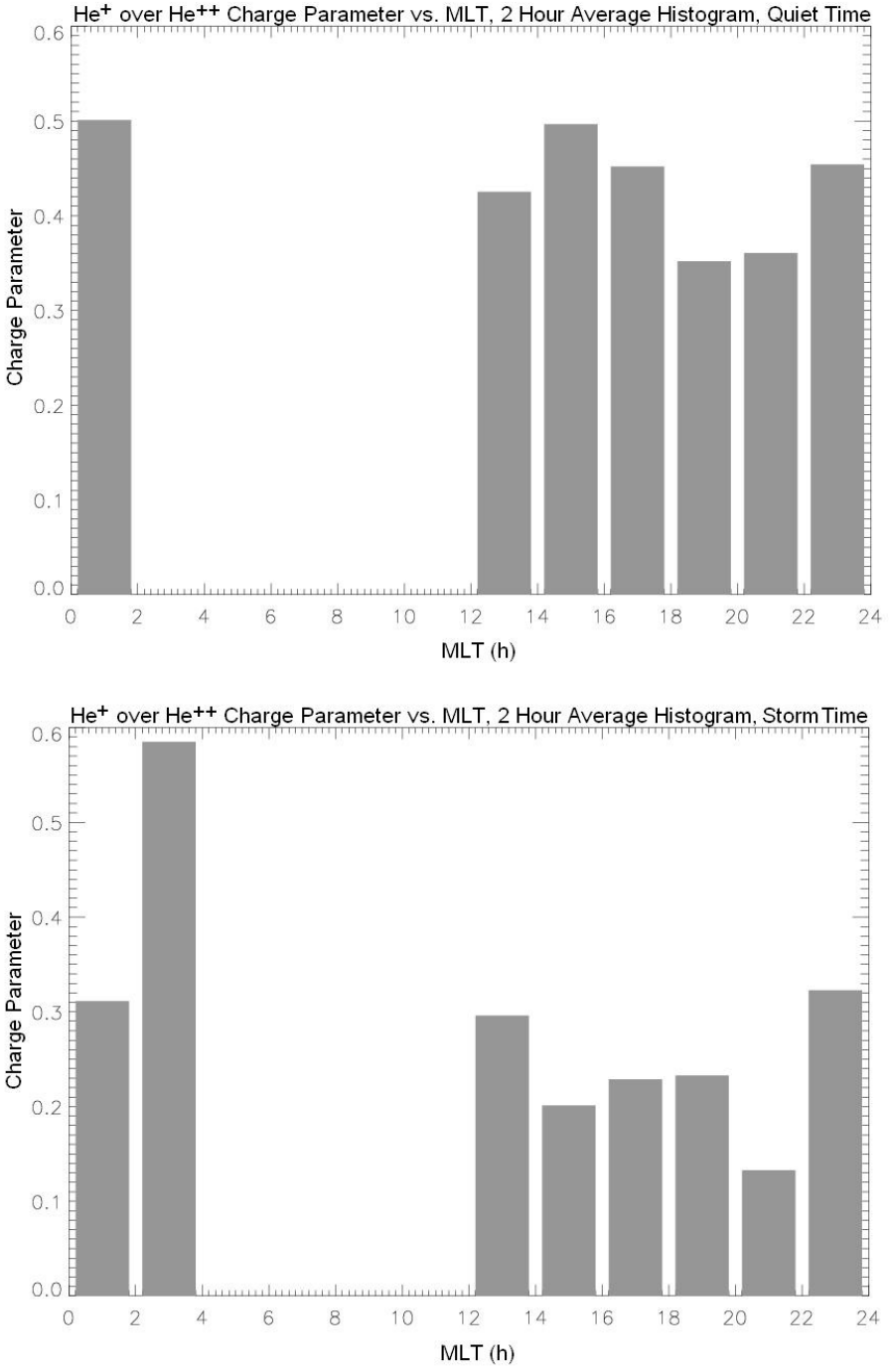

Figure 3.18: 2-hour local time average histograms of charge parameter between L = $4R_E$ and $5R_E$ for quiet (top) and storm (bottom). The gap between 0400 and 1200 MLT is due to CRRES's orbital limitations. During quiet time there appears to be very little evidence of charge exchange for drifting ions. During storm time, the large jump between 1200 and 0400 MLT may be evidence of charge exchange, but this cannot be verified due to MLT limitations. The mean error for each two-hour average was found to be of the order of 10^{-3}, and was hence negligible.

The quiet time plot in figure 3.18 shows a steady increase in the charge parameter in the anticlockwise direction between 2200 and 1200 MLT, which could be evidence of charge exchange. The stormtime plot in figure 3.18 may show a general progression towards He^+ in a westward direction, if the hours across midnight are assumed to be polluted with injected particles. The large MLT gap removes the possibility to test whether this progression is due to charge exchange.

3.6 The Shift in Number Density after a Single CRRES Orbit

3.6.1 Introduction to the Investigation

In the previous section it was shown that there is an average shift in the charge parameter (ratio of ionic helium species) of ~0.003cm^{-3} from He^{++} towards He^+. If all other source/loss mechanisms of the ions are considered equal in ratio, this indicates that charge exchange is occurring to a measurable degree on the timescale of a single drift orbit (~1 hour at outer belt energies). If this is the case, then charge exchange will certainly be observable across the timescale of a single orbit of the CRRES satellite (~10 hours). In this section, a study of the relative number densities of He^+ and He^{++} will be carried out across each subsequent orbit of CRRES, with the large particle influxes associated with stormtime being filtered out of the data using D_{ST} signatures. The prediction is a general shift from He^{++} towards He^+ due to charge exchange.

The CRRES orbit ranged from L ~1.1R_E to ~8.0R_E. The L range of the outer radiation belt is between ~5.0R_E and 7.0R_E, though this is dependant on the amount of storm activity at the time. For this study, the number density of ionic species He^+, He^{++} and O^+ will be considered between L-shells of 5.0R_E and 7.0R_E during the part of the orbit following apogee and the part of the next orbit preceding apogee. This is done in order that the outer belt is comparable with as little source/loss influence, other than charge exchange, as possible, and is shown in figure 3.19.

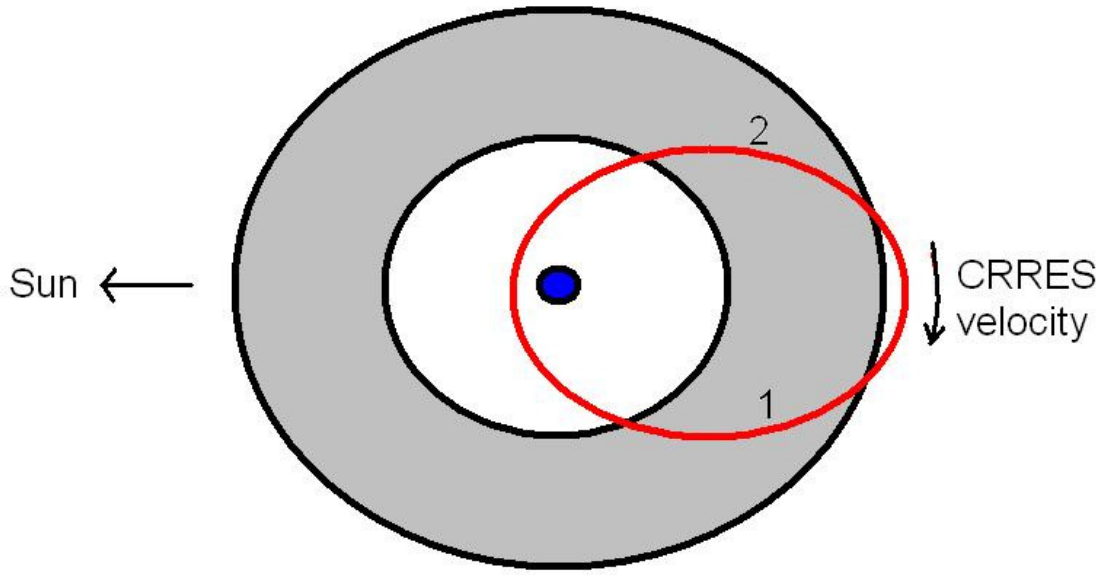

Figure 3.19: an example of a CRRES orbit (red) through the ring current region (grey) is shown. As CRRES passes its apogee, the helium ratio within the belt will be analysed from L= 7.0R_E to 4.0R_E. After passing its perigee, the helium ratio will be found again between these L values. Evidence of shifts from one species to the other will be sought.

3.6.2 Shifts in Number Density and What They May Mean

In order to investigate the number density shift across the timescale of a CRRES orbit, the number density of each ion species will be averaged between L = 5.0R_E and 7.0R_E, and compared across subsequent orbits.

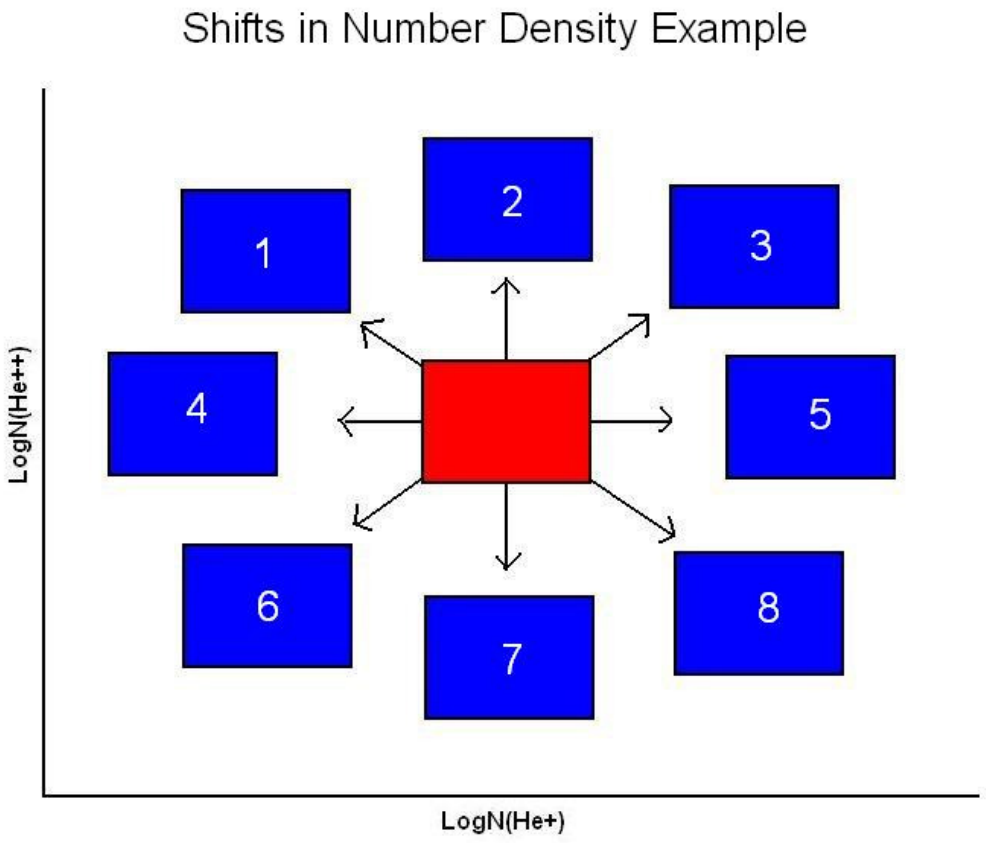

Figure 3.20: Example plot of He^{++} vs. He^{+} number density. The Red region indicates the location of the average number density during the ring current passing after apogee (region 1 from figure 3.19), and the blue regions indicate each possible shift after a CRRES half-orbit (region 2 from figure 3.19). Some shifts can be taken as evidence of charge exchange.

Figure 3.20 shows an illustrative plot of the number density of He^{++} versus that of He^{+}. The central box on the diagram, labelled '1st outer belt visit', represents the population of the outer belt during CRRES's first visit to the outer belt. The surrounding boxes, labelled 1 – 8, are theoretical number densities to which the population could change after the orbit, to be detected by the MICS device when CRRES returns to the outer belt.

Scenario 8 could be taken as evidence of pure charge exchange, with He^{++} being directly converted to He^{+}. As He^{++} and He^{+} will both scatter as a result of other mechanisms, it can be argued that scenario 7 also provides evidence for

the process. All other scenarios involve either an increase in He^{++} or a decrease in He^{+}, and hence would not provide evidence of charge exchange in this study. Finally, there may be no change in number density after the orbit, whereby the population recorded during the second part of the orbit exists within the same location as that recorded during the first. This, of course, provides no evidence for charge exchange.

In order that a charge-exchange study can be correctly carried out using these plots, occasions where there has clearly been an additional input of ions must be discounted. It can easily be seen in the plots themselves when this has occurred, with an increase in He^{++} and/or O^{+} ions not having a likely charge-exchange source. It is possible that some He^{+} ions may lose electrons and become He^{++} ions, or that a solar wind O^{++} population may undergo reactions and become O^{+}, but due to the far lesser chance of either of these processes occurring regularly in the magnetosphere, large increases in either ion will be due to another source. Most of the orbits which involve a new population of particles occur during storm-time, meaning the D_{ST} would be a good parameter by which charge-exchange orbits could be selected. Quiet-time injections of new populations also occur, however, so further care will be required.

3.6.3 Example Orbits for Different Storm Phases

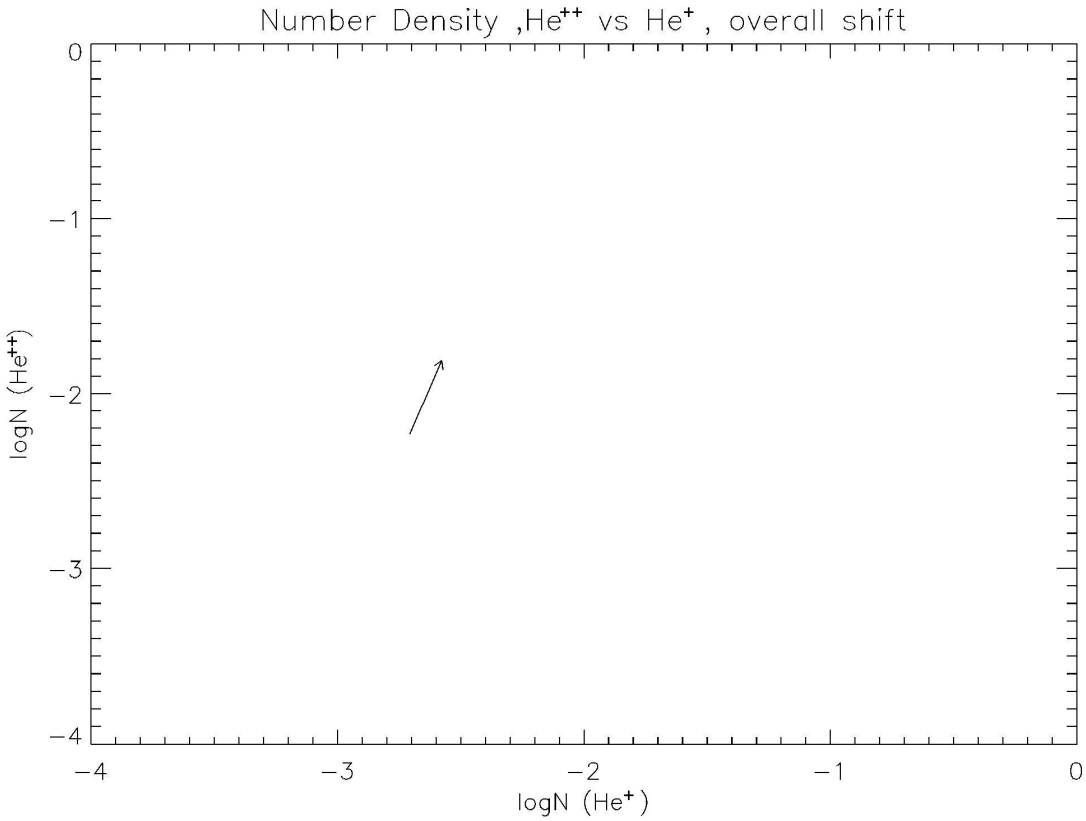

Figure 3.21: CRRES orbit 588 to 589: He^+ vs. He^{++} number density. This shows data taken across the main phase of a magnetic storm. The number density of both ions increases, as would be expected.

Figure 3.21 shows the number density plot of He^+ versus He^{++} across orbit 588 and 589 of CRRES (day 83 of 1991), both taken on 24th March, 1991. On this day, the main phase of the largest storm in the CRRES era occurred. In the figure, the number densities of both species increases, which was expected, as the ion density within the outer belt is known to increase during the main phase of storms. It is expected that all ions will display an increase during storm main phase.

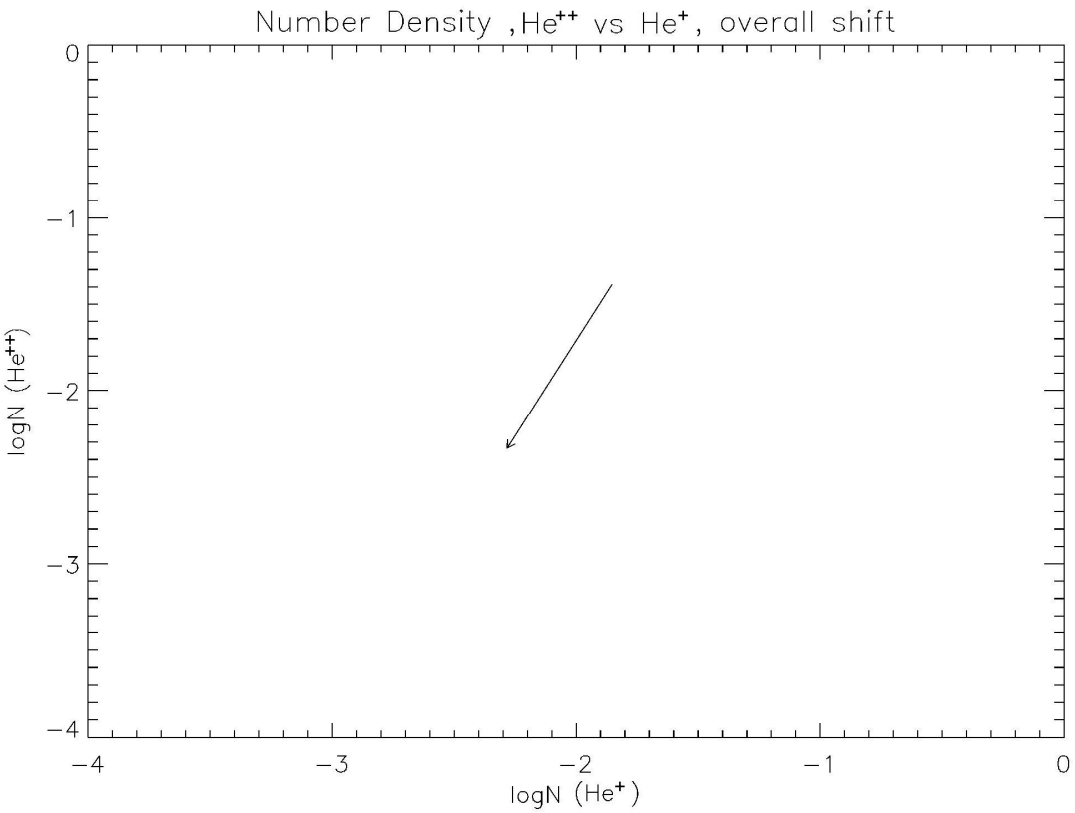

Figure 3.22: CRRES orbit 590 to 591: He^{+} vs. He^{++} number density. This data was taken during the recovery phase immediately following the main phase. A rapid reduction in number density is observed for both ionic species.

Within the period immediately following the main phase of the storm, a temporary rapid recovery begins. Figure 3.22 shows the number density data for orbit 590 to 591, which covers this period. Both ionic species are observed to be rapidly lost during this early part of the recovery phase, with He^{++} decreasing by ~1.0 x $10^{-1}cm^{-3}$ and He+ by 3.6 x $10^{-2}cm^{-3}$. The difference is possibly a result of He^{++} becoming He^{+} due to charge exchange.

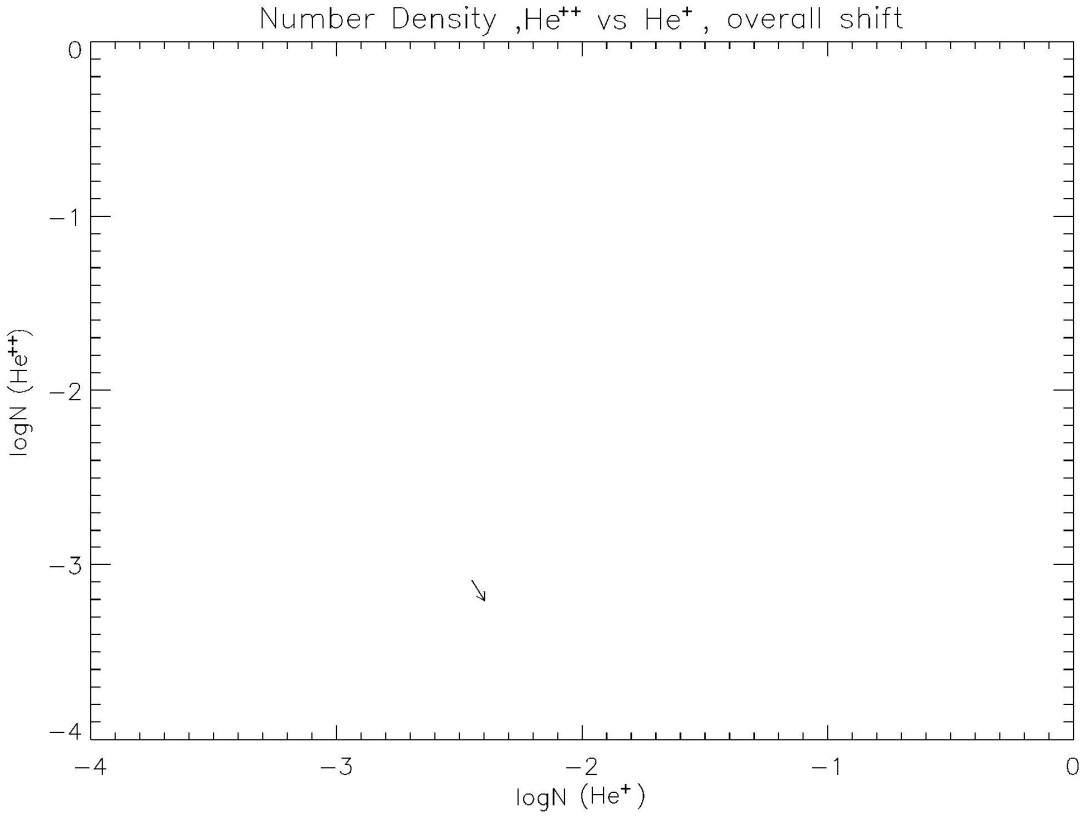

Figure 3.23: CRRES orbit 599 to 600: He^+ vs. He^{++} number density. Data in this plot is taken from a smooth section of the recovery phase. A small decrease in He^{++} is coupled with a small increase in He^+. This is taken as evidence of charge exchange.

Nearing the end of the recovery phase, the D_{ST} gradient is far less steep, and the loss rate of ions is far less than during the early recovery phase. Figure 3.23 shows the shift in number density from orbit 599 to 600, during which period the D_{ST} was undergoing a smooth increase. A small decrease in He^{++} density is coupled with a small increase in He^+ density, which gives evidence for a recovery phase source of He^+, suggested here to be charge exchange. These are only discrete cases, however, and the general shifts in helium populations will be better displayed using an average.

3.6.4 Number Density Shifts for Storm and Quiet Time

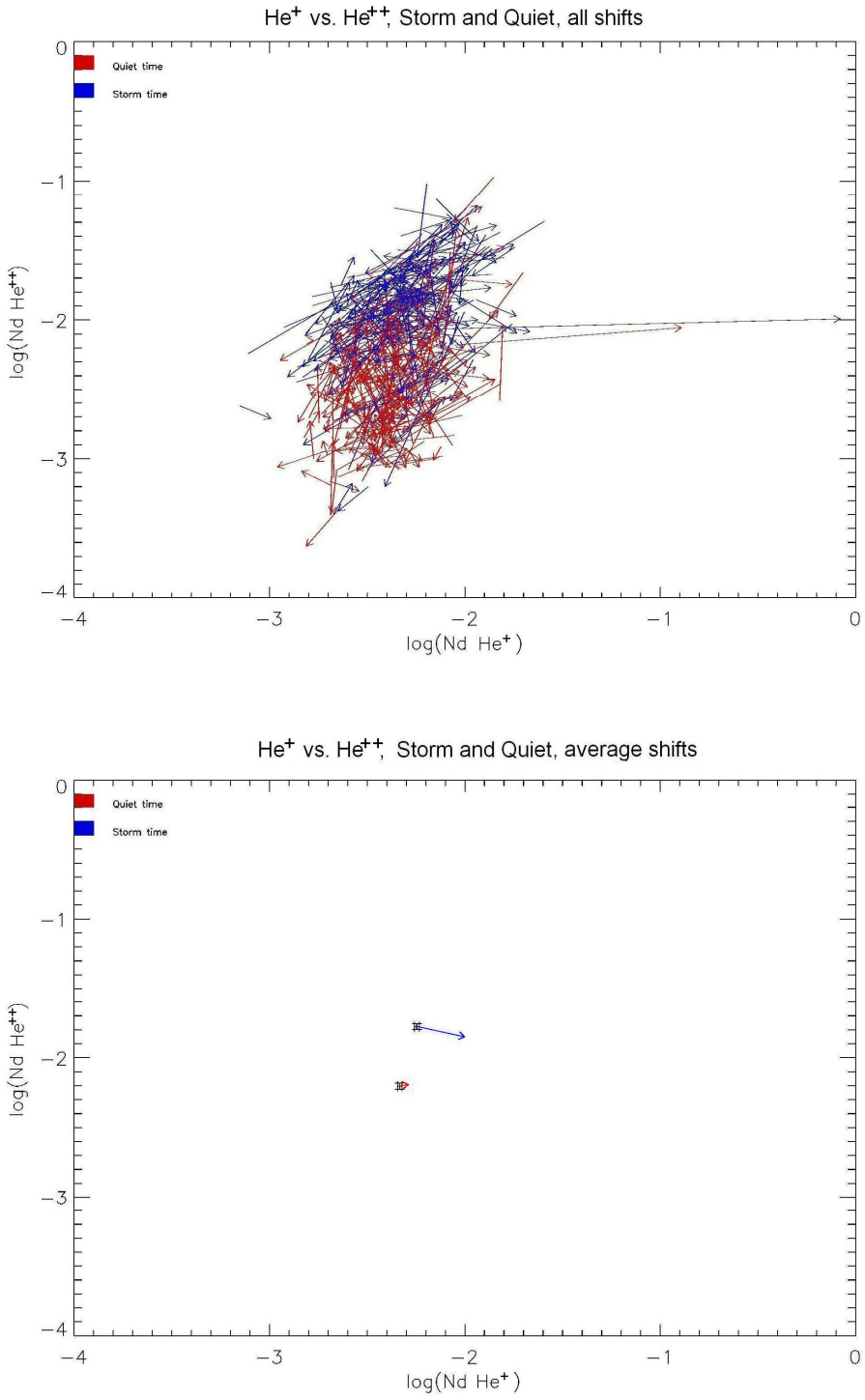

Figure 3.24: (Top) All number density shifts for storm (blue) and quiet (red). (Bottom) Average shift in number density for storm (blue) and quiet (red). The average shift shows a net loss of He^{++} and a gain in He^{+} during storm time. The tiny shift during quiet time is taken as evidence of a steady state for source and loss.

Figure 3.24 shows separate plots of the log of He^{+} vs. He^{++} number density, for data taken during periods of storm and quiet time, where the average D_{ST} across the period of investigation was < -30nT and > -30nT, respectively. Also shown is the average of these swarms of vectors. In the swarm plot, each arrow signifies the number density shift from one orbit of the CRRES satellite to the next. The pair of vectors in the average plot show the overall average of the swarm, with the error bars showing the standard error on the mean. For both storm and quiet time, it is observed that number densities occur in similar regions of the plot, though during stormtime the bulk of the vectors signify higher number densities than during quiet time. This is reflected in the higher number densities during stormtime in the average plot.

The magnitude and direction of the average shift in number density may give further information regarding the outer belt population. During quiet time there is very little change in number density at all, with an average increase of ~5.3 x $10^{-4}cm^{-3}$ in He^{+} and ~1.6 x $10^{-4}cm^{-3}$ in He^{++}. This tiny change in the population signifies a steady state for the magnetosphere during quiet time, in which source and loss mechanisms for helium ions are almost equal. During stormtime, however, the average He^{++} number density is observed to decrease by 2.7 x $10^{-3}cm^{-3}$, while He^{+} is observed to increase by 4.4 x $10^{-3}cm^{-3}$. This shift could be taken as evidence of charge exchange during stormtime. However, for these plots stormtime was defined simply as D_{ST} < -30nT, meaning both main and recovery phases will be included in the average. The main phase of a storm occurs due to the energisation of the outer belt, and a new population of ions in each main phase will pollute the average. Due to the greater relative period of the recovery phase, the average stormtime vector does appear to point in the direction of increasing He^{+} and decreasing He^{++}. In order to further prove that this is due to charge exchange, stormtime will need to be split into main and recovery phase before investigation.

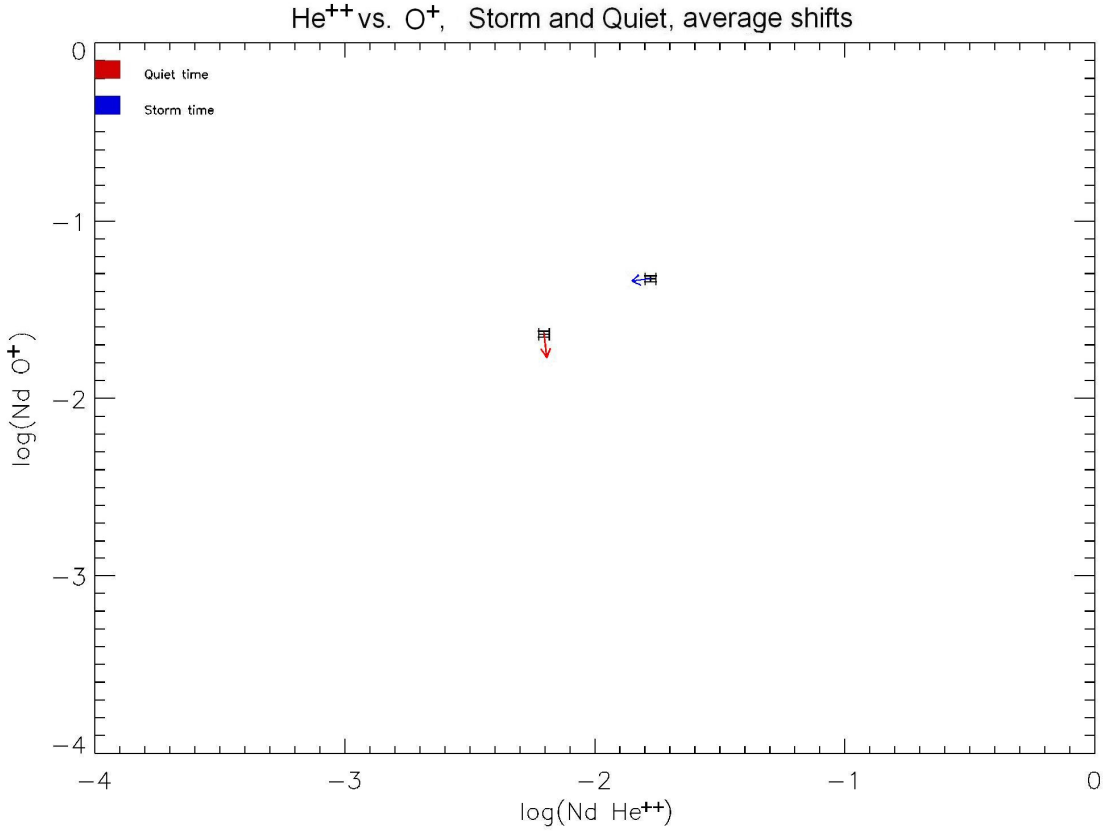

Figure 3.25: Average shift in number density for He^{++} and O^{+} during storm (blue) and quiet (red) time. Both O^{+} and He^{++} appear to decrease during storm time. This is because both the main and recovery phases are considered as storm time using this method, and all newly introduced ions have been lost.

Figure 3.25 shows the overall average plot for He^{++} and O^{+}. It is observed that, during stormtime, which in this plot includes both main phase and recovery, there is little change in the O^{+} content of the outer belt. O^{+} has previously been shown to become dominant in the outer belt during stormtime, so the meaning of this observation is that during the recovery phase of the storm, the newly introduced O^{+} is all lost. The fact that He^{+} increases when O^{+} decreases hints at an alternate source for the He^{+} (as the O^{+} can only come from a terrestrial source). A storm-phase vector plot would show this more clearly.

3.6.5 Number Density Shifts across Different Storm Phases

The previous study, showing number density shifts across consecutive orbits for storm and quiet time, was flawed in that it did not differentiate between the main and recovery phases of the storms. In this section, the ionic population will be considered in terms of storm phase.

3.6.5.1 Locating Main Phases in the Data

The main phase of a geomagnetic storm is characterised by a rapid drop in the D_{ST} index, down to negative values. During 1991, the largest storm occurred on March 24th, with the D_{ST} reaching a value of -298nT. To put this in context, throughout this work a D_{ST} value of -30nT has been regarded as a small storm. It will be necessary to locate main phases in the data if the phases of storms are to be separately investigated. Due to the variable nature of geomagnetic storms, locating all storms in a dataset is not trivial. The parameter used here in order to locate storms is the gradient of the D_{ST} index against time, as it becomes highly negative during the main phase.

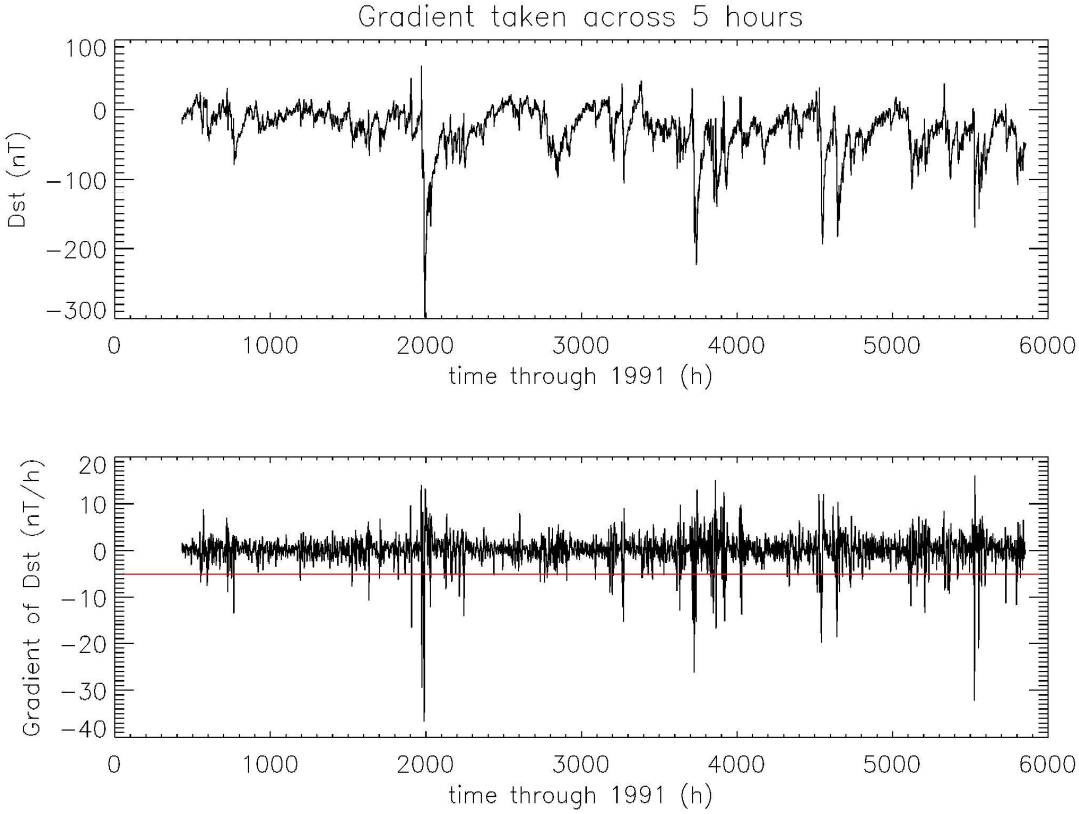

Figure 3.26: (Top) D_{ST}. (Bottom) 5-hour D_{ST} gradient. The red line drawn at –5nT/hour was used to locate the main phases of magnetic storms.

Figure 3.26 shows the D_{ST} profile for 1991 (top) and the D_{ST} gradient taken across 5 hours for each D_{ST} Value (bottom). A value of -5nThr^{-1} locates all of the significant main phases in this dataset. This suited the dataset for 1991 best, as shorter periods often regarded small negative spikes as main phases, and longer periods would overlook small storms altogether. Using these gradients, main phases were located, and their data were compared to data from the previous orbit. If a main phase lasted several orbits, each orbit was compared to the last orbit which did not contain a main phase. Recovery phases were defined as stormtime orbits which do not contain a main phase, in which the outer belt is slowly losing the population enhancement associated with the storm. It is expected that helium charge exchange will be observed in this phase.

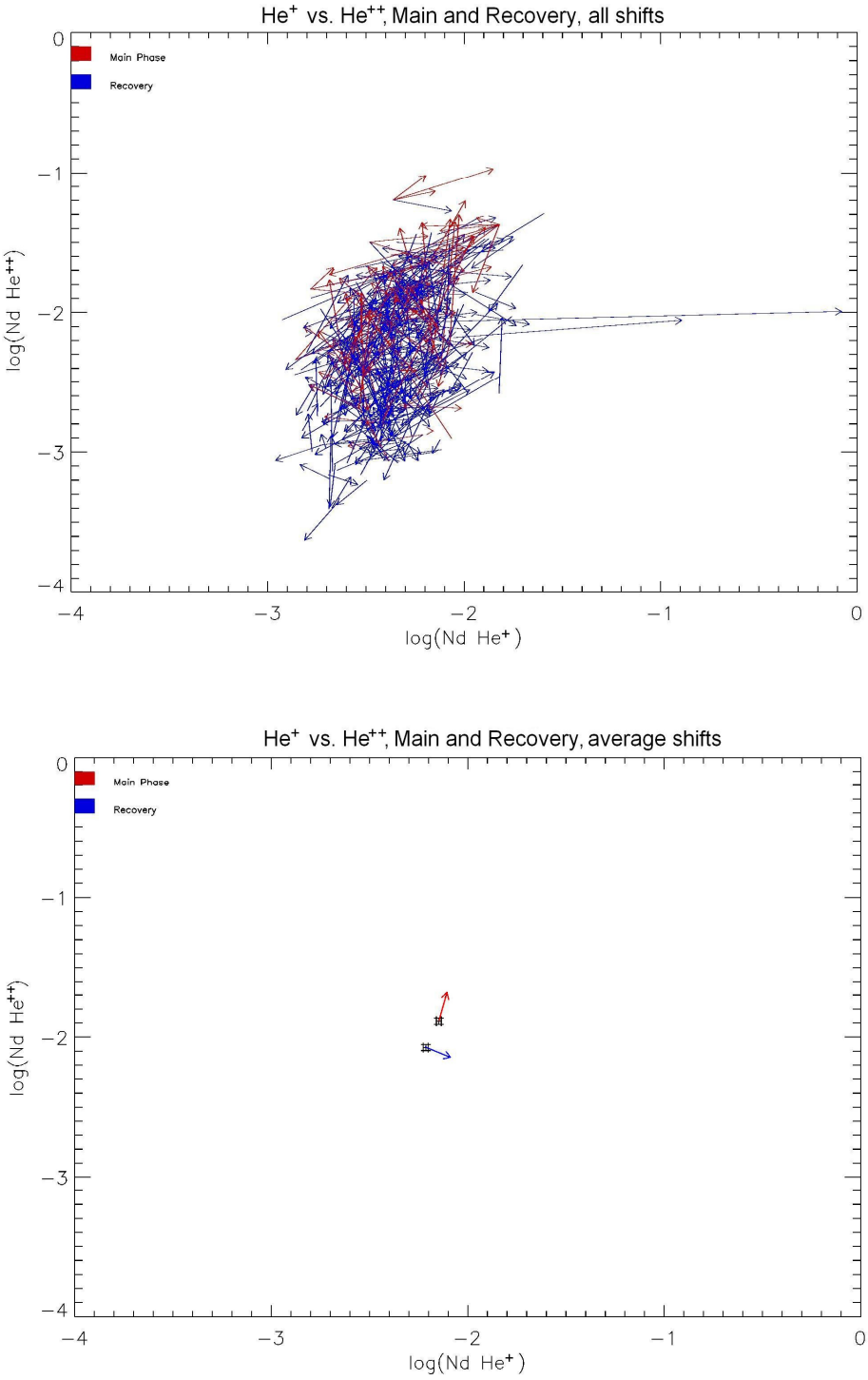

Figure 3.27: (Top) All data. (Bottom) Average for He^{++} vs. He^{+} number density shifts for main phase (red) and recovery phase (blue). During the main phase, both species are observed to increase in number density. During the recovery, He^{++} is observed to decrease, while He^{+} continues to increase.

Figure 3.27 shows the swarm and average plots for the log of He^{+} and He^{++} number densities during the main and recovery phases of geomagnetic storms. As would be expected, far more orbits occur during the recovery phase of storms than the main phase (shown in the higher density of vectors in the recovery phase swarm plot). The main phase vectors appear to show slightly higher number densities than the recovery, and this is again reflected in the average. The average main phase vector shows an increase in He^{++} of ~7.7 x $10^{-3}cm^{-3}$, alongside a far lesser increase of ~7 x $10^{-4}cm^{-3}$ in He^{+} number density. Depending on O^{+}, this may suggest that magnetospheric He^{+} is sourced almost entirely from charge exchange. The recovery phase vector shows a decrease in He^{++} of ~1.3 x $10^{-3}cm^{-3}$ and an increase in He^{+} of ~2.1 x $10^{-3}cm^{-3}$, which indicates a recovery phase source mechanism for He^{+}. This mechanism must be charge exchange.

Figure 3.28 shows the average plot of He^{++} vs. O^{+} for main and recovery phase. During the main phase, a large increase in O^{+} of ~3.2 x $10^{-2}cm^{-3}$ is observed. He^{++} again increases by ~7.7 x $10^{-3}cm^{-3}$. During recovery, both number densities decrease, with O^{+} falling by ~1.2 x $10^{-3}cm^{-3}$ and He^{++} by ~1.3 x $10^{-3}cm^{-3}$. The similarity of the average drop in He^{++} and O^{+} after a single CRRES orbit can be taken as evidence of a near-equal loss rate of both of these ions. With charge exchange, He^{++} would be expected to decrease more rapidly than O^{+}, though some O^{+} will be lost to charge exchange also; taking in an electron and becoming neutral oxygen (no longer magnetically bound). The fact that O^{+} is lost during the recovery phase removes the possibility of an ionospheric source for the singly charged helium enhancement, giving further evidence that charge exchange is the source.

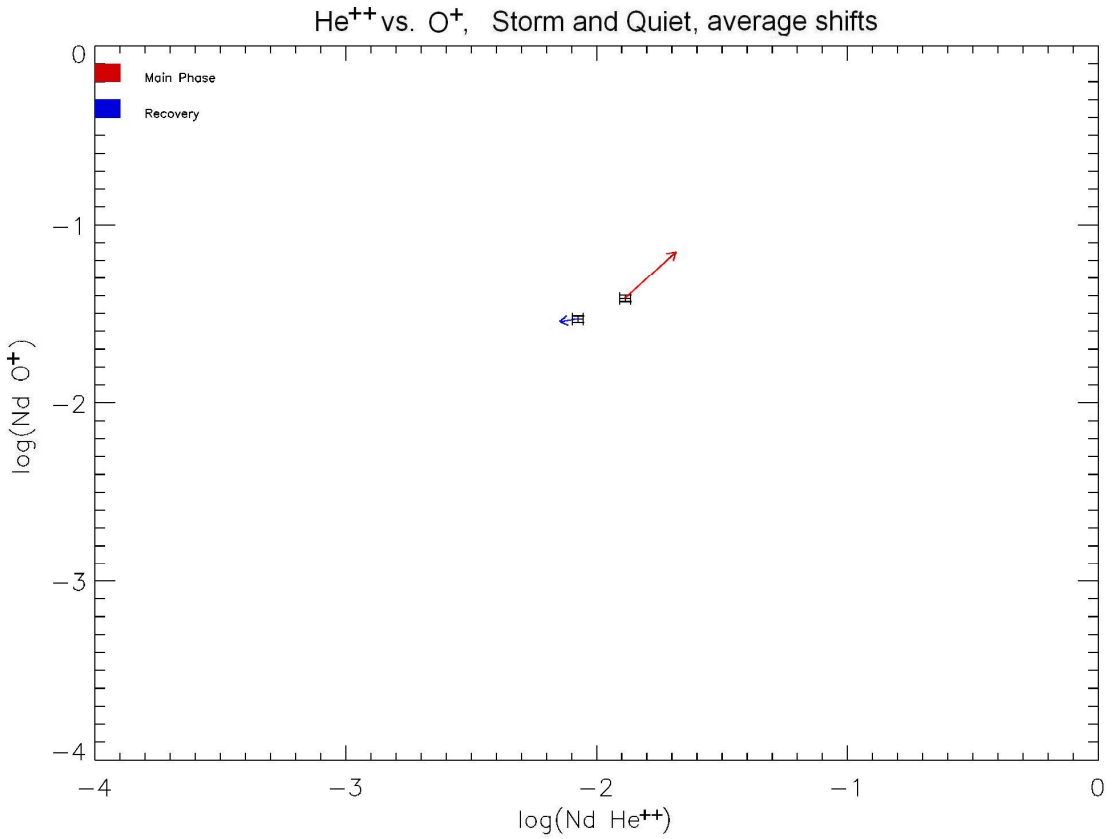

Figure 3.28: He^{++} vs. O^{+}: average shift during main (red) and recovery (blue) phases of magnetic storms. Again, both of these species increase during the main phase, but unlike He^{+}, O^{+} is observed to decrease in the recovery phase, showing that the source for the He^{+} was not terrestrial.

3.7: Chapter Summary

The region of the outer radiation belt was observed to contain a He^{+}/He^{++} maximum (figure 3.8), wherein singly charged helium dominates over doubly charged. This maximum was attributed to charge exchange, specifically the reaction:

$$He^{++} + H \rightarrow He^{+} + H^{+}$$

In this reaction, doubly charged helium, sourced from the solar wind and entering Earth's magnetosphere via reconnection, undergoes charge exchange with a neutral hydrogen atom within Earth's exosphere. The argument was backed up

by the fact that the ratio of O^+ / He^+ does not display a flat signature across the same region (figure 3.11). An investigation into the ratio of helium species within the outer belt across the timescale of a single westward drift showed possible evidence of a small shift from He^{++} towards He^+.

The drift echo of a dispersionless substorm injection, which occurred on 14th February, 1991, during orbit 497 of CRRES, appeared to contain a population of He^+ ions at energies not present in the injection. The possibility that this new population resulted from charge exchange was considered, raising questions as to the expected timescale for charge exchange at outer belt altitudes. This effect is studied in the next chapter.

An investigation of the composition of the outer belt across subsequent CRRES orbits was undertaken in order to find evidence of charge exchange over the time period of a single CRRES orbit (~10 hours). The results suggested that charge exchange may be responsible for the bulk of outer belt He^+ during the recovery phase of geomagnetic storms, when the magnetospheric ion population is enhanced but there is no substantial external ion source.

Chapter 4: Calculating Charge Exchange Cross Sections Using Injections and Drift Echoes

4.1: Introduction: Injections, Drift Echoes and Charge Exchange

Magnetospheric substorms involve a large scale reconfiguration of the Earth's magnetotail. One of the features of substorms is geosynchronous particle injections, which occur across 00:00 MLT at L values of ~ $6R_E$. Given its geostationary transfer orbit, which often had a near-midnight apogee, the CRRES satellite was able to observe these injections as dispersionless signatures. If CRRES remained at high L for the hours following the injection, the injected particles would be observed again, as a dispersed population which had drifted around the Earth.

It was shown in figure 3.18 that, over the timescale of a single drift orbit, a measurable amount of charge exchange will occur. This being the case, it would be expected that, from injection to drift echo, a number of He^{++} ions will have charge-exchanged into He^{+} ions. The cross section of a charge exchange reaction is the physical area around an ion over which charge exchange will occur. If the amount of charge exchange within each energy range were found across the timescale of a drift orbit, an estimation of the cross section for the He^{++}-to-He^{+} reaction within the outer radiation belt could also be found. In this chapter, a method for calculation of the cross section will be presented, and the result discussed in relation to previous work into the cross section.

4.1.1: A Feasibility Study for Charge Exchange of Trapped Ions

In a paper by [Tinsley, 1976] it was suggested that, during the recovery phase of magnetic storms, the dominant species within the ring current changes from protons to He^{+} ions, due to their relatively long charge exchange lifetime. In the previous chapter, it was shown that He^{+} does, indeed, increase in number

density in the recovery phase of magnetic storms, and hence this prediction could be proved using data, but it is not carried out within this thesis.

A simple model was created in order that the expected amount of charge exchange over the short timescale of a couple of drift echoes could be investigated. For this, equation 4.1 was used.

$$T = (n_H \sigma v)^{-1} \qquad \text{Equation 4.1}$$

In equation 4.1, T is the charge exchange lifetime, n_H is the neutral hydrogen density at the given altitude (using data taken from [Tinsley,1976] and a method for averaging across a bounce path, the average n_H was found to be ~1200cm^{-3}. The method is explained in section 4.2.5 of this chapter), σ is the cross section and v is velocity. Values for σv are shown in fig. 4.1 ([Tinsley, 1976]). The model considers an injected population of He^{++} ions, along with a far lesser amount of He^{+} ions, within the energy range of the injection of 497. The ions are assumed to be trapped with perfect stability, with the only loss/source mechanism being charge exchange. Two reactions are considered, given by equations 4.2 and 4.3.

$$He^{++} + H \rightarrow He^{+} + H^{+} \qquad \text{Equation 4.2}$$

$$He^{+} + H \rightarrow He + H^{+} \qquad \text{Equation 4.3}$$

As the charge exchange cross section of equation 4.2 is much larger than that of 4.3, it is expected that, with time, the drifting population will gradually change predominantly from He^{++} to He^{+}, and eventually the He^{++} will all be lost as neutral Helium, which is no longer magnetically bound, via equation 4.3. The protons produced in these reactions would be at a variety of low energies, and so cannot easily be used as proof of charge exchange.

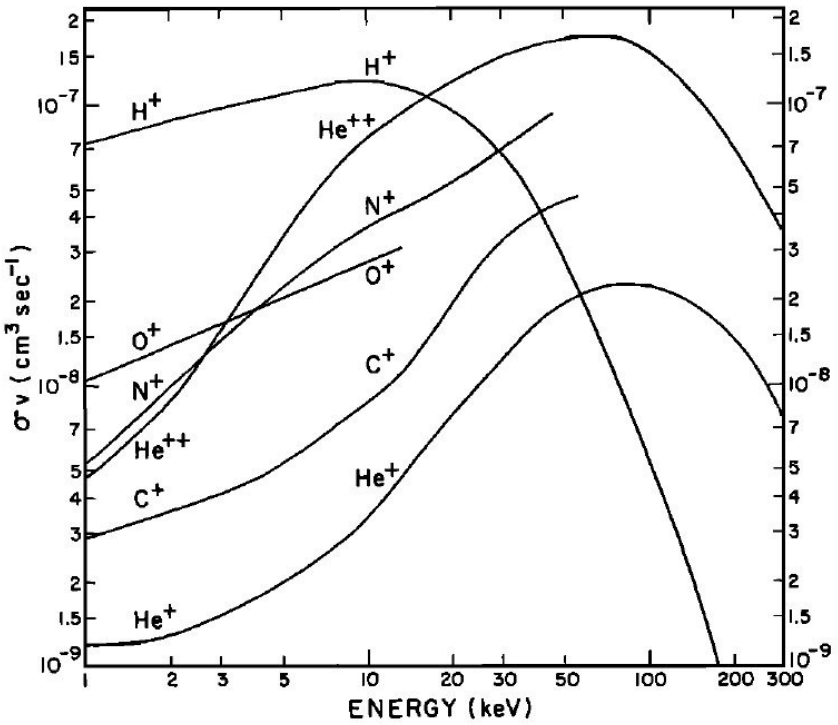

Figure 4.1: Charge exchange cross sections of different ionic species with neutral Hydrogen, multiplied by velocity, from [Tinsley, 1976].

Figure 4.2 shows the modelled evolution of an injection of 6000 He^{++} ions, of energy 90.5 – 101.0 keV. This is around the number that would be observed in an injection, within a relevant energy range. As expected, He^{++} initially decreases, correlating with a He^{+} increase. The He^{+} count reaches a maximum of ~4600 ions, after a time of ~7200s (~2hrs). Using equation 4.9 (discussed later), particle drifts at these energies have a period of ~1.2 to 1.4 hours, so it would be expected that by the second drift echo the maximum He^{+} content would have been reached.

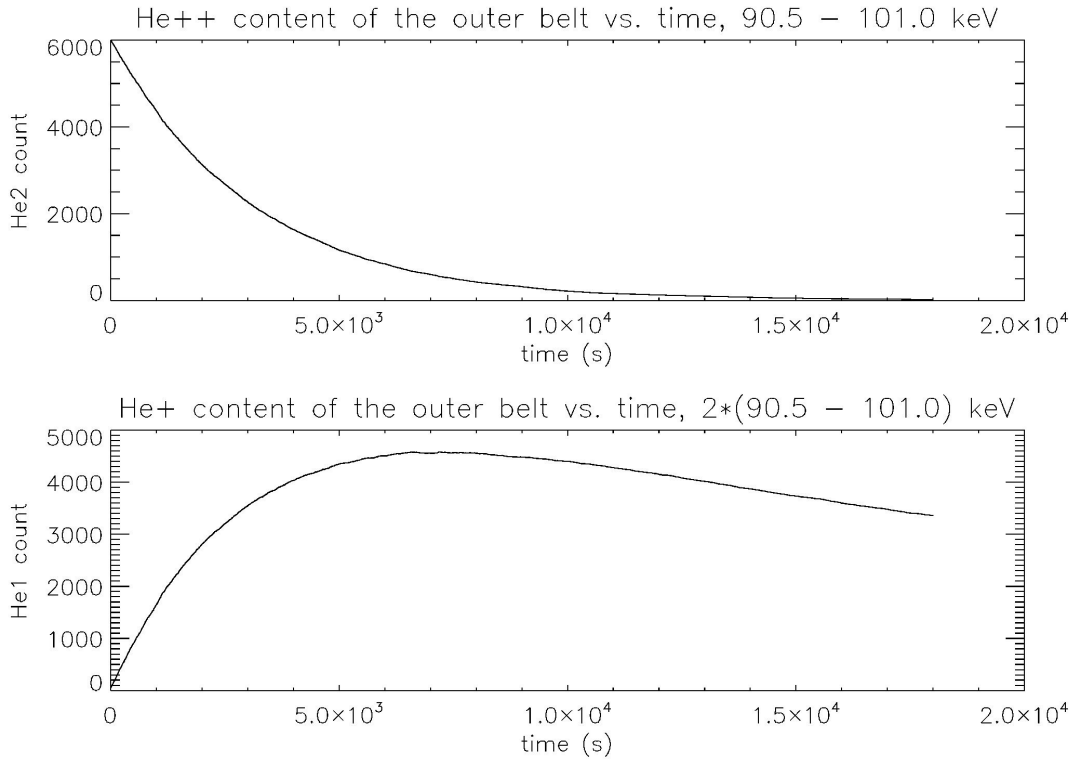

Fig 4.2: (Top) Using Tinsley's cross sections, the loss rate (by charge exchange) of a population of 6000 He^{++} ions of energy 90.5 to 101.0 keV as they change to He^{+} is modelled.
(Bottom) Again using Tinsley's cross sections, the source and loss rate of He^{+} by charge exchange is modelled.

4.2 The Method of Calculation

4.2.1 Charge Exchange Cross Sections

The cross section of a charge exchange reaction is the physical area around the neutral atom which the ion has to pass through in order for charge exchange to occur.

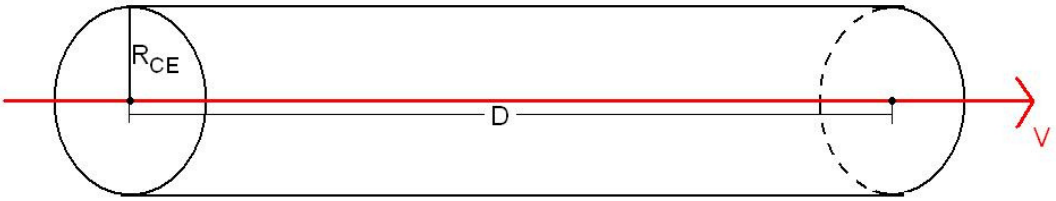

Figure 4.3: The cylinder around the ion's velocity vector (red) shows the total volume in which charge exchange can occur. D and R_{CE} are the distance travelled and the radius of the cross section, respectively.

Figure 4.3 shows a diagram representing the path of a He^{++} ion within the radiation belt. The cylinder enclosing the velocity vector, of cross sectional radius R_{CE}, represents the volume of space over which charge exchange will occur. The charge exchange cross section would be given by equation 4.4

$$\sigma_{CE} = \pi . R_{CE}^{\ 2} \qquad \text{Equation 4.4}$$

By coupling equation 4.4 with the total distance travelled, D, the total volume of the cross-sectional cylinder would be given by equation 4.5.

$$V_{CE} = D . \pi . R_{CE}^{\ 2} \qquad \text{Equation 4.5}$$

In equation 4.5, D needs to take into account the fact that the particle is bouncing, i.e. the path length of a particle will be dependant on the pitch angle, α_{eq}. The number of neutral H particles within this space will be given by multiplying equation 4.5 by N_H, the neutral Hydrogen density. This is shown in equation 4.6.

$$H_{VCE} = N_H . D . \pi . R_{CE}^{\ 2} \qquad \text{Equation 4.6}$$

Any Hydrogen atom within the charge exchange cross section will undergo charge exchange, hence H_{VCE} can be thought of as N_{CE}, the number of charge exchange reactions.

$$N_{CE} = N_H . D . \pi . R_{CE}^{\ 2} \qquad \text{Equation 4.7}$$

Rearranging equation 4.7 for the charge exchange cross section gives:

$$\sigma_{CE} = \frac{N_{CE}}{N_H . D} \qquad \text{Equation 4.8}$$

Within equation 4.8, N_H is a function of altitude. This will need to be averaged for the final calculation.

4.2.2 Dispersionless Injections and Drift Echoes: Orbit 497

Figure 4.4 shows the heavy ion data for orbit 497 of CRRES, taken across 14th and 15th February, 1991. The injection occurs at ~ 23:50 UT, where particles of all energies are observed by the detector at the same time, meaning an injection has occurred locally to the satellite (CRRES L ~5.85R_E, ~00:20 MLT). In O^+ and He^{++}, the injection is clearly visible from the 4th to the 15th energy ranges (denoting E/q values ranging from 54.6 to 240.0 keV). The E/q of He^+ in the injection is limited to lower bins, with very little being injected in the 14th and 15th energy ranges. The first drift appears as a clear arc in energy ranges including those where there was no He^+ in the injection. This is shown in figure 4.5, with the source of the new population of He^+ being suggested as charge exchange.

To further investigate charge exchange across the period of a drift echo, other, similar injections were located. The orbit numbers of these injections are 490, 497, 548, 604 and 612.

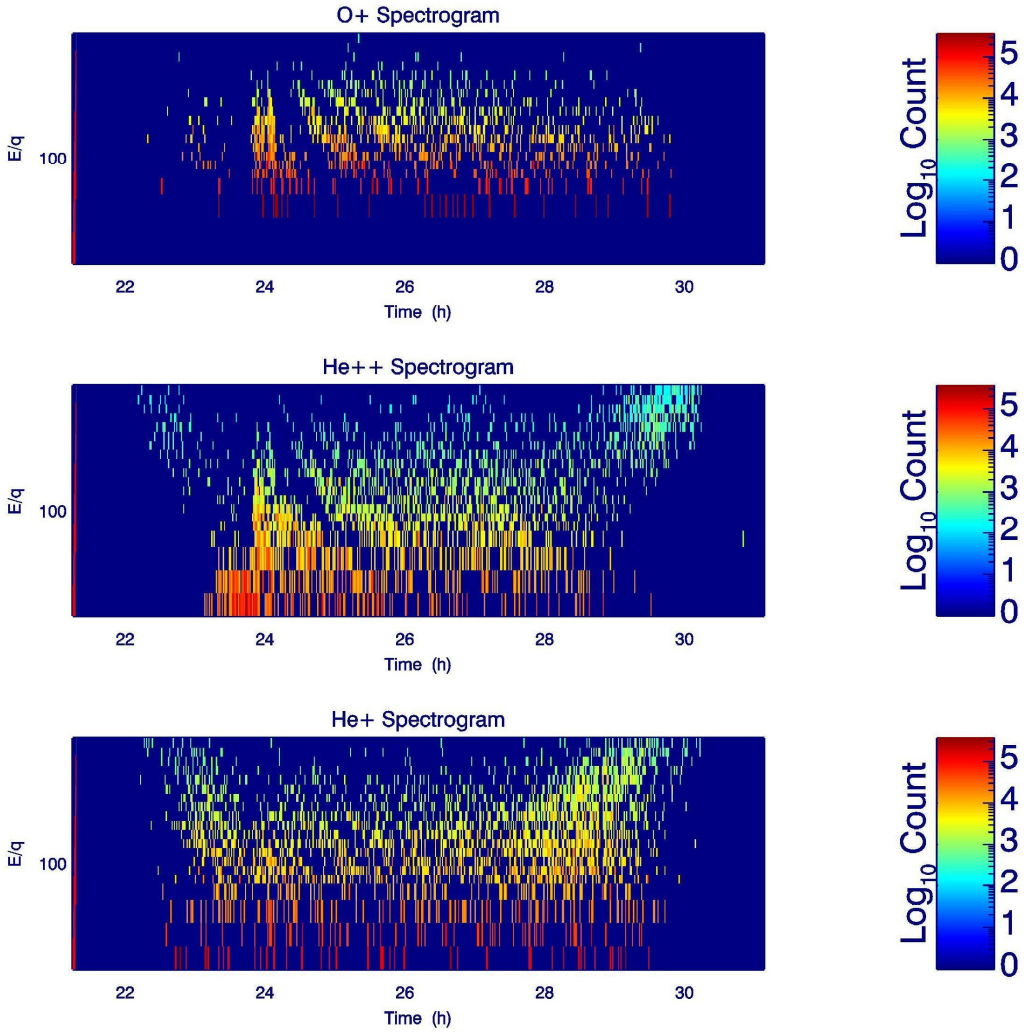

Figure 4.4: Spectrogram of ion data for O^+, He^{++} and He^+ from orbit 497 of CRRES. An injection occurs at ~23:50 UT, rich in O^+ and He^{++}, but lacking He^+.

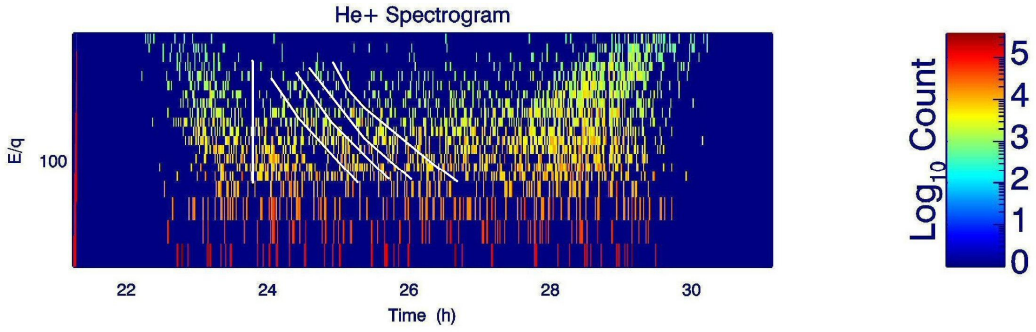

Figure 4.5: He^{++} spectrogram from orbit 497 with injection and drift echo boundaries marked. He^+ in the drift signatures is observed at E/q values not present in the injection.

4.2.3 The Other Injections Included in the Investigation

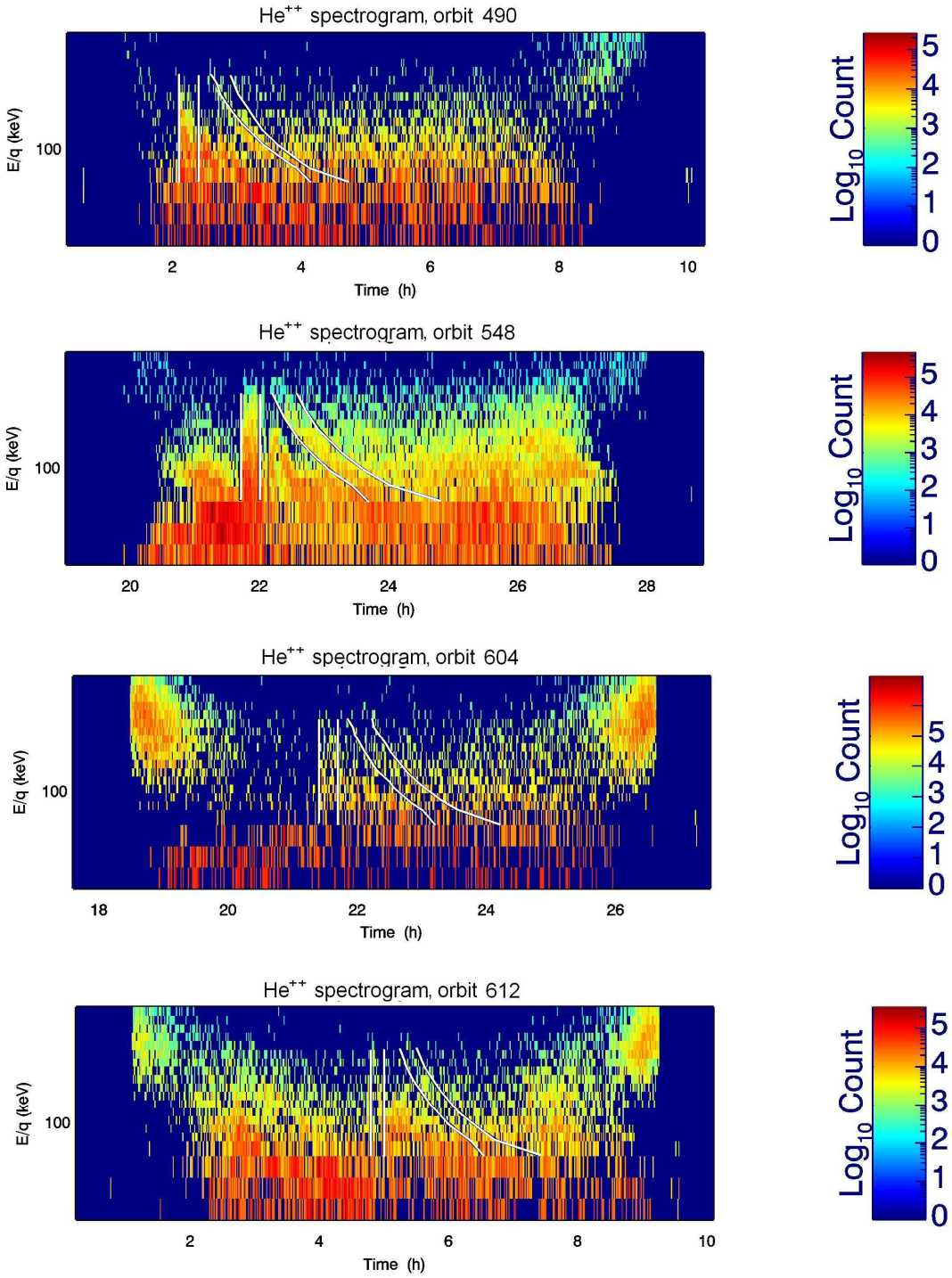

Figure 4.6: He^{++} spectrograms for the remaining four CRRES injections included in the study. Modelled maximum drift times are also shown.

The purpose of this study was to calculate the amount of charge exchange that occurs as a discrete population of particles drifts around the Earth. The first requirement for a CRRES orbit to be included in this study is that it contains a clear substorm injection in He^{++}. Spectrograms were also required to contain two distinct drift echo signatures, in order to increase the time over which the population could be analysed. In order for comparisons to be made across any calculated cross sections, the energy range of the injections will need to be similar. The E/q range of injection 497 was matched by four other injections with two drift echoes, occurring in orbits 490, 548, 604 and 612 of CRRES. These five injections were hence chosen for the study, and are shown in figure 4.6, with the modelled first drift marked.

4.2.4 The Drift Period

$$\frac{\tau}{2} = \left| \frac{1}{12} - \frac{L(k/40keV)}{9.21Z} \right| \qquad \text{Equation 4.9}$$

Equation 4.9, obtained from [Lyons and Schulz, 1989], gives the drift period, τ, in terms of L-value, energy, k, and atomic charge, Z. This equation will be used to calculate the drift period for Helium ions at L ~6.0R_E, and these periods will be compared to the drift echoes visible in the CRRES spectrograms.

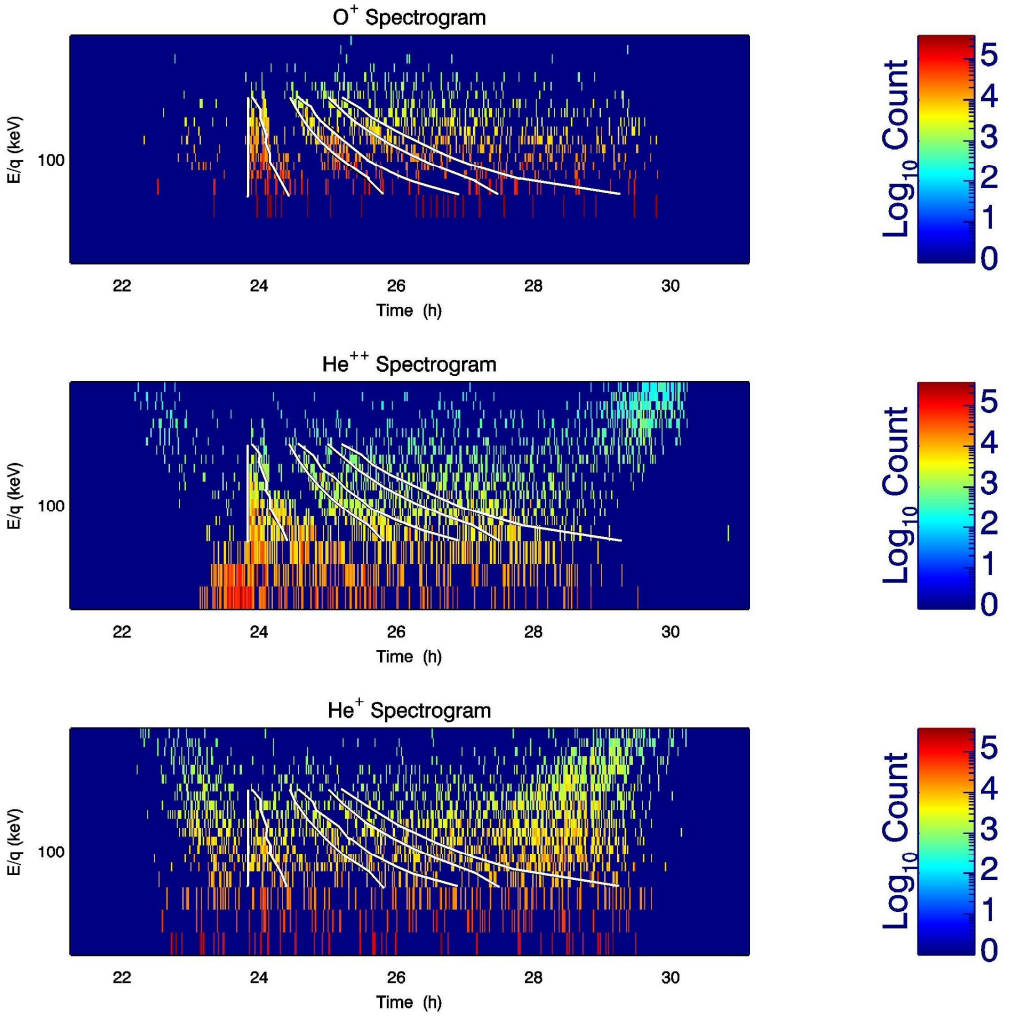

Figure 4.7: Orbit 497 with the drift time, calculated using equation 4.9, plotted over the observed drift echoes. It appears not to match the physical drift time exactly.

Figure 4.7 shows the spectrogram for orbit 497 of CRRES with the modelled drift period plotted as curves. The injection time was used alongside the highest energy of each energy range to calculate the minimum drift period for that range, and an estimation of the time where the main bulk of the injection had occurred was used alongside the minimum energy for the range to calculate the maximum drift period. It can be seen that the equation does not adequately predict the actual drift period for the ions, with the actual drifts occurring slightly more quickly. Due to this, the equation will not be used to calculate the drift period for the charge exchange calculation. Instead, the drift signatures will be

picked from the data by eye, which will add to the unquantifiable errors, especially at lower energies where the drifts overlap quickly due to dispersion. The manually selected drift periods are shown in figure 4.8.

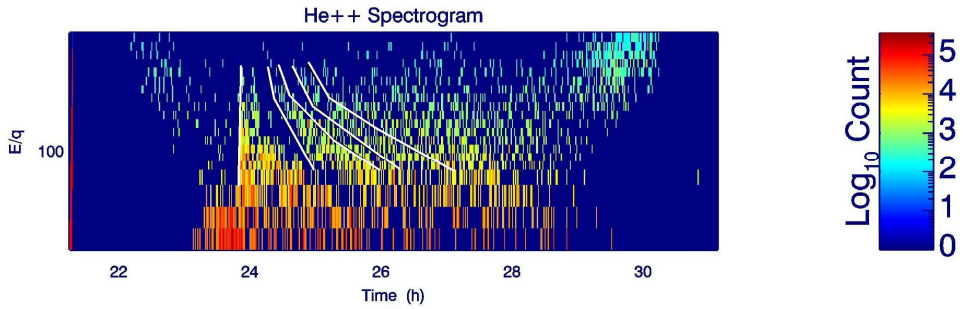

Figure 4.8: He^{++} Spectrogram for obit 497 of CRRES, with handpicked drift arcs.

4.2.5 N_H and Altitude across a Drift-Path

The calculation for charge exchange cross section will require the number density of neutral hydrogen, N_H, through which the particles are moving, to be known. Recent work used measurements of Lyman-α brightness from the Geocoronal Imager (GEO) on the IMAGE satellite to create a model of geocoronal N_H density ([Ostgaard et al., 2003]). This model was not used in this study. Table 4.1 shows values for N_H, taken from [Tinsley, 1976], for various exospheric temperatures. Those of 950K are assumed to be representative of the exosphere at the time, though it is likely that the temperature was higher during this solar maximum period.

Height, R_E	Hydrogen Concentration Models n_H, cm^{-3}					
	750°K	850°K	950°K	1100°K	1300°K	1500°K
1.0785	250000	170000	115000	61000	32000	16000
2	3300	3700	3700	3000	2300	1600
2.5	1200	1400	1600	1400	1200	860
3	530	700	800	750	670	490
3.5	290	400	470	460	420	310
4	180	250	300	300	290	210
4.5	120	170	210	210	210	160
5	85	120	150	160	150	120
5.5	62	93	120	120	120	92

Table 4.1: Exospheric neutral Hydrogen density with altitude from, [Tinsley, 1976]. An exospheric temperature of 950K is assumed.

The values for N_H at L = 1.5 R_E and 6.0R_E were not present in the paper, and were found by interpolation of the log of these N_H data. This is shown in figure 4.9.

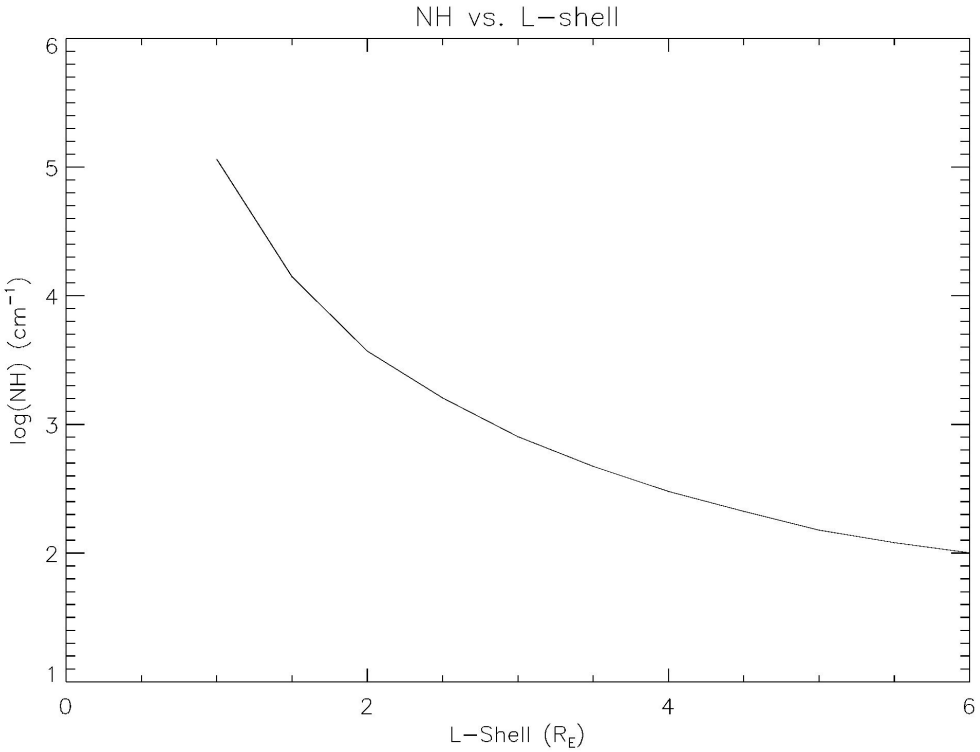

Figure 4.9: N_H with altitude, showing interpolated points at L = 1.5R_E and 6.0R_E.

4.2.5.1 The Altitude of a Bouncing Ion

The altitude of a bouncing ion varies across the bounce path, with the particle drawing closer to the Earth with increasing equatorial pitch angle. The spin axis of the CRRES satellite was along the Earth-Sun axis, meaning the distribution of observed pitch angles would depend upon the magnetic field orientation around the orbit (i.e. the distribution would be restricted if the magnetic field is predominantly in the x_{GSE} direction).

$$\alpha_{loss} = \sin^{-1}\left(\sqrt{\frac{B_{eq}}{B_E}}\right) \qquad \text{Equation 4.10}$$

Equation 4.10 ([5]) gives the value of α which defines the loss cone (α_{loss}), in terms of B_{eq}, the equatorial magnetic field density at the L shell of the bouncing particle, and B_E, the magnetic field density at the foot of the B-field line. B_E should technically be the field strength a few hundred km above the surface of the Earth, where the atmosphere becomes too dense for a bouncing particle to remain unscattered, but with the N_H resolution at 0.5 R_E, using B_E makes little difference. Using magnetic field data from the Tsyganenko model (discussed later), the loss cone for B_{eq} (L=6.0R_E) was calculated to be ~2.8°.

$$B_m = \frac{B_{eq}}{\sin^2 \alpha_{eq}} \qquad \text{Equation 4.11}$$

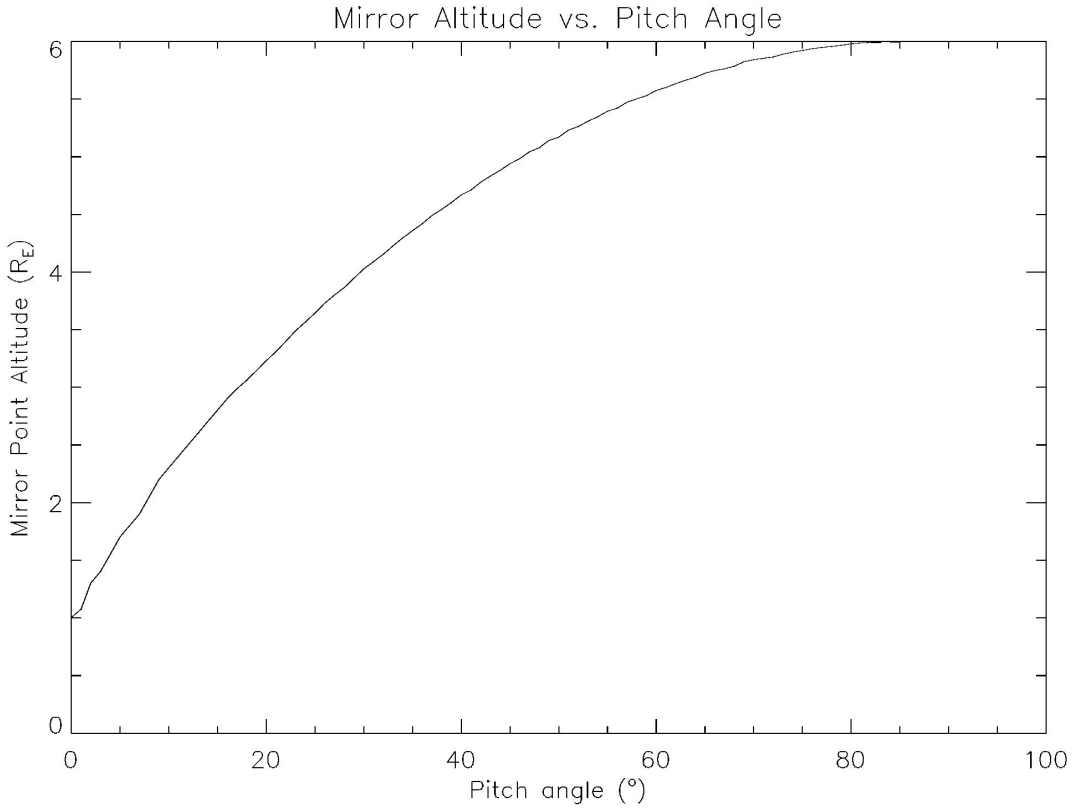

Figure 4.10: Pitch angle vs. mirror altitude for ions trapped at L = 6R_E, calculated using equation 4.11.

Equation 4.11 ([5]) gives the mirror magnetic field density, B_m, in terms of B_{eq} and α_{eq}. The Tsyganenko magnetic field model was used to find the altitude where B = B_m, the mirror altitude, for every integer degree of pitch angle between the loss cone and 90°. The dependence of mirror altitude vs. Equatorial pitch angle is displayed in figure 4.10.

Work by [Hasegawa, 1975], and [Prakash and Diamond, 1999], showed that the motion of a particle can be approximated as simple harmonic if a paraxial approximation for the magnetic field is used i.e.:

$$B_0(z) = B_0(1 + bz^2) \qquad \text{Equation 4.12}$$

In order to approximate the time spent at different altitudes across a bounce path, a simple sine function was used alongside equation 4.11, with the bounce

path-length for particles of different α_{eq} calculated by mapping the trajectory of a field line using the Tsyganenko model. For all pitch angles between 90^o and the approximate loss cone, the bounce path was divided into ten altitude segments. The percentage of time spent in each segment was computed; the time-averaged N_H value for the average drifting particle was found to be ~1200 cm^3.

4.2.6: How Charge Exchange Would Appear in a CRRES Spectrogram

In the drift signature of an injection seen in a CRRES ion spectrogram, it has been suggested that the appearance of He^+ at energies which were not evident in the injection itself may be proof of charge exchange (figure 4.4). How charge exchange would actually manifest itself in CRRES spectrogram will now be investigated.

The reaction that need be considered is that of equation 4.2. First of all, this reaction involves a change in the value of the charge (q). The energy (E) would remain constant, with the change in mass of the Helium ion due to the addition of the electron being negligible, and also the difference in the energy level between the allowed orbitals in Helium could only feasibly create very low energy quantum effects (discussed briefly in section 4.2.8). This essentially means that the value, E/q, will effectively double across this reaction, an effect that would be notable on the y-axis of a CRRES spectrogram.

After the reaction has occurred, the newly introduced He^+ ion, at its new E/q value, will drift much more quickly than previously as He^{++}. This would mean that, if the reaction occurred immediately after initial detection, the resulting He^+ ion would drift around the Earth as if it was present at the head of the injection as a He^+ ion at its new E/q, and would hence be detected within the expected drift echo location. If, however, the He^{++} ion was allowed to drift all the way around the earth, and the charge exchange reaction was to occur immediately before the second detection, the resultant He^+ ion would appear at a much later time. The fact that the E/q values are binned into ranges adds to this effect, as the lowest energy He^{++} ion in a range, probably located at the tail of the injection, would

take the longest amount of time to drift. This effect is explained visually in fig. 4.11.

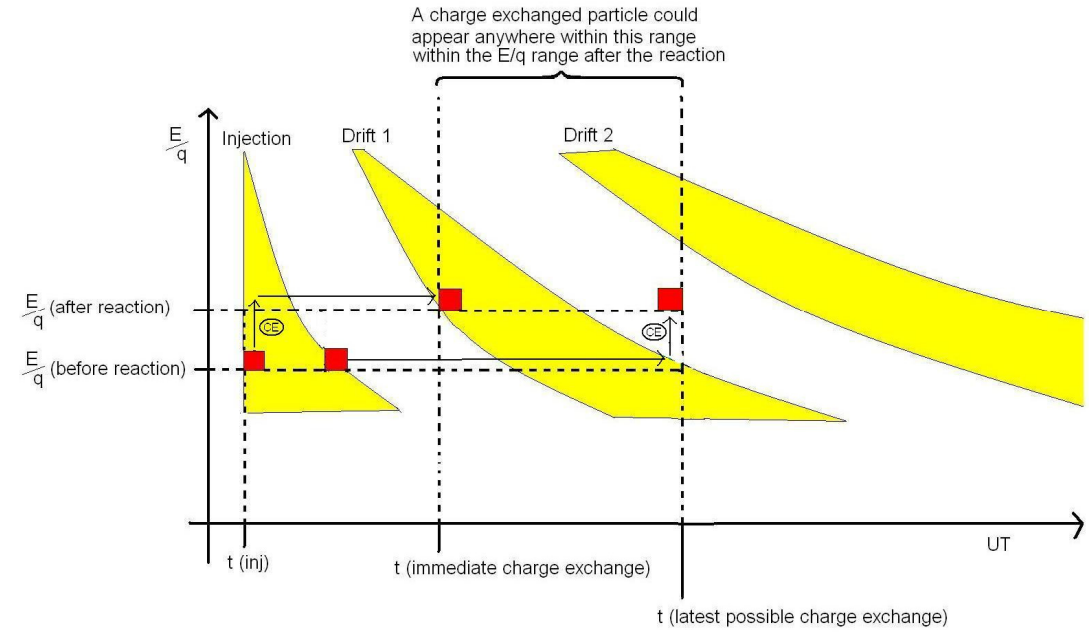

Figure 4.11: The halving of q involved with this reaction would lead to a doubling of E/q, changing the y-position of a charge exchanged He^{++} ion in the He^{+} spectrogram. In the event of uniformly occurring charge exchange, an injected population would be expected to spread across a range of the spectrogram in the time axis.

As can be seen, the expected effect would be a spread of counts in the He^{+} spectrogram with time, although the event of charge exchange happening sooner rather than later (and hence forming a drift echo-like structure in the He^{+} spectrogram) may still be possible, as the majority of the injection is located near the injection's head, especially at the higher energies. However, some inaccuracies at lower energies will occur due to this.

The fact that the energy is sorted onto discrete ranges also poses another problem in the determination of whether a He^{+} ion in a drift echo arose due to charge exchange. To appear in any given bin, an ion must have had one of a range of energies, and if across the reaction E/q is doubled, the resulting particle may fall within one of a number of bins. This will likely lead to some spreading in He^{+} count in the y-axis of a CRRES ion spectrogram, depicted in figure 4.12.

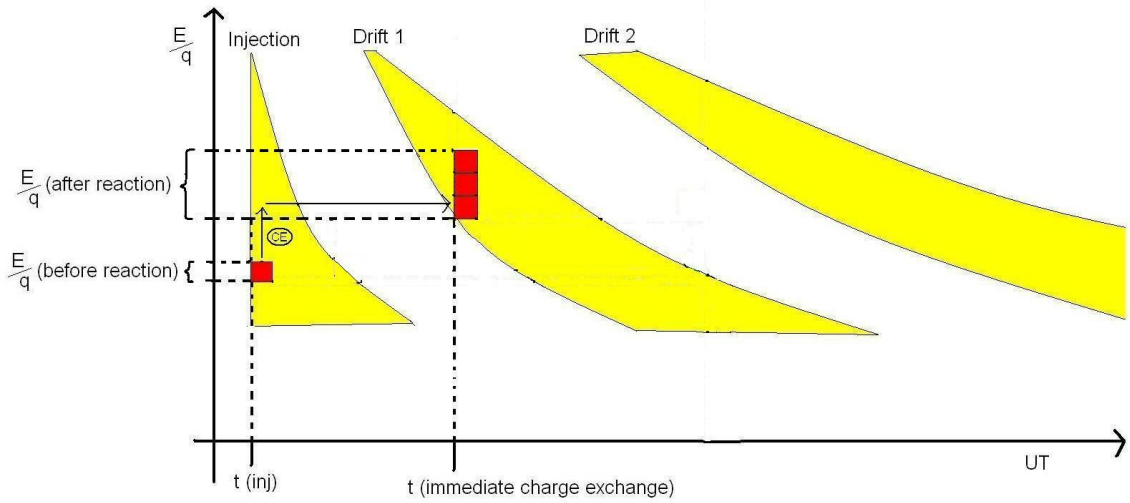

Fig. 4.12: CRRES ions were binned into energy ranges. After charge exchange, a He^{++} ion from a low energy bin could end up in one of two or three bins as He^{+}.

Figure 4.13 depicts the entire energy range into which a He^{+} ion could end up after charge exchange. As the CRRES mission consisted of a single satellite, it is not possible to tell where charge exchange actually happened around the earth, but the likelihood of a charge exchange can be computed.

Due to the impossibility of pinpointing the location around the Earth (MLT) at which charge exchange has occurred, it was assumed that all the charge exchange must have occurred in the early part of the drift orbit (as it would have had to have if the new He^{+} population in 497 arose due to charge exchange). To impose this condition upon the data, only the ions near the head of the injection were considered in the study (first 0.3 hours).

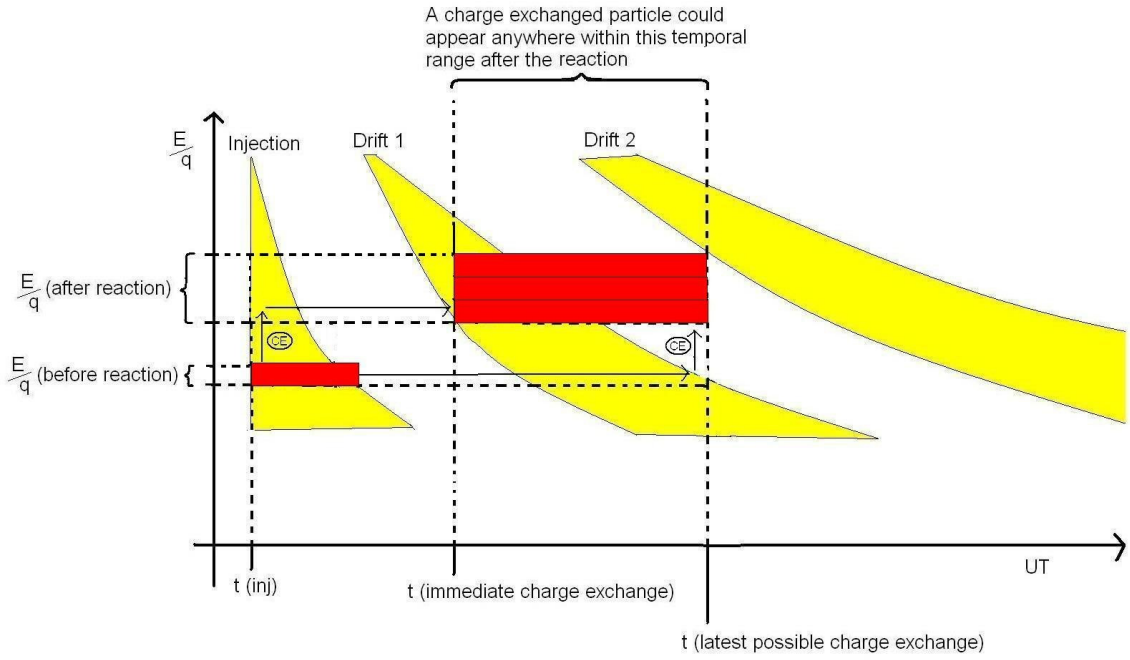

Fig. 4.13: A rough depiction of where He^{++} ions charge exchanged from a single low energy bin could end up, as He^{+}.

4.2.6.1 The Location of Charge Exchanged He^+ on a CRRES Spectrogram

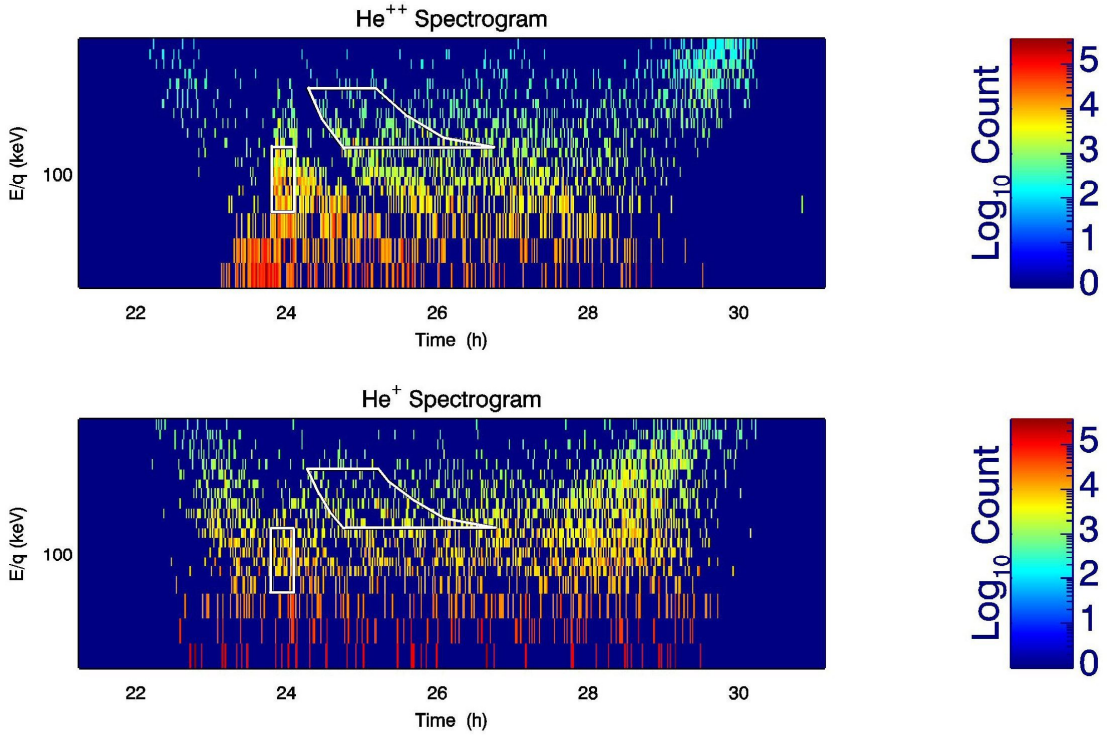

Figure 4.14: CRRES spectrogram for He^{++} and He^+ in orbit 497. The small box encompassing the head of the injection shows the studied input. The box encompassing the drift echoes shows the modeled region of space in which a charge exchanged particle could end up.

The amount of possible spreading of He^+ ions in time due to charge exchange will change with E/q. Figure 4.14 shows the complete region of orbit 497 in which a charge exchanged He^{++} ion from the marked injection region could end up, as He^+, after a single drift. This region encompasses both the first and second drifts. If charge exchange was assumed to be occurring at a constant rate around the Earth, the signature for He^+ would be expected to 'spread' in time. Comparing the appearance of He^+ to He^{++} injections with drift echoes, the boundaries of the He^{++} signatures are generally more clearly defined than those of He^+. This may be evidence of the spreading due to charge exchange. The large area in which a He^+ ion may result after charge exchange can be reduced by only considering a partial drift around the Earth. This is carried out in section 4.3.5.

4.2.7 Accounting for the E/q Range-Spreading

As mentioned in the previous section, following a charge exchange reaction, a He^{++} ion from any E/q range could end up as a He^{+} ion within one of a number of higher E/q ranges. To account for this, the E/q values for the high energy ranges will be halved, in order to find the exact E/q values of He^{++} which will have contributed to their He^{+} after a charge exchange reaction. Using this value, the relative input from all groups which contain He^{++} ions within the desired E/q range will be calculated. The example for the 15th energy range, 220.0 to 240.0 keV, will now be given.

4.2.7.1 Relative He^{++} to He^{+} Input for E/q Bin 15: 220.0 – 240.0 keV

The 15th E/q Range is 220.0 to 240.0 keV. When halved, this means that He^{+} ions would have been sourced as He^{++} ions between 110.0 and 120.0 keV, covering the 7th and 8th E/q bins, of range 101.0 – 113.0 keV and 113.0 – 125.3, respectively. From the 7th range, the total percentage input is given by the effective E/q divided by the total size of the range:

$$\frac{113.00-110.00}{113.00-101.00}=\frac{3.00}{12.00}$$

The same done for the 8th E/q range gives:

$$\frac{120.0-113.0}{125.3-113.0}=\frac{7.0}{12.3}$$

Equation 4.13 gives the relative input of He^{+} from He^{++} in each of these lower ranges, where $N(CE)_{15}$ is the number of new He^{+} particles in a drift relative to the injection, and N_7 and N_8 are the relative inputs from ranges 7 and 8.

$$N(CE)_{15} = \left(\frac{3.00}{12.00}\right).N_8 + \left(\frac{7.00}{12.30}\right).N_9 \qquad \text{Equation 4.13}$$

$$N(CE)_{15} = N_{drift}(He^+)_{15} - N_{inj}(He^+)_{15} \qquad \text{Equation 4.14}$$

4.2.7.2 Relative Input Equations for Other Energy Bins

The above method was used for the other groups into which He^+ will have jumped, giving the following equations.

$$N(CE)_9 = \left(\frac{6.15}{17.80}\right).N_4 \qquad \text{Equation 4.15}$$

$$N(CE)_{10} = \left(\frac{7.35}{17.80}\right).N_4 \qquad \text{Equation 4.16}$$

$$N(CE)_{11} = \left(\frac{2.40}{17.80}\right).N_4 + \left(\frac{6.10}{8.60}\right).N_5 \qquad \text{Equation 4.17}$$

$$N(CE)_{12} = \left(\frac{2.50}{8.60}\right).N_5 + \left(\frac{6.50}{9.50}\right).N_6 \qquad \text{Equation 4.18}$$

$$N(CE)_{13} = \left(\frac{3.00}{9.50}\right).N_6 + \left(\frac{8.00}{10.50}\right).N_7 \qquad \text{Equation 4.19}$$

$$N(CE)_{14} = \left(\frac{2.50}{10.50}\right).N_7 + \left(\frac{9.00}{12.00}\right).N_8 \qquad \text{Equation 4.20}$$

$$N(CE)_{15} = \left(\frac{3.00}{12.00}\right).N_8 + \left(\frac{7.00}{12.30}\right).N_9 \qquad \text{Equation 4.21}$$

4.2.8 The Energy of a Charge Exchange Reaction: Quantum Effects

Photon emission due to charge exchange reactions is presently a subject of interest, due to the relatively recent discovery that comets emit large intensities of x-rays. This was first discovered within comet Hyakutake in 1996

([Lisse et al, 1996]), and it has since been shown for other comets ([Dennerl, Englhauser and Trumper 1997]). The widely accepted explanation for these x-rays is that highly ionised heavy (z > 2) ions undergo charge exchange with cometary neutrals ([Cravens, 2000]), leaving the solar wind ion in an excited state. The subsequent relaxation of the electron results in the release of a photon; in the case of the heavy solar wind ions, this photon will be a matter of a few ten to a few hundred eV.

Alpha particles carry a charge of +2e. This makes high state orbitals unstable, and therefore most of the energy jumps will be relatively small, releasing low energy photons. These photons will not cause substantial losses in the energy of the alpha particles themselves.

4.2.9 Modelled Magnetic Field Data

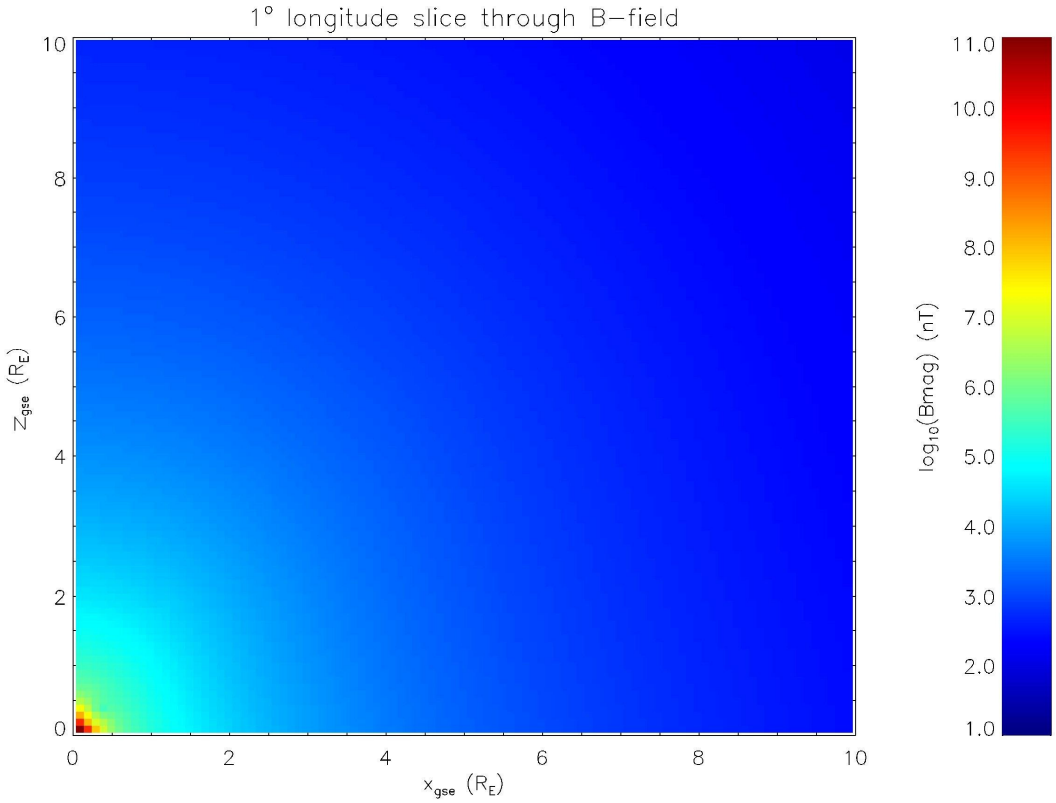

Figure 4.15: Tsyganenko 2004 model of Magnetic field for 14th February, 1991, at a slice through 1° longitude. B is shown to drop off rapidly with distance. The x and y axes show co-ordinates in GSE.

In order to find the altitude of the mirror point, B_m, a global-magnetospheric model was required. Tsyganenko's 2004 model was used, which is semi-empirical, using data from a variety of spacecraft. As well as the data, the effects of various magnetospheric current systems, such as the ring current and cross tail current, are taken into account.

The model was used to create B-field data within the magnetosphere for the dates of the injections, and these were used to find the altitude at which B = B_m and $\lambda = \lambda_m$, where λ_m, the mirror latitude, is given in equation 4.22.

$$\sin^2 \alpha_{eq} = \frac{\cos^6 \lambda_m}{\left(1 + 3\sin^2 \lambda_m\right)^{1/2}} \qquad \text{Equation 4.22}$$

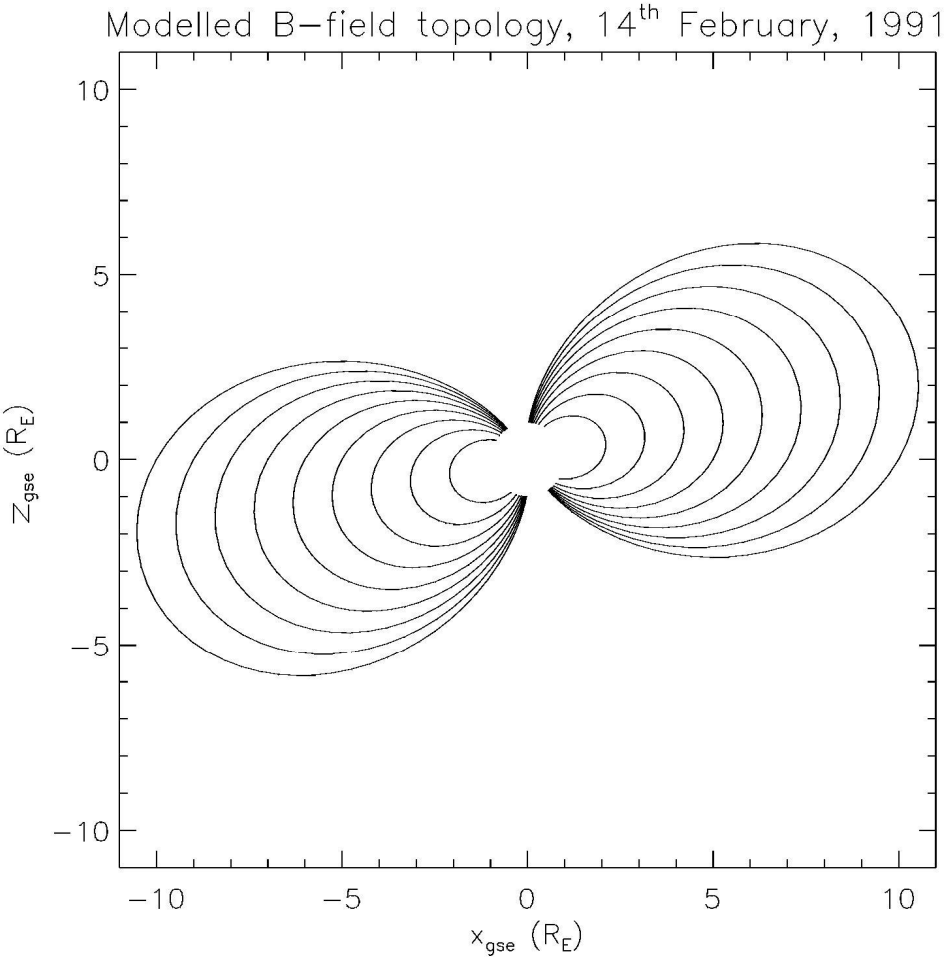

Figure 4.16: Topology of Earth's magnetic field from L = 1R_E to 10R_E for 14th February, 1991, made using the Tsyganenko model.

The mirror altitude was found for each degree in longitude.

The model was also used as a means of following the altitude of a particle as it moved along the field line. When given the L value of any field line, the model was able to map the field line as a function of altitude. Figure 4.16 shows the modelled geomagnetic field from L = $1.0R_E$ to $10.0R_E$ for 14th February, 1991.

4.3 Results

4.3.1 The Cross Sections from Orbit 497

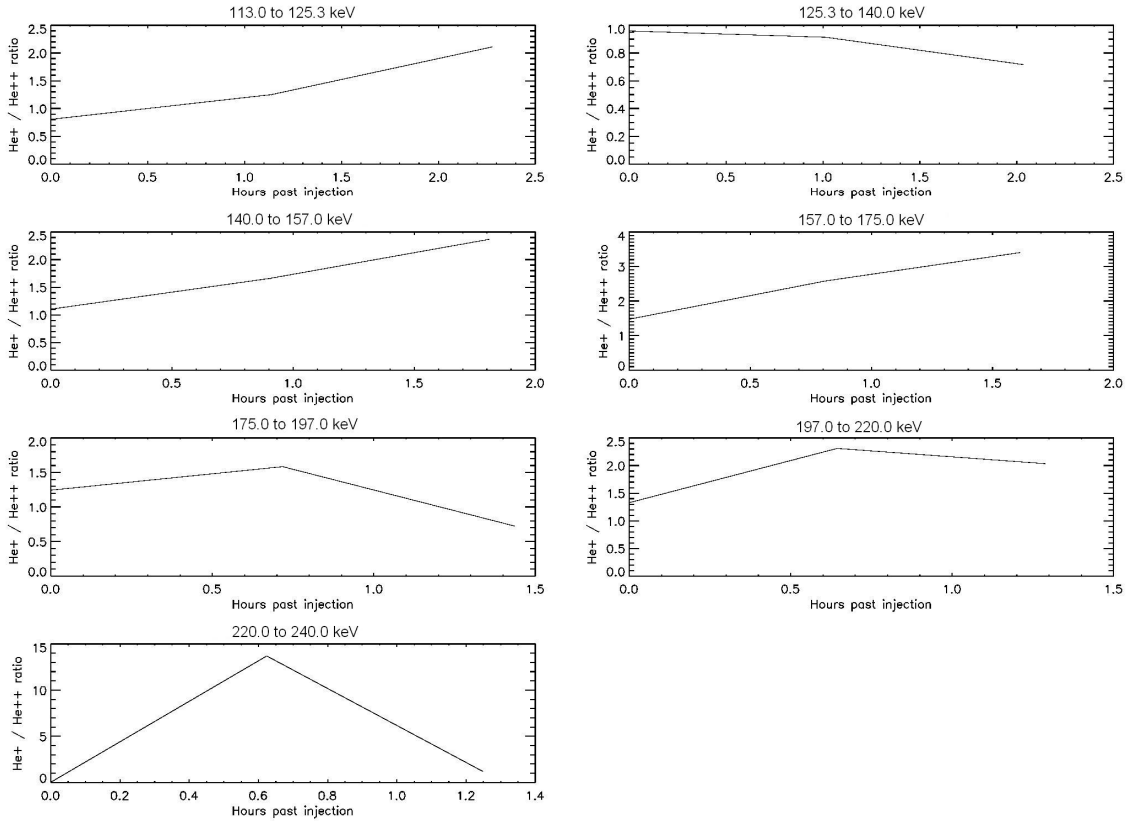

Figure 4.17: Helium ratio against time for energy ranges in the injection of orbit 497. The energy range denotes the E/q of the resulting He^+. A shift towards He^+ is generally observed after the first drift. Due to the large database, the error on the mean for each point was negligible, ranging between 0.003 and 0.05.

Figure 4.17 shows the shift in helium ratio as a function of time for the first and second drifts after the injection in orbit 497. This plot examines the

progression of the ratio as the helium ions drift, and is not concerned with the E/q range of the charge exchange source of the ions (the source He^{++} ions would be at half the E/q value). In this orbit, there is a net-shift from He^{++} to He^{+} after one drift, but after the particles have drifted a second time, the ratio in many energy ranges has reduced, indicating a greater density of He^{++}. There are a few possible explanations for this. The first is that new He^{++} has entered the outer belt from outside, though it seems unlikely, as no further injection was observed to occur. The second possibility is that the amount of He^{+} in the signature has increased enough for the charge exchange reaction given in equation 4.3 becomes prominent, and a greater amount of He^{+} is being lost as neutral helium. Finally, it is possible that dispersion has caused error in the measurement of the second drift echo.

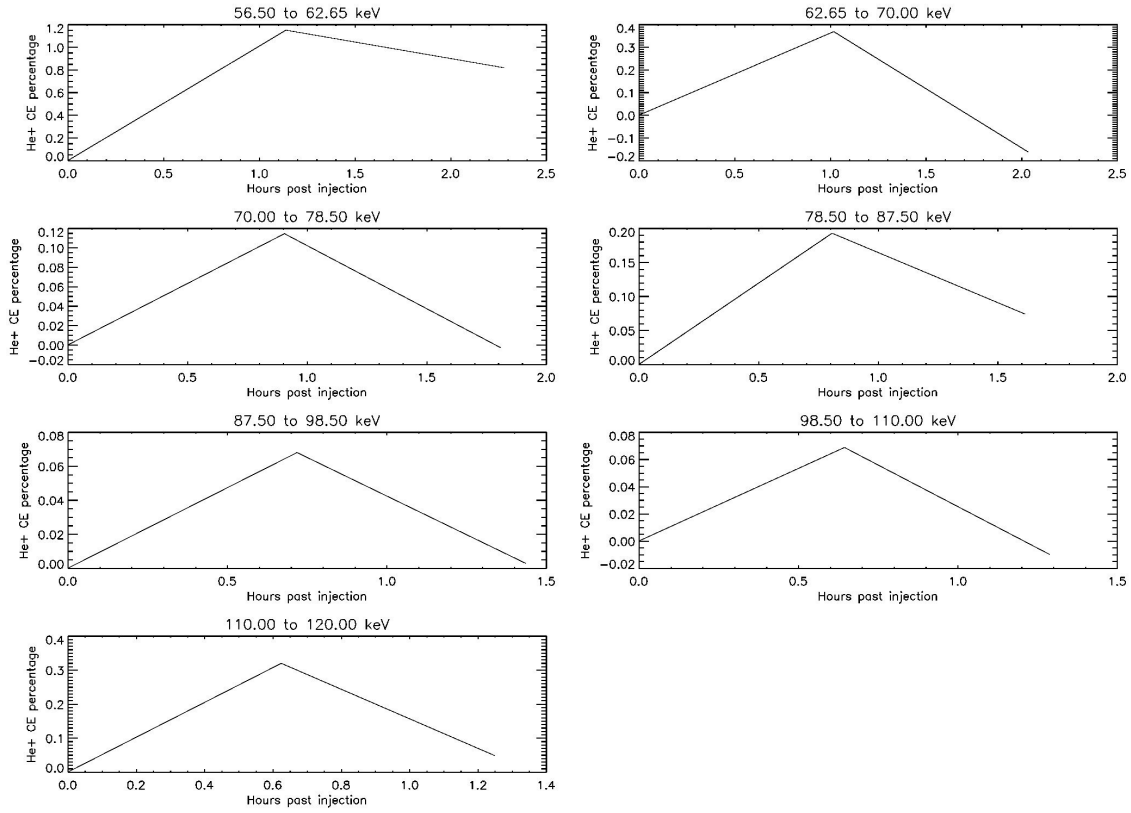

Figure 4.18: The percentage of the input He^{++} which has appeared as He^{+} due to charge exchange. The amount of new He^{+} in the drift echo is divided by the total He^{++} input from lower energy groups in the injection. The result is displayed against time, with one point for each drift.

In figure 4.17, the final energy range (of value 220.0 – 240.0 keV) held the entirely new population of He^+ in the first drift. The final plot in figure 4.18 shows that there is, indeed, a huge He^+ increase after a single drift, but it has been mostly lost after the second drift. This means that the appearance of the new population of He^+ was unlikely due entirely to charge exchange, though a terrestrial source for the new population is also unlikely, as the effect is not observed in the O^+ data for the same period.

Figure 4.18 shows the percentage of new helium against time for orbit 497. For this plot, the amount of new He^+ in the higher energy range of the drift echo is shown as a percentage of the He^{++} lost from the lower energy range. It is again observed that after a single drift, the shift is always toward He^+. Furthermore, it is worth noting that after a second drift, it appears that the reaction always goes in the opposite direction. This may be taken as evidence that increased He^+ alongside decreased He^{++} content has caused reaction 4.3 to become more prominent, though this seems unlikely as He^{++} has not decreased significantly and the relative physical cross sections should not change. It is also worth noting that the large number of charge exchanged He^+ ions which appeared at 220 – 240 keV was coupled with a large He^{++} injection at half of the E/q value, and so it may actually be reasonable to attribute it to charge exchange.

After a single drift, the general shift in helium ratio towards He^+ may be evidence of charge exchange. Using the method described in the first part of this chapter, the cross section for the charge exchange reaction was calculated. The results for orbit 497's first drift were multiplied by the relevant velocity for comparison with the work by [Tinsley, 1976], and are displayed in figure 4.19. Across the energy range under study, Tinsley calculated the product σv to range from ~1.5 x $10^{-7}cm^3s^{-1}$ at 60keV, down to ~1.0 x $10^{-7}cm^3s^{-1}$ at 115keV. The values for orbit 497 appear to be higher, starting at ~6.2 x 10^{-6} cm^3s^{-1} at 60keV, and reaching a minimum of 6.5 x $10^{-7}cm^3s^{-1}$ at 104.25keV, and finally with the high value of ~2.4 x 10^{-6} cm^3s^{-1} at 115keV.

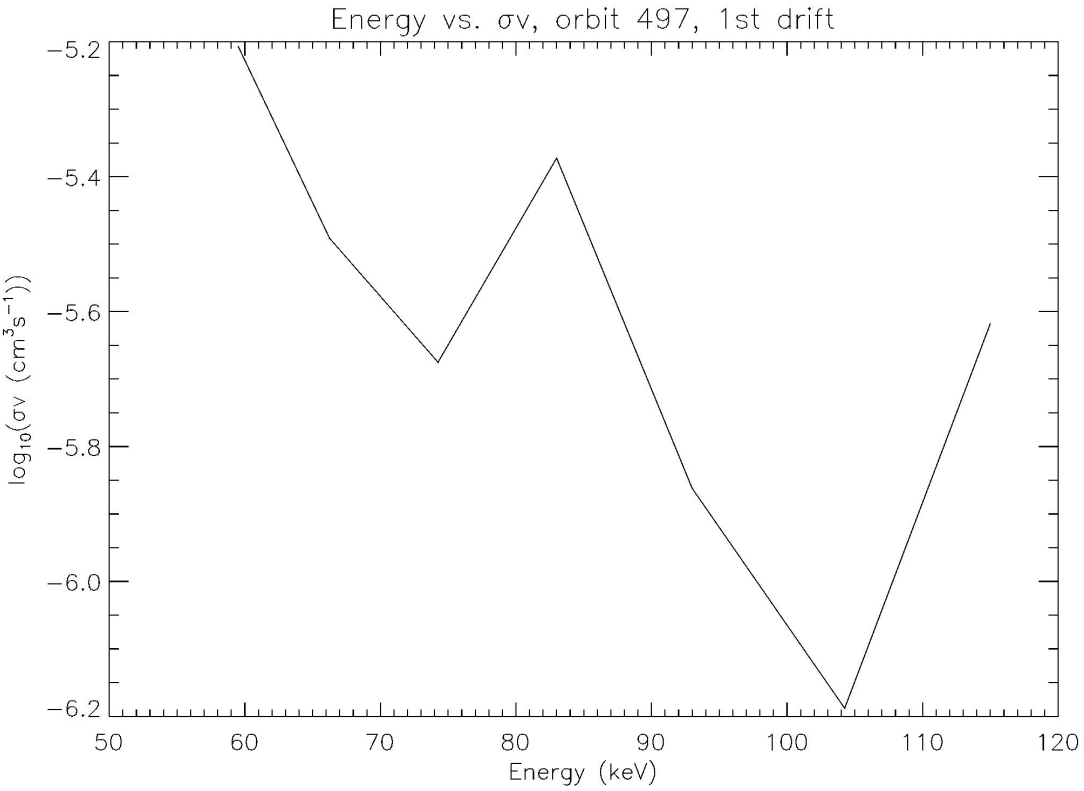

Figure 4.19: Calculated charge exchange cross section for 497, 1st drift. This cross section is ~10 times larger than those presented by [Tinsley, 1976].

As was observed in figure 4.18, the second drift of 497 showed evidence of the ratio moving in the He^{++} direction, and hence the cross sections were limited and not shown here.

4.3.2 The Cross Sections from Orbit 490

The first drift of orbit 497 showed He^{+} increases at all seven energies, and hence the cross section could be calculated for each. Within the other injections, there were sometimes occurrences of He^{++} increase after a single drift, due either to contamination or error in the drift time, which limited the energies at which cross sections could be calculated. Figure 4.20 shows the calculated cross section for orbit 490 of CRRES. Within the gap between 66.25 and 93.0 keV, the shift in number density was not indicative of charge exchange, meaning no cross

section could be calculated. At other energies, however, the cross sections are similar to those calculated from orbit 497, ranging between 2.5 x 10^{-7} cm^3s^{-1} to 4.7 x 10^{-6} cm^3s^{-1}, at 93.0 keV and 115.0 keV, respectively.

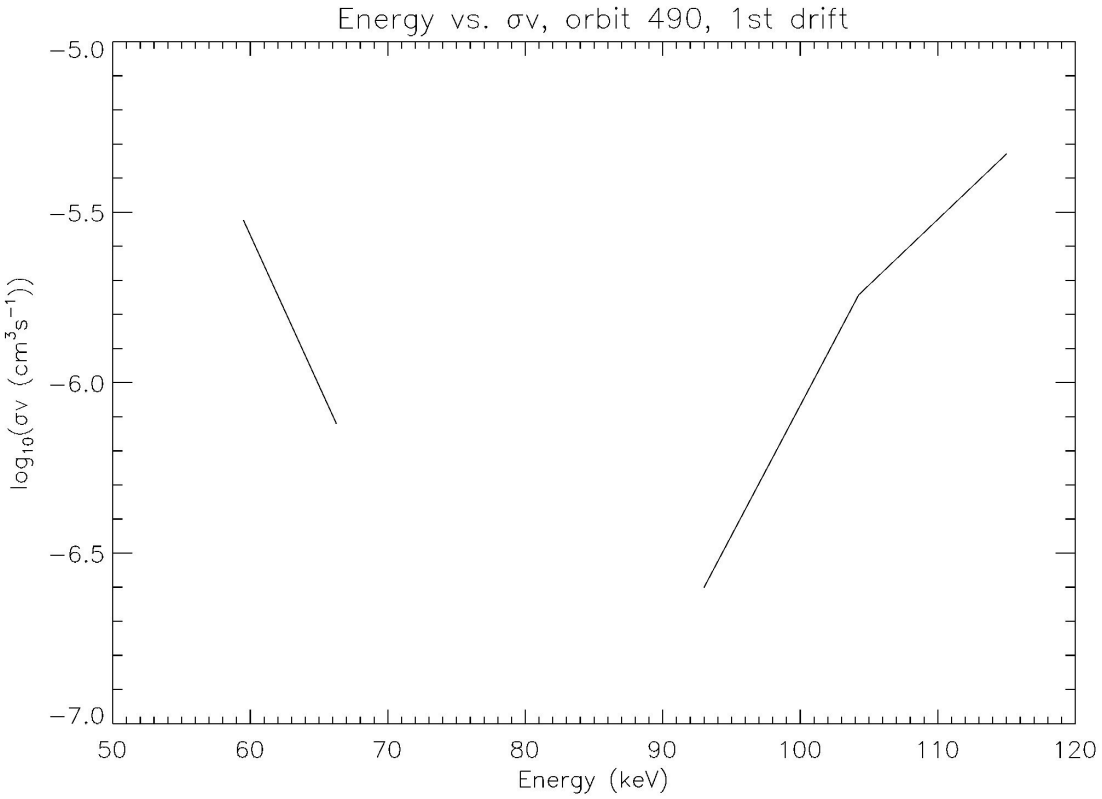

Figure 4.20: Calculated charge exchange cross section for 490, 1st drift. These values are similar to those from 497.

4.3.3 The Average Cross Section

Figure 4.21 shows a linear average of the cross section using all data from drift 1. The error bars indicate the standard deviation for each energy range. It is observed that the points do fit closely to the linear pattern, with the standard deviation usually generally being around an order of magnitude.

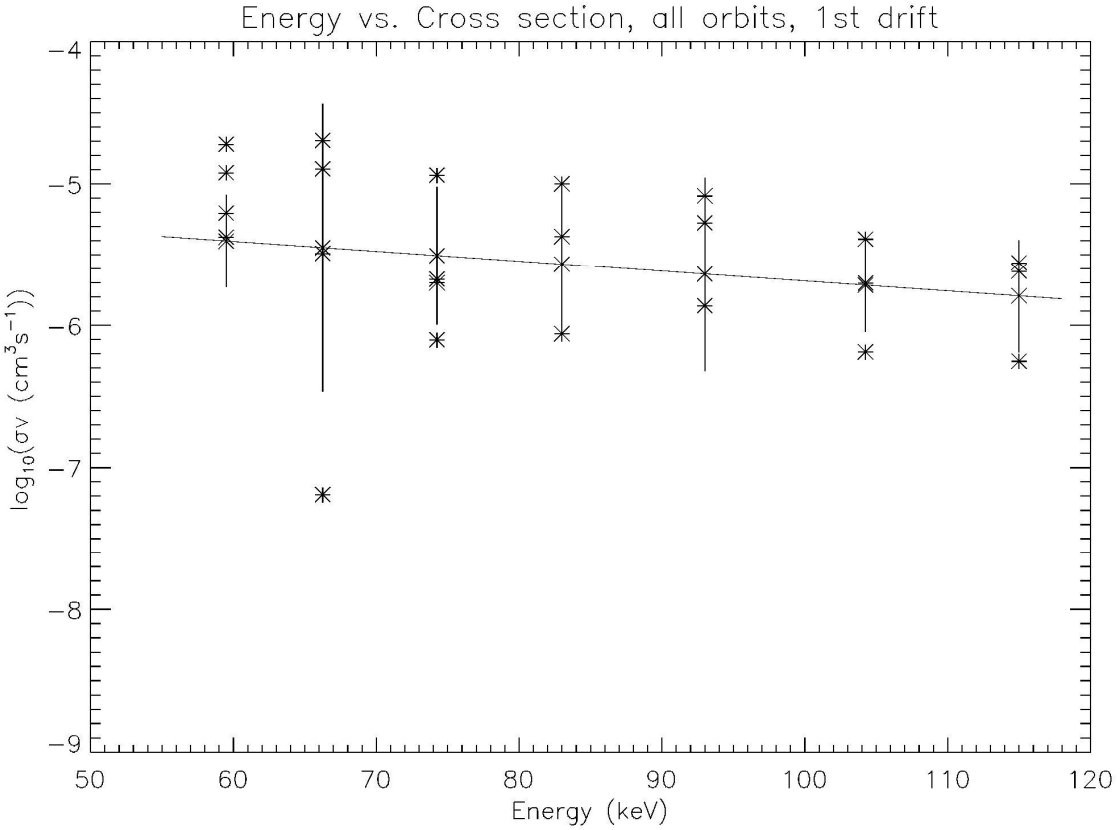

Figure 4.21: Averaged cross section using all values from the first drift. Error bars show the standard deviation at each energy. This is approximately an order of magnitude.

Figure 4.22 shows Tinsley's equivalent cross section plot, with the He^{++} cross section marked approximately between the relevant energy ranges in red. The data for this plot was taken from [Rapp, 1974], who compared modelled cross sectional data to experimental results. Between the relevant energy ranges, Tinsley's graph shows a peak in the cross section of around 1.5 x 10^{-7} cm^3s^{-1}, which begins to decline at higher energies, reaching ~1.0 x 10^{-7} cm^3s^{-1} at 120 keV. The values calculated in this study, presented in figure 4.22, range from a maximum of 4.3 x 10^{-6} cm^3s^{-1} down to 1.5 x 10^{-6} cm^3s^{-1}, around an order of magnitude larger than Tinsley's.

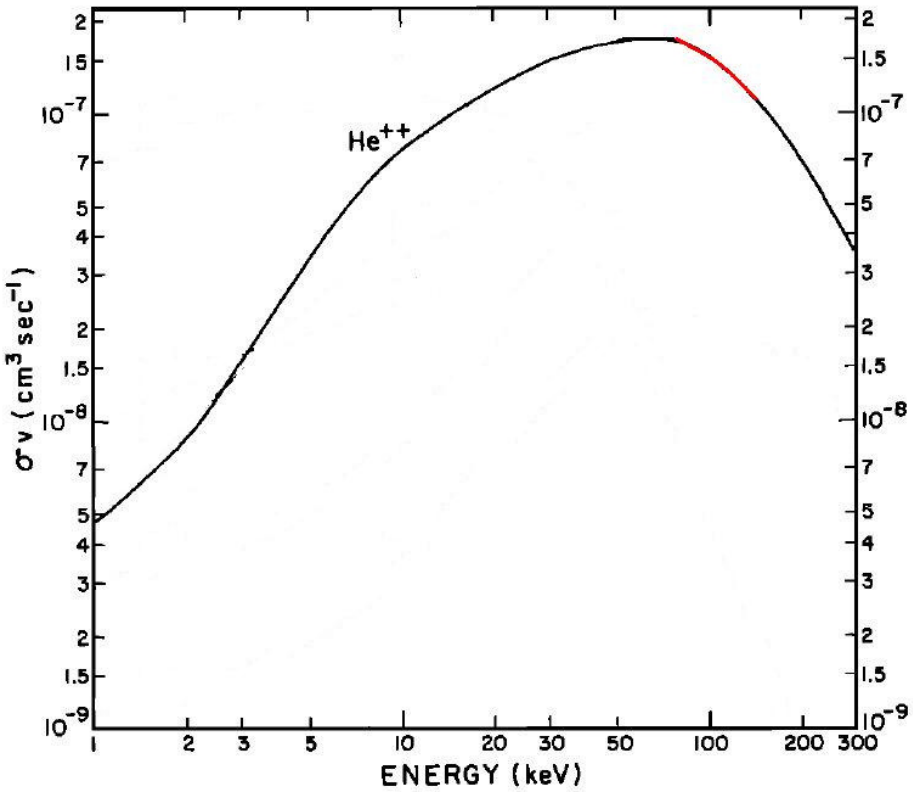

Figure 4.22: Tinsley's cross section plot for the reaction. The energy range under investigation is marked in red. The cross sectional values of 10-7cm^{3}s^{-1} are ~10 times smaller than those calculated in this work.

Figure 4.23 shows the average cross section after two drifts. The value of this cross section at 60 keV has a value of ~4.4 x 10^{-6} cm^{2}s^{-1}, very similar to that of the first drift. The more-negative slope of the data, however, leads to a lower minimum cross section of ~2.7 x 10^{-7} cm^{2}s^{-1} at 115 keV. The tendency for the cross section to decrease with energy after a second drift could be taken as evidence that decreased He^{++} alongside increased He^{+} has caused charge exchange reaction 4.3 to become relatively more prominent for the injected population, as it would appear that less charge exchange had occurred. The physical cross section itself would not be expected to change, but the calculated cross section may have been affected by the pitch angle distribution moving towards 90^o after drifting, lowering the average N_H density and decreasing the amount of charge exchange occurring. The effect of the reaction 4.3 was not been considered in this study.

Due to the assumption that all charge exchange occurred in the early part of the orbit (discussed later, alongside other assumptions), the continuation into drift 2 may not actually provide any useful information, as a large amount of charge exchange is expected to have been missed between drifts. Computing the charge exchange cross section between the first and second drifts is also not possible, as more often than not the He^{+} to He^{++} has shifted in the other direction.

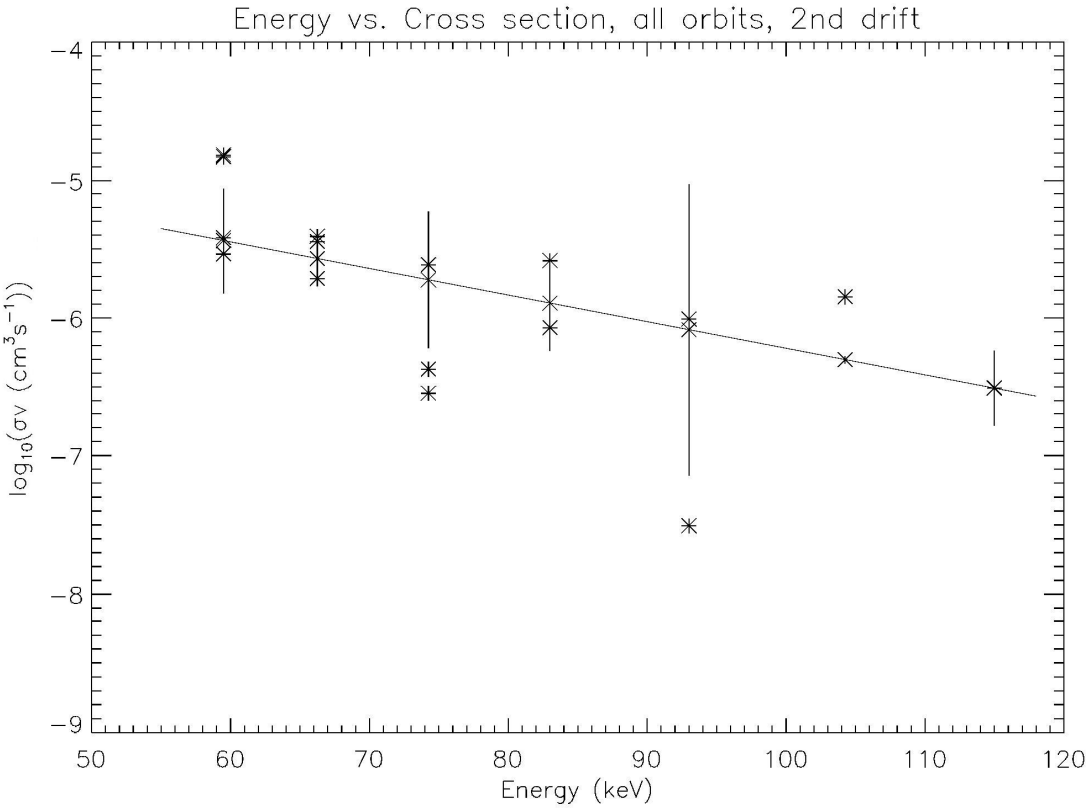

Figure 4.23: Averaged cross section using all values from the second drift. The slope of this graph is more negative than that of the first drift, but cross sectional values are similarly large.

4.3.4 Comparison of Cross Sections with Recent Work

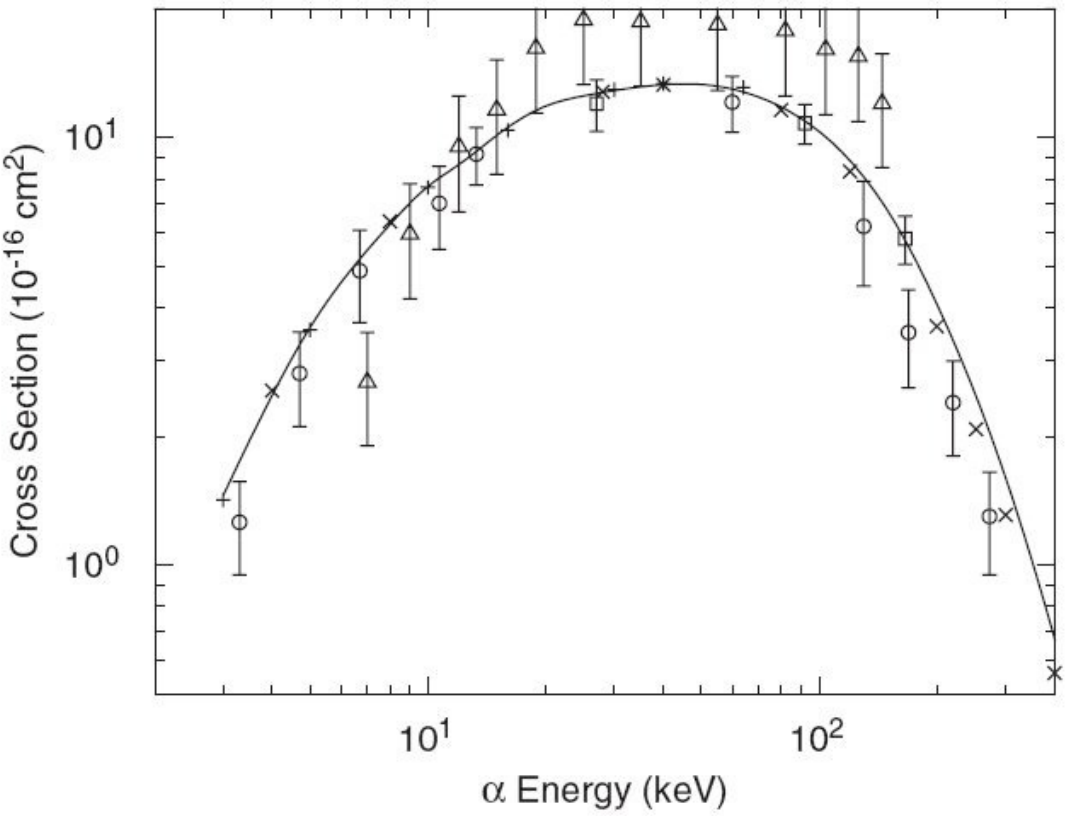

Figure 4.24: Compilation of more recent cross section data for the reaction from [Winter, 2007], showing both modelled and experimental results.

Figure 4.24 shows the average cross section for all possible electron shell transfers, taken from [Winter, 2007]. This plot shows both modelled and experimental data. Experimental data include the triangles, from [Bayfield and Khayrallah, 1975]; the circles, from [Shah and Gilbody, 1978] and [Nutt et al., 1978], and the squares, from [Olson et al., 1977]. The crosses represent a two-centre Gaussian model [Toshima, 1994] and the solid line represents the two-centre Sturmian model discussed in the paper itself. At the energies relevant to this study, experimental cross sections have a maximum of ~10^{-15} cm^2, and a high-energy drop reaching values of ~10^{-16} cm^2.

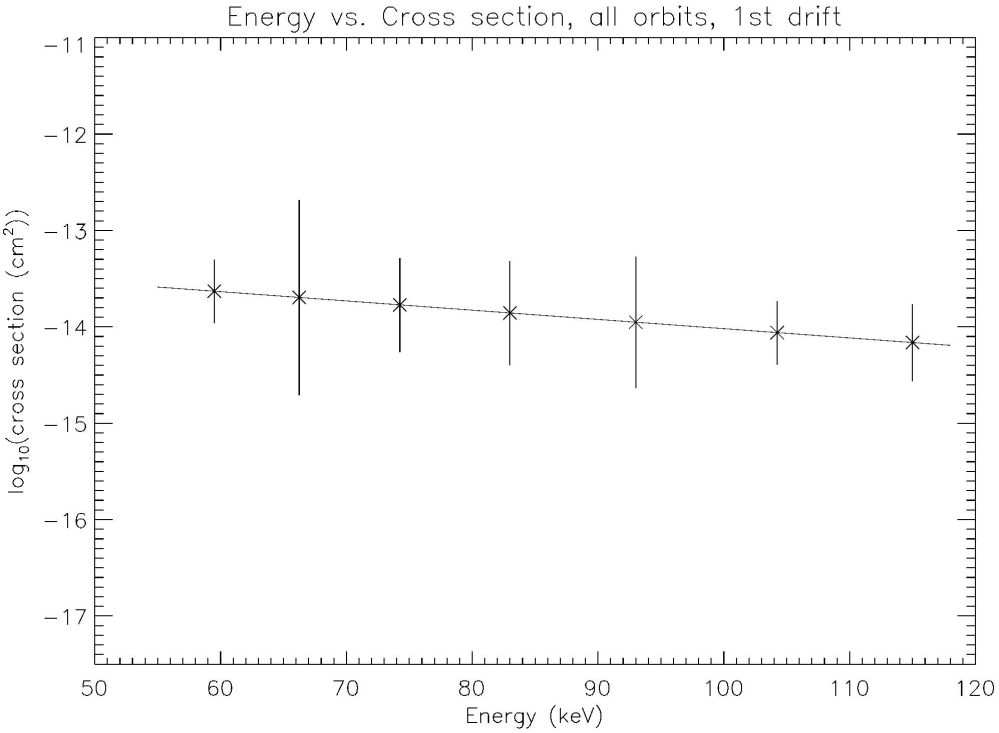

Figure 4.25: Calculated cross section for the first drift, approximately ten times larger than those in 4.24. Error bars show that the standard deviation is approximately an order of magnitude.

Figure 4.25 shows a linear regression of the calculated cross sections for drift 1. The slope of this graph is in the expected direction, with the lower end of the energy range having the larger cross section. The calculated values for the cross sections are larger than those from the work displayed in figure 4.24. Ranging from ~2.6 x 10^{-14} cm^2 at 60 keV, down to ~6.4 x 10^{-15} cm^2 at 115 keV, they are approximately a factor of 10 greater. Although this seems, at first, likely to be incorrect, in a paper by [Smith and Bewtra, 1978], the charge exchange lifetimes of ring current ions were found to be shorter than predicted, and recommended re-examining the composition of the ring current during the recovery phase of magnetic storms. In their paper, cross sections for the various charge exchange reactions were taken from previous work by many different authors, with those of the reaction under study here calculated by [Fite et al., 1962]. Shorter charge exchange lifetimes would lead to larger cross sections in this study, which may explain the relatively large cross sections calculated.

4.3.5 Consequences of the Assumptions

It is possible that the large cross sections may be explained by investigating the effect that some of the assumptions made to complete this work may have had. The assumption that charge exchange occurred within the early part of the orbit possibly had the greatest effect. As there is not a rapid loss of He^{++} (He^{++} drift echoes are clearly observed), the average cross section itself may be inaccurate. This could be explained by the pitch angle shifting toward 90^{o}, which would decrease the average N_H value across a bounce path and hence increase the calculated cross section.

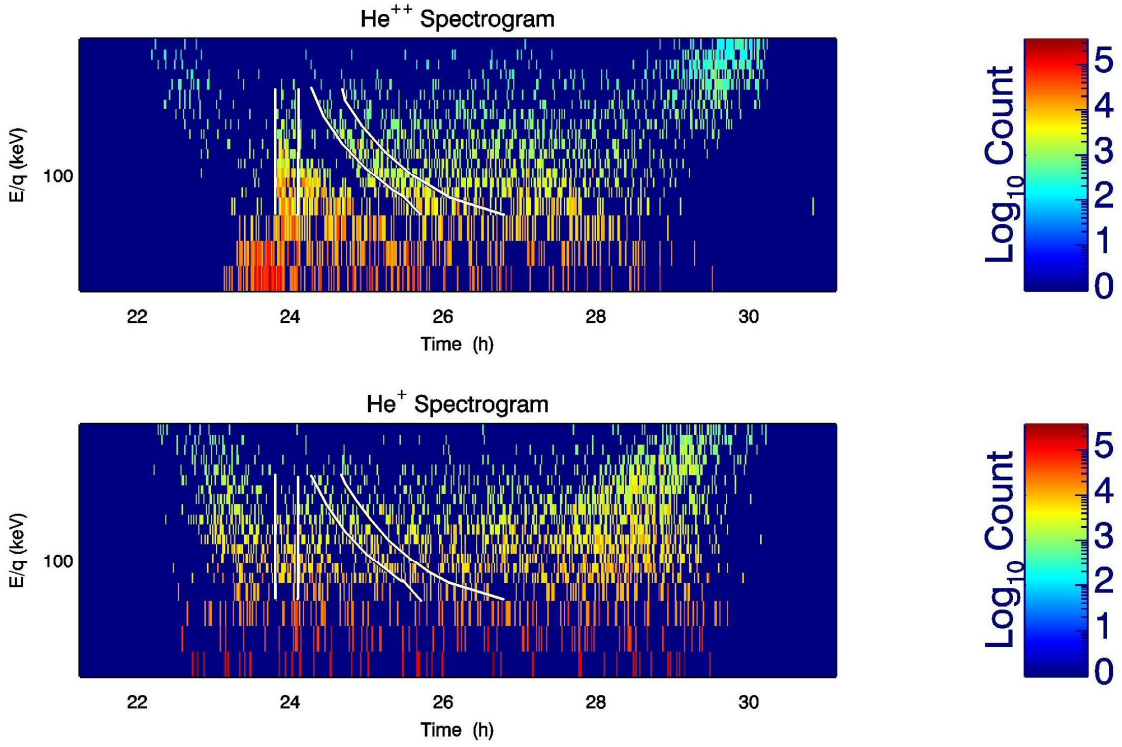

Figure 4.26: He^{++} and He^{+} spectrograms for orbit 497 of CRRES, marked with the modelled location of injected charge-exchanged particles if a partial drift is considered. In this spectrogram, all charge exchange is assumed to have occurred in the duration between the vertical lines encompassing the injection. With this imposed, all charge exchanged He^{++} ions would result as He^{+} in the upper part of the drift echo in the He^{+} spectrogram.

If the distance over which the particles must have travelled is reduced to allow for this, the calculated cross sections become larger. It is worth noting that, in order for the new population to have fallen within the drift echo, the particle would have had to have occurred across this timescale, and hence the cross sections would be expected to be large. Figure 4.26 shows CRRES orbit 497 spectrograms for He^{+} and He^{++} with the drift period for the maximum duration of the partial drift marked. The first drift echo is encompassed well using this method. The distance travelled over this partial drift is dependant on velocity; the time taken for the partial drift being fixed. A time of 0.3 hours was chosen in this study, as it encompassed the first drift echo well.

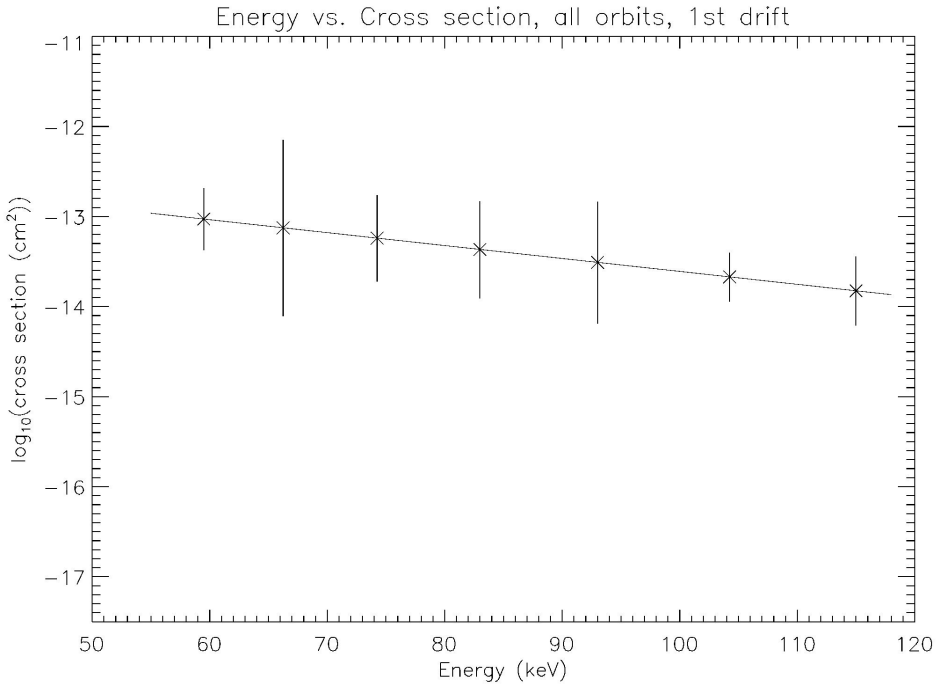

Figure 4.27: Averaged cross section, taking into account the partial distance around the earth for rapid charge exchange, after which He^{+} could end up within the first drift echo. In doing this, the cross section is increased by approximately half an order of magnitude.

In figure 4.27, the cross section was taken across the partial distance defined by 0.3 times velocity, as depicted in figure 4.26. As predicted, the cross section is larger when partial drift is given allowance, with the new maximum of

the average at 60keV being 1.0 x 10^{-13} cm^2, and the minimum at 115keV being 1.3 x 10^{-14} cm^2. Though larger, it can be seen that these values have not changed radically due to the decrease in path length. There is also a large overlap of actual values with the initially calculated, showing that the average may not be a good representation of the truth due to there only being few data points. This is shown in figure 4.28.

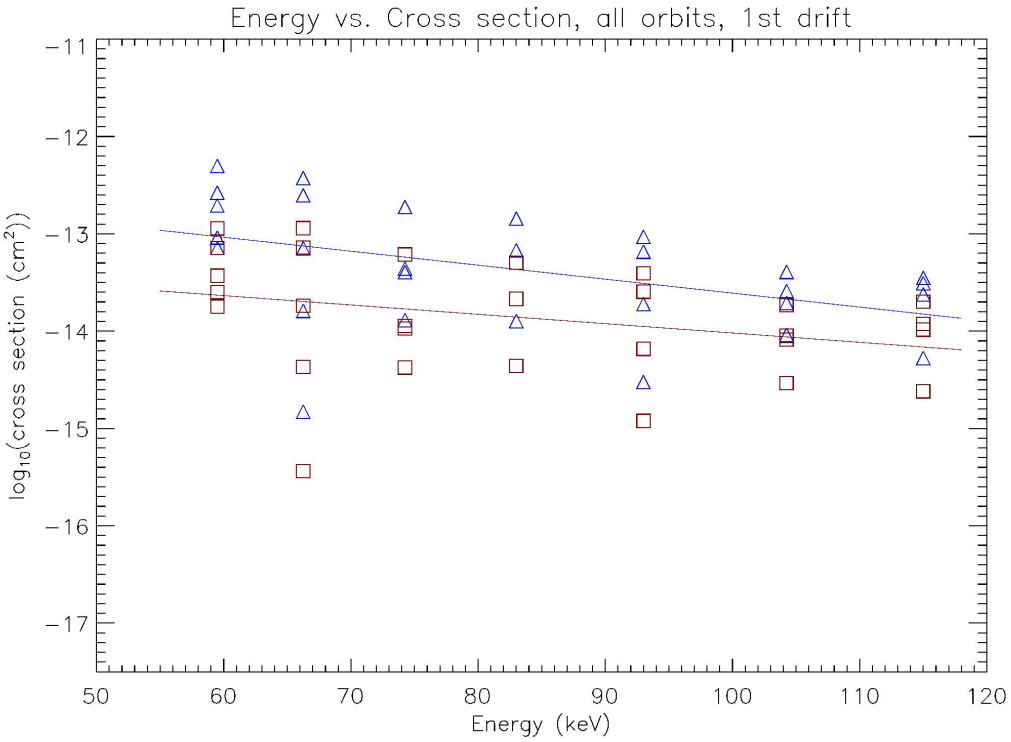

Figure 4.28: Comparison of full (red squares) to partial (blue triangles) drift cross sections. The amount of deviation of points from the average is shown to be greater than the difference in cross section, meaning that the difference in cross section due to the consideration of a partial drift is smaller than the deviation of points from the mean.

Another assumption which may have affected the cross section was that the time taken by a particle's bounce could be approximated using simple harmonic motion. In a paper by [Hasegawa, 1975], it was shown that a particle's bounce motion could be approximated as simple harmonic using a paraxial approximation for the geomagnetic field, given by equation 4.12. The SHM approximation was used to calculate the average number density of hydrogen

across a bounce path. This value was calculated as ~1200cm^{-3}, assuming an isotropic pitch angle distribution. It is to be expected that this value may be a large source for error in the cross section, as multiplying by a factor of x will result in the same factor difference in the cross section.

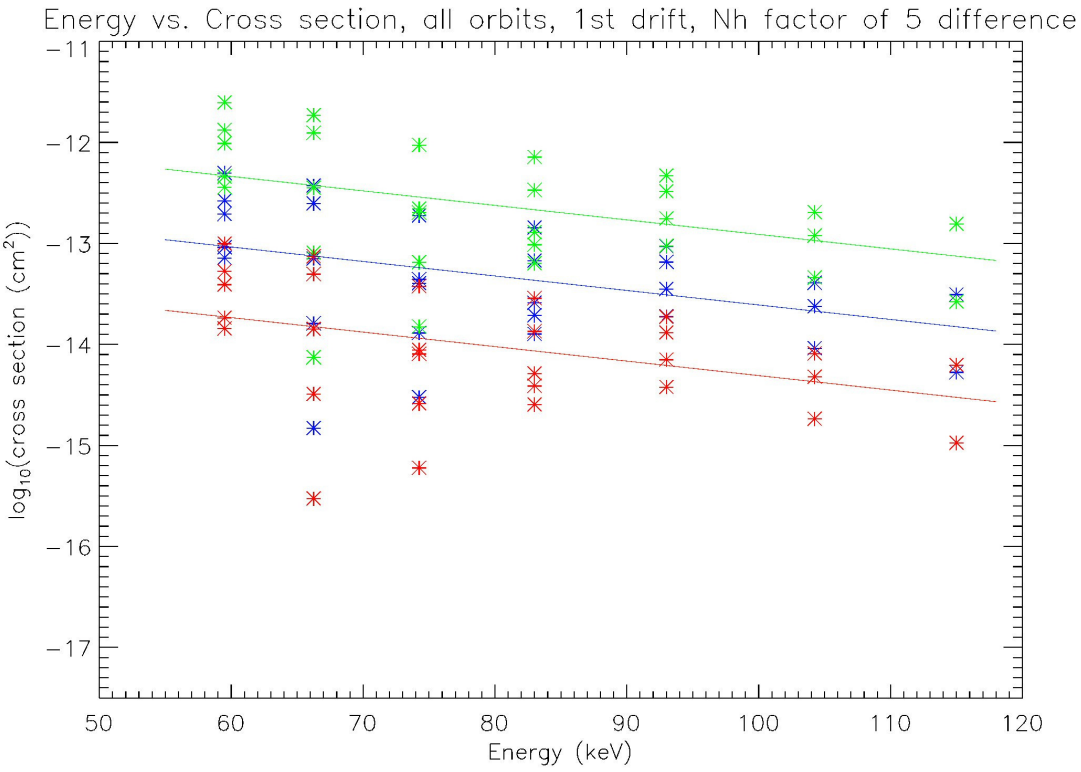

Figure 4.29: The effect on the partial drift (blue) of multiplying (green) and dividing (red) the average N_H value by a factor of 5. Again, the deviation of points is shown to be greater than the cross sectional difference.

Figure 4.29 shows this effect if the cross section (for the partial orbit from the above section) is multiplied or divided by a factor of 5, coloured red and green, respectively. The blue line shows the original cross section, corrected for path length. It is observed that a larger density of neutral hydrogen would have meant smaller cross sections. An accurate description of the time spent at different altitudes along a bounce path would be a good improvement to this work.

The exospheric temperature was chosen to be 950K by comparison to Lepine's work. During this solar maximum period, however, it is possible that the

temperature would have been higher. With reference to Table 4.1, higher temperatures lead to lower exospheric neutral hydrogen densities, and hence a higher temperature would lead to a larger cross section. This does, therefore, not explain the large cross sections.

4.4 Discussion and Conclusions

Multiplication with velocity of the calculated cross sections initially showed that increases in He^+ with drift may be due to charge exchange, being only a factor of 10 greater than values from [Tinsley, 1976], with the standard deviation indicating that the cross section could reach lower values. Across most of the injections, He^+ tended to increase after the first drift, which gave further support for charge exchange occurring. After the second drift, the difference in He^+ had usually become less, and the possibility that the shift from He^{++} to He^+ had made the charge exchange reaction 4.3 more prominent was suggested, with He^+ being lost as neutral helium. As only a small population of He^{++} were considered, because they were in the only part of the injection which could feasibly have ended up as He^+ in the first drift, the helium ratio for the second drift will not compare closely to that of the injection. Due to this, the possibility of calculating the cross section for the charge exchange reaction which results in neutral helium was not carried out, but would be a good extension to the work in future.

The average cross sections were calculated to range from ~2.6 x 10^{-14} cm^2 at 60 keV down to ~6.4 x 10^{-15} cm^2 at 115 keV, which are approximately a factor of ten greater than previous experimental work by [Bayfield and Khayrallah, 1975], [Shah and Gilbody, 1978], [Nutt et al., 1978] and [Olson et al., 1977]. The cross sections calculated here match most closely those of [Bayfield and Khayrallah, 1975], especially at the highest energies. Larger error in the lower energy calculation is likely due to a large amount of charge exchange occurring in the tail of the injection, which was not considered in this study.

If the duration of charge exchange across which a He^{++} ion could feasibly end up as a He^+ ion within the first drift echo is taken into account for, the shorter

distance over which charge exchange must be occurring increases the cross section by a factor of ~5, though slightly less at high energy than low, as can be seen in the steeper gradient of the larger cross section in 4.27. This small difference is likely to be due to the greater accuracy at high energies. The newly calculated cross sections range from ~1.0 x 10^{-13} cm^2 at 60keV, down to 1.3 x 10^{-14} cm^2 at 115keV.

It is possible that the average N_H value of ~1200 cm^{-3} was not correct. This may have been due to errors caused by the approximation of bounce timing using simple harmonic motion. If SHM does not adequately describe the motion of the particle, the percentage of time spent at low altitude may have been larger, which would lead to smaller cross sections for the same amount of charge exchange. It was shown that any factor difference in average N_H would translate to the same factor of difference in cross section.

A comparison of the cross sections calculated here to a plot by [Winter, 2007], which showed recent experimental results and modelled data, showed that the method of calculation using dispersionless substorm injections and their drift echoes yields cross sections which are larger than suggested by other work by a maximum factor of ~50. It is clear that these values are unphysically large, but it is still possible that charge exchange is responsible for the new population in helium, as in a previous paper by [Smith and Bewtra, 1978] the rate of charge exchange within the ring current was found to be faster than expected. It is believed that the method of using dispersionless particle injections and their drift echoes to calculate charge exchange cross sections was reasonable, with the limitations of the CRRES satellite causing the errors in the cross sections which were found. In order for the study to be carried out to a greater degree of accuracy, multiple satellite measurements of the radiation belt would be required simultaneously, in order to actually follow the population as it drifted around the Earth. Future magnetospheric research may accommodate this need. With the limitation to the study of using a single satellite, alongside the problems faced while investigating the helium ratio within the second drift echo, a good idea to further investigate the effect would be to study all occurrences of injections with

only a single drift echo visible. This would create a much larger statistical dataset, improving the accuracy of the final cross sections.

Although some evidence of charge exchange has been presented, the likelihood that the "new" population, which appeared at high energy in orbit 497 was not entirely due to charge exchange, as the He^{++} was unlikely to have formed a drift echo; the complete duration in which a particle could have ended up being shown in figure 4.15. Another possible explanation for this particular event would be that the injection has an MLT-varied composition, and that the He^{+}, which must have been at the head of the injection, was simply missed by the satellite. However, this explanation also seems unlikely, as none of the injections appeared to contain much He^{+}. A study of the He^{+} content of injections depending of the MLT of the satellite at the time of injection would be necessary to investigate this.

Chapter 5: Geomagnetic Storms which do not Contain Substorms

5.1 Storms with no Substorms

5.1.1 Introduction

Tsurutani has shown instances ([Tsurutani et al, 2003]) of geomagnetic storm periods which show no evidence of substorm activity in auroral data (i.e. no large scale expansions). Out of eleven storms during 1997, which were specifically chosen due to the nature of the ICMEs which caused them, five were not observed to contain substorms. He attributed the lack of substorm expansion phases during these events to the smooth, negative B_z profiles of the magnetic clouds within the ICMEs, the expectation being that steady reconnection allowed the magnetosphere to convect smoothly while under the influence of this solar wind discontinuity. In this chapter, LANL electron data during the storms are examined for evidence of substorm injections. Following on from this, any substorm injections will be investigated, with focus on the solar wind precursor to these injections. A similar study using data from 2000 – 2003 is also carried out.

5.1.2 ICMEs with Magnetic Clouds

In the paper, the eleven storms Tsurutani studied were caused by fast ICMEs containing magnetic clouds, identified by R. P. Lepping. Though certain characteristics are expected within a magnetic cloud, Tsurutani et al. note that there is no unique set of criteria, as concluded by [Zwickl et al., 1983]. Generally, a magnetic cloud within an ICME would be expected to show a decrease in ram pressure and an increase in magnetic field density, and a smooth rotation in the direction of the magnetic field vector. The B_z rotation was especially important in the study, as it aimed to prove that substorms were not visible in auroral data during the theorised steady magnetospheric convection that occurs during the events. Figure 5.1 shows the solar wind parameters of Ram Pressure, B

magnitude and B_z for an ICME containing a magnetic cloud, as well as the AE and D_{ST} indices for a geomagnetic storm ([Tsurutani et al., 2003]).

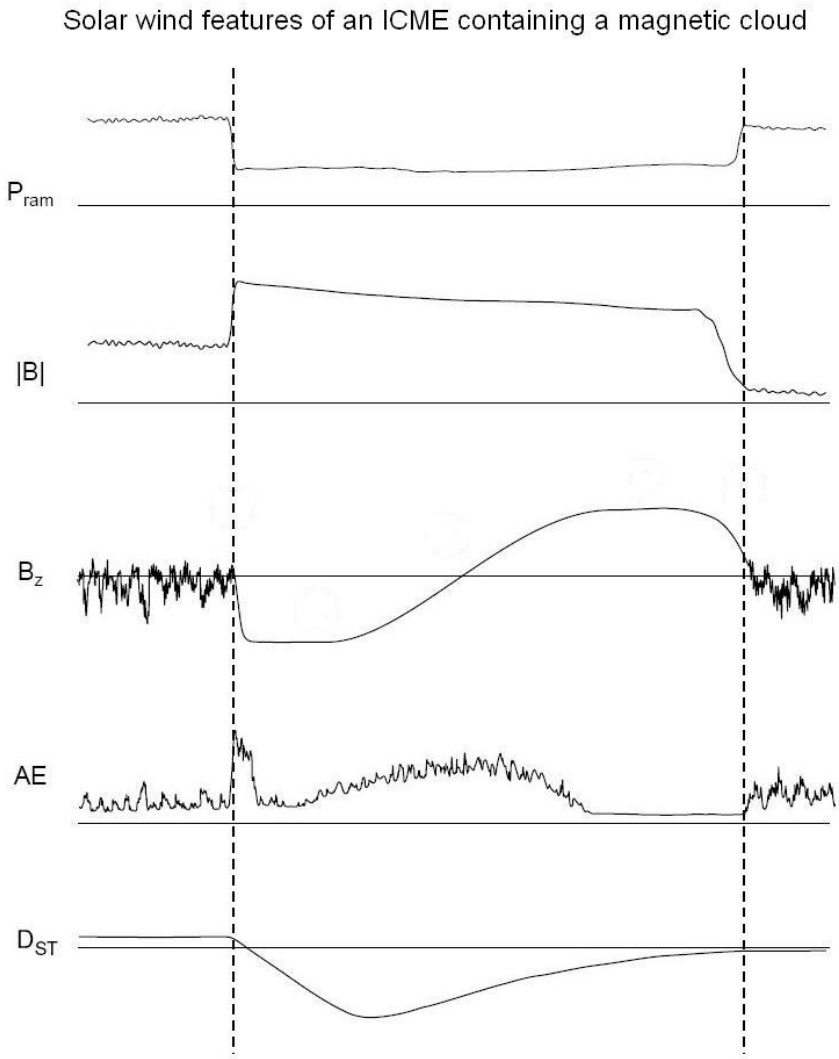

Figure 5.1: Solar wind features of an ICME containing a magnetic cloud, from [Tsurutani et al., 2003]. During the negative B_z portion of the cloud, it was theorised that steady magnetospheric convection would lead to a lack of substorm activity.

5.2 Geosynchronous Altitude Electrons during the Substormless Storms of 1997

The storms of 1997 which did not contain substorm expansions in auroral data may contain other evidence of substorm activity. Another signature of the magnetospheric substorm is geosynchronous particle injections across magnetic midnight. The substormless-storms of 1997 will now be investigated in particle data. Due to the geosynchronous nature of the injections, electron data from the Los Alamos National Laboratory (LANL) geosynchronous satellites are ideal, as they offer near-constant coverage of the relevant altitude across the period.

5.2.1 LANL Electron Spectrograms

The spectrograms presented in this section show data merged from three separate instruments; the Magnetospheric Plasma Analyser (MPA), Synchronous Orbit Particle Analyser (SOPA) and Energetic Spectrometer for Particles (ESP) ([4]). In this study, data will be used from satellites 1989-046, 1990-095, 1991-080, 1994-084 and LANL-97A, all of which carried these instruments.

MPA Capable of detecting particles between energies of ~1eV/e and 40keV/e. Low energy substorm injections would be expected at the upper end of this range.

SOPA Split into ten differential channels, this device can detect particles from 50keV to above 1.5MeV. The most energetic substorm-related electrons would fall into the lower part of this range.

ESP This device detects the high energy particles, with its nine channels capable of observing energies ranging from 0.7MeV to 26MeV. These high energies are not generally associated with substorm injections.

One would therefore expect substorm injections to appear across the MPA and SOPA partition in LANL spectrograms.

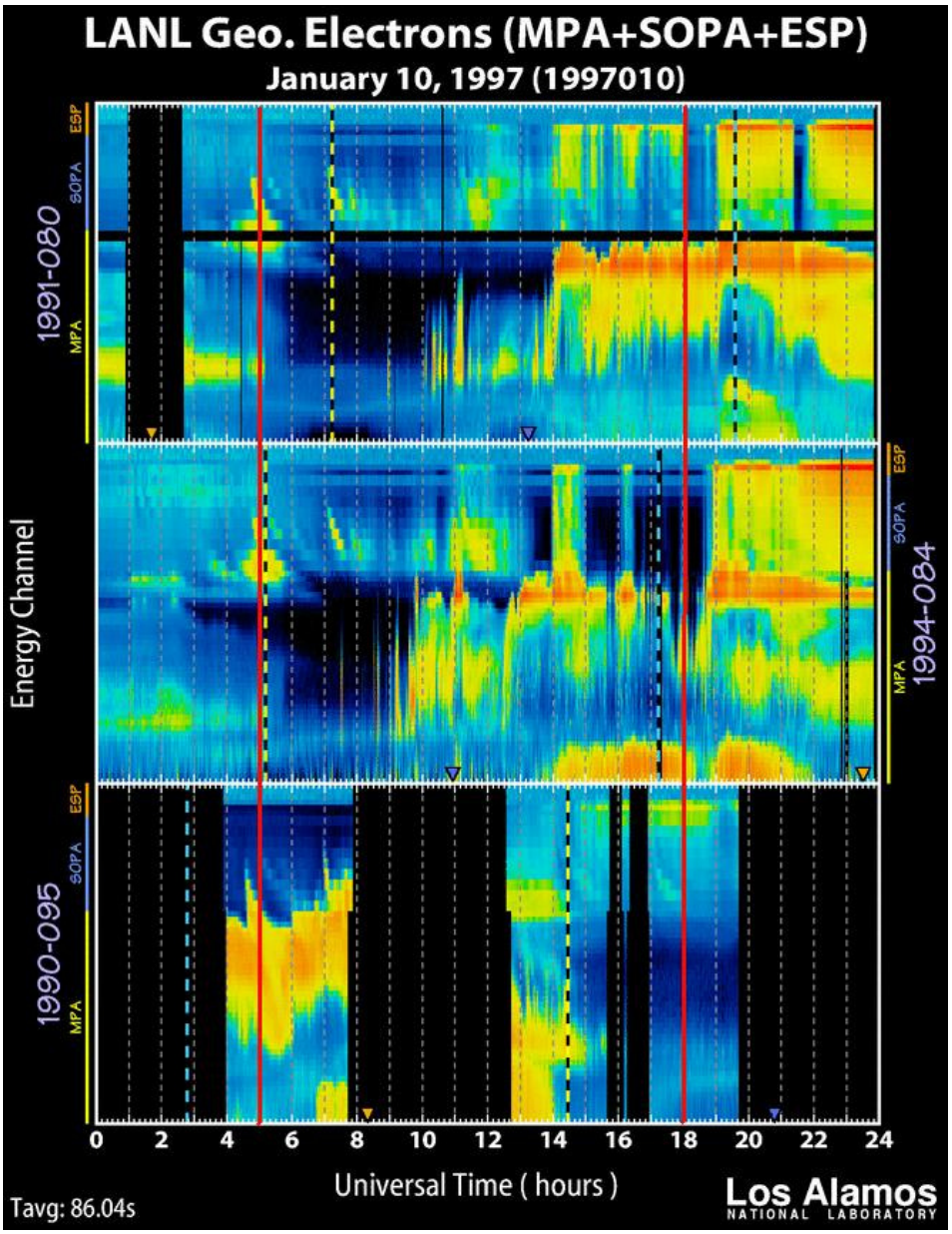

Figure 5.2a LANL Electron Spectrogram, January 10th, 1997, taken from [4]. The B_z negative portion of the magnetic cloud is marked between the red lines at 05:00 and 18:00 UT. Dispersionless injections appear in a similar form as in ion data, with electrons of multiple energies reaching the detector at the same time. Each of the three plots in this figure show data from a different LANL satellite, with the x-axis showing UT and the Y axis showing energy. The vertical dotted lines represent each satellite's passing of midnight (blue) and midday (yellow) MLT.

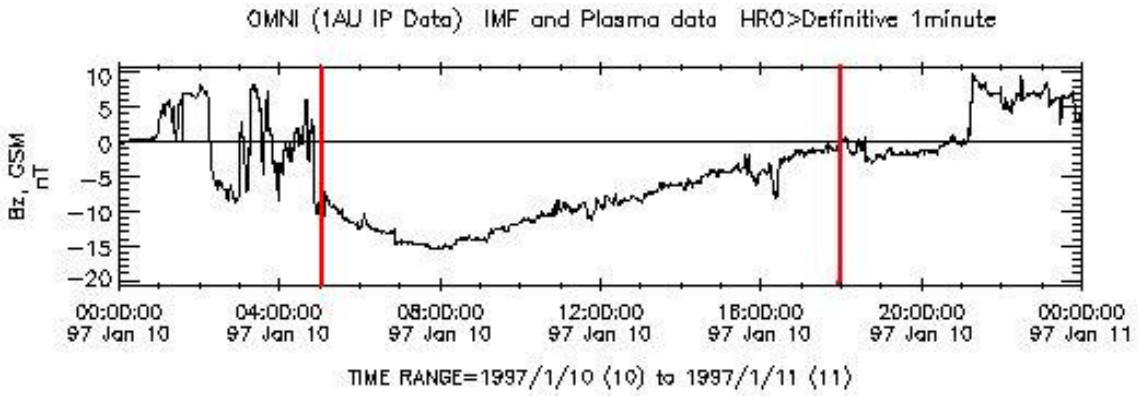

Figure 5.2b: Smooth negative B_z portion of the fast-CME magnetic cloud of January 10th, 1997; data from [King and Papitashvili, 2005]. The negative section is enclosed by the red lines.

Figure 5.2a shows LANL electron data for January 10th, 1997. This is the first of the storms in 1997 reported as having no auroral substorm. The duration of the negative-B_z portion of the cloud can be seen in 5.2b between ~05:00 UT and 18:00 UT. The LANL electron data covers the period entirely, with three separate satellites in operation. A near-dispersionless injection signature is observed to occur at ~04:30 UT by satellite 1990-095, whose location is ~01:54 MLT. The proximity of this satellite to midnight is further evidence of this being a dispersionless substorm injection. The same signature is then detected by 1991-080 and 1991-084 (located at ~09:15 MLT and 09:21 MLT, respectively), though it has dispersed somewhat during the short interval of drift. This injection occurs immediately before the cloud interval, meaning the magnetotail may have released its excess energy before the steady-reconnection period - this possibly explains the lack of substorm expansion phases. At ~11:07 UT, a dispersed signature is observed by 1994-084, located at 18:11 MLT. The satellite nearest to midnight, 1990-095, took no data during this period. At 14:00 UT, 1994-084 observes another injection signature, which is then observed by 1990-080 moments later. The locations of these satellites are ~20:55 MLT and ~18:55 MLT respectively, suggesting this injection has drifted oppositely to electron flow. The short timescale over which these two observations occur, however, suggests that they are both the same injection, with the later observation being the tail end.

This could be due to the injection's energisation region spreading across midnight. The maximum energy of this injection is lesser for the tail-end observation.

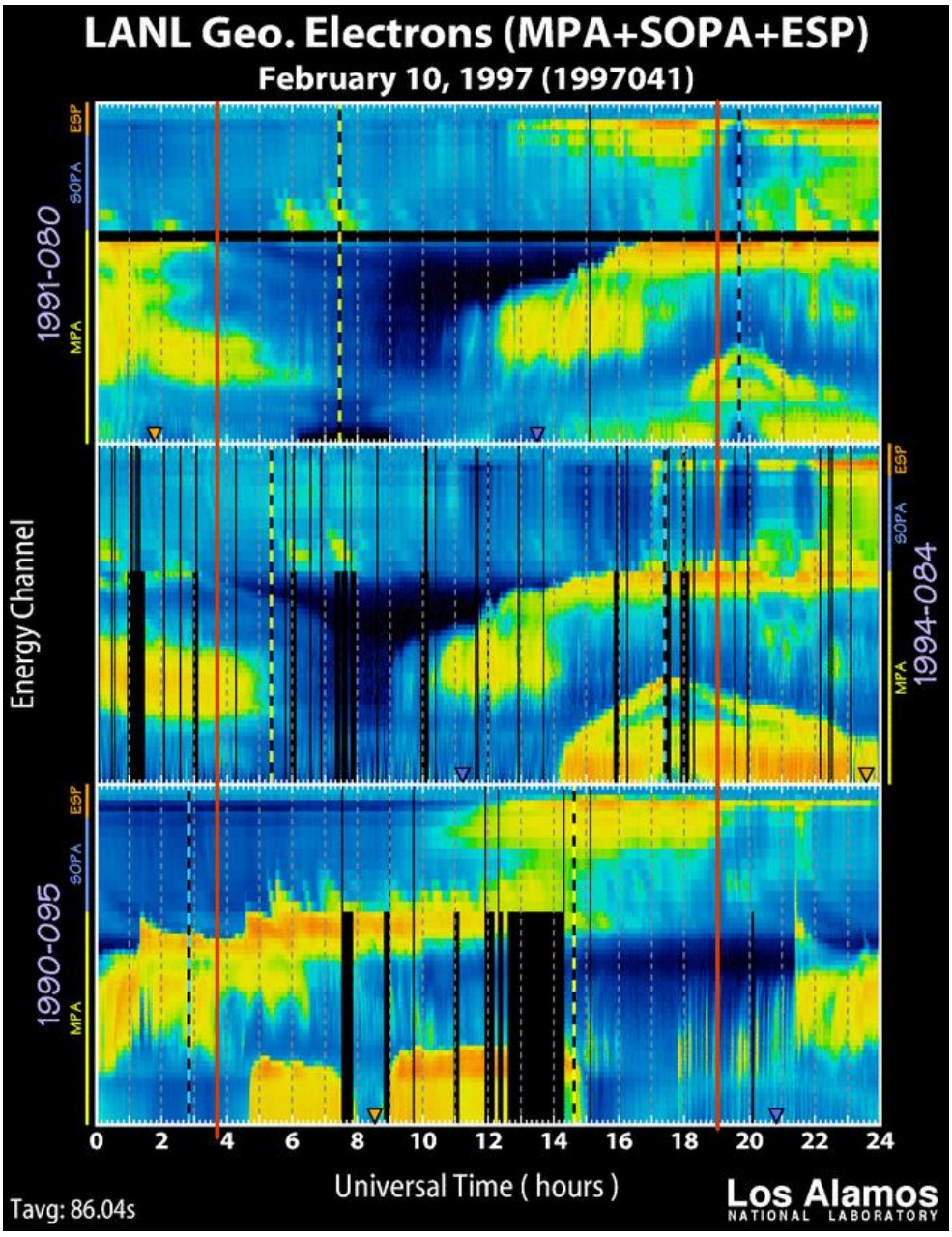

Figure 5.3a LANL Electron Spectrogram, February 10th, 1997, taken from [4]. The B_z negative portion of the magnetic cloud is marked between the red lines at 04:00 and 19:00 UT.

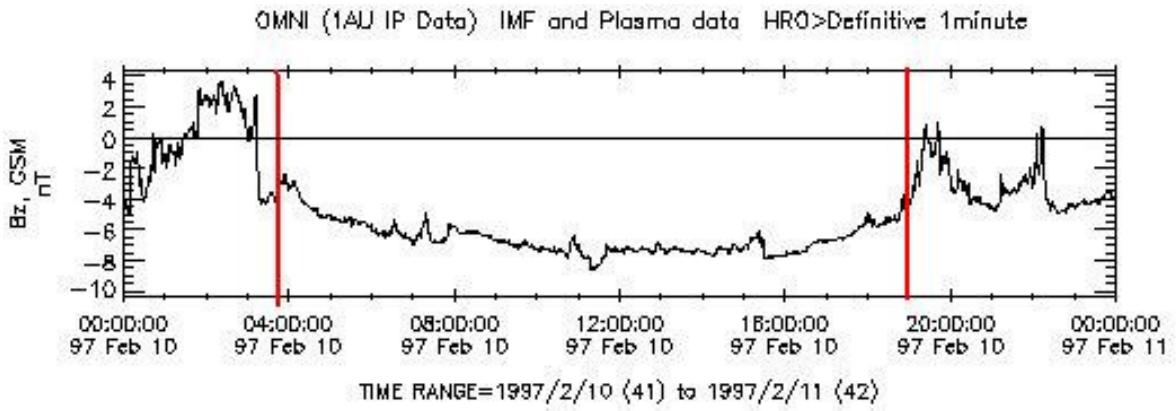

Figure 5.3b: Smooth negative B_z portion of the fast-CME magnetic cloud of February 10th, 1997; data from [King and Papitashvili, 2005]. The negative section is enclosed by the red lines.

Figure 5.3a shows LANL electron data from 10th February, 1997. In figure 5.3b it can be seen that the IMF B_z is negative, and relatively stable, from ~04:00 UT to ~ 19:00 UT. The magnitude of the negative excursion is, however, quite low, reaching a minimum of only -8nT. In the spectrogram, a clear injection is observed by 1990-095 at 05:27 UT, which at the Universal Time was located at ~02:45 MLT. This injection is also observed as a dispersed signature by 1991-080 and 1994-084. Tsurutani reported no substorm expansion phases during this time period, and so this injection must have been caused by a pseudobreakup, which will be discussed in section 5.2.2 of this chapter.

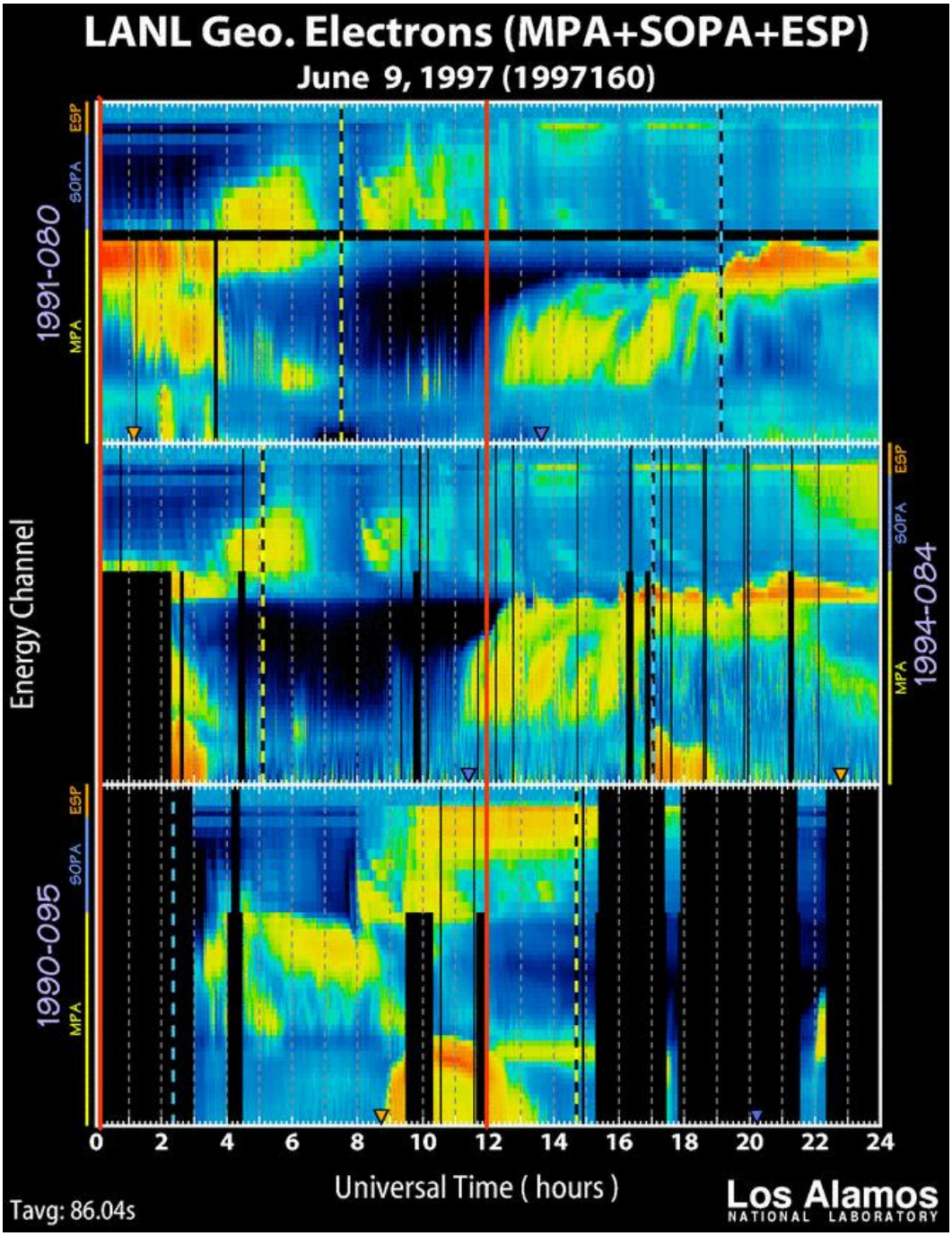

Figure 5.4a LANL Electron Spectrogram, June 9th, 1997, taken from [4]. The B_z negative portion of the magnetic cloud is marked between the red lines at 00:00 and 12:00 UT.

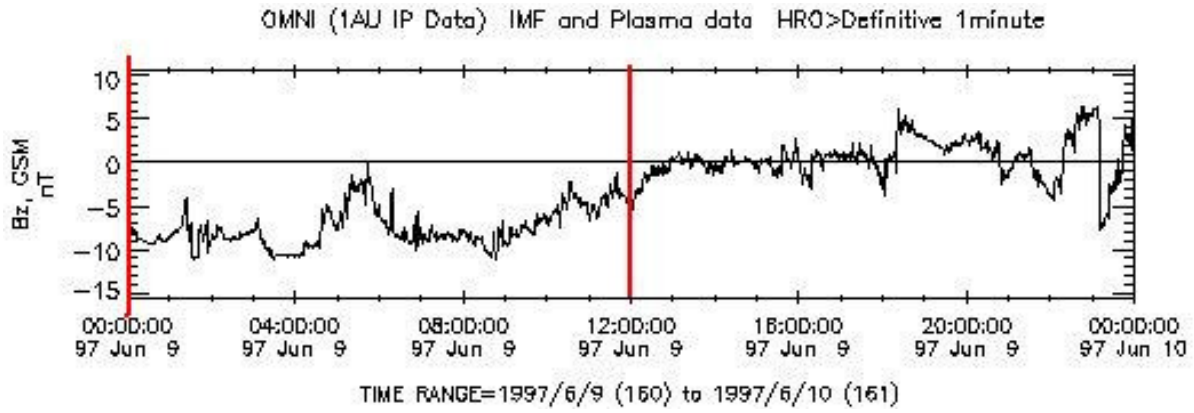

Figure 5.4b: Smooth negative B_z portion of the fast-CME magnetic cloud of June 9th, 1997; data from [King and Papitashvili, 2005]. The negative section is enclosed by the red lines.

Figure 5.4a displays data from 9th June, 1997; the third occurrence of a geomagnetic storm which was not accompanied by substorm expansions. The negative B_z portion of the cloud is shown in figure 5.4b to occur during the first half of the day, from ~00:00 UT till 12:00 UT, though it is not a very smooth profile. Looking at the electron spectrogram for this period, a single, slightly dispersed injection signature is seen by 1990-095 at 07:56 UT. The satellite was located at 05:16 MLT; the slight dispersion in energy is likely due to its distance from midnight. The drifting population is then observed by 1991-080 (12:26 MLT) at 07:59 UT, and finally 1994-084 (14:47 MLT) at 08:04 UT.

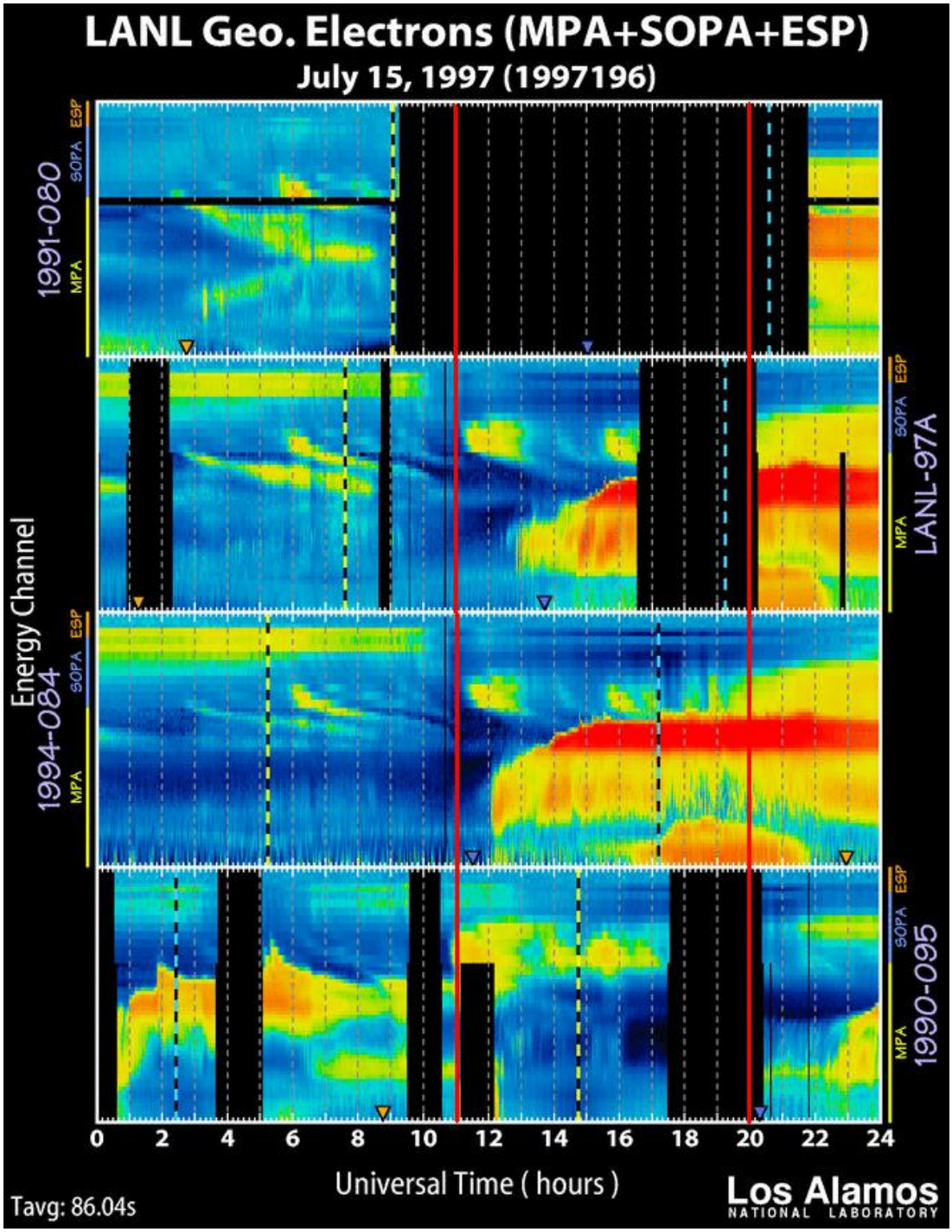

Figure 5.5a LANL Electron Spectrogram, July 15th, 1997, taken from [4]. The B_z negative portion of the magnetic cloud is marked between the red lines at 11:00 and 20:00 UT.

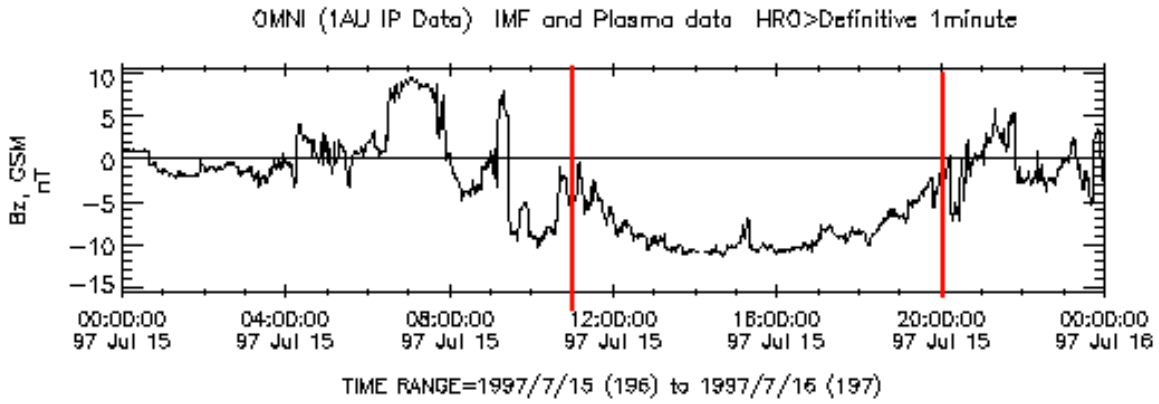

Figure 5.5b: Smooth negative B_z portion of the fast-CME magnetic cloud of July 15th, 1997; data from [King and Papitashvili, 2005]. The negative section is enclosed by the red lines.

In figure 5.5a, LANL data is shown for July 15th, 1997. The smooth, B_z-negative portion of the magnetic cloud exists between ~11:00 UT and 20:00 UT, shown in figure 5.5b. Two injections are observed to occur before the negative B_z interval begins. 1990-095 observes dispersionless signatures, and dispersed drift signatures are observed by 1991-080, LANL-97A and 1994-084. A blob in the electron spectrogram occurs immediately before the smooth negative period, being detected first by 1990-084 (located at ~08:00 MLT) at 10:50 UT. The initial blob does not clearly resemble an injection, but the subsequent drift echoes, as observed by LANL-97A (15:25 MLT) and 1994-084 (17:45 MLT), at 11:10 UT and 11:18 UT, respectively. This blob is most likely due to the spike that occurs immediately before the negative B_z section. Within the smooth, negative part of the cloud, a large enhancement of low energy electrons occurs. A single narrow injection signature is observed by 1994-084 at ~18:50 UT. No other satellites are able to observe this injection, as the region starts to fill with higher energy electrons. Again, there appears to be evidence of substorm activity in particle data for this storm.

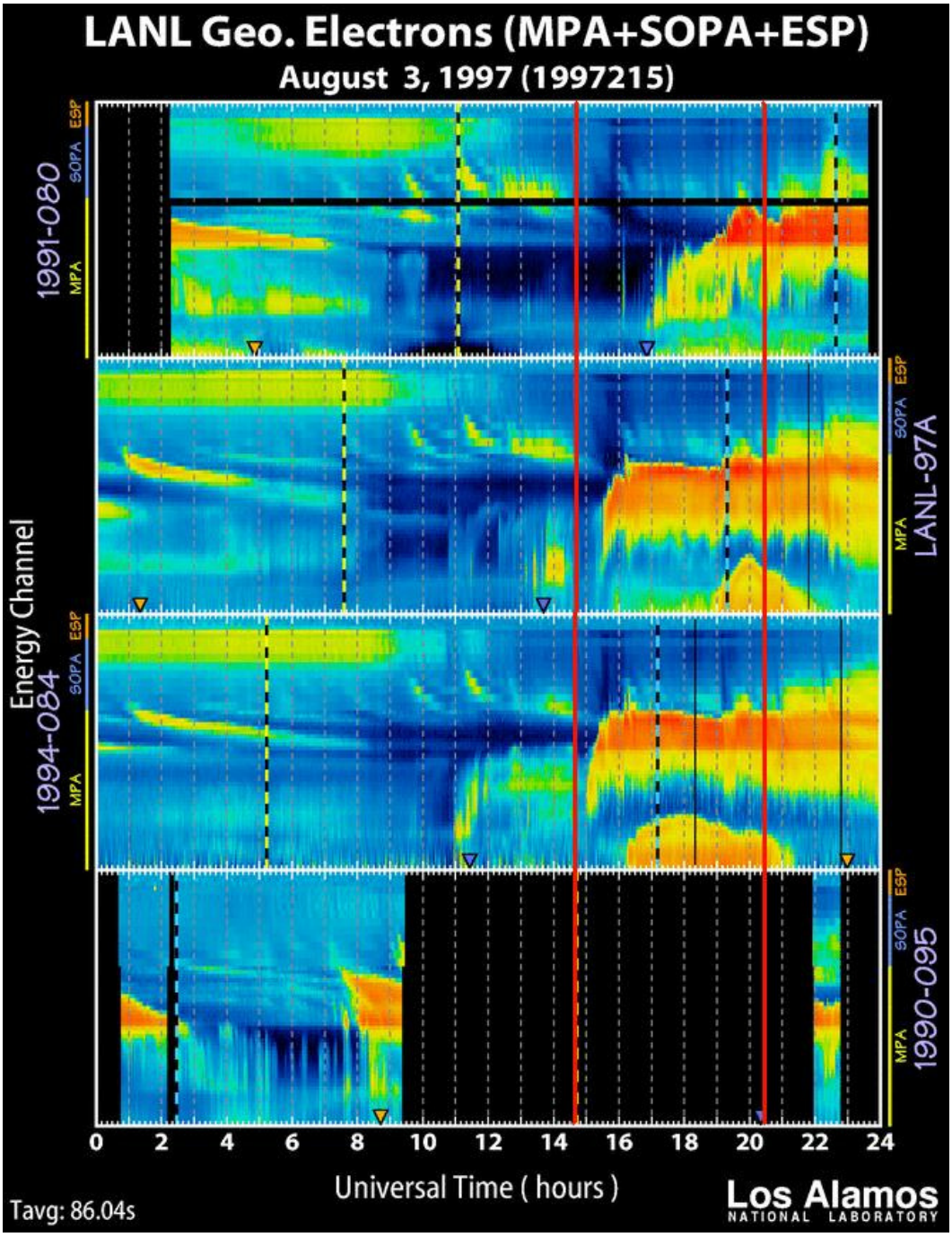

Figure 5.6a: LANL Electron Spectrogram, Aug 3rd, 1997, taken from [4]. The B_z negative portion of the magnetic cloud is marked between the red lines at 15:00 and 20:00 UT.

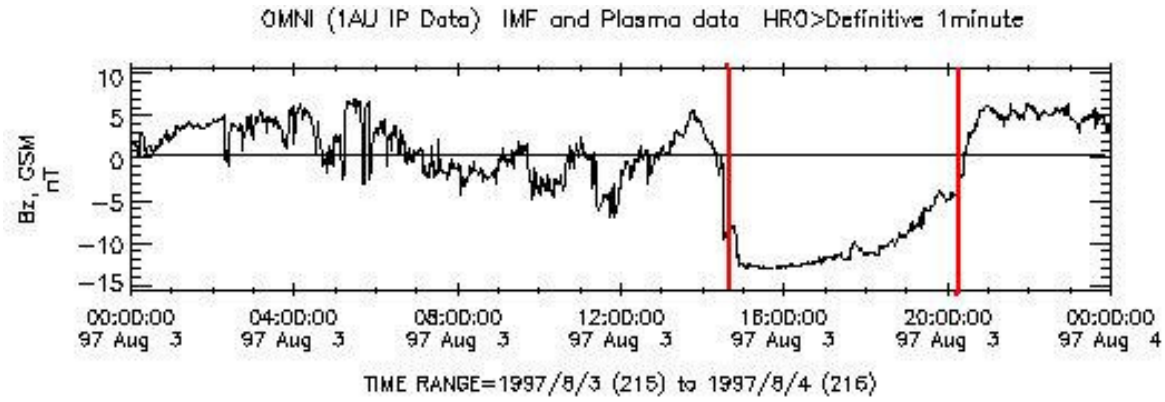

Figure 5.6b: Smooth negative B_z portion of the fast-CME magnetic cloud of August 3rd, 1997; data from [King and Papitashvili, 2005]. The negative section is enclosed by the red lines.

LANL data for the final storm that did not contain substorm expansions is shown in figure 5.6a, occurring on August 3rd, 1997. The negative-B_z portion of the cloud is shown in 5.6b, occurring between ~15:00 UT and 21:00 UT, and is remarkably smooth throughout. All satellites taking data during this period are far from midnight, and so injections would be expected to have dispersed somewhat before detection. Two separate dispersed populations are observed during the 6 hours prior to the negative section, along with another signature which may be a group of dispersed echoes. When the negative B_z portion reaches the Earth, the same low energy electron enhancement then appears to spread to higher energies. Throughout the negative-cloud period, the three satellites: 1994-084, LANL-97A and 1991-080 are located across midnight, and some small injections are seen within the large enhancement. The first is observed by LANL-97A at ~16:10 UT, and by 1994-084 at ~16:20 UT (satellites were located at ~20:40 MLT and ~23:00 MLT, respectively). This injection is small, but very clear. A final injection-like signature is clearly observed by all satellites at ~19:40UT, when they are located across midnight.

5.2.2 Pseudobreakups

Having located dispersionless injection signatures during intervals where no auroral expansions were observed, their cause must have been

pseudobreakup activity rather than substorms. Pseudobreakups contain many of the same features as substorms, such as enhanced AE, dispersionless injections and magnetotail dipolarisation, though not on such a large scale as substorms ([Kullen and Karlsson, 2004]). A good future study would investigate, in depth, the differences between substorm and pseudobreakup injections, involving comparisons of energy, composition and MLT-range.

The most notable difference between substorms and pseudobreakups is that pseudobreakups lack an auroral expansion phase, with enhancements in the brightness of the aurora seemingly unable to reach the threshold for onset. Pseudobreakups are often observed to occur as a precursor to substorms, within their growth phase ([Koskinen et al, 1993]), but have also been observed during substorm recovery, SMC events and quiet time ([Aikio et al., 1999]). One present explanation for this phenomenon is that pseudobreakups are small, localised substorms, in which the energy threshold for larger-scale substorm occurrence is not met. Recent work by [Kullen and Karlsson, 2004] came to this conclusion.

In a paper by [Arballo et al., 1998], pseudobreakups were confirmed to have occurred on 10th January, 1997; the first occurrence noted by Tsurutani et al. of a geomagnetic storm with no substorms. This means that any injections observed were associated with the pseudobreakups, and though the energy threshold was not met, small substorms were occurring. It is likely that this applies to injections within the other substormless-storm periods.

5.3 The Energies of Injected Electrons

If a pseudobreakup is a substorm in which the threshold for large-scale reconnection is not met, there may be a difference between the two in terms of the energy of the injected particles. Each pixel on a LANL spectrogram relates to a specific energy range, and so the maximum energy of an injection can easily be found. The expectation is that substorm-related injections will have a higher energy than pseudobreakup-related injections, due to the greater energy involved in the mass-restructuring of the tail.

5.3.1 Injections during Substormless Storms

Date (1997)	Time (UT)	Range (low) (keV)	Range (high) (keV)	Mean range (keV)
10th January'	4:32	315	500	407.5
10th January	14:00	750	1100	925
10th February'	1:18	50	75	62.5
10th February	5:27	75	105	90
10th February	6:58	225	315	270
10th February*	21:25	225	315	270
9th June	8:00	315	500	407.5
9th June*	16:00	50	75	62.5
9th June*	20:22	50	75	62.5
15th July'	1:49	50	75	62.5
15th July'	5:16	150	225	187.5
15th July	18:45	225	315	270
3rd August'	7:06	105	150	127.5
3rd August	16:08	225	315	270
3rd August	19:35	105	150	127.5
3rd August	20:54	105	150	127.5
3rd August*	22:12	750	1100	925

Table 5.1: Injections during substormless storms, showing the date, time (UT) and the highest energy range of the injected electrons, alongside the mean of that range.
‘ before negative B_z interval
** after negative B_z interval*

Table 5.1 shows injections that occurred during the storm periods of 1997 which contained no substorm expansions, along with the approximate range of the highest energies reached. The mean value of the range is also given. As this is simply the average of the two defined energies in each range, the modal value across all these pseudobreakup-related injections will tell us something about the average pseudobreakup injection energy. For these substormless storms, this appears to be both 270keV and 62.5keV. The former is near the expected energy for substorm injections; the latter is very low. All of these maxima were in the SOPA range. Injections marked as before or after the negative B_z event may have been due to substorms, as their occurrence would not have been included in Tsurutani’s study. They have been included in this work in case substorms occurred immediately before or after the negative B_z period. The average value of the mean energies for pseudobreakup injections that occurred during the B_z-negative events is 206.6 keV.

5.3.2 Injections during Storms with Substorms

Date (1997)	Time (UT)	Range (low) (keV)	Range (high) (keV)	Mean of range (keV)
21st April	12:47	500	750	625
22nd Apil	2:44	105	150	127.5
22nd Apil*	18:35	105	150	127.5
23rd April*	0:15	<50	<50	n/a
23rd April*	0:41	<50	<50	<50
23rd April*	1:31	<50	<50	<50
23rd April*	18:48	500	750	625
23rd April*	23:36	225	315	270
15th May	7:22	315	500	407.5
16th May*	4:08	75	105	90
16th May*	14:58	105	150	127.5
1st October-DE	11:40	500	750	625
1st October'	16:08	315	500	407.5
1st October'	17:14	315	500	407.5
2nd October'	2:08	<50	<50	<50
10th October'	0:20	150	225	187.5
10th October'	16:40	<50	<50	<50
10th October	22:07	315	500	407.5
11th October	4:45	315	500	407.5
11th October	8:04	105	150	127.5

Table 5.2: Injections during storms which contained substorm expansions, showing the date, time (UT) and the highest energy range of the injected electrons, alongside the mean of that range.
‘ before negative B_z interval
** after negative B_z interval*
DE = Drift echo

Table 5.2 shows the maximum energy range for injections which occurred during the storms in which at least one substorm did occur. The energy of electrons detected by the MPA device were very low, and have been labelled as <50. The event on 1st October is labelled as DE, due to the fact that a clear drift echo was observed when no operational satellite was near midnight to see the injection. It is worth noting that, during these events, low energy pseudobreakup injections may also occur. For each event, the presence of at least one higher energy substorm injection is expected within the duration of the cloud.

Date (1997)	Time (UT)	Range (low) (keV)	Range (high) (keV)	Mean of range (keV)
10th January	14:00	75	105	90
10th February	5:27	75	105	90
10th February	6:58	225	315	270
9th June	8:00	315	500	407.5
15th July	18:45	225	315	270
3rd August	16:08	225	315	270
3rd August	19:35	105	150	127.5
				average 217.9

Table 5.3a: The energies of injections in substormless storms that occurred within the negative B_z duration. The average mean of maximum energy range is shown to be 217.9 keV.

Date (1997)	Time (UT)	Range (low) (keV)	Range (high) (keV)	Mean of range (keV)
21st April	12:47	500	750	625
22nd April	2:44	105	150	127.5
15th May	7:22	315	500	407.5
1st October - DE	11:40	500	750	625
10th October	22:07	315	500	407.5
11th October	4:45	315	500	407.5
11th October	8:04	105	150	127.5
				average 389.6

Table 5.3b: The energies of injections in storms which contained substorm expansions that occurred within the negative B_z duration. The average mean of maximum energy range is shown to be 389.6 keV.
DE = Drift echo

Table 5.3a and 5.3b contain the dates, times and energies of injections which occurred during the IMF B_z-negative period of the storms which did not, and did, contain substorm expansions respectively. Since no substorm expansions were observed during the events of 5.3a, all injections observed must have been due to pseudobreakups. In 5.3b, at least one injection per event must have been due to a substorm. The events in the latter table do generally occur at higher energies than those of the former, the average being 389.6keV. Each magnetic cloud also led to an injection of > 407.5keV, while those for the known pseudobreakups were generally of a lower energy, the average being 217.9 keV.

5.3.3 Solar Wind Correlation with Injections

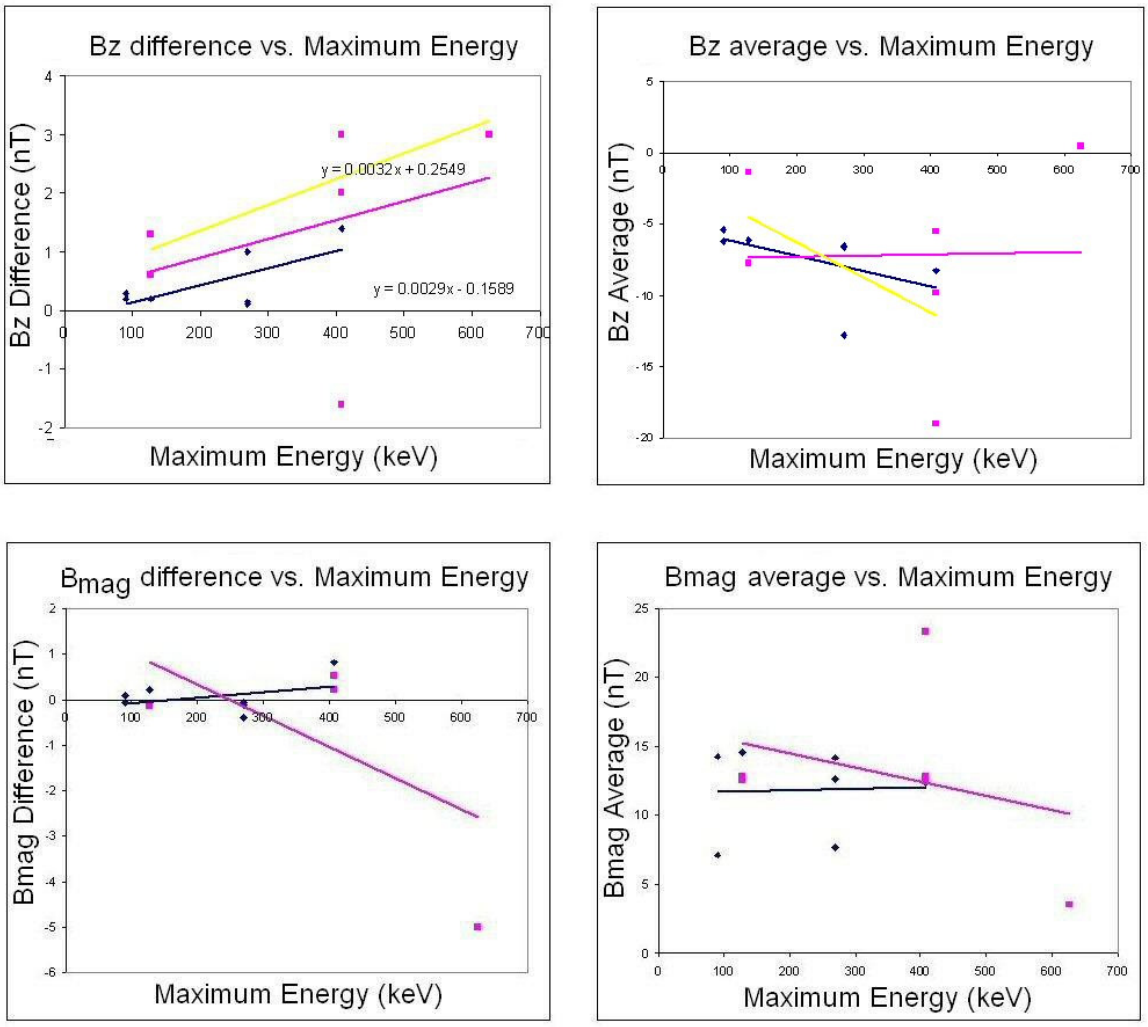

Figure 5.7a: Visual analysis of solar wind parameters during the 20 minutes preceding the injection, showing maximum spike magnitude (left) and overall average (right). Injections from substorms are shown in pink; injections from pseudobreakups are shown in blue. Parameters shown are B_z and B magnitude. The yellow line on the B_z difference and pressure graphs (top) show the data for substorm injections (pink points), discounting the single anomalous point in each. This point was not from the same injection for both graphs.

The high energy injections from Table 5.3b were coupled with auroral expansions, while the lower energy injections from table 5.3a were not. Solar wind conditions will now be compared for all events. The solar wind data were provided by OMNI ([King and Papitashvili, 2005]), which contains a combination

of Wind and IMP 8 data, shifted in time to align with the nose of the bow shock. Due to this, only a few minutes of time will have to be considered between a solar wind event and its effect upon the magnetosphere, though some time must be allowed for full convection to the nightside reconnection region.

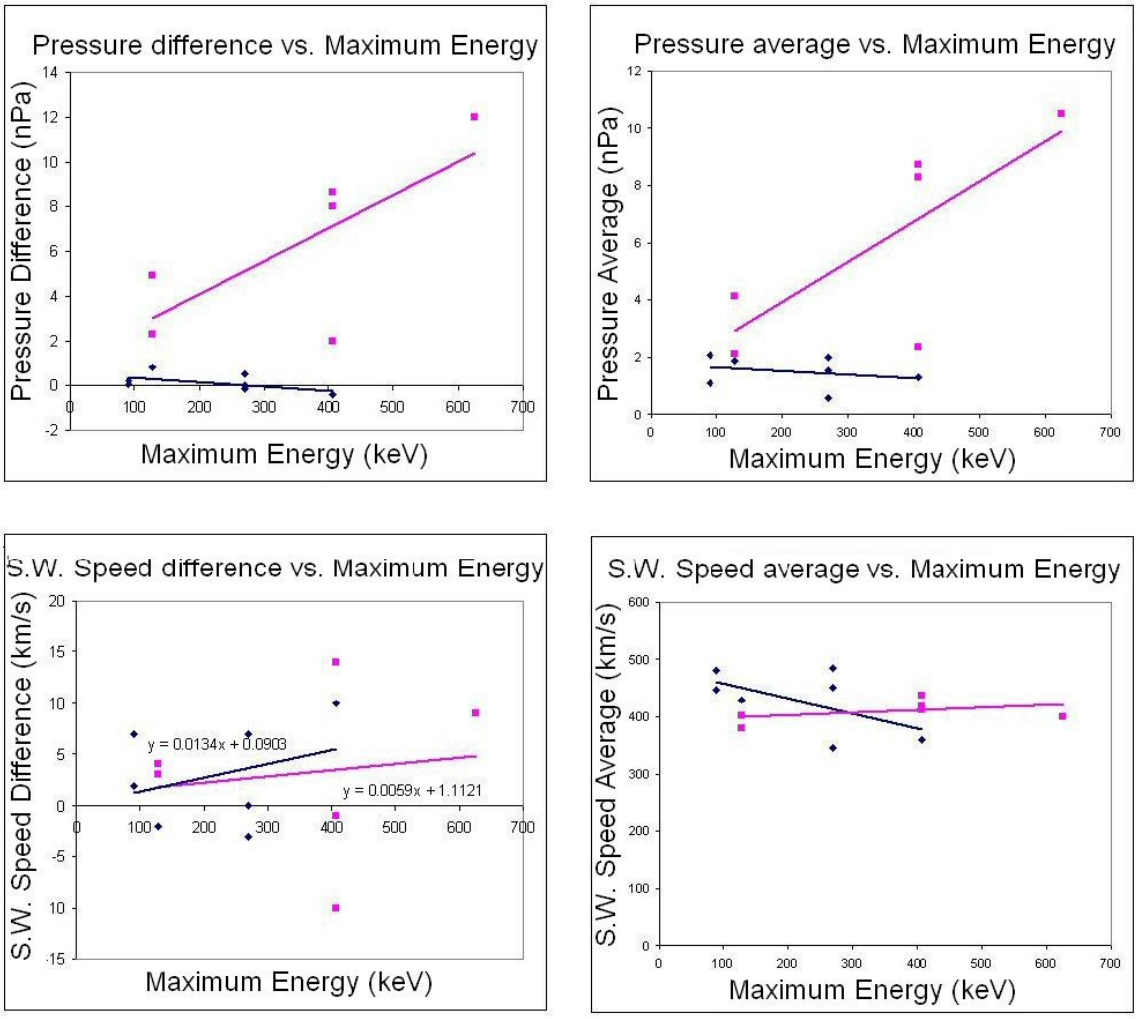

Figure 5.7b: Visual analysis of solar wind parameters during the 20 minutes preceding the injection, showing maximum spike magnitude (left) and overall average (right). Injections from substorms are shown in pink; injections from pseudobreakups are shown in blue. Parameters shown are flow pressure and solar wind speed. Pressure shows a striking correlation for pseudobreakups and substorms, with substorms occurring for high pressure jumps and average pressures.

For each injection, the solar wind conditions were investigated for regular patterns during the twenty minutes before occurrence. Parameters under investigation were B magnitude, B_z component of the IMF, solar wind flow speed and solar wind flow pressure.

Figure 5.7a and 5.7b show the results of the analysis of the solar wind during the twenty minutes before injection occurrence, this being done by manual visual analysis. The pink lines show the linear average for injections which occurred during storms which contained substorm expansions; the blue lines contain data for those that did not. In both figures, the left-hand plots show the difference between the maximum and minimum, and the right-hand plots show the average of these data. The deviation of many points on these plots from the linear average is striking, but some correlations are observed nonetheless.

In 5.7b the pressure graphs (top) suggest that increases in pressure lead to the occurrence of substorms, with higher average pressures or greater (positive) pressure differences leading to higher energy injections (pink line). The data for pseudobreakups, however, appears in both cases to produce a fairly flat average, suggesting that pseudobreakups of all energies require no pressure pulse to occur.

There is also a notable difference between substorms and pseudobreakups in IMF B_z difference, shown in 5.7a, with substorms occurring generally due to higher B_z jumps. The energy dependence on these B_z spikes is, however, very similar for both substorms and pseudobreakups, as the gradient showing the injection energy-dependence is very similar for both (~0.003). A single occurrence of a substorm injection showed no B_z spike prior to injection, and in fact showed a small B_z drop (1.6nT, October 10th, 22:07 UT). The yellow line on the graph shows the linear regression of the data with the anomalous point removed, and follows the pattern of the remaining points closely. The occurrence of a substorm during this period, however, implicates B_z jumps as a requirement for substorms. Regardless, there is evidence that the energy of both substorm and pseudobreakup injections is a function of the magnitude of positive B_z jumps.

At first, the plot showing average B_z prior to injections seems to show very little correlation for substorms, suggesting that the magnitude of the negativity of B_z is unimportant. However, there is again a point that may be considered anomalous, being the only one with a positive average. This was the event on 21st April 1997, where the high energy of the substorm may be accounted for by the large B_z spike into positive values. The yellow linear-fit discounts this point, and a clear negative correlation is observed, as it is for pseudobreakups. It seems likely then that a greater negativity of IMF B_z leads to higher energies of both substorms and pseudobreakups, though this fact alone does not separate them, as highly-negative B_z appears to be a precursor to both events.

5.3.4 Maximum Gradient of the Solar Wind Pressure and B_z for the events of 1997

The above method for the determination of jumps and averages was highly susceptible to human error. A more accurate method for determination of the importance of sudden jumps in solar wind pressure and B_z to substorm occurrence would involve the use of the running gradient, which could easily be split into spikes and dips. In this study, the maximum positive gradient within the period starting twenty minutes prior to injection, and ending five minutes after, will be plotted against the maximum energy of the injection, for both substorms and pseudobreakups.

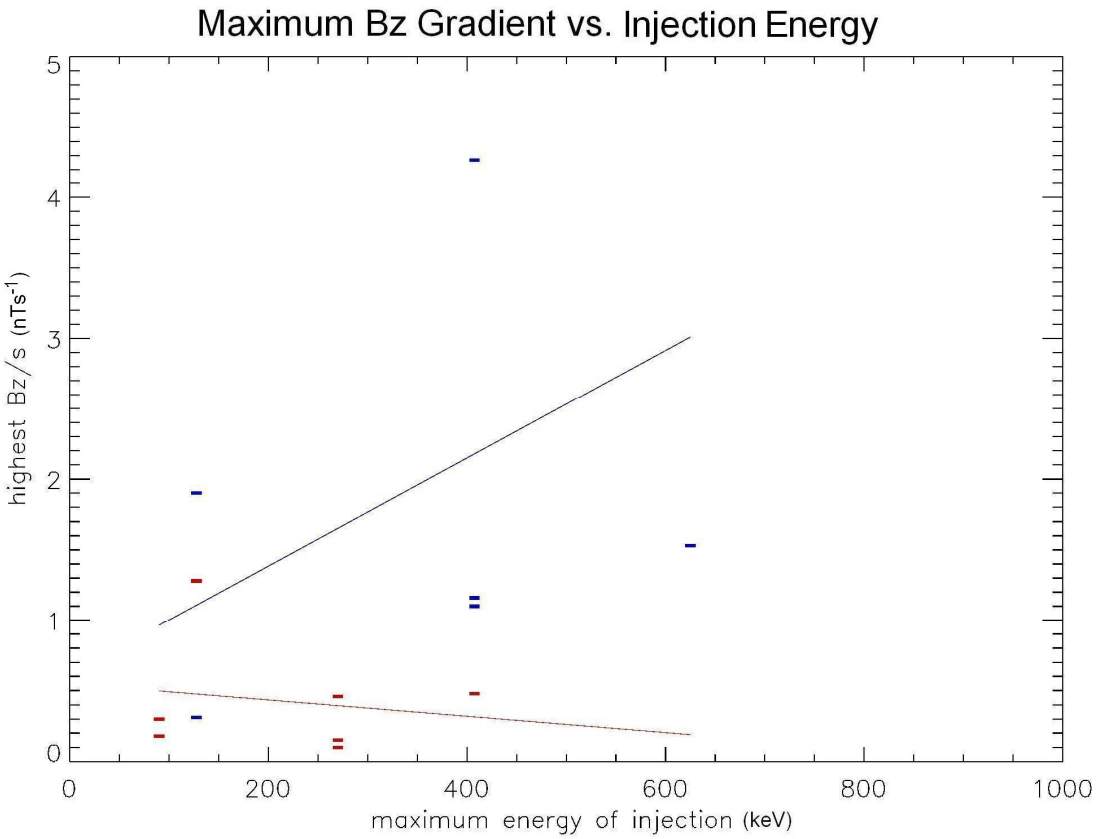

Figure 5.8: The maximum gradient of B_z spike in the 20 minutes preceding the injection against maximum energy reached by the injection. Events containing substorm expansions are blue; events containing no expansion are red. The graph gives evidence that larger B_z spikes lead to substorms. The pearson coefficient of 0.39 for substorms and -0.17 for pseudobreakups give evidence against linear correlation between these parameters.

Figure 5.8 shows the maximum positive gradient of B_z, for the same temporal range as the above study, against maximum energy of the injection. For substorms, it shows a similar correlation to the earlier by-eye plots, with injection energies increasing with the gradient of B_z spikes. Pseudobreakup injection energy, however, does not appear to correlate positively with B_z gradient. It is apparent in this graph that larger spikes in B_z lead to substorms, while lesser spikes result in pseudobreakups. While these patterns are clear, there is too little data with too large a spread to deduce much from the linear-fits themselves. This is especially true for the substorm injections.

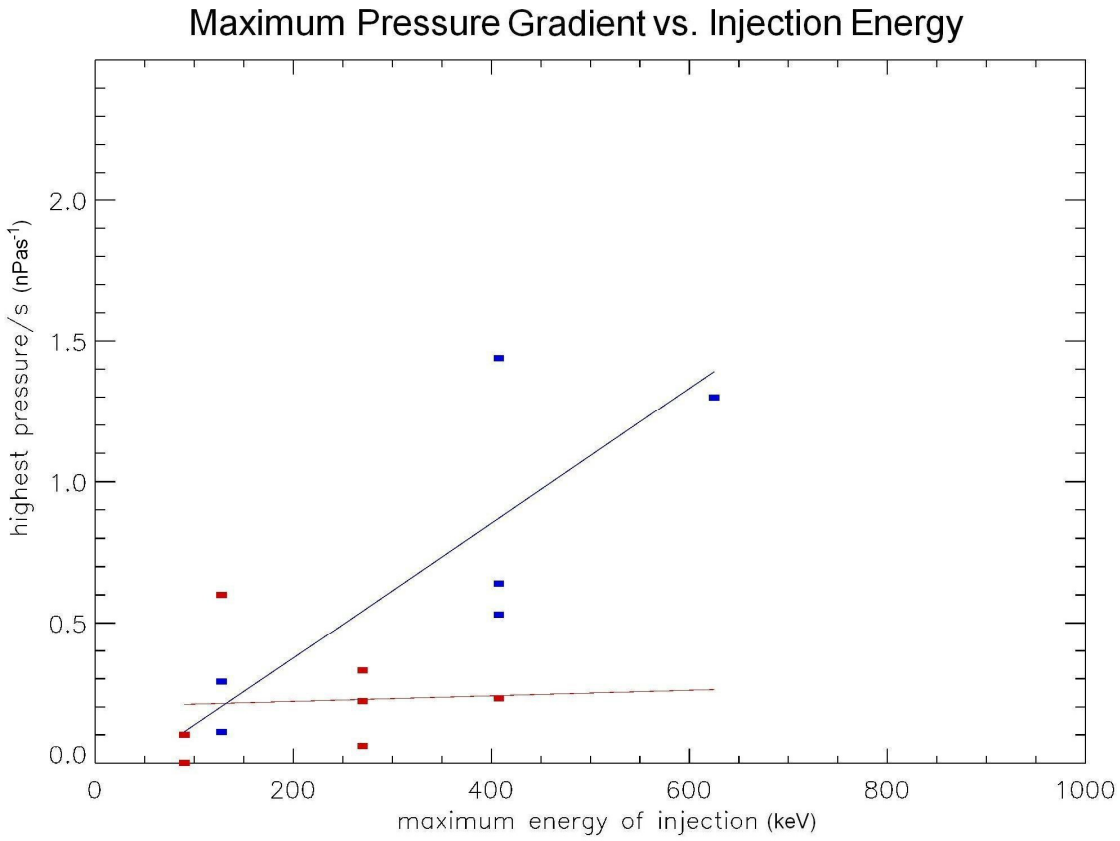

Figure 5.9: The maximum gradient of Ram pressure spike in the 20 minutes preceding the injection against maximum energy reached by the injection. Events containing substorm expansions are blue; events containing no expansion are red. The graph gives evidence that larger Ram Pressure spikes lead to substorms. The pearson coefficient for substorms is 0.72, showing some evidence of a linear correlation. For pseudobreakups, the pearson coefficient is only 0.06.

Figure 5.9 is the same style of plot as 5.8, with the y-axis showing maximum pressure gradient rather than B_z. The same pattern as in the earlier plot is observed, and points appear not to deviate greatly from the linear-fits; the pearson coefficient of 0.72 indicating reasonable linear correlation for substorm injections. As with the earlier plot, spikes in pressure seem to lead to higher energy substorm injections, with pseudobreakup injection energy not appearing to change with pressure. A more accurate representation of the relationship between pseudobreakup injection energy and pressure spike-gradient requires a larger statistical study. Such a study is attempted later in this chapter. The

magnitude of the IMF and solar wind velocity were also investigated in terms of substorm occurrence, but no evidence was found to suggest that it plays any role.

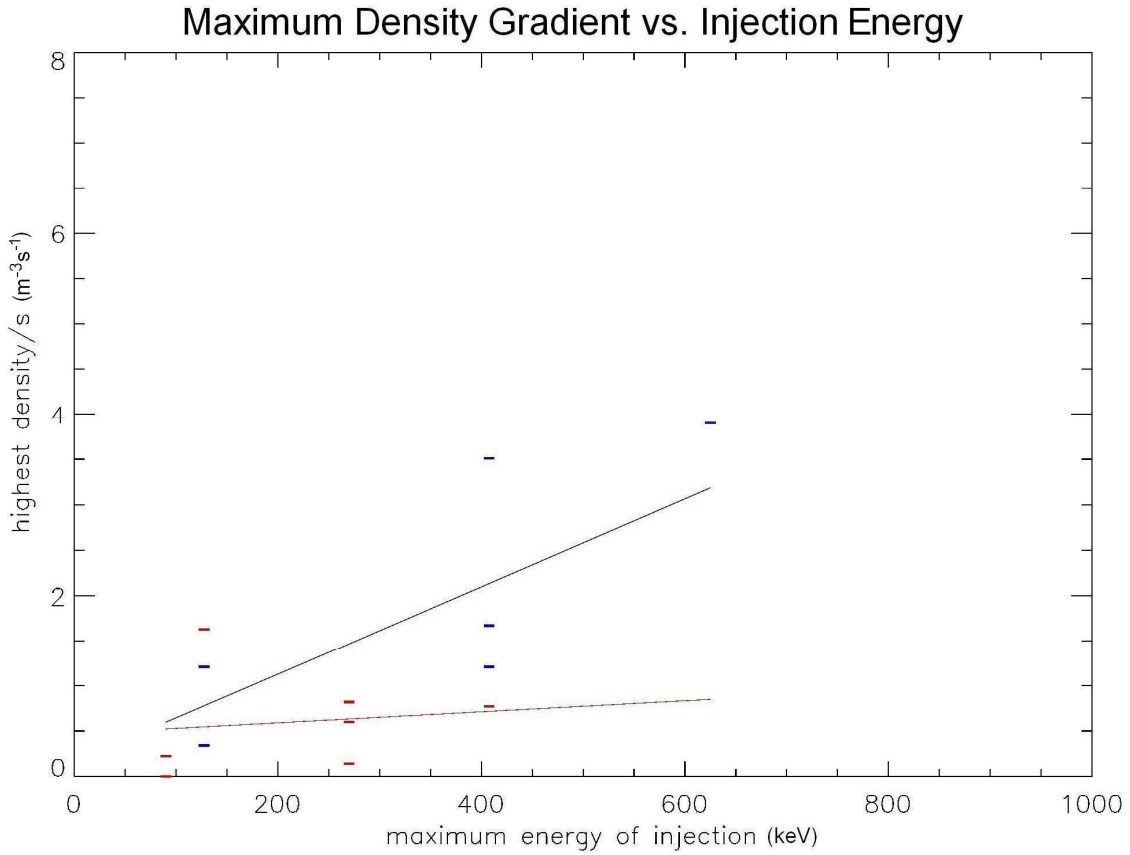

Figure 5.10: The maximum gradient of solar wind density spike in the 20 minutes preceding the injection against maximum energy reached by the injection. Events containing substorm expansions are blue; events containing no expansion are red. The graph gives evidence that larger density spikes lead to substorms. The pearson coefficient for substorms is 0.63, so a reasonable linear correlation may exist. Pseudobreakups have an pearson coefficient of 0.13. Density is related to pressure by ρv^2.

Figure 5.10 shows the relationship between injection energy and maximum density gradient for substorms and pseudobreakups. Figure 5.9 showed that a pressure spike may be responsible for substorm occurrence. Flow pressure is

related to density by the relationship $P = \rho v^2$, and as can be observed in figure 5.10, this correlation is more likely due to a period of increased density. This may be explainable using the solar wind pressure catastrophe model for substorm occurrence (e.g. [Erickson and Wolf, 1980]), as a sudden increase in the density may trigger a substorm after it has undergone nightside reconnection and convected back towards the Earth. This would also explain the apparent necessity for a lag of up to 20 minutes after the density enhancement has reached the bow shock, as time will be required for transport to the pressure-catastrophe region.

5.4 Pseudobreakup or Substorm Occurrence: A Brief Summary

Five of eleven magnetic cloud induced storms during 1997 were identified by Tsurutani et al. to contain no substorm expansion phases in the aurora. It has been shown in this study that LANL data contain evidence of numerous particle injections during all of these storms. In the cases where expansion phases were not observed, these injections are attributed to pseudobreakup activity. It has been shown that the injections during the non-substorm periods were generally of a lower energy than those that occurred during the periods with expansions. The average of the maximum energy range for each injection was then analysed in relation to the solar wind during the twenty-minute period prior to injection. It was found that the energy of substorm injections increases with the magnitude of a positive B_z spike prior to injection, and also greater magnitudes of B_z-negativity. It was also shown that substorms may require a spike in the solar wind flow pressure, or density, to occur; the magnitude of the spike showing positive correlation with the energy of the resulting injection. Pseudobreakups, however, appear to occur when the difference in pressure is very tiny, or zero. Using this evidence it is suggested that substorms occur when a B_z spike is coupled with a pressure (or density) spike, while pseudobreakups result from B_z spikes alone.

5.5: Storms With No Substorms: 2000 - 2003

The result of the 1997 study is interesting, as it suggests that the threshold for substorm occurrence may be related to the solar wind density/pressure. This would be supported strongly if the same effect were observed using a larger set of injections. If substorm versus pseudobreakup occurrence does depend upon small enhancements in the solar wind pressure, the effect should not have a dependence on the stage of the solar cycle, save that a greater number of substorms than pseudobreakups should occur during solar maximum. For this reason, it is expected that a period across solar maximum would be ideal for this study, with the years 2000 – 2003 being selected.

During this period, the IMAGE satellite observed the Earth from orbit, taking data such as UV and Electron flux. Auroral expansions can be seen in this data, and hence it will be used to determine whether injections occurred due to substorm or pseudobreakup activity.

5.5.1: Geomagnetic Storms during the Period

All occurrences of storms which contain a period of steadily negative IMF B_z will be considered in this study. The smooth negative profile of B_z is still required in order that any results can be compared to the 1997 study.

Table 5.4 shows details of solar wind parameters for all storms during the period. The data are once again taken from the OMNI dataset, which was discussed earlier in this chapter. Out of 111 storms during the period, 39 were found to contain long-duration, smoothly negative B_z structures.

Year	Month	Day	~Duration of negative B_z (h)	~Start, negative B_z (UT)	~End, negative B_z (UT)	Minimum B_z (nT)
2000	1	22	9	1800	300	-17
2000	2	5	3	1700	2000	-14
2000	2	12	3	800	1100	-21
2000	3	1	12	400	400	-6
2000	3	30	23	100	0	-7
2000	4	6	23	200	100	-30
2000	4	15	9	1800	300	-11
2000	4	24	4	1000	1400	-13
2000	6	26	11	1300	0	-7
2000	7	15	5	2000	100	-60
2000	8	10	21	2100	1800	-13
2000	9	12	9	900	1800	
2000	9	17	3	1900	2200	
2000	10	4	20	400	0	-14
2000	10	13	21	2100	1800	-10
2000	10	28	25	2200	2300	-18
2000	11	6	22	1400	1200	-15
2000	11	20	9	600	1500	-7
2001	1	24	12	900	2100	-7
2001	2	13	12	1800	600	-10
2001	3	4	12	1500	300	-13
2001	3	19	31	1500	2200	-20
2001	3	31	6	1500	2100	-40
2001	4	22	17	500	0	-14
2001	5	28	12	900	2100	-10
2001	7	8	8	1900	300	-8
2001	8	17	3	1700	2000	-24
2001	9	23	3	1700	2000	-12
2001	10	21	10	900	1900	-13
2001	10	28	10	200	1200	-19
2002	2	1	6	300	900	-14
2002	2	28	9	1800	300	-15
2002	3	23	16	1700	900	-11
2002	4	17	24	0	0	-11
2002	8	20	24	1600	1600	-9
2002	9	3	3	200	500	-20
2002	10	1	10	700	1700	-23
2003	2	1	24(with separation)	2000	2000	-11
2003	4	20	2	2300	100	-7
2003	4	29	6	1200	1800	-10
2003	6	15	15	900	0	-10
2003	8	17	21	300	0	-17
2003	11	20	13	1200	100	-50

Table 5.4: Storms containing periods of steadily negative B_z from 200 –2003. Shown is date, duration of negative B_z, start and end times and minimum B_z.

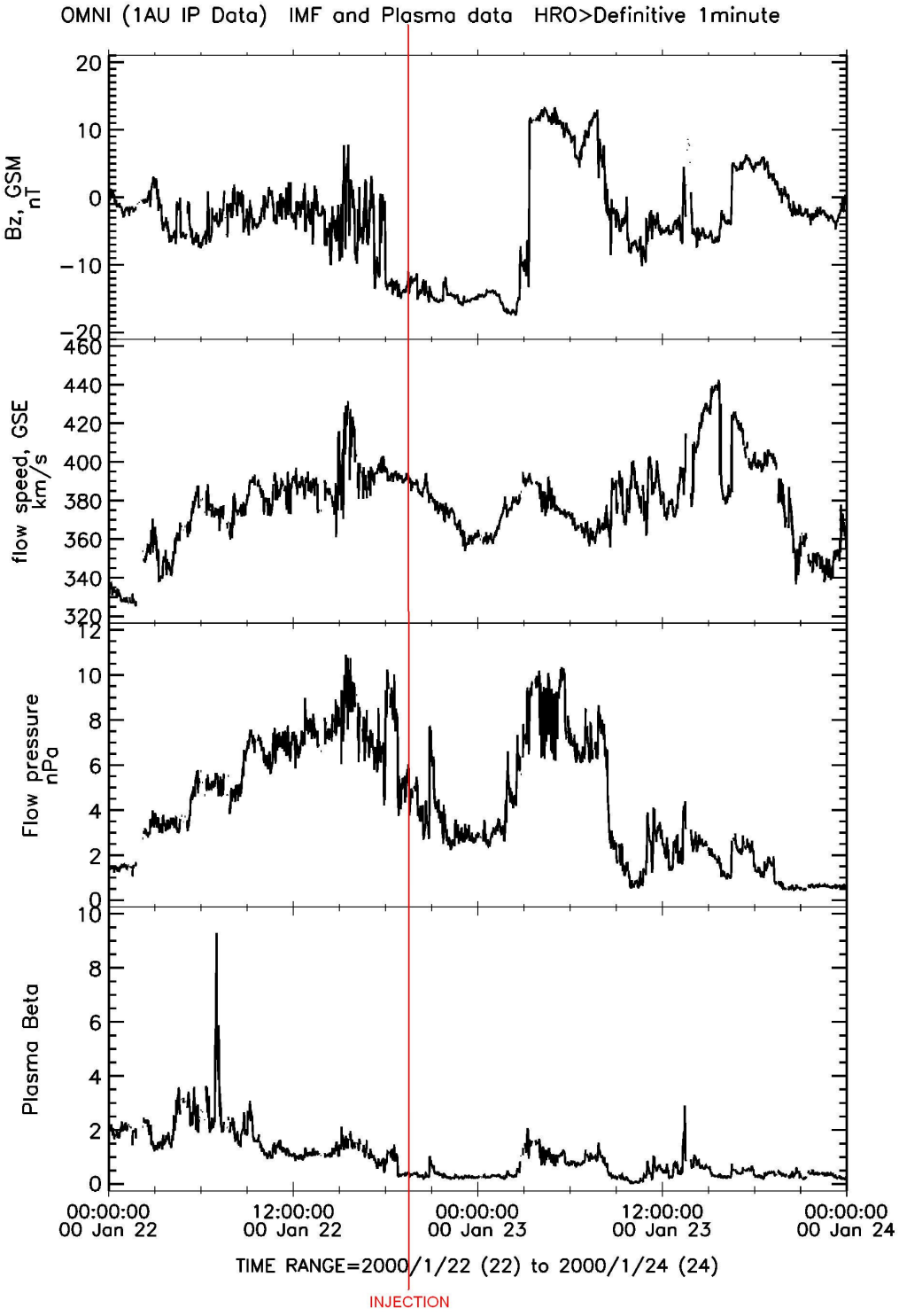

Figure 5.11: Solar Wind data from January 22nd to 23rd, 2000, with injection time marked. Parameters shown (from top) are B_z, flow speed, flow pressure and plasma beta. This injection correlated with a substorm expansion phase. OMNI data is from [King and Papitashvili, 2005].

Figure 5.11 shows an example of a smooth, negative B_z event, between ~18:00 UT on January 22nd to ~03:00 UT on January 23rd. An injection was observed to occur at ~19:40, which correlated with a substorm expansion phase (discussed later).

5.5.2: Electron Injections during the Storms of 2000 – 2003

Once again, LANL electron spectrograms appear to be the best option for the study of substorm or pseudobreakup occurrence. Details of all injections that occurred during the storms of the years 2000 – 2003 which contained negative B_z events are given in appendix C. Many of the injections occurred outside the duration of the bubble, and these will be discounted from the analysis. The maximum energy of each injection was again found, as this parameter is expected to be useful in determining whether the injection occurred due to a substorm or pseudobreakup. The UT assigned to each injection has been carefully approximated using the LANL summary-plot database, but due to this an error in the timing of ±3 minutes is incurred, due to the time-resolution of LANL plots on the site ([4]).

Coupled with the extra human error involved with this, and also the error involved regarding the MLT of the satellite relative to the location of injection occurrence (across 00:00 MLT), it will have to be accepted that the substorm/pseudobreakup which caused the injection could have occurred a number of minutes before the injection was detected.

To counter this, only the injections which were detected as dispersionless signatures when the satellite was near midnight will be considered. Even so, a period of 20 minutes before the injection to five minutes after will be considered in the analysis of solar wind parameters (a large amount of time beforehand to give a few minutes for transport and convection within the magnetosphere).

Figure 5.12 shows the LANL electron data for during the negative B_z event shown in figure 5.11. The clearly marked injection occurs at 19:40 UT, observed by 1994-084, and is subsequently observed as a drift signature by 1991-080.

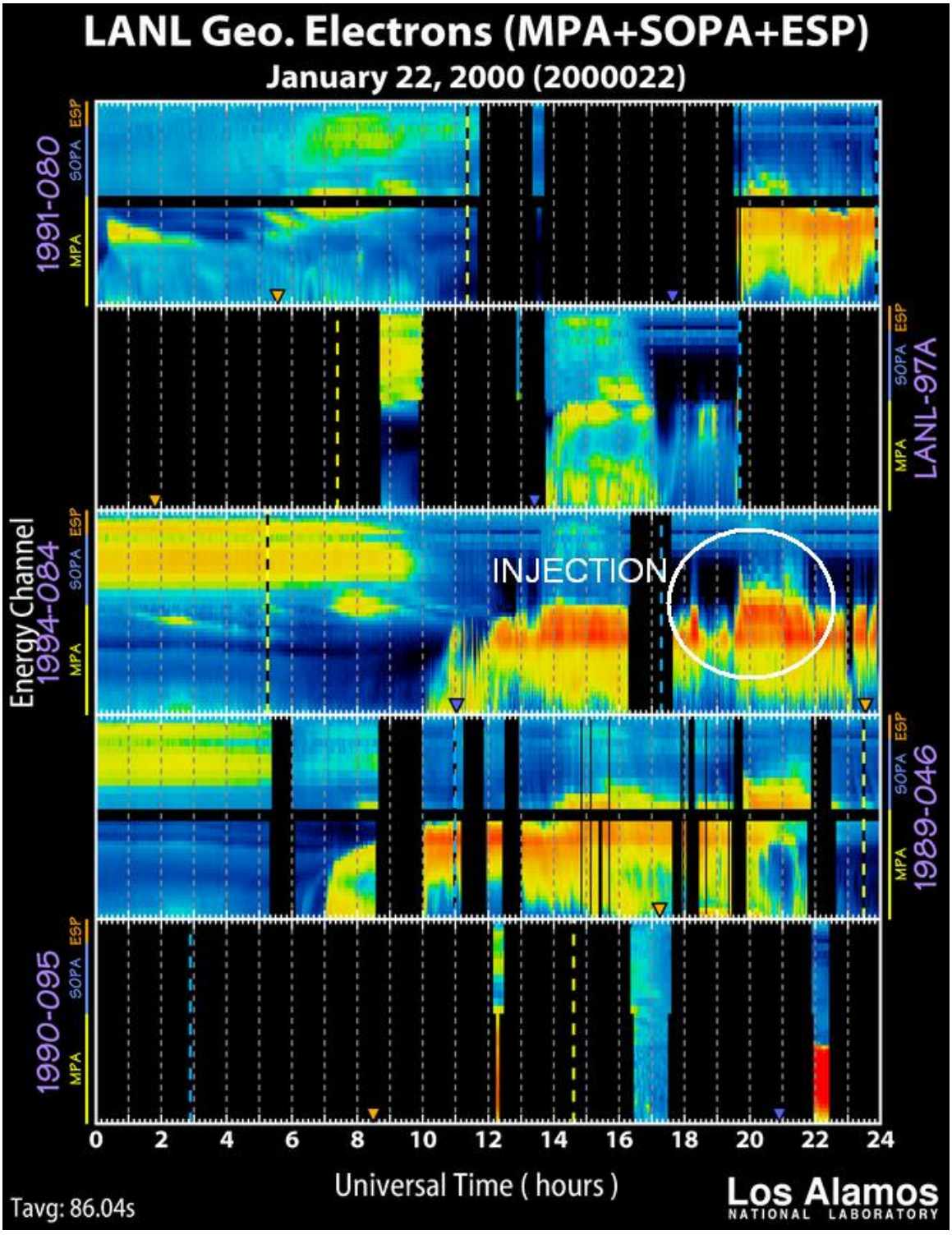

Figure 5.12: LANL electron spectrogram, January 22nd, 2000, taken from [4]. The marked injection was first observed by satellite 1994-084, which had just passed 00:00 MLT (the vertical blue dotted line), and is subsequently observed by 1991-080, as a dispersed drift signature.

5.5.3: IMAGE Data for 2000 – 2003

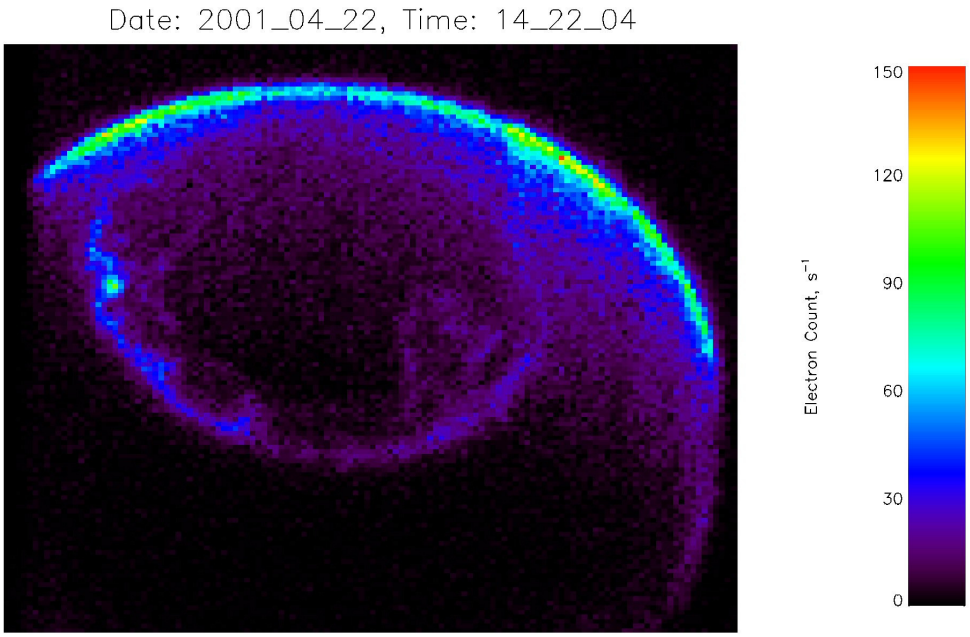

Figure 5.13: IMAGE raw electron data plot of aurora, from 2001/04/22, 14:22:04 UT. Expansion phases would be seen only if IMAGE was facing the aurora at the time of injection.

For this study, IMAGE electron data was first considered as a means of determining whether auroral expansion phases were occurring. The data available from IMAGE were spectrographically plotted, and showed the earth from the location of the satellite at a particular time. Data was available with two-minute intervals, which is a suitable time resolution for the determination of substorm onsets.

Figure 5.13 shows the aurora as it appears in IMAGE electron data. During substorm growth phase, the aurora would move to lower latitudes. At substorm onset, the narrow, stretched auroral arc would be observed to suddenly brighten, and expand to higher latitudes, with a westward surge of the brightening. As the spacecraft was not always directly facing the aurora, however, it was often difficult to deduce whether substorm expansions were occurring. Ideally, keograms of IMAGE data would be used instead, but these

were not available. IMAGE data was unfortunately found to be unsuitable for use in this study.

5.5.4: All-Sky Keograms for 2000 - 2003

Due to the limitations of the IMAGE data with regard to this study, another method for the determination of occurrence of auroral expansions was required. In the work of Tsurutani et al. on the 'storms with no substorms' from 1997 ([Tsurutani et al., 2003]), night-side UV images of the aurora from the POLAR satellite were used. For the work presented here, All-Sky auroral keograms are used.

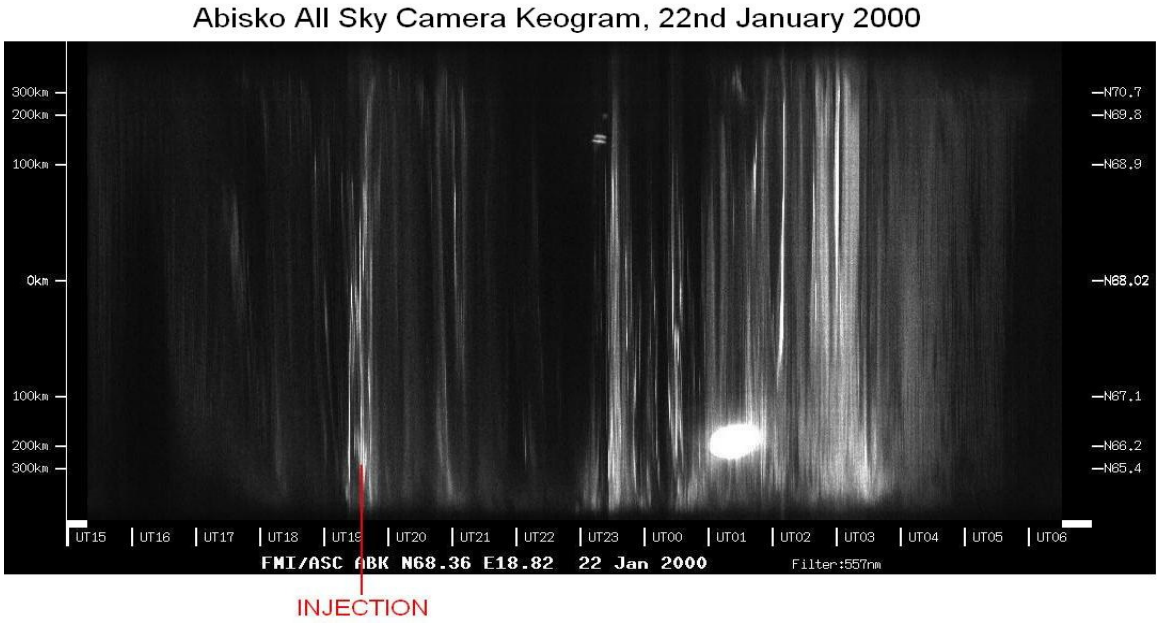

Figure 5.14: Abisko All-Sky keogram from 22nd January, 2000. The x-axis shows UT and the y-axis shows latitude. The Injection time is marked, and the brightening and poleward motion of the aurora indicate that this injection was due to a substorm with an expansion phase.

A keogram shows a local-time section of the night sky in Universal Time and latitude. Auroral keograms are made by stacking a Local-Time slice through the aurora against its relevant Universal Time. In a keogram, the brightness and

latitudinal motion of the aurora can be observed, and hence they are a useful tool for locating substorm onsets. The specification for substorm occurrence in this investigation will be an intensification of the aurora followed by a poleward latitudinal expansion.

Figure 5.14 shows an example keogram, which shows the progression of the aurora through the high-latitude night sky for 22nd January, 2000. The x-axis shows UT, with the date referring to the pre-midnight hours within the left partition of the plot (post-midnight is the next day, rather than the one labelled), and the y-axis is latitude. At ~19:30 UT, a large brightening is observed, which proceeds to expand to high latitudes. This is the auroral manifestation of a substorm, and will likely correlate to most of the electron injections under investigation. A dispersionless electron injection was observed by LANL satellite 1994-084 at ~19:40 UT (figure 5.12).

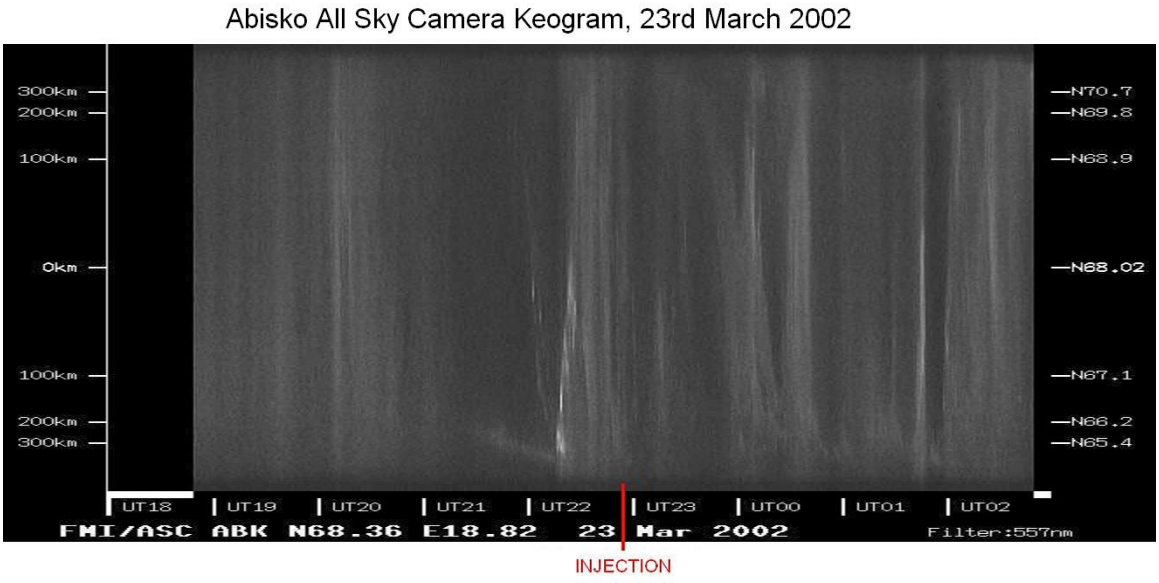

Figure 5.15 Abisko All-Sky keogram from 23rd March, 2002. The injection occurs much later than the earlier substorm expansion, and is attributed to a recovery-phase pseudobreakup.

In All-Sky keograms, pseudobreakups will not manifest themselves in the same way, as they will lack the expansion phase. It is expected that some

brightening will occur. Regardless, any injection which is observed to occur without a large-scale expansion will be counted as a pseudobreakup injection.

Figure 5.15 shows an example keogram from 23rd March, 2002. On this day, an injection was observed to occur at ~22:55 UT. As can be seen in the keograms, the main brightening and expansion occurred just after 22:00 UT, meaning this later injection was due to a substorm recovery phase pseudobreakup.

The availability of All-Sky data is quite limited in relation to the times of the injections. Due to the position of each of the All-Sky cameras, which are fixed upon the Earth, certain Universal Times will be unseen by any camera. The UT period which is covered by the available cameras is between ~15:00 UT and 06:00 UT, meaning any injections between 06:00 UT and 15:00 UT cannot be studied. Couple this with downtime and poor visibility (due to clouds) and, as with IMAGE, there is little knowledge of the number of injections which occurred due to substorms as opposed to those that occurred due to pseudobreakups. Due to these limitations, out of the 32 injections only six could be confirmed as containing expansion phases, and only three could be confirmed not to. Despite this very limited data set, correlations will be sought. All sky keograms were available from observatories in Abisko, Kilpisjarvi, Kevo and Muonio.

Year	Month	Day	Hour (UT)	Minute (UT)	Median of Maximum energy range (keV)	expansion
2000	1	22	19	40	270	yes
2000	2	5	19	5	187.5	yes
2000	2	12	17	0	187.5	yes
2000	3	1	19	5	127.5	yes
2000	10	4	17	25	187.5	no
2001	3	31	20	25	407.5	yes
2001	9	23	19	15	270	yes
2002	3	23	22	55	270	no
2003	2	1	19	35	187.5	no

Table 5.6: All injections used in the study, showing date, time, maximum energy reached and whether a substorm expansion phase was observed.

5.5.5 Results of the 2000-2003 Study

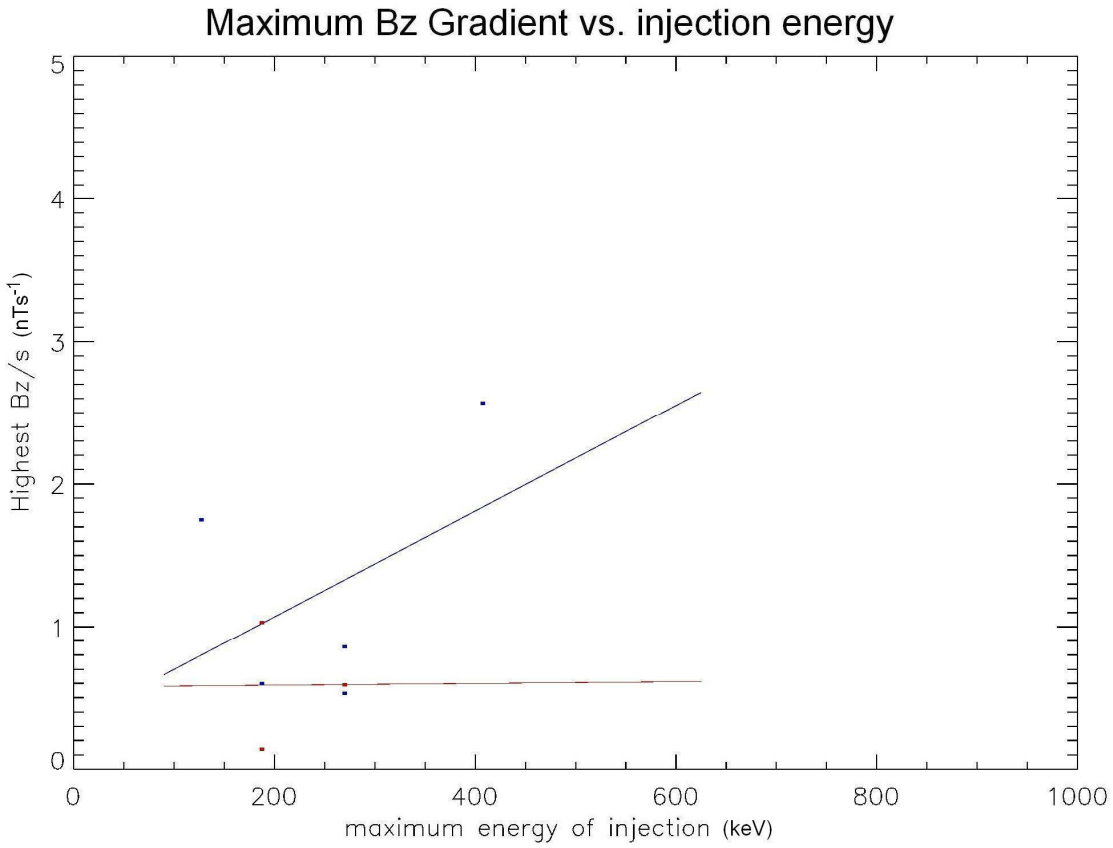

Figure 5.16: The maximum gradient of B_z spike in the 20 minutes preceding the injection against maximum energy reached by the injection. Events containing substorm expansions are blue; events containing no expansion are red. The pearson coefficient is 0.45 for substorms and 0.01 for pseudobreakups, meaning there is little evidence of a linear relationship in this graph. While the lack of many data points makes the gradient of the regression lines unsuitable to make solid conclusions, it is still evident that higher B_z spikes lead to substorms.

The results of this solar maximum study are very similar to those of the work shown in the first part of this chapter. The mean-maximum energy of the substorm injections is 366.75 keV, again much higher than that of the pseudobreakup injections, which is 190.21 keV. During this solar maximum period, only three of the injections were observed not to contain substorm expansions, all occurring during the recovery phase of previous substorms. This is most likely a result of the greater amount of solar activity during solar maximum.

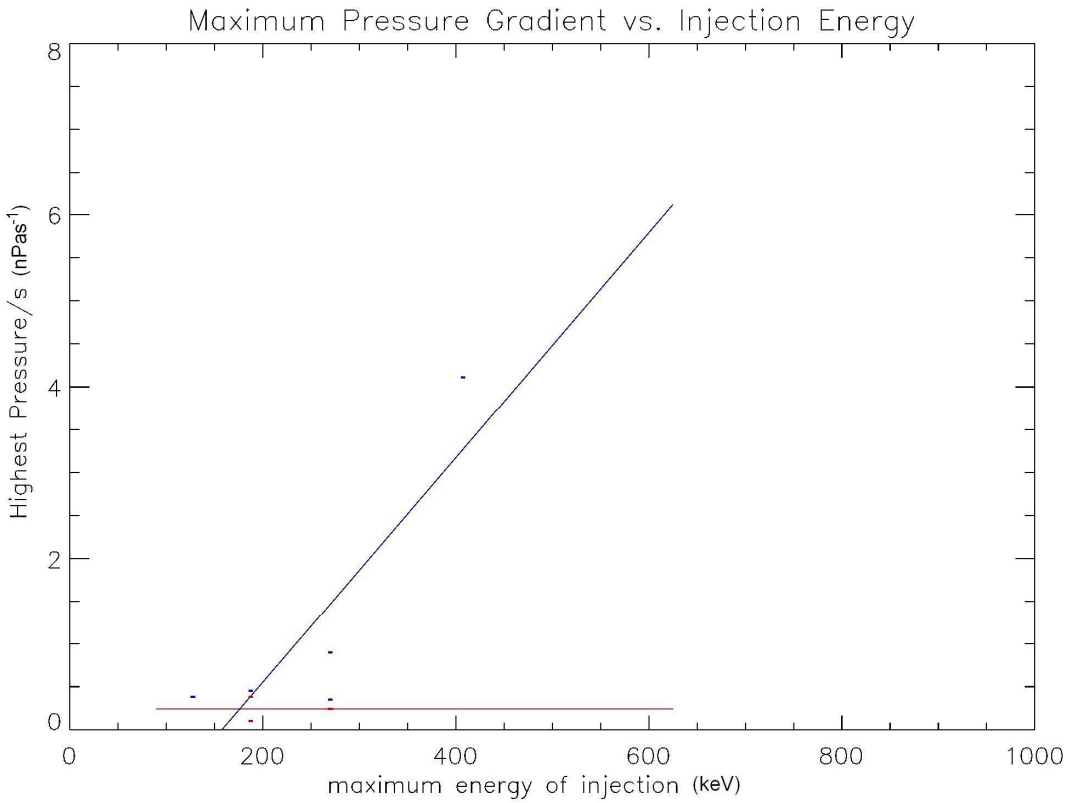

Figure 5.17: The maximum gradient of flow pressure spike in the 20 minutes preceding the injection against maximum energy reached by the injection. Events containing substorm expansions are blue; events containing no expansion are red. Again, data is lacking, but it is clear that larger pressure pulses lead to substorms. The pearson coefficient for substorms is 0.85, meaning that some linear correlation is observed. For pseudobreakups, the pearson coefficient is ~0, but this may be due to the lack of data points.

Figure 5.16 shows the maximum energy of injected particles against the largest B_z gradient, before the injection, for substorm (blue) and pseudobreakup (red) injections. Largest B_z gradient refers to the greatest positive jump in IMF B_z within the twenty minutes before the injection. The same plot for 1997 data showed two distinct populations for substorms and pseudobreakups, separated in B_z, and with increasing B_z gradients leading to increased injection energies. Although there are fewer points, the 2000 – 2003 data also shows this correlation, with the linear-fits behaving similarly. The points which make up this plot deviate from the linear-fits somewhat, and with the limited data, linear correlation cannot be proved. There is still evidence, however, that larger B_z

spikes lead to substorms and smaller spikes lead to pseudobreakups, and that substorm injection energy shows positive correlation with the size of the B_z spike, while pseudobreakup injection energy does not.

Figure 5.17 is the same style of plot as figure 5.16, for gradient-jumps in pressure rather than B_z. In the 1997 study this plot yielded another interesting result, with substorm injection energy increasing alongside pressure-spike magnitude, and pseudobreakups occurring when the pressure underwent very little in the way of a spike. In the 2000 – 2003 plot, the same is observed, with substorms occurrence following the larger pressure spikes. The linear fit does show the same correlation as that of the 1997 plot, though again the small amount of data detracts from the precision of any conclusions drawn.

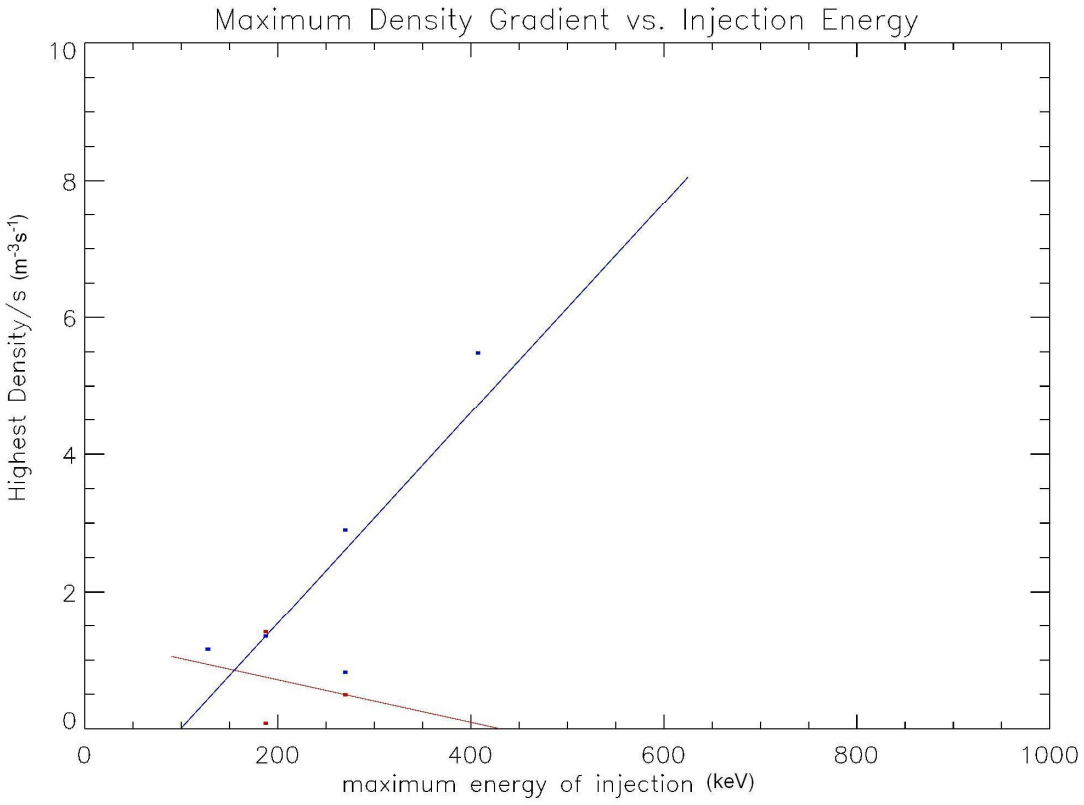

Figure 5.18: The maximum gradient in solar wind density spike in the 20 minutes preceding the injection against maximum energy reached by the injection. Events containing substorm expansions are blue; events containing no expansion are red. Reasonable correlation is seen between injection energy and density spike magnitude for substorms. The pearson coefficient is 0.83 for substorms, so a linear relationship may exist. That of pseudobreakups is only -0.21.

Figure 5.18 shows the maximum gradient in density, and despite the lack of many points, good correlation is observed with substorm occurrence. Pseudobreakup injections appear to be associated with lower densities. These observations were also made in the 1997 data.

5.5.6 Storms with No Substorms: A feature of Slow Magnetic Clouds?

A particular type of solar phenomena which may be of importance to this study is a Slow Magnetic Cloud. Slow Magnetic Clouds were studied by [Lepping et al., 1990], who categorised them as a manifestation of coronal mass ejections. Also known as Slow, or Late-Acceleration CMEs, these magnetic bubble-like structures do not burst from the Sun's corona like fast CMEs, but instead accelerate slowly with the ambient solar wind. Their general structure consists of a closed magnetic loop, or cloud, with rotation of the magnetic field components and an increased magnetic field magnitude. Due to the slow acceleration, there is no shock at the forefront of a Slow Magnetic Cloud. Despite the lack of a pressure pulse, Slow Magnetic Clouds have been shown to be surprisingly geoeffective ([Tsurutani et al., 2004]).

5.5.7 A Theory for Slow CMEs and Substorm Occurrence

In the first part of this chapter it was shown that for 1997 data there was evidence that substorm occurrence relied on a small spike in pressure as well as B_z, while pseudobreakups occurred with the B_z spike only. A statistical study of Slow CMEs could therefore prove interesting, as they are known to induce geomagnetic storms and should not have as turbulent a pressure profile as fast CMEs. Figure 5.19 shows the solar wind speed, pressure, magnetic field magnitude, B_z and Beta which would be expected within a slow CME. As it is essentially a bubble of magnetic field, the magnitude of the field would be expected to rise and the Beta to drop to near-zero values. The z-component of

the magnetic field would rotate smoothly, with a sinusoidal profile. As it slowly accelerates with the solar wind, no sudden jump in speed or pressure would be observed to occur. If pressure is indeed important with relation to substorm occurrence, the smoother profile involved with slow CMEs would be expected to cause a greater amount of pseudobreakups, with very few full substorm expansions occurring.

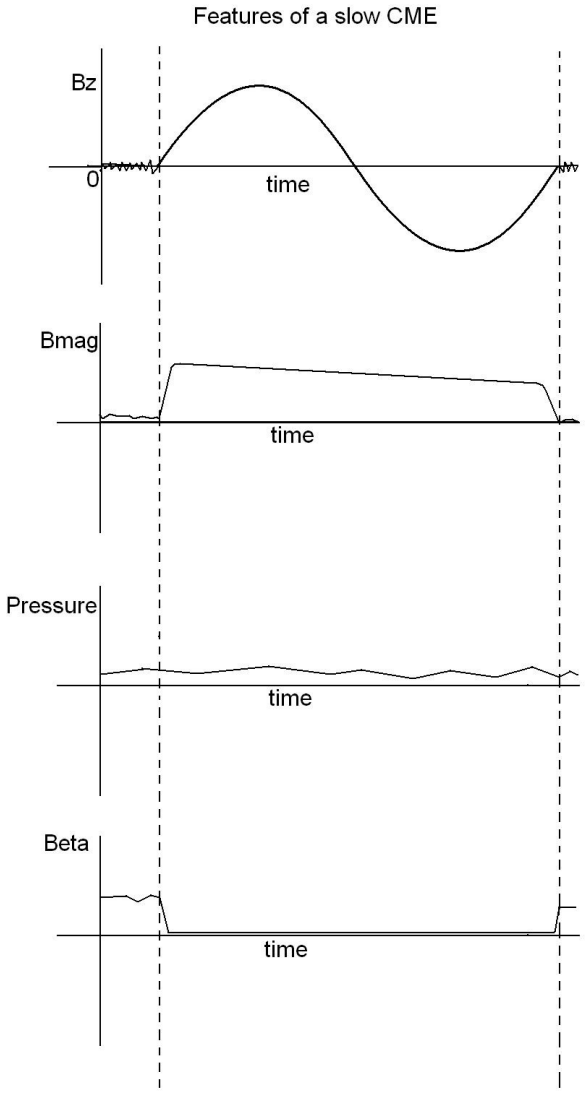

Figure 5.19: A cartoon showing some features of a Slow CME. The smoothly rotating IMF B_z and lack of a shocked region at the head are the two primary features, though an enhancement of B magnitude and low Beta value are also expected.

In the period under study, no geomagnetic storms were caused by interaction with a Slow Magnetic Cloud. It is possible that, at solar maximum, the greater level of solar activity tends to produce less of these less energetic phenomena.

5.5.8: Storms with No Substorms during the THEMIS Era

The recent THEMIS mission allows the opportunity to study the differences in magnetotail reconfiguration between substorms and pseudobreakups. It has been previously shown by [Ohtani et al., 1993] that some dipolarisation of the field occurs during pseudobreakups, though only locally. Using the THEMIS dataset, alongside all-sky data which could be used to differentiate between substorms and pseudobreakups, the entire region of the near- to far-earth magnetotail could be investigated simultaneously during both phenomena. This would be a good future extension to the work within this chapter.

5.6: Chapter Conclusions

Five geomagnetic storms that occurred in 1997 which did not contain any auroral expansions were investigated using LANL electron data. Across the duration of each storm, dispersionless injection signatures were observed, signifying evidence of substorm activity where none was seen in auroral data. These injections were attributed as being due to pseudobreakup activity, with the threshold for full substorm occurrence not being met. In an investigation of the maximum energy reached by the injections, it was found that storms which did not contain substorm expansion phases generally contained lower energy injections than those which did.

Solar wind data were then used to investigate the possible threshold which must be met in order for a full substorm to occur. A study carried out by

eye, alongside computed investigations that considered solar wind parameters in the 20 minutes prior to substorm occurrence, suggested that the number density and pressure of solar wind material was an important factor for substorm occurrence. Spikes in B_z were also correlated to substorm occurrence, with smaller spikes instead resulting in pseudobreakups.

A further study was undertaken using data from 2000 to 2003. Insufficient coverage of the aurora by the IMAGE satellite during the relevant periods meant that All-Sky data from various cameras were required to ascertain whether expansions had occurred, and due to their fixed positions on earth, important auroral data were again very limited. The few occurrences of storms in which the occurrence or lack of substorm expansions could be confirmed showed a similar correlation to the 1997 study, firstly with substorm injections being of a higher energy than pseudobreakup injections, and secondly with the solar wind parameters of density, pressure and B_z showing a similar correlation with injection energy and substorm/pseudobreakup occurrence.

It is suggested that spikes in the density of solar wind material within events which energise the magnetosphere will lead to a more rapid build-up of pressure within the reconnection region on the nightside than for events of small or average solar wind density. The rapid pressure build up would lead to a full substorm, while a slower pressure increase would cause only pseudobreakup activity.

Chapter 6: Summary, Conclusions and Further Work

6.1 Summary of the Work

6.1.1 Charge Exchange as a Source of Outer Belt He^+

Invariant Latitude plots of Helium charge state ratio showed that He^+ existed in greater number density than He^{++} in the outer belt region. Oxygen was generally the dominant magnetospheric heavy ion, especially at high latitude (high L-Shell), but within the region of the outer belt the number density of He^+ came close to matching that of O^+. As O^+ and He^+ do not display a flat ratio across invariant latitude, they cannot be sourced entirely from the same region. Charge exchange of solar wind alpha particles with exospheric neutral hydrogen was suggested as the source of this He^+, with the stability of trapping in the region allowing particles to populate the belt for many days before they are lost. A further charge exchange reaction would neutralise the He^+ and cause it to be lost, but relative to the other aforementioned reaction, the smaller cross sectional area over which this charge exchange can occur would lead to a build-up in He^+, assuming a continuous input of He^{++}.

The number density ratio of He^+ to He^{++} within the outer belt region was investigated as a function of MLT. It was found that there was a slight shift towards He^+ in a westward direction around the Earth. The ring current flows in this direction, and it was suggested that this may be evidence of a small amount of charge exchange after a single drift orbit. Alongside this, a population of He^+ which appeared in the drift echo of a dispersionless particle injection at energies not apparent within the injection itself was suggested as being due to charge exchange.

If charge exchange is occurring visibly on this short timescale, one would expect it to be observed across the period of a single CRRES orbit. Shifts in the number density of ionic helium species were investigated on an orbit-to-orbit basis, and the data was sorted by storm main and recovery phase. It was shown

that during the main phase of a storm all ionic species common to the ring current increase in number density, indicating both solar wind and ionospheric input. During the recovery phase, however, He^+ was shown to increase in number density, while the O^+ and He^{++} content decreased. This is evidence of a recovery phase source for He^+, here suggested to be charge exchange.

6.1.2 Calculating the Charge Exchange Cross Section Using Distinct Populations of Drifting Particles

A new population of He^+ was observed to appear at energies in the drift echo of a dispersionless particle injection which occurred on 14th February, 1991, during orbit 497 of CRRES. This population was in an energy range which was not present in the injection. The possibility of this He^+ having arisen as a result of charge exchange was investigated. Due to the expected 'spreading' of He^+ on a CRRES energy spectrogram in the event of charge exchange, it was concluded that this new population could not have been entirely be explained by the reaction.

The helium composition of five injections in which two clear drift echoes were observed was investigated with each drift. It was found that, after a single drift, the He^+/He^{++} ratio always increased, i.e. the helium content was shifting towards He^+. Shifts in the second drift signature were less clear, often moving in the opposite direction. It was shown that a charge exchanged He^{++} ion could end up in either of the drift echoes, or anywhere in between them, after a single drift, adding complications to the study. The modelled drift time was, however, shown not to perfectly fit the actual drift time, with the particles often drifting more quickly than predicted.

Calculated cross sections using the first drift were found to be, at minimum, ten times larger than previously published work. The cross sections were larger at the lower end of the energy range than the higher, probably due to the larger level of contamination by ambient, uninjected drifting ions. The spread in data showed a standard deviation of ~1 order of magnitude, meaning

previously calculated cross sections were within the error at the highest energies. In a previous paper by Smith and Bewtra, charge exchange lifetimes were found to be larger than predicted by laboratory measurements and theory. This effect may have manifested itself as the large cross section calculated in this study.

6.1.3: Storms with No Substorms: A Study of Substorm and Pseudobreakup Occurrence

A recent paper by [Tsurutani et al., 2003] reported that five of eleven magnetic storms in 1997, all caused by interplanetary coronal mass ejections containing magnetic clouds, did not contain evidence of substorm expansion phases in auroral data. It was suggested that steady convection of the magnetosphere, in response to reconnection with the smoothly negative IMF B_z profile associated with the magnetic clouds, was the reason for this unusual lack of substorms.

An investigation of LANL electron data showed that many energetic electron injections occurred within the duration of the magnetic clouds, indicating that expansionless substorms were occurring. These expansionless onsets are referred to as pseudobreakups, and a recent investigation of the features of substorms and pseudobreakups by [Kullen and Karlsson, 2004] concluded that the two phenomena are essentially the same thing, with pseudobreakups simply being the weakest possible form of a substorm. Hence, it was shown that during the storms which held no substorm expansions, very weak substorms were occurring.

The maximum energies of the injections which occurred during the five 'expansionless' storms were compared to those of the storms which contained substorm expansion phases, and it was found that the injections were generally of greater energy if a substorm expansion had occurred. This is likely a result of the full expansion being the more energetic process. The average maximum energy for a pseudobreakup injection was found to be 217.9 keV, and that of substorm injections was calculated at 389.6 keV.

For the events studied in Tsurutani's paper, solar wind parameters, corrected for their impact with the nose of the Bow Shock, were investigated across the 20 minutes prior to injection. Using a few methods, including a manual examination of data and a gradient-based investigation of spikes and discontinuities, evidence was presented that solar wind with large number density (and pressure, as it is related to density) enhancements led to substorms, while pseudobreakup occurrence required no such spike. Positive Spikes in B_z were shown to correlate positively with the energy of injected particles, and full substorms appeared to be preceded by greater positive B_z spikes than pseudobreakups. It was also shown that highly negative B_z was required for the occurrence of both substorms and pseudobreakups, with some evidence that more highly negative B_z was required for substorms. Injection energy showed positive correlation with average B_z negativity for both substorms and pseudobreakups.

A similar study was carried out using data from 2000 – 2003, across solar maximum. Due to a lack of useful auroral data from IMAGE, limited All-Sky Camera data from various high-latitude observatories were used to find expansions. The limitations presented by this method due to the observatories being fixed in latitude and longitude made the dataset small, but even with the limitations similar correlations were observed across all investigated solar wind parameters. The average energy of injections due to pseudobreakups and substorms also showed a similar trend, with the average maximum energy being 190.21 keV and 366.75 keV, respectively.

6.2 Conclusions and Further Work

6.2.1 Charge Exchange as a Source of Outer Belt He^+

Evidence of charge exchange as a source of He^+ in the outer belt has been presented, and it is concluded that charge exchange is a prominent source

of magnetospheric He^+. Charge exchange is suggested as the mechanism responsible for the storm recovery phase source of He^+.

Improvements could be made in the CRRES orbit-by orbit study by refining the storm phase-finding algorithm, as it is possible that some quiet time data may have been regarded as recovery phase. This would have contaminated the shift in species, pushing it toward the 'steady state' for the sources and losses of ions, shown to exist during quiet time. A more refined investigation into charge exchange during the recovery phase would also be a good idea, as the loss rate during the initial recovery is far greater than during the late recovery.

6.2.2 Calculating the Charge Exchange Cross Section Using Distinct Populations of Drifting Particles

The shift in Helium ratio after a single drift is suggested as evidence of charge exchange. Due to unavoidable problems due to using data from a single satellite it is hard to argue that this is the case. However, the method of calculating charge exchange cross sections using an injected population of He^{++} and its drift echoes was sound, and future missions involving multiple geosynchronous satellites (with MICS devices in their payload) could better observe shifts in the drifting population.

The method of calculation of cross section used in this chapter could be greatly improved. Firstly, more accurate modelling of the drift period would remove the need for handpicking, which may have caused inaccuracies in lower energy ranges, where energy dispersion and uninjected ions cause the most error. A more accurate method of determining the time spent at different altitudes across a bounce path, alongside a higher resolution model for neutral hydrogen density with altitude, would also have improved the accuracy of the final cross section. With regard to the calculated cross sections, a good extension to this work would be to create modelled spectrograms of He^+ and He^{++}, and compare them to actual data. Modelled spectrograms could also be made using cross sections from other work, to see whether there is a greater likeness.

The CRRES mission was not ideal for this study, as it involved a single satellite, and had no way of ascertaining where, in MLT, a charge exchange reaction occurred. If the study could be undertaken with multiple satellites, taking detailed ion data at various geosynchronous locations, better results could be achieved. A mission similar to LANL would be ideal, with each probe having a MICS device.

6.2.3 Storms with no Substorms: a Study of Substorm and Pseudobreakup Occurrence

Due to the occurrence of dispersionless electron injections in the stormtime periods which did not contain full expansions, it was concluded that small substorms (pseudobreakups) were occurring. This suggests that Continuous Steady Magnetospheric Convection (SMC) with an absence of any substorm activity is not possible. Full substorm occurrence was correlated to enhancements in the density of the solar wind within the 20 minutes prior to onset. This is explained in relation to substorms being the solution to the pressure catastrophe, as predicted by [Erickson and Wolf, 1980], with the spike in density initiating the formation of a NENL.

In order to confirm the conclusions of this chapter, a large statistical study of the solar wind parameters leading to substorms and pseudobreakups, especially density, should be carried out. If a pseudobreakup is indeed simply the smallest variety of substorm, perhaps some measure of substorm intensity should be created for this study, such as brightness at onset, or the amount of poleward expansion.

Intensity could be studied for the substorms which occur as a result of Slow Magnetic Cloud-induced storms. It is possible that the smoothly rotating B_z period of these solar wind phenomena would cause pseudobreakups, or very low-energy substorms. Alongside this investigation, the density of the solar wind within each Magnetic Cloud could be compared to the intensity of any substorm-activity which was induced.

Finally, an investigation of THEMIS data across the entire magnetotail during pseudobreakups and substorms would be an excellent addition to the work presented here, as current disruption and Near-Earth reconnection could be examined with regard to the intensity of the substorm.

6.3 Summary of Conclusions

Evidence of charge exchange as a source of He^+ in the outer belt has been presented, beginning with a tendency for He^+ to exist in greater number densities than He^{++} in the Outer Radiation belt. A shift in the average ratio of He^+ to He^{++}, with MLT, in the Outer Belt region suggests a short timescale for charge exchange. He^+ is shown to increase in number density during the recovery phase of geomagnetic storms, and charge exchange is suggested as the source. It is concluded that charge exchange is a primary source for Outer Belt He^+.

The helium composition of five substorm injections and their subsequent drift echoes were investigated for evidence of charge exchange. After a single drift, a shift from He^{++} towards He^+ composition was observed. Charge exchange cross sections were calculated from these data, and were found to be far larger than those from previous work. It was concluded that charge exchange cannot be entirely responsible for the observation.

Five storm intervals during 1997 which did not contain auroral substorm expansions were found to contain dispersionless substorm injections in LANL electron data. These injections were attributed to pseudobreakup occurrence, and their energies were found to be generally lower than those of full substorms. A study of precursor solar wind parameters suggested that solar wind density enhancements are required for full substorm occurrence. This is explained in relation to the pressure catastrophe ([Erickson and Wolf, 1980]). A study using data taken from 2000 – 2003 gave a similar result. It is concluded that all storms contain some level of substorm activity, and that substorm versus pseudobreakup occurrence depends upon the density of material within the precursor solar wind.

Bibliography

[1] http://silas.psfc.mit.edu/introplasma/figures/chap1/exbdrift13.png

[2] http://www-spof.gsfc.nasa.gov/Education/Figures/Dungey.gif

[3]leadbelly.lanl.gov/lanl_ep_data/information/energies/cpa_electron_energies.gif

[4] http://leadbelly.lanl.gov

[5] Fitzpatrick, R., The Physics of Plasmas, 2008

[Aikio et al., 1999] Aikio, A.T., Sergeev, V. A., Shukhtina, M. A., Vagina, L. I., Angelopoulos, V., Reeves, G. D., Characteristics of pseudobreakups and substorms observed in the ionosphere, at geosynchronous orbit, and in the midtail, Journal of Geophysical Research, Volume 104, 12263-12287, 1999

[Akasofu, 1968] Akasofu,S .-I., Polar and Magnetospheric Substorms, Astrophysics and Space Sciences Library, Volume 11, 1968

[Angelopoulos, 2008] Angelopoulos, V., The THEMIS Mission, Space Science Reviews, Volume 141, 5-34, 2008

[Arballo et al., 1998] Arballo, J. K., Ho, C. M., Lakhina, G. S., Tsurutani, B. T., Zhou, X. –Y., Kamide, Y., Shue, J. –H., Akasofu, S. –I., Lepping, R. P., Goodrich, C. C., Papadopoulos, K., Sharma, A. S., Lyon, J. G., Pseudobreakups During January 10, 1997, Substorms-4: International Conference on Substorms-4, Lake Hamana, Japan, Astrophysics and Space Sciences Library, Volume 238, 315, 1998

Bibliography

[Baker et al., 1984] Baker, D. N., Bame, S. J., Birn, J., Feldman, W. C., Gosling, J. T., Hones, E. W., Zwickl, R. D., Slavin, J. A., Smith, E. J., Tsurutani, B. T., Sibeck, D. G., Direct Observations of Passages of the Distant Neutral Line (80-140RE) Following Substorm Onsets: ISEE-3, Geophysical Research Letters, Volume 11, 1042-1045, 1984

[Baker et al., 1996]] Baker, D. N., Pulkkinen, T. I., Angelopoulos, V., Baumjohann, W., McPherron, R. L., Neutral Line Model of Substorms: Past Results and Present View, Journal of Geophysical Research-Space Physics, Volume 101, Issue A6, 12975-13010, 1996

[Baumjohann et al., 1989] Baumjohann, W., Paschmann, G., Cattell, C. A., Average Plasma Properties in the Central Plasma Sheet, Journal of Geophysical Research-Space Physics, Volume 94, Issue A6, 6597-6604, 1989

[Bayfield and Khayrallah, 1975] Bayfield, J. E., Khayrallah, G. A., Electron Transfer in keV-energy $^4He^{++}$ Collisions. 3. Experimental Tests of the Close-Coupling Calculations for $^4He^{++}$ -H(1s) Collisions, Physical Review A: Atomic, Molecular and Optical Physics, Volume 12, Issue 3, 869-875, 1975

[Chapman, 1962] Chapman, S., Earth Storms: Retrospect and prospect, J. Phys. Soc. Jpn., Volume 17,6-16, 1962

[Cravens, 2000] Cravens, T. E., Heliospheric X-Ray Emmission Associated with Charge Transfer of the Solar Wind with Interstellar Neutrals, Astrophysical Journal, Volume 532, Issue 2, L153-L156, 2000

[Daglis et al., 1999] Daglis, I. A., Thorne, R. M., Baumjohann, W., Orsini, S., The Terrestrial Ring Current: Origin, Formation, and Decay, Reviews of Geophysics, Volume 37, 407-438, 1999

[DeForest and McIlwain, 1971] DeForest, S. E., McIlwain, C. E., Plasma Clouds in the Magnetosphere, Journal of Geophysical Research, Volume 76, no. 16, 3578-3611, 1971

[Dennerl, Englhauser and Trumper, 1997] Dennerl, K., Englhauser, J., Trumper, J., X-Rat Emissions from Comets detected in the Rontgen X-Ray Satellite All-Sky Survey, Science, Volume 277, Issue 5332, 1625-1630, 1997

[Dessler and Parker, 1959] Dessler, A. J., Parker, E. N., Hydromagnetic Theory of Geomagnetic Storms, Journal of Geophysical Research, Volume 64, 2239-2252, 1959

[Dungey, 1961] Dungey, J. W., Interplanetary Magnetic Field and the Auroral Zones, Phys. Rev. Lett., Volume 6, 47-48, 1961

[Elvey, 1957] Elvey, C. T., Problems of Auroral Morphology, Proceedings of the Nat. Academy of Sciences of the USA, Volume 43, 63-75, 1957

[Erickson and Wolf, 1980] Erickson, G. M., Wolf, R. A., Is Steady Convection Possible in the Earth's Magnetotail?, Geophysical Research Letters, Volume 7, 897-900, 1980

[Fillingim et al., 2000] Fillingim, M. O., Parks, G. K., Chen, L. J., Brittnacher, M., Germany, G. A., Spann, J. F., Larson, D., Lin, R. P., Coincident POLAR/UVI and WIND Observations of Pseudobreakups, Geophysical Research Letters, Volume 27, no. 9, 1379-1382, 2000

[Fite et al., 1962] Fite, W. L., Smith, A. C. H., Stebbings, R. F., Charge Transfer in Collisions Involving Symmetric and Asymmetric Resonance, Proceedings of the Royal Society of London Series A - Mathematical and Physical Sciences, Volume 268, Issue 1335, 527-&, 1962

[Freden, 1968], Freden, S. C., Inner-Belt Van Allen Radiation, Space Science Reviews, Volume 9, Issue 2, 198-242, 1968

[Gonzalez and Tsurutani, 1987] Gonzalez, W. D., Tsurutani, B. T., Criteria of Interplanetary Parameters Causing Intense Magnetic Storms (DST less-than- 100-nT), Planetary and Space Science, Volume 35, Issue 9, 1101-1109, 1987

[Gonzalez et al., 1994] Gonzalez, W. D., Joselyn, J. A., Kamide, Y., Kroehl, H. Rostoker, W. G., B . T. Tsurutani, V. M. Vasyliuna, What is a Geomagnetic Storm?, Journal of Geophysical Research, 99, 5771-5792, 1994

[Gosling et. al, 1991] Gosling, J. T., McComas, D. J., Phillips, J. L., Bame, S. J., Geomagnetic Activity Associated with Earth Passage of Interplanetary Shock Disturbances and Coronal Mass Ejections, Journal of Geophysical Research, Volume 96, No. A5, 7831-7839, 1991

[Grande et al., 1992] Grande, M., Perry, C. H., Hall, D. S., Wilken, B., Livi, s., Soraas, F., Fennell, J. F., Composition Signatures of Substorm Injections, Proceedings of the International Conference on Substorms (ICS-1), Kiruna, Sweden, ESA SP-335),485--490, 1992

[Grande et al., 1996] Grande, M., Perry, C. H., Blake, J. B., Chen, M. W., Fennell, J. F., Wilken, B., Observations of Iron, Silicon, and Other Heavy Ions in the Geostationary Altitude Region During Late March 1991, Journal of Geophysical Research, Volume 101, No. A11, 24707-24718, 1996

[Grande et al., 1997] Grande, M., Perry, C. H., Hall, A., Fennell, J., Wilken, B., Survey of Ring Current Composition During Magnetic Storms, Adv. Space Res. Vol. 20, No. 3, 321-326, 1997

[Hall et al., 1998] Hall, A. M., Perry, C. H., Grande, M., Lester, M., Wilken, B., Survey of Dispersionless Substorm Ion Injections Observed by CRRES, Adv. Space Res., Volume 21, No. 4, 615-618, 1998

[Hasegawa, 1975] Hasagawa, A., Plasma Instabilities and Nonlinear effects, Springer Verlag, New York Heidelberg Berlin, 52-62, 1975

[Hudson et al., 2008] Hudson, M. K., Kress, B. T., Mueller, H., Zastrow, J. A., Blake, J. B., Relationship of the Van Allen Radiation belts to solar wind drivers, Journal of Atmospheric and Solar Terrestrial Physics, 70, 708-729, 2008

[Hones, 1976] Hones E. W. Jr., The Magnetotail: Its Generation and Dissipation, in Physics of Solar Planetary environments, edited By D. J. Williams, AGU, Volume 558, 1976

[Hones et al., 1972] Hones, E. W. Jr., Asbridge, J. R., Bame, S. J., Montgomery, M. D., Singer, S., Akasofu, S. –I., Measurements of Magnetotail Plasma Flow made with Vela 4B, Journal of Geophysical Research, Volume 77, No. 28, 1972

[Johnson et al., 1992] Johnson, M. H., Kierein, J., Combined Release and Radiation Effects Satellite (CRRES) – Spacecraft and Mission, Journal of Spacecraft and Rockets, Volume 29, No. 4, 556-563, 1992

[Kaufmann, 1987] Kaufmann, R. L., Substorm Currents: Growth Phase and Onset, Journal of Geophysical Research, Volume 92, 7471, 1987

[King and Papitashvili, 2005] King, J. H., Papitashvili, N. E., Solar Wind Spatial Scales in and Comparisons of Hourly Wind and ACE Plasma and Magnetic Field Data, Journal of Geophysical Research – Space Physics, Volume 110, Issue A2, Article Number A02104, 2005

[Koskinen et al., 1993] Koskinen, H. E. J., Lopez, R. E., Pellinen, R. J., Pulkkinen, T. I., Baker, D. N., Bosinger, T., Pseudobreakup and Substorm Growth Phase in the Ionosphere and Magnetosphere, Journal of Geophysical Research, Volume 98, 5801, 1993

[Kullen and Karlsson, 2004] Kullen, A., Karlsson, T., On the Relation Between Solar Wind, Pseudobreakups, and Substorms, Journal of Geophysical Research, Volume 109, 2004

[Lepping et al., 1990] Lepping, R. P., Jones, J. A., Burlaga, L. F., Magnetic Field Structure of Interplanetary Magnetic Clouds at 1 AU, Journal of Geophysical Research, Volume 95, No. A8, 11957-11965, 1990

[Lisse et al., 1996] Lisse, C. M., Dennerl, K., Englhauser, J., et al., Science, Volume 274, Issue 5285, 205-209, 1996

[Lui, 1996] Lui, A. T. Y., Current Disruption in the Earth's Magnetosphere: Observations and Models, Journal of Geophysical Research-Space Physics, Volume 101, Issue A6, 13067-13088, 1996

[Lui and Burrows, 1978] Lui, A. T. Y., Burrows, J. R., On the Location of Auroral Arcs Near Substorm Onsets, Journal of Geophysical Research, Volume 83, 3342, 1978

[Lyons and Schulz, 1989] Lyons, L. R., Schulz, M., Access of Energetic Particles to Storm Time Ring Current through Enhanced Radial “Diffusion”, Journal of Geophysical Research, Volume 94, No. A5, 5491-5496, 1989

[Lyons et al., 1999] Lyons, L. R., Nagai, T., Blanchard, G. T., Samson, J. C., Yamamoto, T., Mukai, T., Nishida, A., Kokubun, S., Association Between Geotail Plasma Flows and Auroral Poleward Boundary Intensifications observed by CANOPUS Photometers, Journal of Geophysical Research, Volume 104, 4485, 1999

[McPherron et al., 1973] McPherron, R. L., Aubry, M. P., Russel, C. T., Coleman, P. J., Satellite Studies of Magnetospheric Substorms on August 15, 1968 .4. OGO-5 Magnetic-Field Observations, Transactions-American Geophysical Union, Volume 54, Issue 4, 205-205, 1973

[McPherron, 1991] McPherron, R. L., Physical Processes Producing Magnetospheric Substorms and Magnetic Storms, Geomagnetism, Volume 4, 593-739, 1991

[Nagai et al., 1998] Nagai, T., Fujimoto, M., Saito, Y., Machida, S., Terasawa, T., Nakamura, R., Yamamoto, T., Mukai, T., Nishida, A., Kokubun, S., Structure and Dynamics of Magnetic Reconnection for Substorm Onsets With Geotail Observations, Journal of Geophysical Research-Space Physics, Volume 103, Issue A3, 4419-4440, 1998

[Nakada and Mead, 1965] Nakada, M. P., Mead, G. D., Diffusion of Protons in the Outer Radiation belt, Journal of Geophysical Research, Volume 70, No. 19, 1965

[Nutt et al., 1978] Nutt, W. L., McCullough, R. W., Brady, K., Shah, M. B., Gilbody, H. B., Electron Capture by He^{2+} Ions with H and H_2 at Impact Energies Below 10keV, Journal of Physics B: Atomic and Molecular Physics, Volume 11, No. 8, 1457, 1978

[Ohtani et al., 1993] Ohtani, S., Anderson, B. J., Sibeck, D. G., Newell, P. T., Zanetti, L. J., Potemra, T. A., Takahshi, K., Lopez, R. E., Angelopoulos, V., Nakamura, R., Klumpar, D. M., Russell, C. T., A Multi Satellite Study of Pseudo-Substorm Onset in the Near-Earth Magnetotail, Journal of Geophysical Research, Volume 98, No. A11, 19355-19367, 1993

[Olson et al., 1977] Olson, R. E., Salop, A., Phaneuf, R. A., Meyer, F. W., Electron Loss by Atomic and Molecular Hydrogen in Collisions with $^3He^{++}$ and $^4He^+$, Physical Review A: Atomic, Molecular, and Optical Physics, Volume 16, 1867-1872, 1977

[Ostgaard et al., 2003] Ostgaard, N., Mende, S. B., Frey, H. U., Gladstone, G. R., Lauche, H., Neutral Hydrogen Density Profiles Derived from Geocoronal Imaging, Journal of Geophysical Research, Volume 108, No, A7, 1300, 2003

[Paulikas and Blake, 1979] Paulikas, G. A., Blake, J. B, Effects of the Solar Wind on Magnetospheric Dynamics: Energetic Electrons at the Synchronous Orbit, Quantitative Modeling of Magnetospheric Processes, Geophysical Monograph Series, Volume 21, 180-202, 1979

[Prakash and Diamond, 1999] Prakash, M., Diamond, P. H., The Role of Nonlinear Landau Damping and the Bounce Motion of Protons in the Formation of Dissipative Structures in the Solar Wind Plasma, Nonlinear Processes in Geophysics, Volume 6, 161-167, 1999

[Rapp, 1974] Rapp, D., Electron capture and Excitation in Collision of He^{++} with H, 2, Convergence of the Atomic Expansion, Journal of Chemical Physics, Volume 61, Issue 9, 3777, 1974

[Reeves et al., 2011] Reeves, G. D., Morley, S. K., Friedel, H. W. R., Henderson, M. G., Cayton, T. E., Cunningham, G., Blake, J. B., Christensen, R. A., Thomsen, D., On the Relationship Between Relativistic Electron Flux and Solar Wind Velocity: Paulikas and Blake Revisited, Journal of Geophysical Research, Volume 116, A02213, 2011

[Rostoker, 1998] Rostoker, G., On the Place of the pseudo-breakup in a Magnetospheric Substorm, Geophysical Research Letters, Volume 25, No. 2, 217-220,1998

[Sckopke, 1966] Sckopke, N., A General Relation Between the Energy of Trapped Particles and the Disturbance Field over the Earth, Journal of Geophysical Research, Volume 71, 3125-3130, 1966

[Shah and Gilbody, 1978], Shah, M. B., Gilbody, H. B., Electron Capture and He^{+} (2s) sormation in fast He^{2+} -H and He^{+} -H Collisions, Journal of Physics B: Atomic and Molecular Physics, Volume 11, 121, 1978

[Smith and Bewtra, 1978] Smith, P. H., Bewtra, N. K., Charge Exchange Lifetimes for Ring Current Ions, Space Science Reviews, Volume 22, 301-318, 1978

[Tinsley, 1976] Tinsley, B. A., Evidence that the Recovery Phase Ring Current Consists of Helium Ions, Journal of Geophysical Research, 81, No. 34, 1976

[Toshima, 1994] Toshima, N., Ionisation and Charge-Transfer of Atomic-Hydrogen in Collision with Multiply-Charged Ions, Physical Review A, Volume 50, Issue 5, 3940-3947, 1994

[Tsurutani et al., 2003] Tsurutani, B. T., Zhou, X, -Y, Gonzalez, W. D., A Lack of Substorm Expansion Phases During Magnetic Storms Induced by Magnetic Clouds, Disturbances in Geospace: The Storm-Substorm Relationship, Geophysical Monograph 142, American Geophysical Union, 23-36, 2003

[Tsurutani et al., 2004] Tsurutani, B. T., Gonzalez, W. D., Zhou, X, -Y, Lepping, R. P., Bothmer, V., Properties of Slow Magnetic Clouds, Journal of Atmospheric and Solar-Terrestrial Physics, Volume 66, 147-151, 2004

[Van Allen et al., 1958] Van Allen, J. A., G. H. Ludwig, E. C. Ray, and C. E. McIlwain, Observations of high intensity radiation by satellites 1958 Alpha and Gamma, Jet Propul., 28, 588-592, 1958

[Voronkov et al., 2003] Voronkov, I. O., Donovan, E. F., Samson, J. C., Observations of the Phases of the Substorm, Journal of Geophysical Research, Volume 108 (A2), 1073, 2003

[Wilken et al., 1992] Wilken, B., Weiβ, W., Hall, D., Grande, M., Søraas, F., Fennell, J. F., Magnetospheric Ion Composition Spectrometer Onboard the CRRES Spacecraft, Journal of Spacecraft and Rockets, Volume 29, No. 4, 1992

[Williams, 1987] Williams, D. J., Ring Current and Radiation Belts, Reviews of Geophysics, 25, 570-578, 1987

[Winter, 2007] Winter, T. G., Electron Transfer, excitation, and ionization in α-H Collisions studied with a Sturmian Basis, Physical Review A, Volume 76, Issue 6, 2007

[Zwickl et al., 1983] Zwickl, R. D., Ashbridge, J. R., Bame, S. J., Feldman, W. C., Gosling, J. T., Smith, E. J., Plasma Properties of Driver Gas following Interplanetary Shocks observed by ISEE-3, Solar Wind Five, Nasa Conf. Publ. CP-2280, 711, 1983

Appendix A: Number Density Shifts in Helium

The Study of shifts in Helium population across CRRES's subsequent visits to the outer belt was carried out in chapter 3. Certain graphs which did not contribute to the investigation, but are nonetheless important, are presented here.

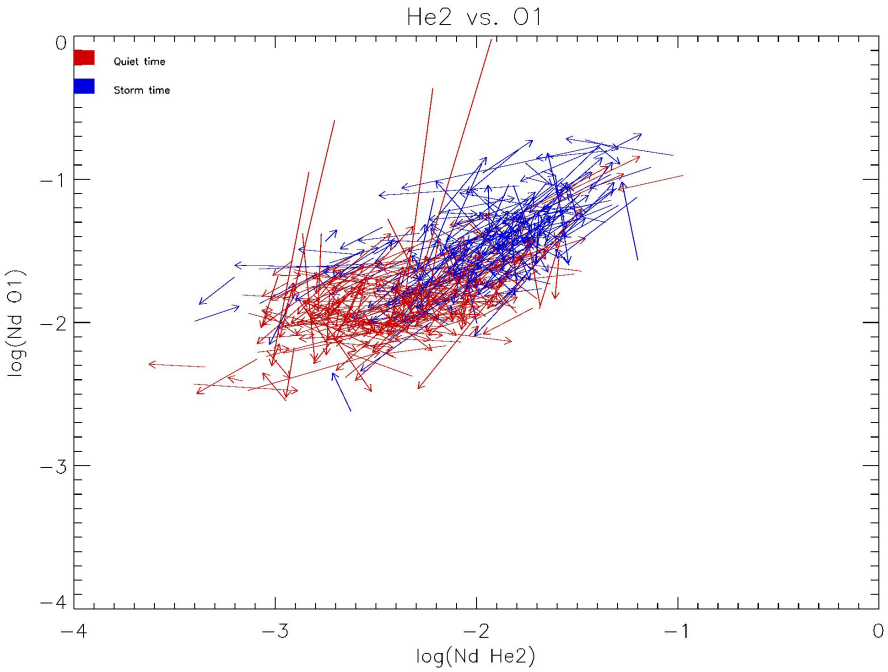

Figure A.1: Log vs. log plot of O^{+} number density vs. He^{++} number density, showing the average population shifts for each orbit-to-subsequent-orbit of CRRES. Quiet time data, taken as DST > -30nT, is red. Stormtime data, taken as DST < -30nT, is blue.

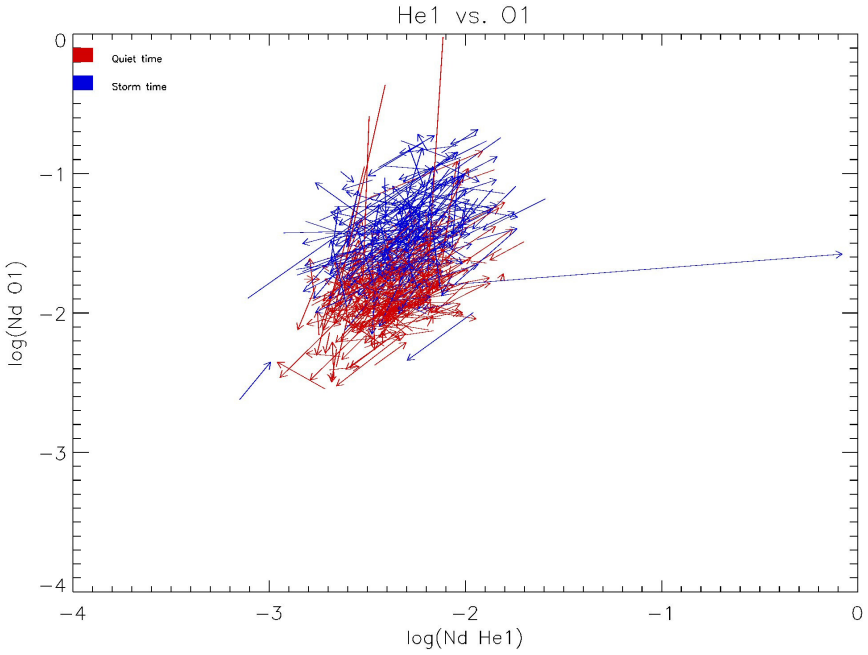

Figure A.2: Log vs. log plot of O^+ number density vs. He^+ number density, showing the average population shifts for each orbit-to-subsequent-orbit of CRRES. Quiet time data, taken as DST > -30nT, is red. Stormtime data, taken as DST < -30nT, is blue.

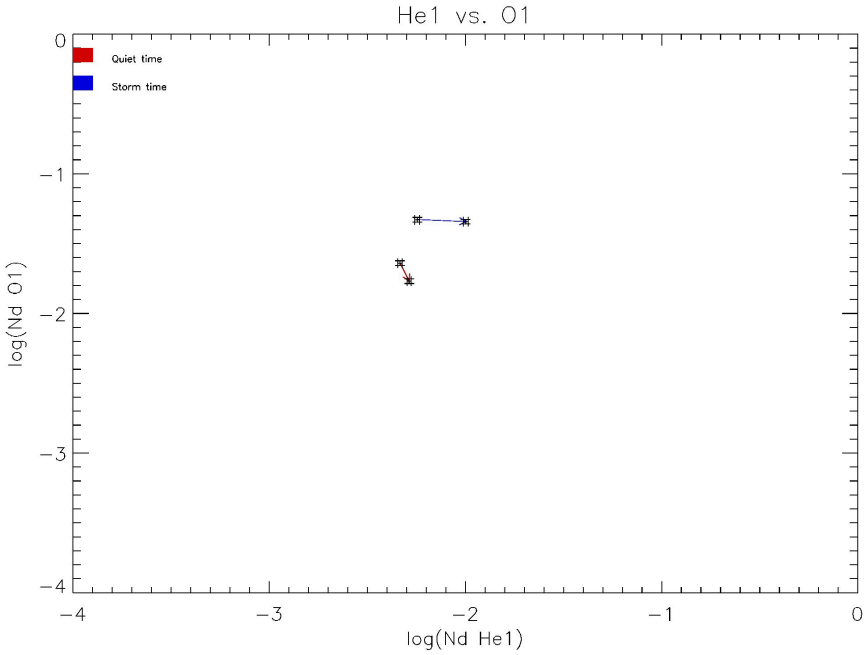

Figure A.3: Log vs. log plot of O^+ number density vs. He^+ number density, showing the overall average population shift across all subsequent-orbits of CRRES. Quiet time data, taken as DST > -30nT, is red. Stormtime data, taken as DST < -30nT, is blue.

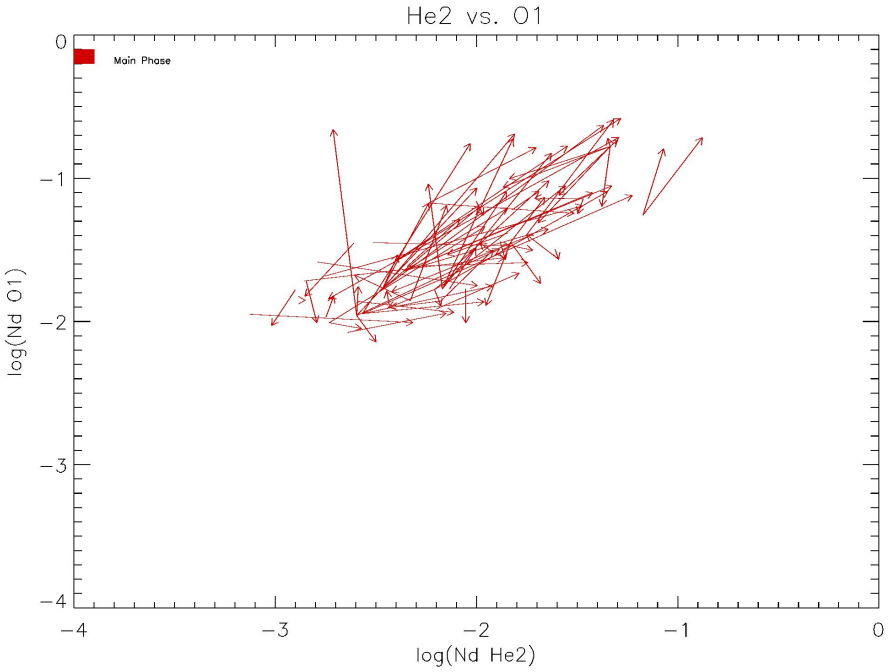

Figure A.4: Log vs. log plot of O^{+} number density vs. He^{++} number density, showing the average population shifts for each orbit-to-subsequent-orbit of CRRES across the main phase of geomagnetic storms.

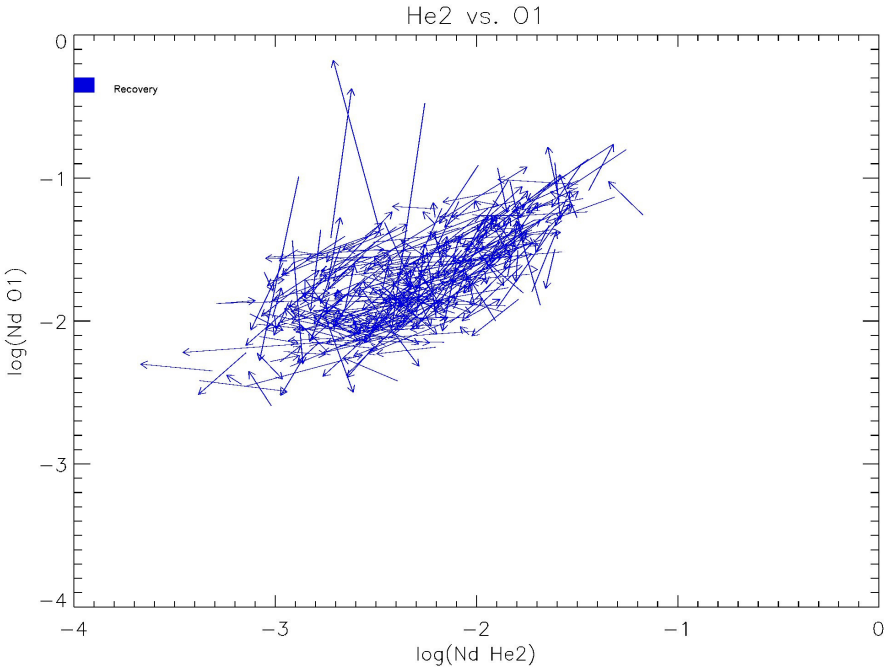

Figure A.5: Log vs. log plot of O^{+} number density vs. He^{++} number density, showing the average population shifts for each orbit-to-subsequent-orbit of CRRES across the recovery phase of geomagnetic storms.

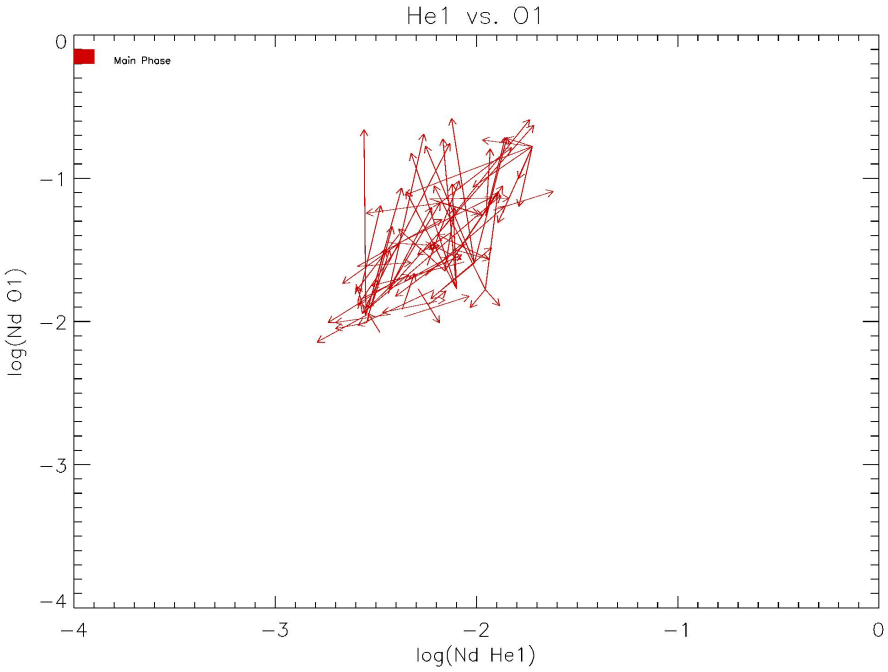

Figure A.6: Log vs. log plot of O^+ number density vs. He^+ number density, showing the average population shifts for each orbit-to-subsequent-orbit of CRRES across the main phase of geomagnetic storms.

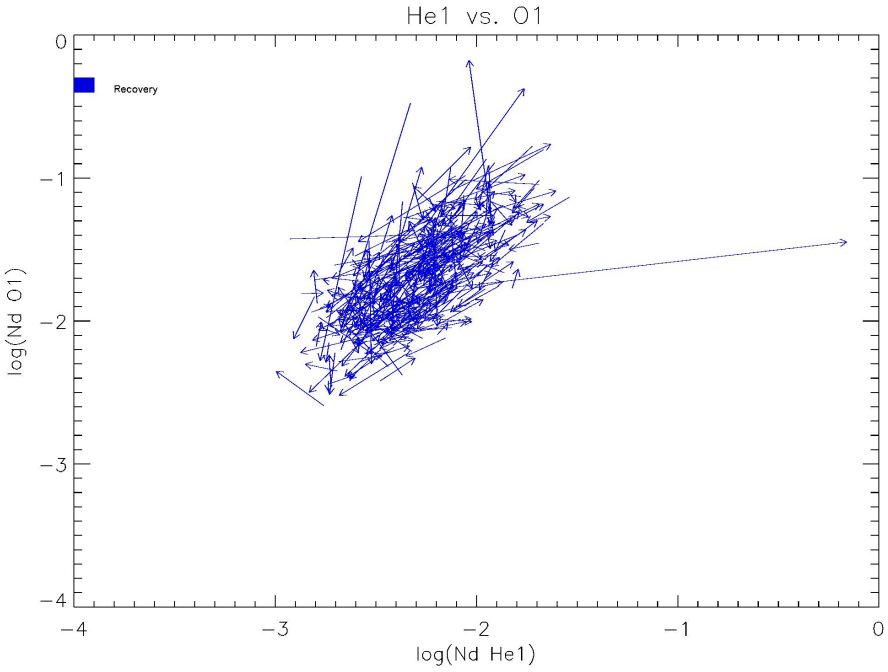

Figure A.7: Log vs. log plot of O^+ number density vs. He^+ number density, showing the average population shifts for each orbit-to-subsequent-orbit of CRRES across the recovery phase of geomagnetic storms.

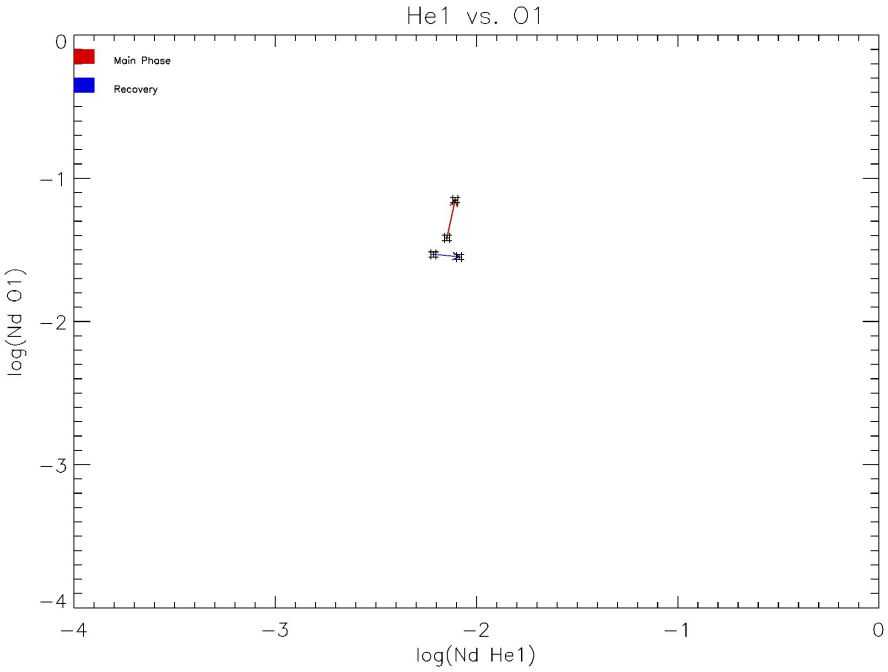

Figure A.8: Log vs. log plot of O^+ number density vs. He^+ number density, showing the overall average population shift across all subsequent-orbits of CRRES. Main Phase data is shown in red, recovery phase data in blue.

Appendix B: Cross Sections from Individual Orbits

In chapter 4, charge exchange cross sections for alpha particles reacting with neutral Hydrogen were calculated from five instances of injections followed by clear drift signatures. The Cross sections from each orbit not shown within the chapter itself are presented here.

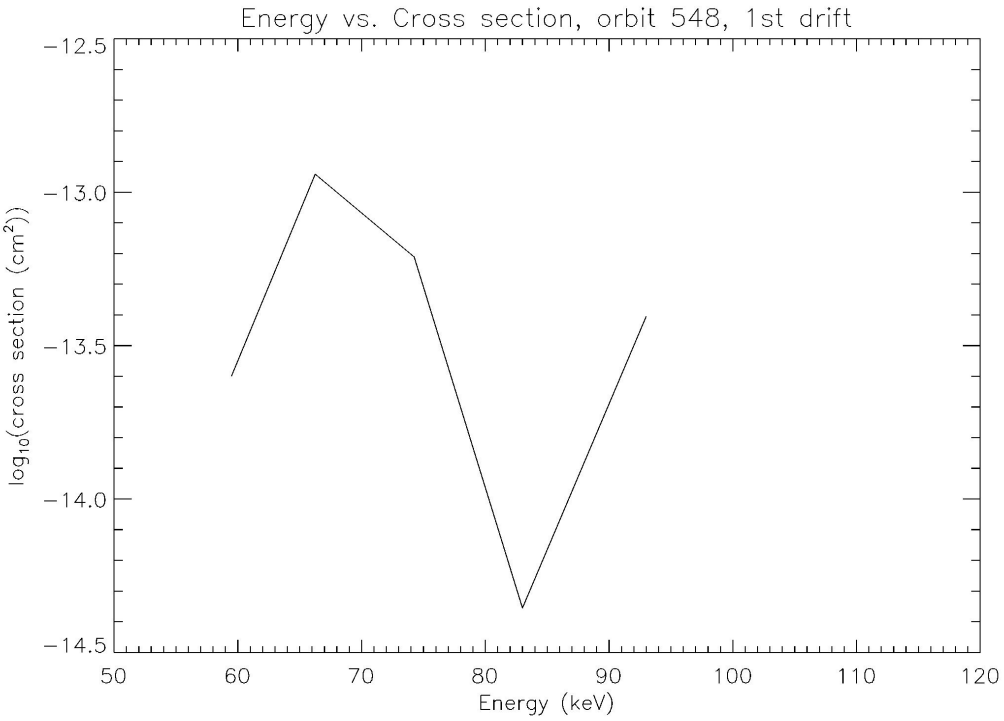

Figure B.1: Charge exchange cross section vs. energy from the injection and its first drift echo within orbit 548 of CRRES.

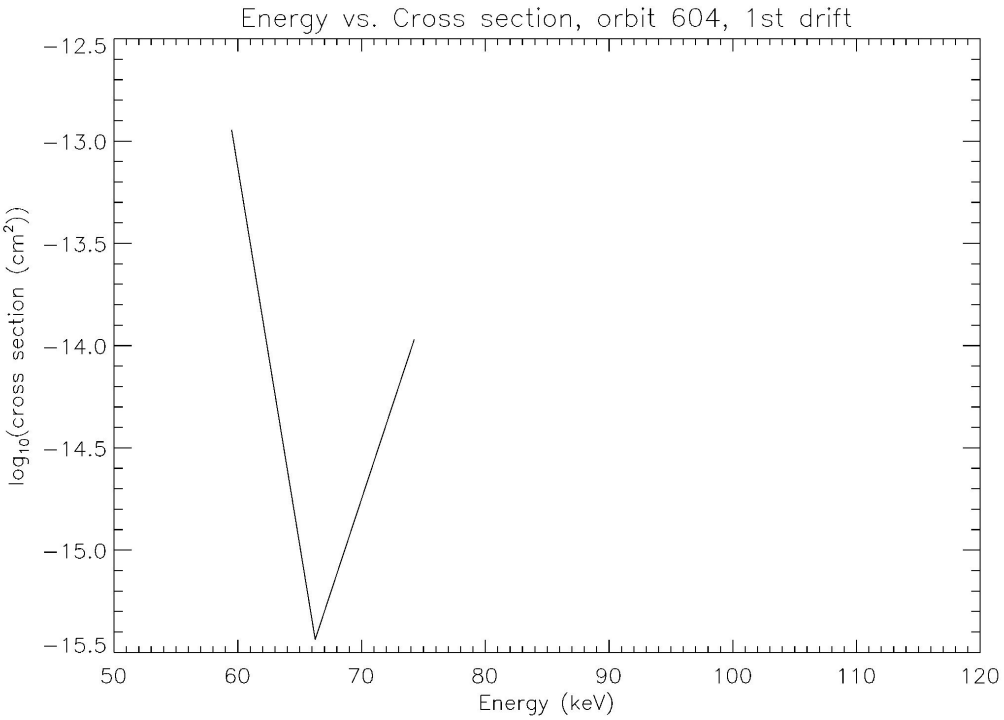

Figure B.2: Charge exchange cross section vs. energy from the injection and its first drift echo within orbit 604 of CRRES.

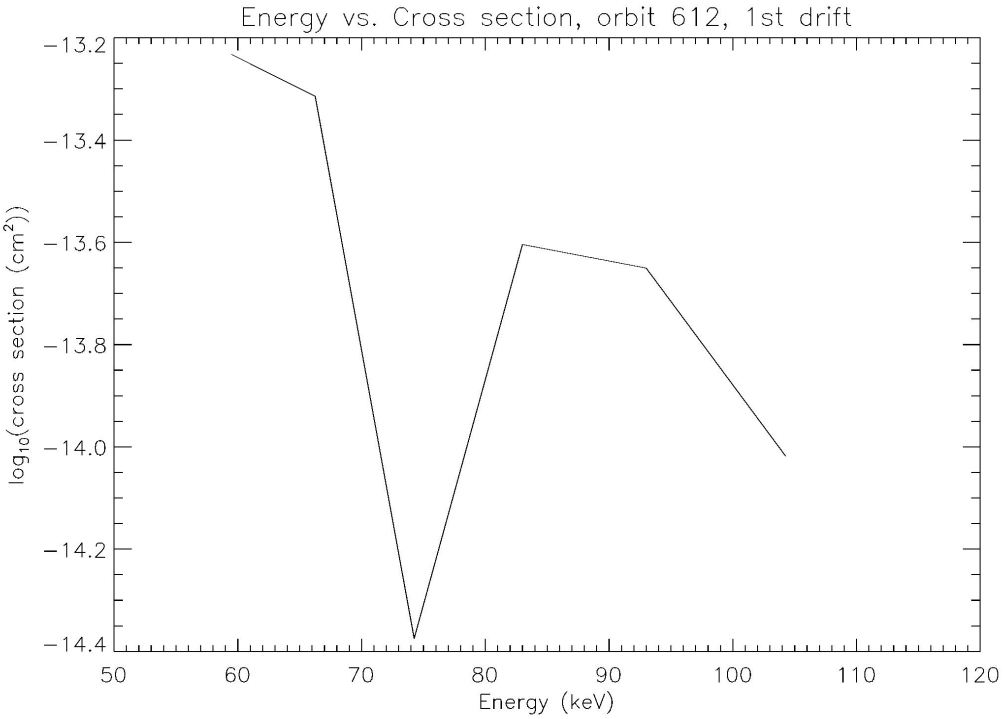

Figure B.3: Charge exchange cross section vs. energy from the injection and its first drift echo within orbit 612 of CRRES.

Appendix C: LANL injections during the Period 2000 - 2003

Chapter 5 contained a study of substorm and pseudobreakup injections within the period 2000–2003. Some of the data from the work are shown here.

Year	Month	Day	Hour (UT)	Minute (UT)	Median of max. energy range (keV)	i/o negative B_z
2000	1	22	19	40	270	1
2000	2	5	19	0	187.5	1
2000	2	12	11	30	407.5	0
2000	2	12	17	0	187.5	0
2000	3	1	10	30	187.5	1
2000	3	1	13	40	187.5	1
2000	3	1	15	20	187.5	1
2000	3	1	19	30	127.5	1
2000	3	30	14	39	62.5	1
2000	4	6	3	15	127.5	1
2000	4	6	16	42	270	1
2000	4	15	19	20	90	1
2000	4	15	20	10	187.5	1
2000	4	15	20	55	187.5	1
2000	4	24	11	55	127.5	1
2000	6	26	13	0	270	1
2000	6	26	20	15	270	1
2000	7	15	20	25	925	1
2000	7	15	22	40	925	1
2000	8	10	23	20	187.5	1
2000	9	12	13	10	407.5	1
2000	9	17	21	30	270	1
2000	10	4	6	50	407.5	1
2000	10	4	9	45	187.5	1
2000	10	4	14	15	925	1
2000	10	4	17	25	187.5	1
2000	10	4	21	45	407.5	1
2000	10	13	13	50	270	1
2000	10	13	17	50	187.5	1
2000	10	29	0	10	187.5	1
2000	10	29	3	13	187.5	1
2000	10	29	10	0	187.5	1
2000	11	6	14	0	270	1
2000	11	6	16	10	270	1
2000	11	7	2	25	270	1
2000	11	20	12	10	<50	1
2000	11	20	15	25	90	0

Table C.1: Stormtime electron injections during negative B_z periods, 2000 data.

Year	Month	Day	Hour (UT)	Minute (UT)	Median of max. energy range (keV)	i/o negative B_z
2001	1	24	11	30	187.5	1
2001	1	24	19	0	270	1
2001	2	13	22	0	407.5	1
2001	2	14	1	0	270	1
2001	2	14	3	35	187.5	1
2001	2	14	4	30	407.5	1
2001	3	4	13	5	187.5	0
2001	3	4	15	35	270	1
2001	3	4	17	20	407.5	1
2001	3	4	20	30	270	1
2001	3	5	1	15	270	1
2001	3	19	18	35	407.5	1
2001	3	19	19	5	407.5	1
2001	3	31	16	15	407.5	1
2001	3	31	18	5	925	1
2001	3	31	20	30	407.5	1
2001	4	22	10	25	<50	1
2001	4	22	13	30	187.5	1
2001	4	22	14	30	187.5	1
2001	4	22	17	35	270	1
2001	5	28	12	15	270	1
2001	5	28	16	20	187.5	1
2001	5	28	19	5	62.5	1
2001	5	28	19	50	127.5	1
2001	7	8	18	20	62.5	0
2001	7	8	21	50	127.5	1
2001	7	8	22	55	407.5	1
2001	7	9	2	25	187.5	1
2001	8	17	18	40	127.5	1
2001	8	17	19	25	187.5	1
2001	8	17	20	20	127.5	1
2001	9	23	16	10	407.5	0
2001	9	23	19	45	407.5	1
2001	10	22	11	25	925	1
2001	10	22	18	20	1300	1
2001	10	28	10	10	187.5	1

Table C.2: Stormtime electron injections during negative B_z periods, 2001 data.

Year	Month	Day	Hour (UT)	Minute (UT)	Median of max. energy range (keV)	i/o negative B_z
2002	2	2	6	10	127.5	1
2002	2	28	21	10	925	1
2002	3	1	2	40	187.5	1
2002	3	23	17	45	90	1
2002	3	23	22	55	270	1
2002	3	24	6	55	407.5	1
2002	4	17	3	15	62.5	1
2002	4	17	4	5	62.5	1
2002	4	17	7	30	62.5	1
2002	4	17	16	5	90	1
2002	4	17	20	45	90	1
2002	4	17	21	35	90	1
2002	4	17	22	25	90	1
2002	8	20	21	0	187.5	1
2002	9	4	3	10	90	1
2002	9	4	4	5	187.5	1
2002	10	1	13	15	270	1
2002	10	1	16	25	407.5	1

Table C.3: Stormtime electron injections during negative B_z periods, 2002 data

Year	Month	Day	Hour (UT)	Minute (UT)	Median of max. energy range (keV)	i/o negative B_z
2003	2	1	19	40	187.5	1
2003	2	2	7	40	187.5	1
2003	2	2	15	45	187.5	1
2003	4	20	3	30	187.5	1
2003	4	29	14	30	407.5	1
2003	6	16	11	20	90	1
2003	6	16	12	15	62.5	1
2003	6	16	21	35	187.5	1
2003	8	18	4	30	1300	1
2003	8	18	11	20	407.5	1
2003	8	18	16	30	925	1
2003	8	18	19	45	187.5	1
2003	11	20	21	10	407.5	1
2003	11	20	22	35	187.5	1

Table C.4: Stormtime electron injections during negative B_z periods, 2003 data

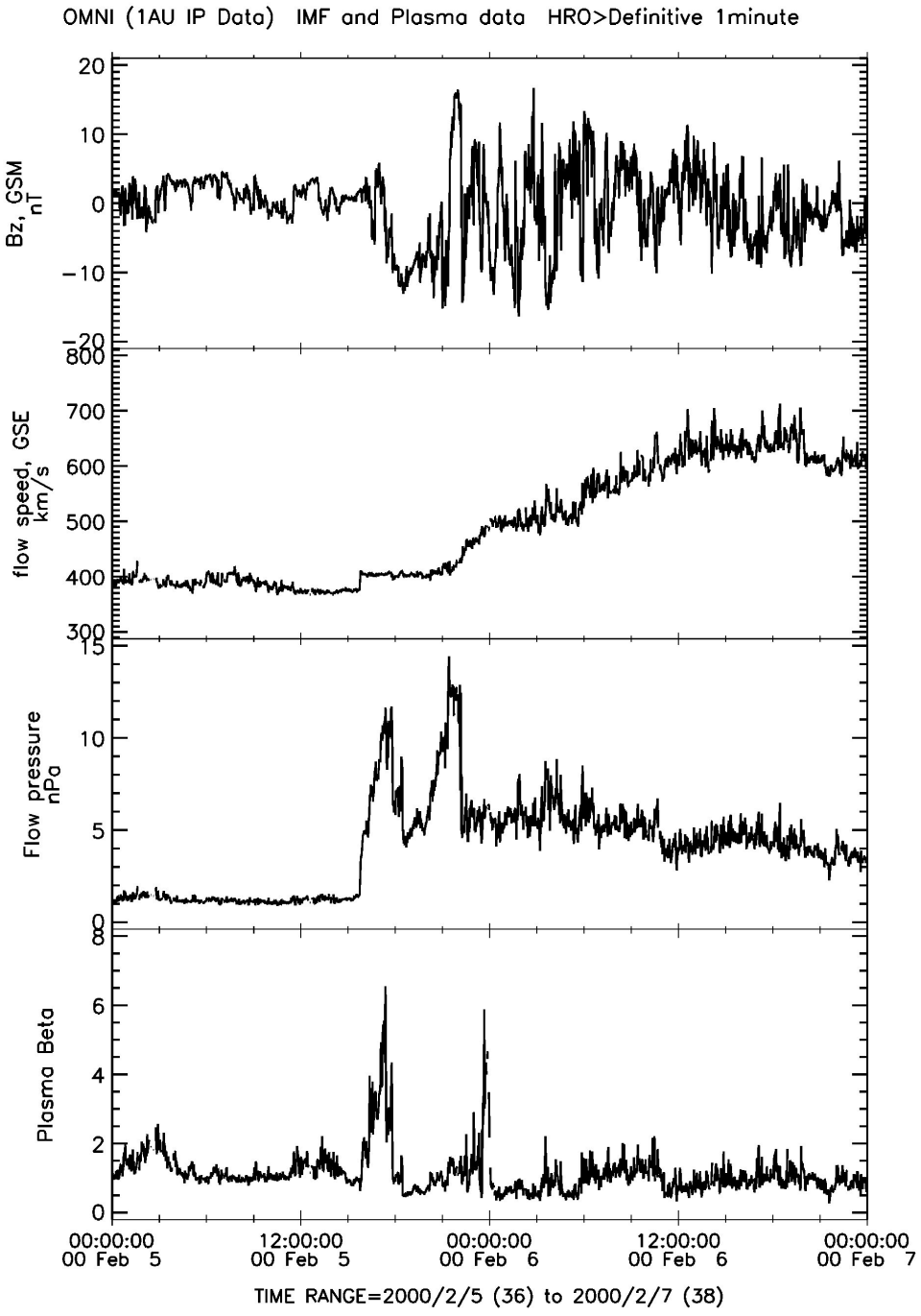

Figure C.1: Solar wind data from 5th – 6th February, 2000. A short duration of negative Bz is observed between ~17:00 UT and 20:00 UT on the 5th. OMNI data is from [King and Papitashvili, 2005].

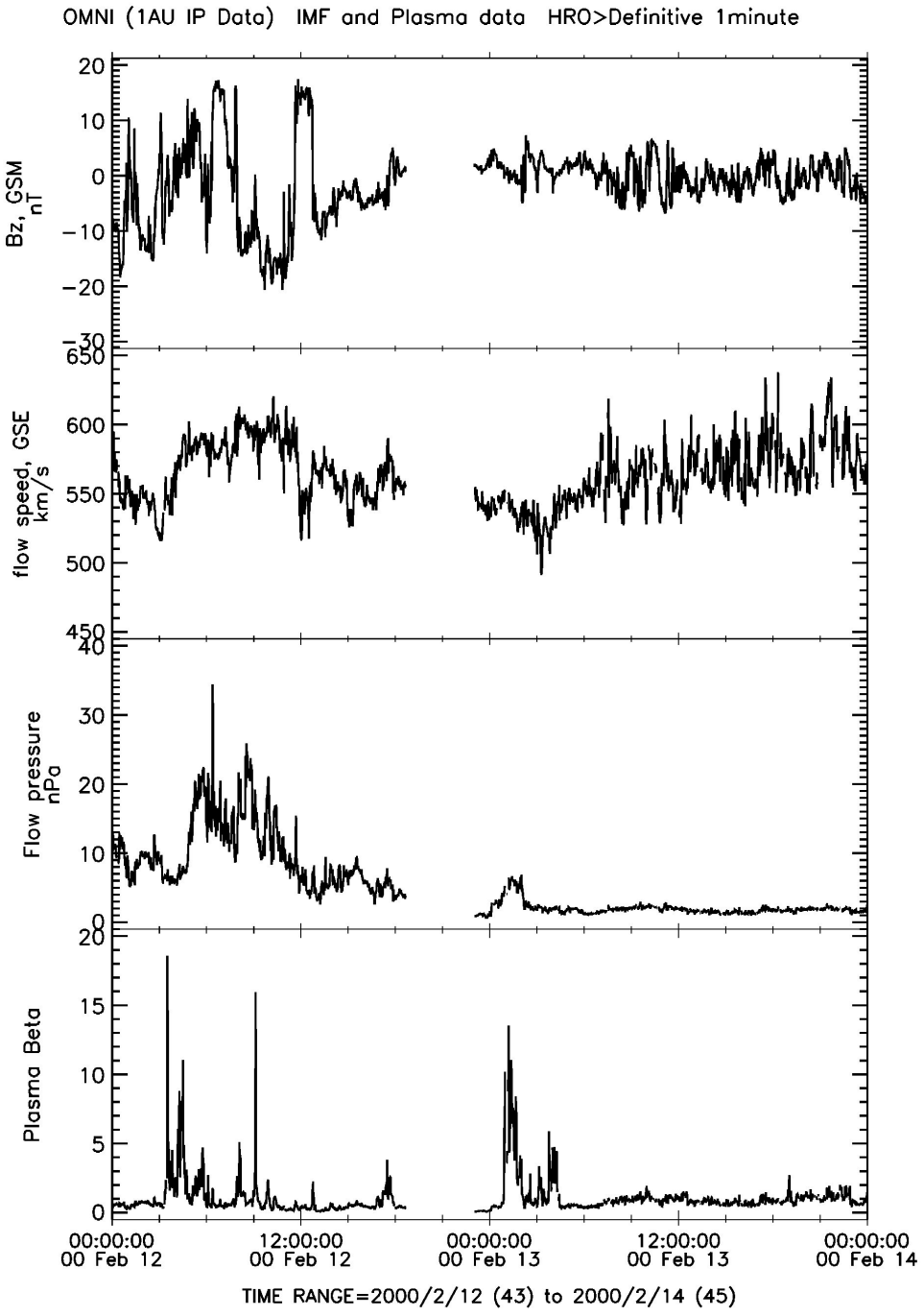

Figure C.2: Solar wind data from 12th – 13th February, 2000. A short duration of negative Bz is observed between ~06:00 UT and 11:00 UT on the 12th. OMNI data is from [King and Papitashvili, 2005].

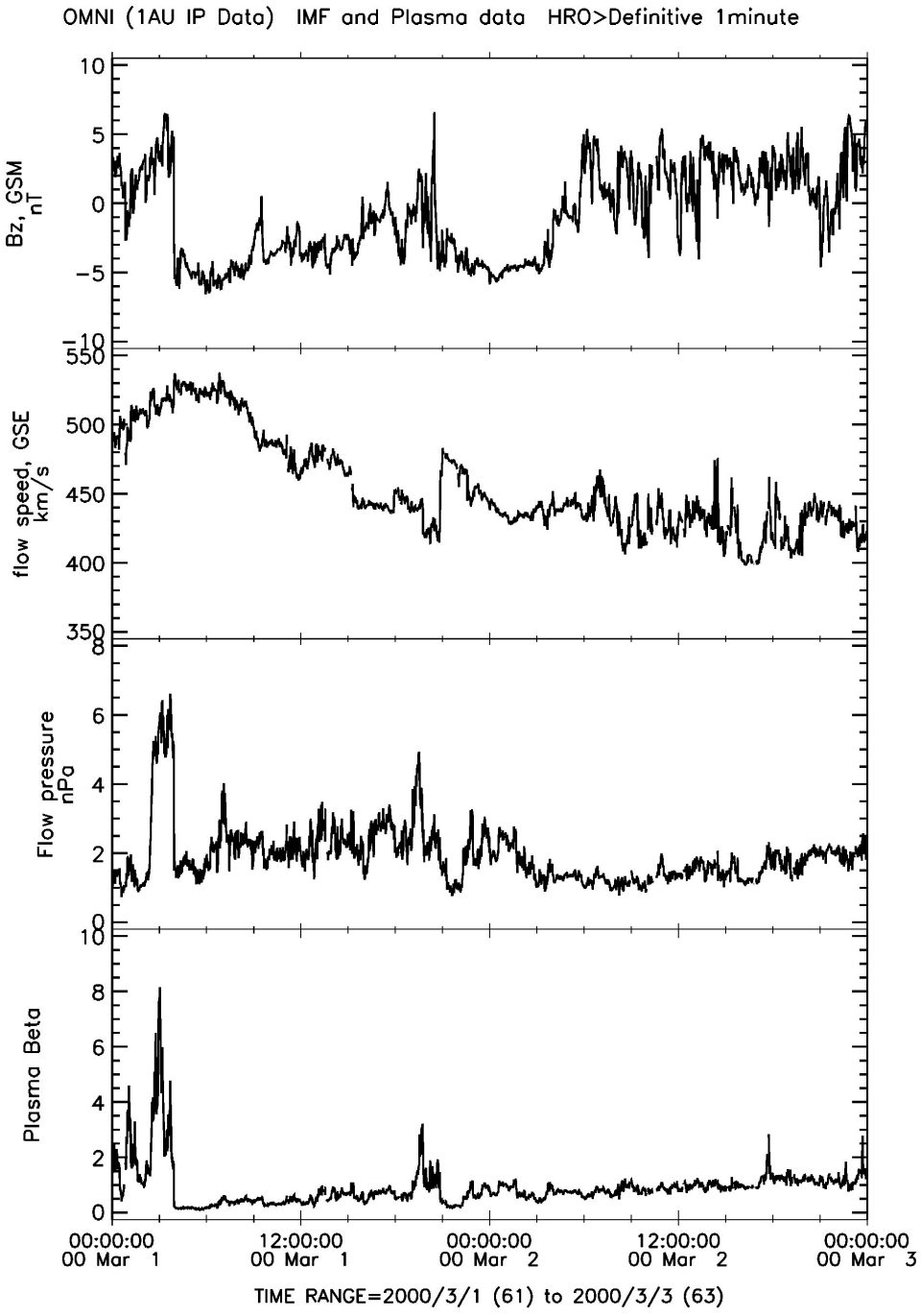

Figure C.3: Solar wind data from 1st – 2nd March, 2000. Bz is negative between ~04:00 UT and 18:00 UT on the 1st. OMNI data is from [King and Papitashvili, 2005].

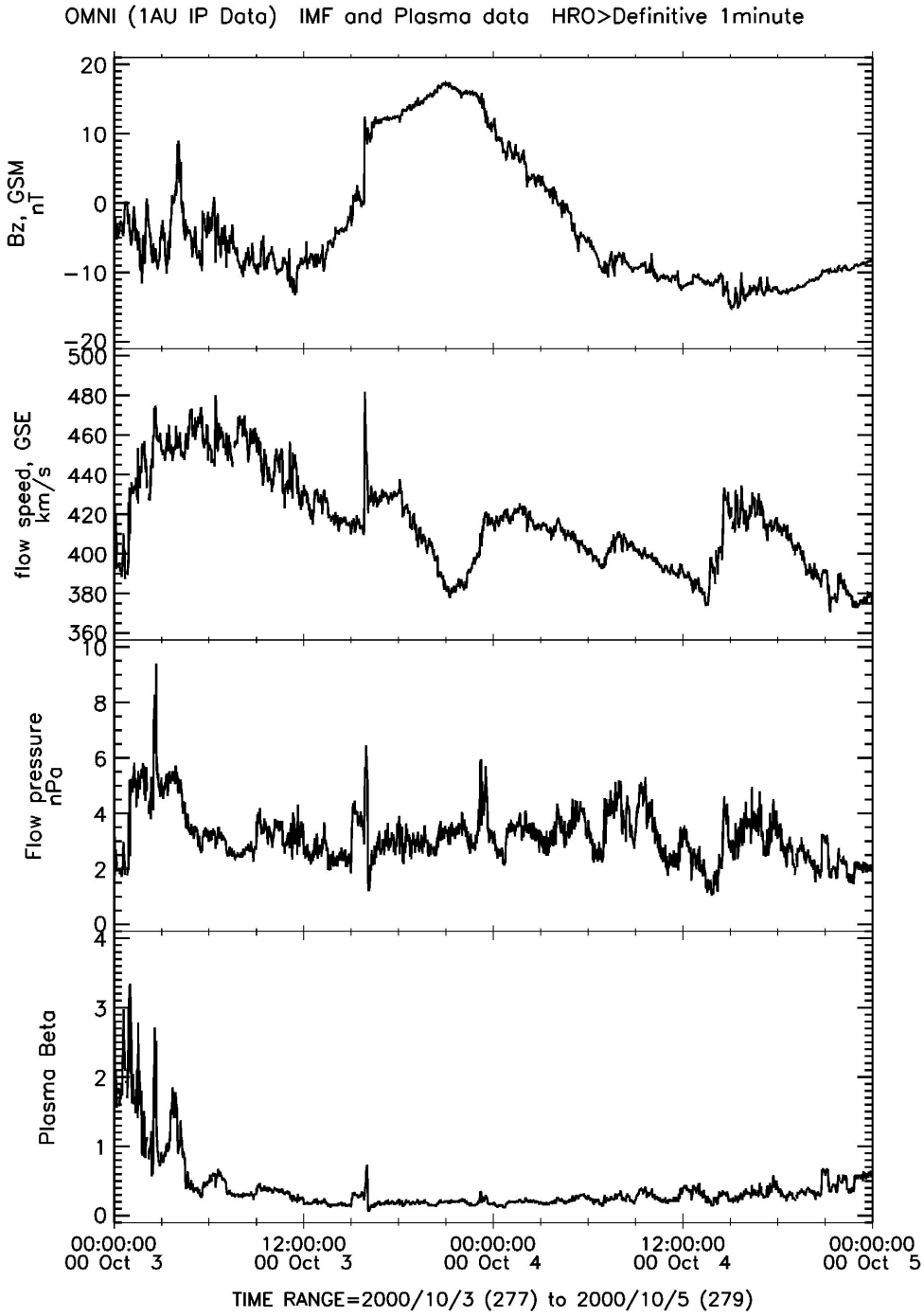

Figure C.4: Solar wind data from 3rd – 4th October, 2000. Bz is negative between ~06:00 UT on the 4th and 00:00 UT on the 5th. OMNI data is from [King and Papitashvili, 2005].

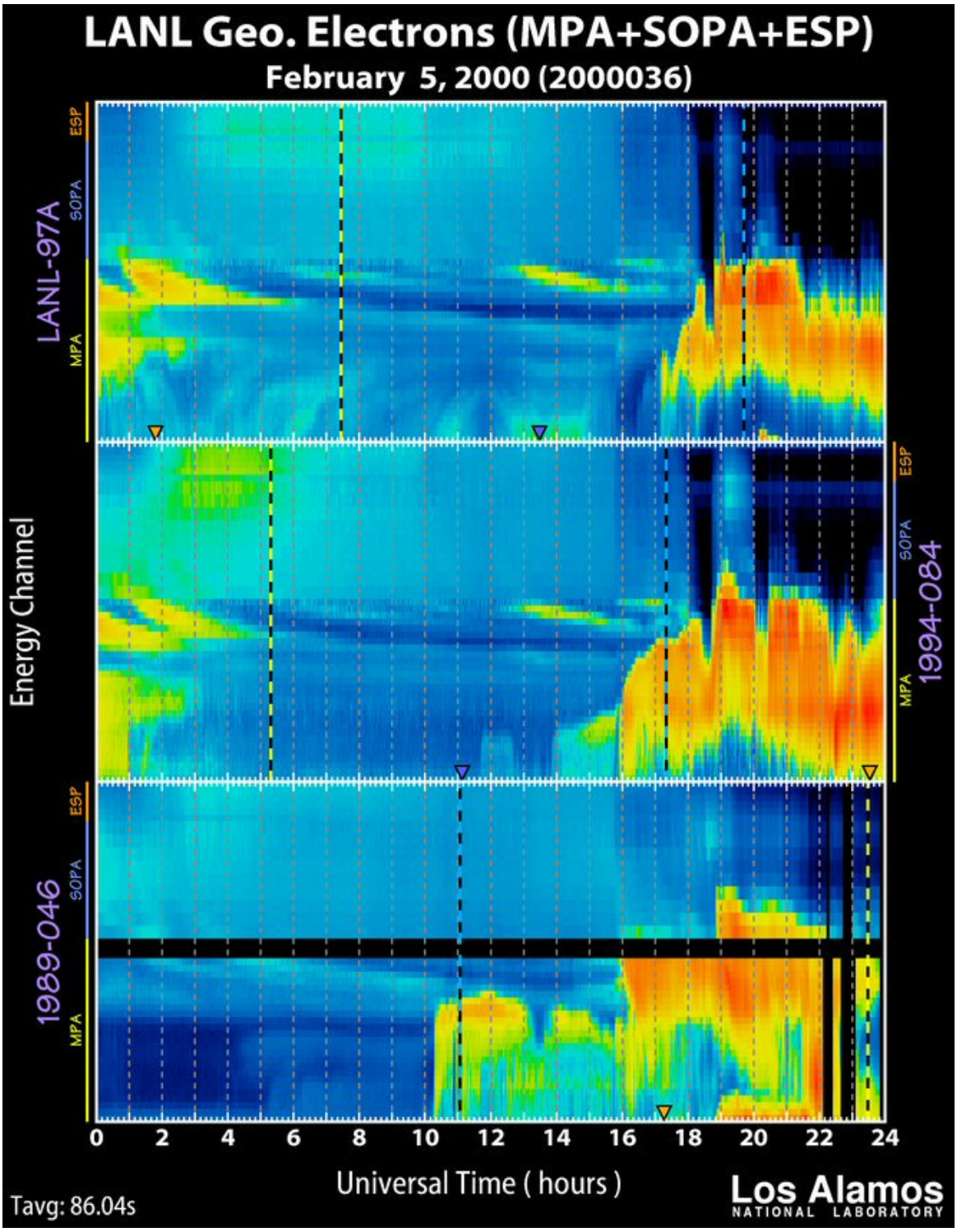

Figure C.5: LANL electron data from 5th February, 2000. Table C.1 details all injection signatures.

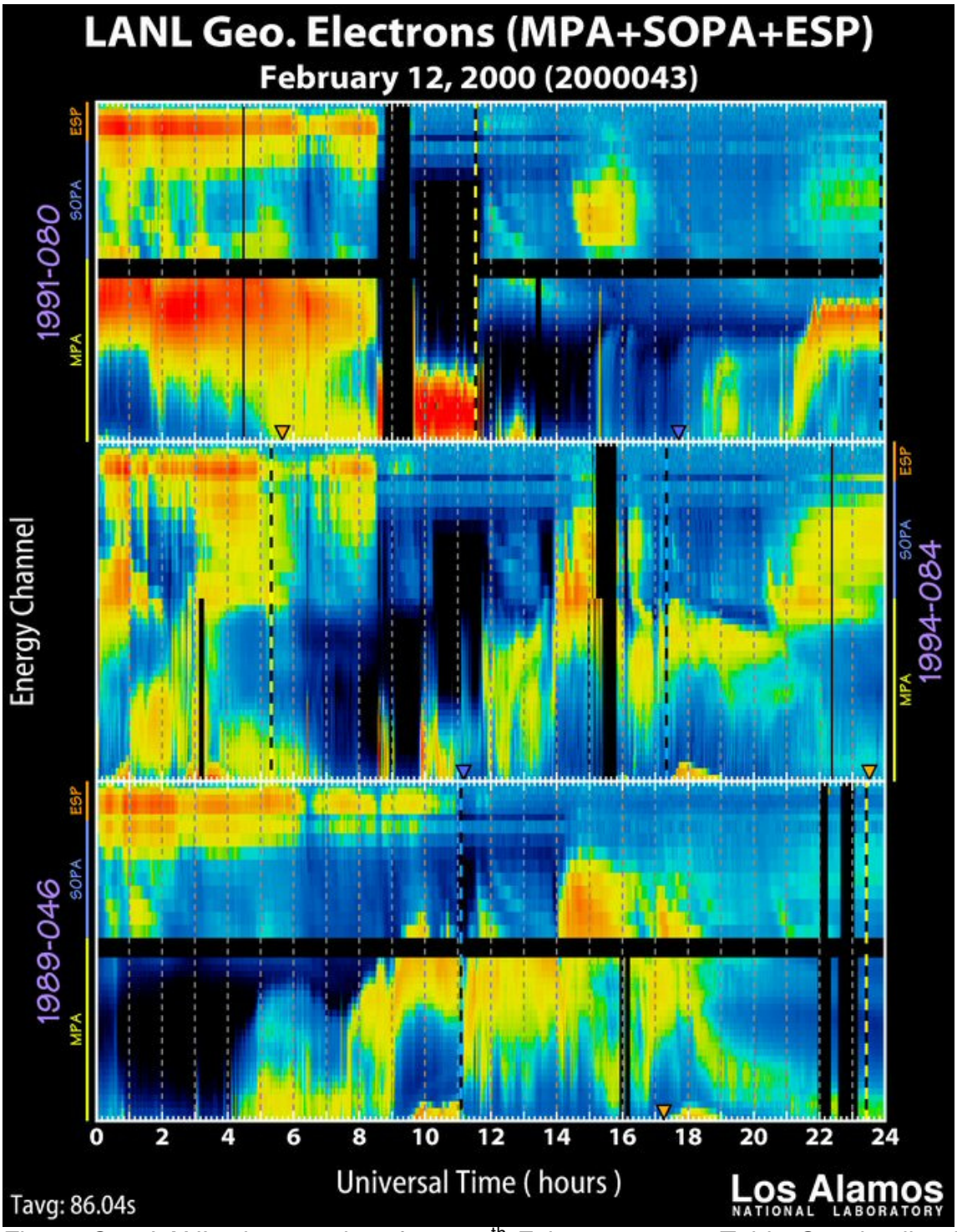

Figure C.6: LANL electron data from 12th February, 2000. Table C.1 details all injection signatures.

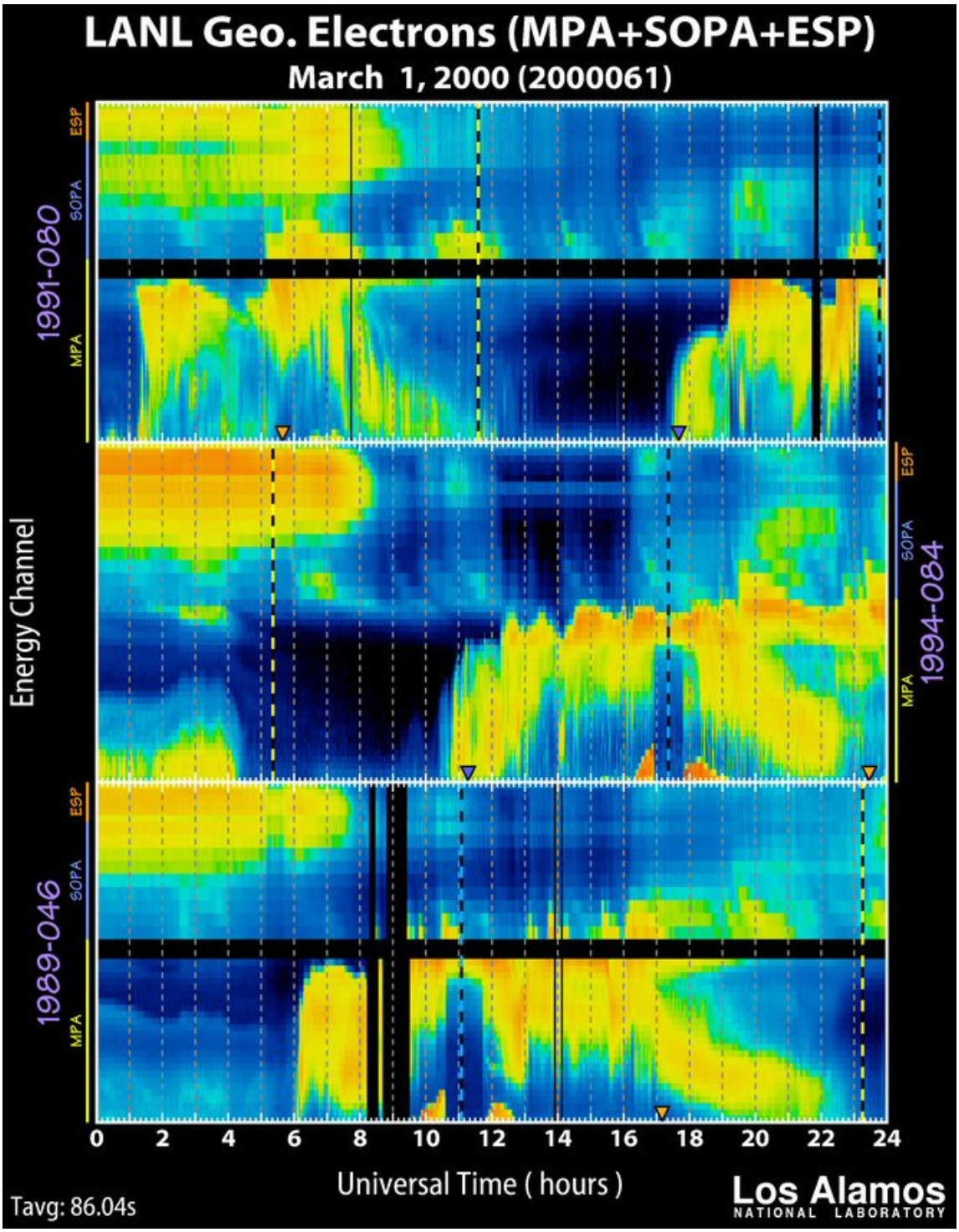

Figure C.7: LANL electron data from 1st March, 2000. Table C.1 details all injection signatures.

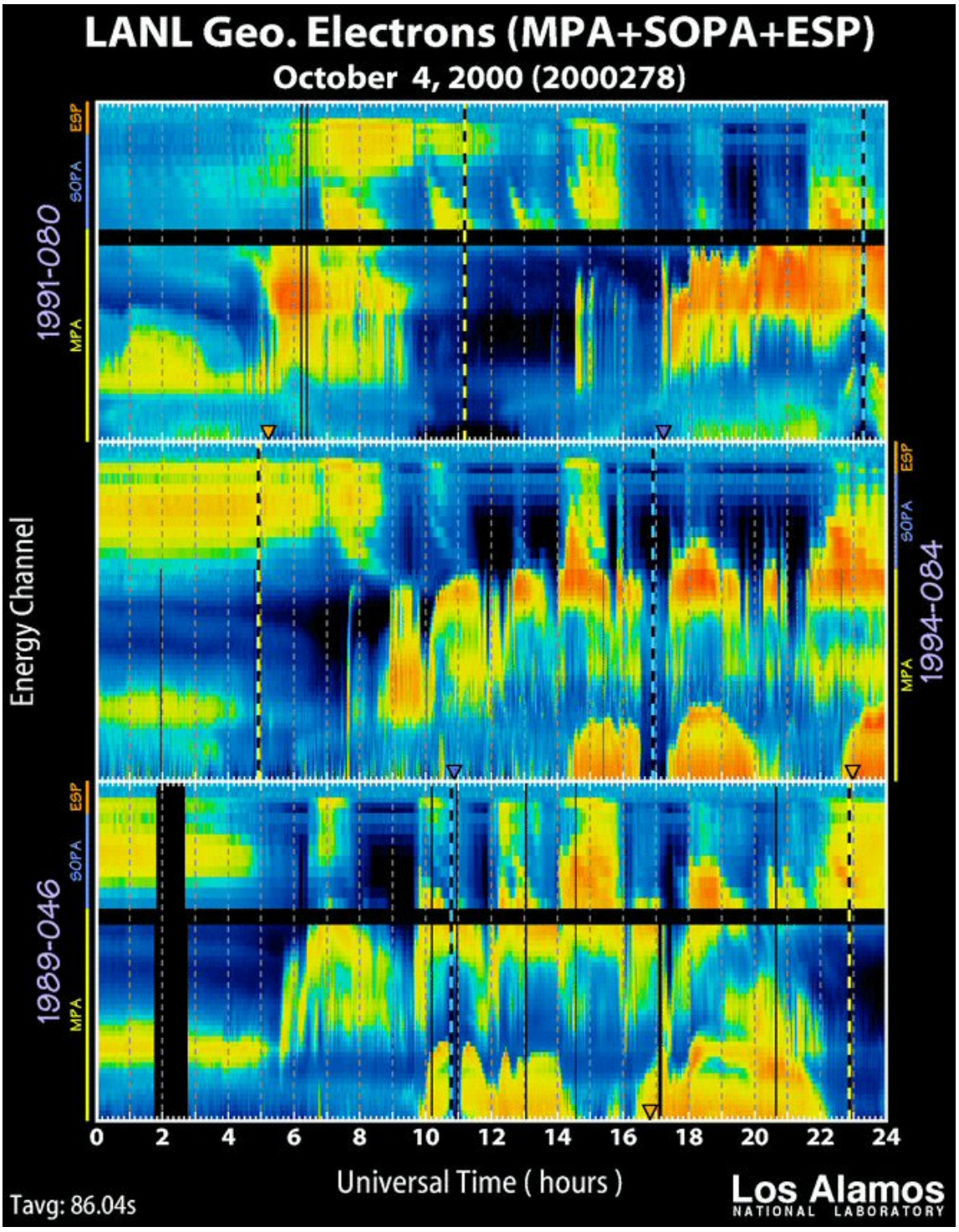

Figure C.8: LANL electron data from 4th October, 2000. Table C.1 details all injection signatures.

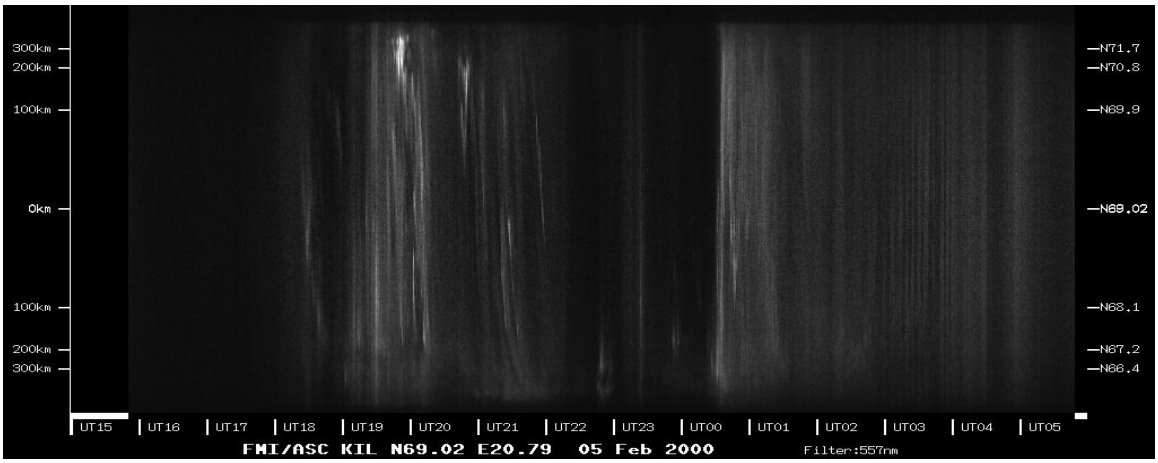

Figure C.9: All-Sky Keogram for 5th February, 2000, from Kilpisjarvi. A brightening and expansion is observed at ~19:00 UT.

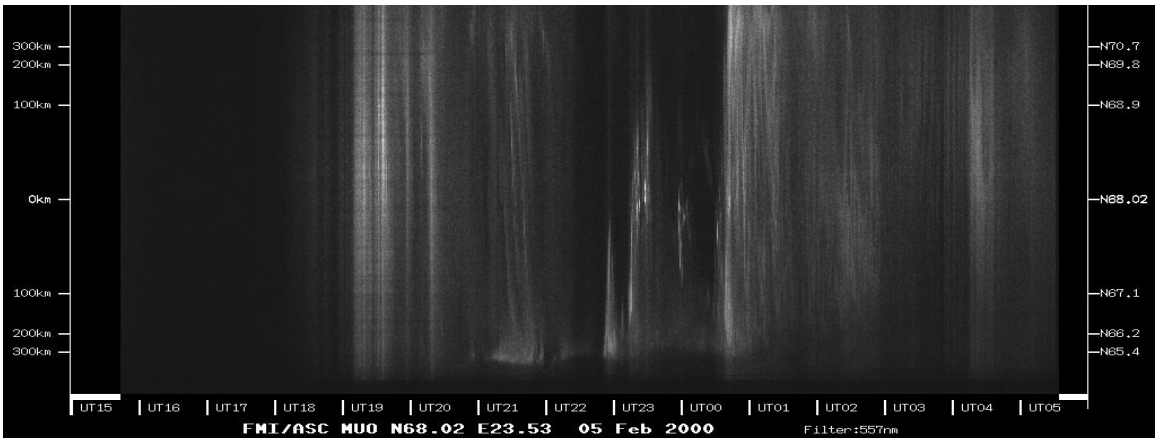

Figure C.10: All-Sky Keogram for 5th February, 2000, from Muonio. A brightening and expansion is observed at ~19:00 UT.

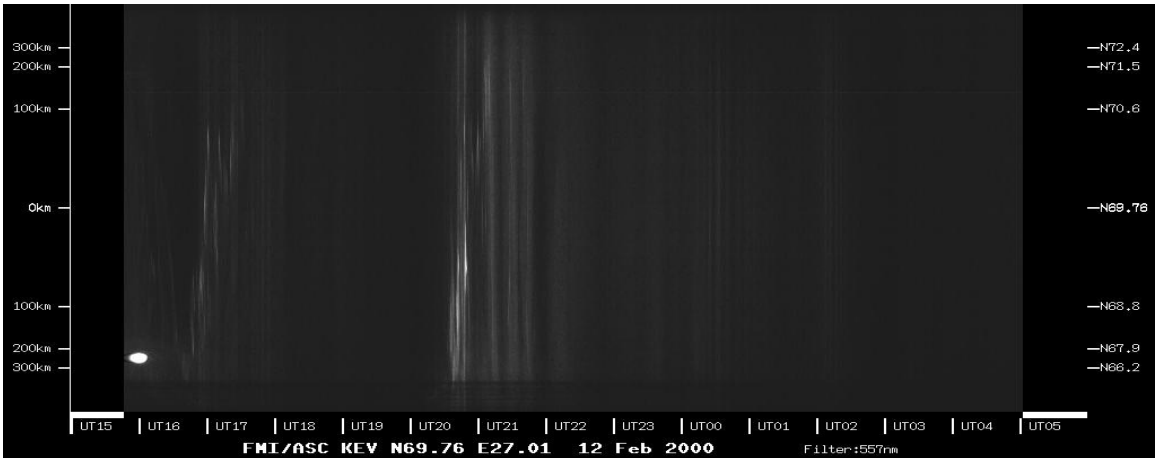

Figure C.11: All-Sky Keogram for 12th February, 2000, from Kevo. Brightenings with expansions are observed at ~17:00 UT and 20:40 UT.

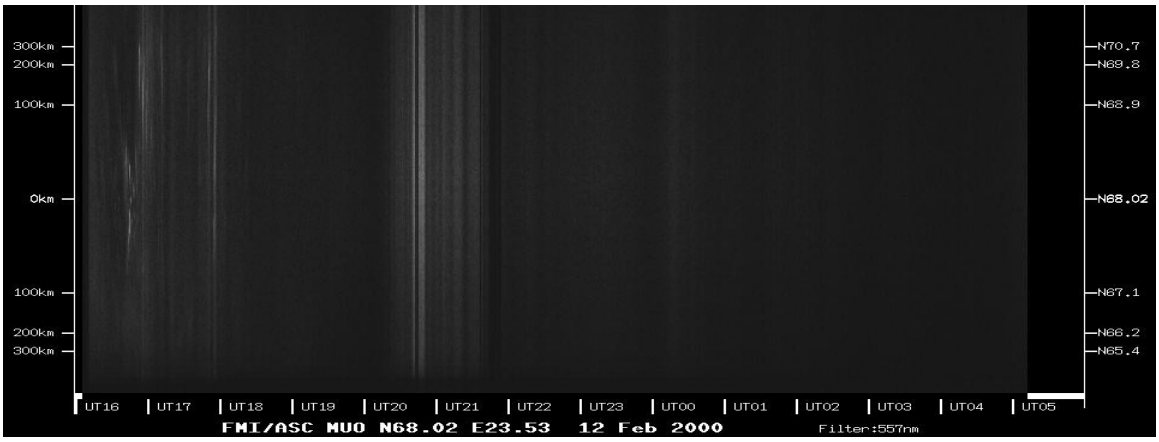

Figure C.12: All-Sky Keogram for 12th February, 2000, from Muonio. Brightenings with expansions are observed at ~17:00 UT and 20:40 UT.

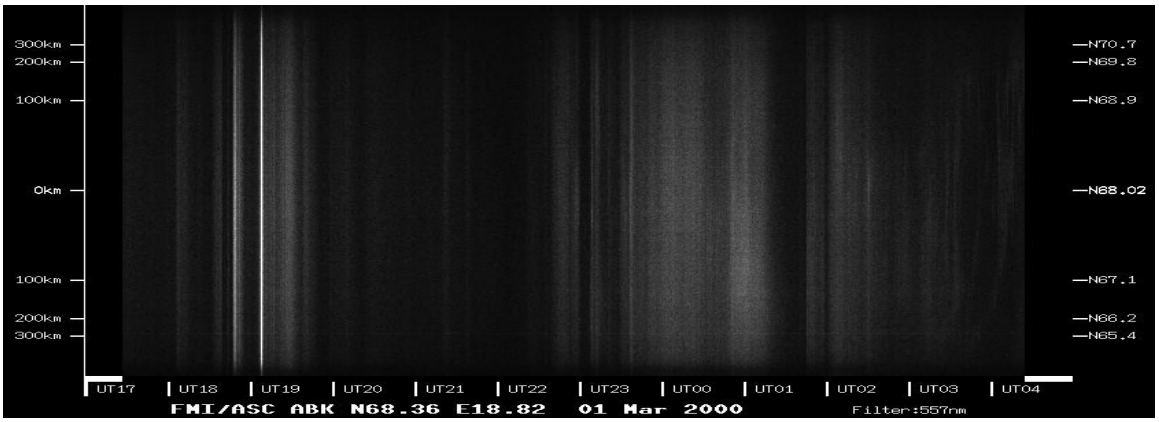

Figure C.13: All-Sky Keogram for 1st March, 2000, from Abisko. Multiple expansions are observed.

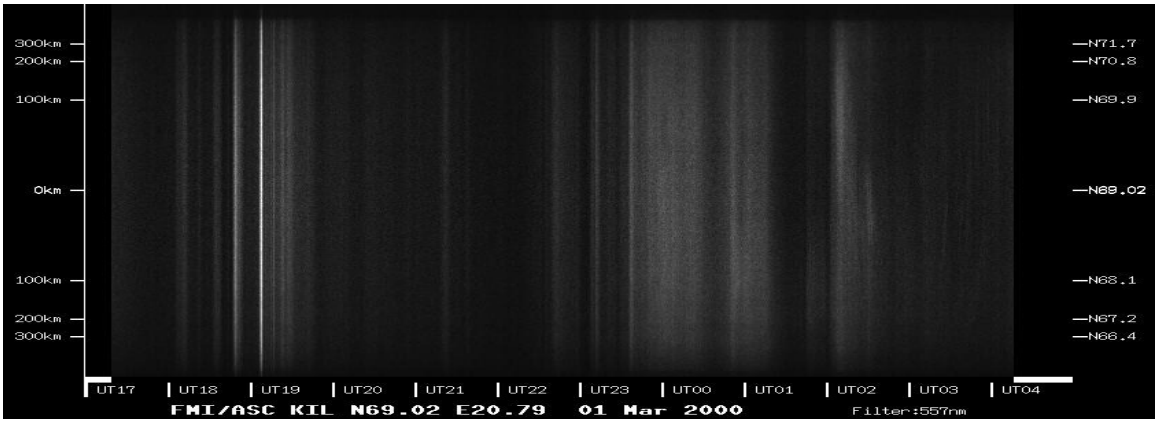

Figure C.14: All-Sky Keogram for 1st March, 2000, from Kilpisjarvi. Multiple expansions are observed.

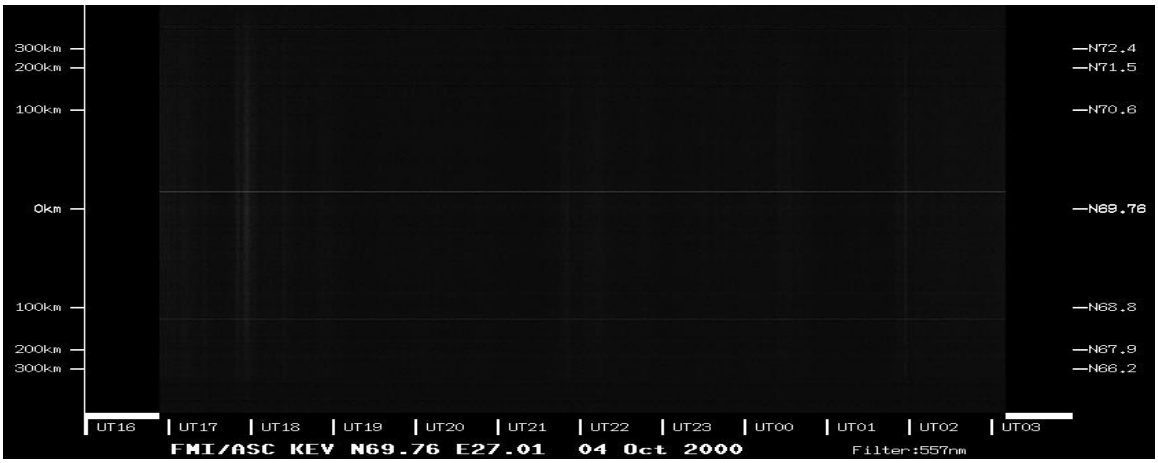

Figure C.15: All-Sky Keogram for 4th October, 2000, from Kevo. Very little is observed around 15:30. The injection which occurs was attributed to a growth phase pseudobreakup for the slight expansion which occurs at ~18:00.